



The dynamic organization of the neuronal postsynaptic membrane

Manon Westra

The dynamic organization of the neuronal postsynaptic membrane

Manon Westra

2023

The dynamic organization of the neuronal postsynaptic membrane

Manon Westra

ISBN: 978-94-6483-216-7

DOI: 10.33540/1831

The studies described in this thesis were performed at the division of Cell Biology, Neurobiology and Biophysics at the Faculty of Science of Utrecht University in Utrecht, The Netherlands

Cover design: Manon Westra

Layout: Manon Westra

Printed by Ridderprint

Copyright © 2023 by Manon Westra

All rights reserved

The dynamic organization of the neuronal postsynaptic membrane

De dynamische organisatie van het neuronale postsynaptische membraan

(met een samenvatting in het Nederlands)

Proefschrift

ter verkrijging van de graad van doctor aan de
Universiteit Utrecht
op gezag van de
rector magnificus, prof.dr. H.R.B.M. Kummeling,
ingevolge het besluit van het college voor promoties
in het openbaar te verdedigen op

woensdag 6 september 2023 des middags te 2.15 uur

door

Manon Westra

geboren op 10 februari 1994
te Amstelveen

Promotor:

Prof. dr. L.C. Kapitein

Copromotor:

Dr. H.D. MacGillavry

Beoordelingscommissie:

Prof. dr. A.S. Akhmanova

Prof. dr. E.M. Hol

Prof. dr. H.W.H.G. Kessels

Prof. dr. M.M. Maurice

Prof. dr. B.M. Mulder



Contents

I	General introduction	7
2	Contribution of membrane lipids to postsynaptic protein organization	19
3	Single-molecule localization microscopy of subcellular protein distribution in neurons	41
4	Precise detection and visualization of nanoscale temporal confinement in single-molecule tracking analysis	59
5	Resolving the dynamic subsynaptic distribution of GluA1- and GluA3-containing AMPA receptors	89
6	mGluR5 is transiently confined in perisynaptic nanodomains to shape synaptic function	113
7	Methods to study the dynamic lipid organization in the postsynaptic membrane	153
8	General discussion	173
&	Addendum	185
	<i>Nederlandse samenvatting</i>	
	<i>Curriculum vitae</i>	
	<i>List of publications</i>	
	<i>Dankwoord</i>	

The image features a large, white, serif capital letter 'I' centered on a background of marbled paper. The marbling consists of intricate, organic patterns in shades of light blue, dark blue, and black, creating a complex, textured appearance. The letter 'I' is simple and bold, standing out prominently against the busy, multi-colored background.

I



General introduction

Manon Westra

The brain is a fascinating organ consisting of approximately 86 billion neurons forming a complex network (Azevedo et al., 2009). The point at which two neurons interact is called the synapse, with each neuron potentially having hundreds to thousands of these points of contact. To transfer signals from a presynaptic neuron to a postsynaptic neuron, neurotransmitters are released from the presynaptic site into the synaptic cleft where they subsequently bind to their corresponding receptors on the postsynaptic site. A variety of factors play a role in this process of synaptic transmission, however, this thesis will focus on the organization of the postsynaptic membrane of excitatory synapses, which is fundamental to efficient neuronal signaling. In particular, the dynamic behavior of individual membrane components collectively contributes to the efficient transfer of signals across the synapse. The synaptic membrane contains transmembrane neurotransmitter receptors and synaptic protein complexes that are embedded in a heterogeneous mixture of lipids. However, we know little about the subsynaptic organization of individual glutamate receptor subtypes and the dynamics of synaptic lipids and their contribution to synaptic transmission. This thesis aims to contribute to the understanding of the relationship between postsynaptic membrane organization and neuronal functioning. The remainder of this introduction covers an overview of the key concepts that are the basis of the research presented in this thesis.

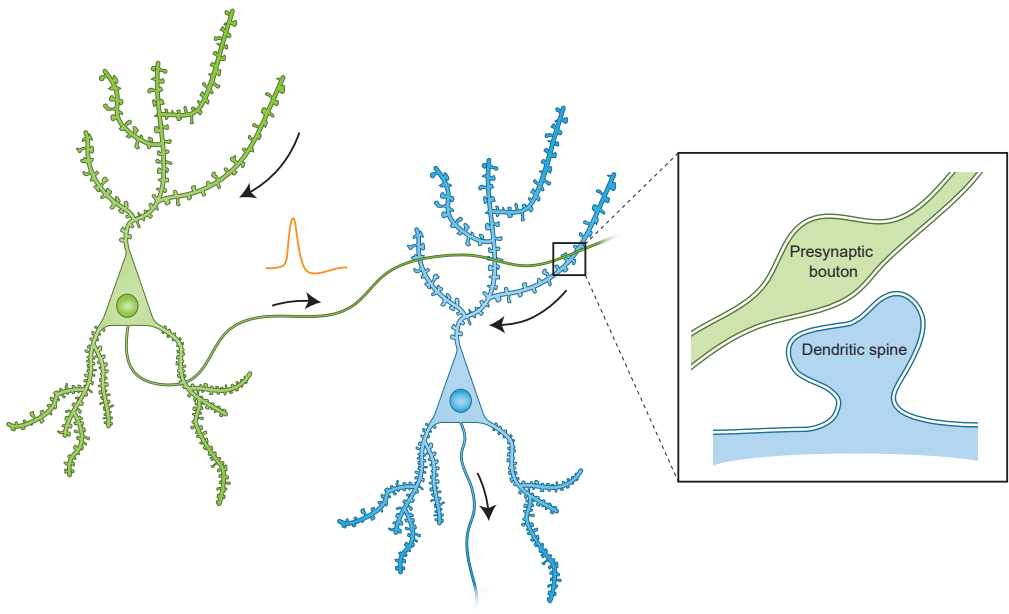


Figure 1. Excitatory synaptic transmission

The axon is a long, thin structure that transmits signals in the form of action potentials (orange) from the sending neuron (green) to the synapse, shown in the zoom. At the synapse, neurotransmitters are released from the presynaptic bouton and bind to receptors located in the dendritic spine of the receiving neuron (blue). Synaptic signals are integrated in the soma, and finally, determine whether an action potential is generated to transmit the signal to connecting neurons via the axon.

Synaptic transmission

Neurons have specialized projections called axons and dendrites (Figure 1). The axon is a long, thin structure in which at the initial segment action potentials are generated, which travel down the axon. The axon thus sends the message, while dendrites receive synaptic inputs from other axons. The sum of all the incoming inputs, either excitatory or inhibitory, determines whether the neuron fires an action potential. Synapses are the sites where the signal is transmitted from axon to dendrite. The presynaptic bouton contains synaptic vesicles filled with neurotransmitters such as glutamate. Upon the arrival of an action potential at the bouton, voltage-gated calcium channels open and the influx of calcium promotes the fusion of synaptic vesicles with the membrane. Glutamate released from the vesicles into the synaptic cleft binds glutamate receptors that are localized at the postsynaptic membrane on protrusions of the receiving dendrite called spines. This activation of glutamate receptors results in depolarization of the postsynaptic membrane. Synaptic signals from the different dendrites are integrated at the soma. If the summed depolarization, from either multiple inputs or repeated inputs, reaches the threshold potential, this will elicit an action potential at the axon initial segment of the receiving neuron.

Glutamate receptors

A wide variety of neurotransmitter receptors exists that can be broadly divided into two groups: ionotropic receptors and metabotropic receptors. The ionotropic receptors consist of a membrane-spanning domain that forms an ion channel. Binding of neurotransmitters to these receptors results in a fast postsynaptic response because the channel will open and allow the passage of specific ions. On the other hand, metabotropic receptors are not ion channels, but their activation results in downstream signaling pathways that modulate postsynaptic responses on a longer timescale. The glutamate receptors at the postsynaptic membrane are the ionotropic glutamate receptors: AMPA-, NMDA-, and kainate receptors, and the group I metabotropic glutamate receptors (mGluRs). Most synapses in the brain possess both AMPARs and NMDARs. AMPARs are the primary mediators of fast excitatory transmission in the brain, whereas NMDARs are primarily responsible for initiating long-term plasticity processes such as long-term potentiation (LTP) and depression (LTD).

AMPA receptors

AMPARs are synthesized in the endoplasmic reticulum and composed of four subunits forming a tetrameric complex. There are four different subunits, GluA1–4, of which GluA4 is mainly expressed during development and only sparsely at later stages (Zhu et al., 2000; Lohmann and Kessels, 2014; Henley and Wilkinson, 2016). The different subunits are highly similar in their ligand binding domain and transmembrane region but differ in their extracellular N-terminal domain and cytoplasmic C-terminal tail. The cytoplasmic tail of AMPAR subunits can be modified by a variety of posttranslational modifications, like phosphorylation and palmitoylation. Phosphorylation of specific sites on a subunit can regulate the conductance and open probability of the AMPAR (Derkach et al., 1999; Banke et al., 2000). In addition, the N-terminal domain was found to play a crucial role in the synaptic targeting of AMPARs in a subunit-specific manner (Díaz-Alonso et al., 2017; Watson et al., 2017).

In the hippocampus, the brain area of focus in this thesis, the most prevalent subunit combinations are GluA1/2 and GluA2/3 with a small proportion of GluA1 homomers (Wenthold

et al., 1996; Mansour et al., 2001; Kessels et al., 2009; Lu et al., 2009). The AMPAR subunit composition has important implications for its ion channel function. GluA2-lacking receptors, like the GluA1 homomers, are calcium permeable, whereas most GluA2-containing receptors are calcium impermeable (Hollmann et al., 1991; Hume et al., 1991; Isaac et al., 2007). Furthermore, the function of AMPARs is modulated by their auxiliary subunits, of which the transmembrane AMPAR regulatory proteins (TARPs) and cornichon homologs (CNIHs) are the most prevalent in the hippocampus (Schwenk et al., 2014). Thus, the combination of subunit-specific posttranslational modifications, their formation into heterotetramers, and binding to auxiliary subunits leads to multiple types of AMPARs, with their own specific channel properties.

Metabotropic glutamate receptors

The metabotropic glutamate receptors are G-protein coupled receptors (GPCRs) that bind glutamate with their large N-terminal extracellular domain and trigger a variety of signaling pathways that modulate synaptic transmission and plasticity. The group I mGluRs, mGluR1 and mGluR5, are primarily found at postsynaptic sites. mGluRs form dimers to become functional receptors. Group I mGluRs are mainly coupled to the activation of phospholipase C (PLC) via Gq. PLC hydrolyzes phosphoinositide phospholipids in the plasma membrane, leading to the formation of IP₃ and diacylglycerol (DAG). This pathway results in release of Ca²⁺ from intracellular stores and the activation of protein kinase C (PKC). Group I mGluRs can also trigger additional signaling pathways like mitogen-activated protein kinase (MAPK) and mammalian target of rapamycin (mTOR) signaling pathways (Niswender and Conn, 2010). The activation of these downstream signaling pathways can thus have longer-lasting physiological effects than activation of ionotropic receptors.

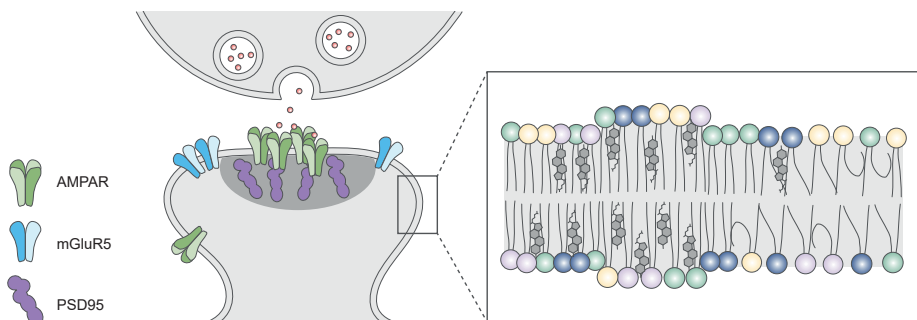


Figure 2. Synapse organization

Glutamate is released from synaptic vesicles in the presynaptic bouton. The neurotransmitters bind to glutamate receptors on the dendritic spine. AMPARs are concentrated in the PSD and anchored by PSD95, the PSD's core protein. mGluR5 resides in the perisynaptic area surrounding the PSD. The glutamate receptors are embedded in a membrane composed of a diverse population of lipid types that differ in their head group, tail length, and saturation levels.

Importance of receptor dynamics for synaptic plasticity

The localization of glutamate receptors is often depicted as extremely static, where each receptor is bound to its own specific location. However, glutamate receptors are highly dynamic. These dynamics are important in the brain for concepts like learning and memory that are mediated by synaptic plasticity. The general idea behind synaptic plasticity is that synapses with more activity become stronger, whereas the less active synapses become weaker. We call these processes long-term potentiation (LTP) and long-term depression (LTD). It is called long-term because these particular activities can have effects on synapses that last for hours. During LTP, repetitive activation of AMPARs relieves the NMDAR blockade by Mg^{2+} to allow Ca^{2+} entry into the postsynaptic neuron, inducing signaling cascades resulting in synaptic potentiation. AMPARs play a critical role in changing synaptic strength. During LTP, AMPARs are inserted in the postsynaptic membrane via exocytosis and lateral diffusion. In contrast, during LTD, AMPARs are removed from the postsynaptic membrane via endocytosis. Many studies have found subunit-specific rules for these activity-dependent trafficking events of AMPARs. In general, it is assumed that LTP induction promotes the trafficking of GluA1/2 receptors to the synapse, whereas GluA2/3 receptors are constitutively recycled at the synapse. Indeed, the GluA1 subunit has been found to be essential for the induction of LTP (Zamanillo et al., 1999; Hayashi et al., 2000; Shi et al., 2001; Boehm et al., 2006), although not all studies found this specific subunit requirement for LTP induction (Granger et al., 2013).

Postsynaptic membrane organization into nanodomains

AMPA receptors are concentrated in the postsynaptic density (PSD), which is a dense accumulation of scaffolding proteins, signaling molecules, and adhesion complexes (Figure 2). PSD95 is one of the core proteins of the PSD and anchors AMPARs at the PSD via binding to TARPs. On the other hand, mGluR5 is primarily localized in a perisynaptic ring around the PSD (Nusser et al., 1994; Luján et al., 1996; Scheefhals et al., 2023). Glutamate receptors have a low affinity for glutamate, thus only receptors located close to the presynaptic release site will become activated. Under basal conditions, the activated receptors will be ionotropic receptors that localize inside the PSD. In these situations, the glutamate concentration will not be high enough to activate mGluRs that are located just around the PSD. Only during high-frequency stimulation the concentration at the border of the PSD will be high enough to activate mGluRs and trigger intracellular signaling cascades. This reveals another mechanism to precisely tune synaptic transmission and plasticity (Scheefhals and MacGillavry, 2018). The spatial segregation of glutamate receptors results in distinct activation probabilities, which leads to diverse postsynaptic responses depending on the mode of activation. Thus, the organization and localization of receptors at the postsynaptic membrane are of great importance for proper synaptic functioning.

Previous studies found that the PSD protein PSD95 is organized in so-called nanodomains in which ionotropic glutamate receptors are enriched (MacGillavry et al., 2013; Nair et al., 2013). Furthermore, these postsynaptic nanodomains were found to be aligned with the presynaptic release site of neurotransmitters (Tang et al., 2016). Combining this information with the fact that glutamate receptors have a low affinity for glutamate, the alignment or misalignment of neurotransmitter release and postsynaptic receptors can be of great influence for synaptic transmission (Figure 3). Thus, for efficient synaptic potentiation, it is critical to not only incorporate more AMPARs at the synapse, but also to increase their density at

sites opposite to the presynaptic release, specifically. Insight into the nanoscale localization and dynamics of different AMPAR subtypes and postsynaptic mGluRs could thus help in understanding the underlying principles of efficient synaptic transmission.

Contribution of membrane lipids to postsynaptic protein organization

Research over the past decades has been dedicated particularly to the protein-protein interactions that are responsible for the dynamics and localization of postsynaptic glutamate receptors. However, it is often overlooked that receptors are embedded in a sea of lipids that greatly contribute to the structure and organization of the membrane. Lipids are the most abundant components of the plasma membrane and can be categorized based on their head groups, fatty acid chain lengths, and degree of saturation (Figure 2). The characteristic biophysical properties of different lipids contribute to membrane organization. Lipids with longer acyl chains can reduce membrane fluidity, whereas unsaturated lipids prevent tight packing and therefore promote membrane fluidity. Several models have been proposed to describe the contribution of lipids to membrane organization. These include the contribution of lipids to membrane fluidity, thickness, and formation of ordered lipid domains (Singer and Nicolson, 1972; Saffman and Delbrück, 1975; Mouritsen and Bloom, 1984; Simons and Ikonen, 1997). Most likely, the interplay between the different biophysical properties of lipids and transmembrane proteins determines the plasma membrane organization.

The synaptic membrane was found to be enriched in specific lipids such as cholesterol, sphingomyelin, and polyunsaturated fatty acids (PUFAs) (Cotman et al., 1969; Breckenridge et al., 1972). This distinct lipid composition can have several important implications for synapse organization and function. For instance, the lipid composition can adjust the viscosity of the membrane, thereby regulating the diffusion of proteins like glutamate receptors within the membrane. Furthermore, the abundance of cholesterol, sphingolipids, and PUFAs in the synaptic membrane could increase the organization into ordered membrane domains. For PUFAs this might seem counterintuitive because these are unsaturated lipids and therefore less

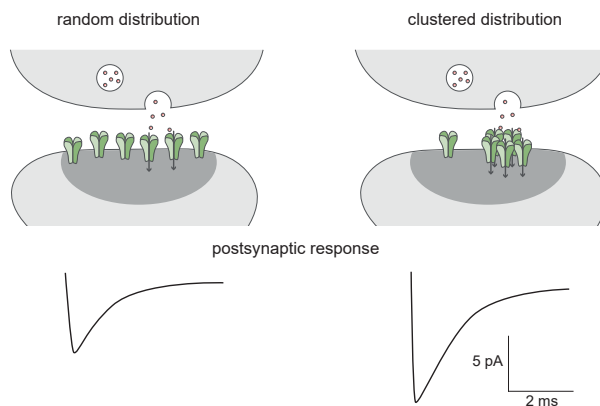


Figure 3. Synaptic receptor nanodomains increase synaptic efficiency

Because more glutamate receptors become activated, release of glutamate on a cluster of receptors results in excitatory postsynaptic currents (EPSCs) with increased amplitudes compared to release on a random distribution of receptors. Adapted from (MacGillivray et al., 2013).

efficiently packed, however, they have been found to increase the formation and stabilization of ordered domains (Wassall and Stillwell, 2009; Levental et al., 2016, 2017). Interestingly, it has been found that the lipid composition of the PSD changes over development and this change includes an increase in domain-promoting lipids (Tulodziecka et al., 2016). Thus, it could be hypothesized that the specific lipid composition at synapses could contribute to the heterogeneous nanodomain organization of glutamate receptors.

Studies that changed the levels of certain lipids found that lipids can modulate synaptic transmission. Depleting cholesterol, for example, has been shown to reduce NMDAR open probability and the fraction of synaptic immobile NMDARs (Korinek et al., 2015, 2020). In addition, lowering cholesterol increased AMPAR basal internalization (Hering et al., 2003). Similarly, modulating the levels of PUFAs, specifically DHA, has been reported to affect synaptic functioning. For example, the addition of DHA led to higher protein levels of both AMPARs and NMDARs (Cao et al., 2009). Furthermore, the abundant interactions between proteins and lipids should not be neglected, considering post-translational lipid modifications and proteins containing lipid-interacting domains. AMPARs are activity-dependent palmitoylated at specific sites and this palmitoylation is controlling trafficking and recycling (Greaves and Chamberlain, 2007; Yang et al., 2009). And for example, mGluR1 has a cholesterol recognition/interaction amino acid consensus (CRAC) motif, that was discovered to be involved in the agonist-dependent downstream pathway activation (Kumari et al., 2013). A more elaborate review of the contribution of membrane lipids to postsynaptic protein organization can be found in **Chapter 2**.

Altogether, the interplay between protein and lipid organization likely contributes to the complex nanoarchitecture of the postsynaptic membrane. This highly complicated organization is of great importance for both basal transmission and synaptic plasticity. Glutamate receptors traffic in and out of the synapse or are confined just at the border of the PSD, and these processes should be perfectly regulated so the receptors are in the right place at the right time. The work in this thesis is dedicated to unraveling more of the secrets behind this complex organization.

Super-resolution microscopy to investigate the organization of the synaptic membrane

It is important to realize that all of the processes described in the sections above are happening at the scale of a few hundred nanometers. In our research, we are interested in the subsynaptic organization of receptors and lipids, thus we should be able to study these molecules at the nanoscale. As the diffraction limit of microscopes is around 200–300 nm, conventional microscopy does not allow us to resolve the localization and dynamics of these molecules within individual synapses. Luckily, in recent years, several super-resolution microscopy techniques have been developed that can resolve structures beyond this diffraction limit. One of these methods is stimulated emission depletion (STED) microscopy (Hell and Wichmann, 1994; Klar and Hell, 1999). The principle behind STED microscopy is that it reduces the area of excitation by a doughnut-shaped de-excitation STED beam and thereby overcomes the diffraction-limited resolution of a confocal microscope. It thus depletes fluorescence in specific regions at the outer regions of the excitation laser focus while leaving the central spot to emit fluorescence. Because of the need for a high-intensity STED beam, leading to

progressive bleaching of fluorophores, dyes with high photostability are a requirement for STED imaging.

The other approach is single-molecule imaging, where instead of acquiring all fluorescent molecules at the same time, only subsets of single molecules are visualized at a time to make sure their point spread functions (PSFs) do not overlap. After obtaining multiple diffraction-limited images with different subsets of single molecules, the centers of the diffraction-limited spots can be derived by fitting and these spatial coordinates together can be used to reconstruct the super-resolved image (Lelek et al., 2021). The question is how to obtain fluorescence from only a subset of molecules. This process relies on the stochastic switching of fluorescent molecules between their 'on' and 'off' states. With photoactivated localization microscopy (PALM) the fluorescent molecules can be photoactivated or photoswitched with light of a specific wavelength. On the other hand, during stochastic optical reconstruction microscopy (STORM) specific dyes are used that can photoswitch when they are inside special STORM buffers that often include an oxygen-scavenging system. In **Chapter 3**, we describe an elaborate protocol to perform single-molecule localization microscopy to resolve neuronal synapses.

To study the dynamics of molecules we can use a technique based on the same principle as single-molecule localization microscopy. During single-molecule tracking, individual molecules are localized in multiple frames over time and these localizations are later combined into trajectories by tracking algorithms (Manzo and Garcia-Parajo, 2015). From these trajectories we can estimate the diffusion coefficient and thereby learn more about the diffusion of different molecules within the plasma membrane. Furthermore, we can investigate the subdiffusive behavior of molecules to discriminate between Brownian, confined, and anomalous diffusion. The study of temporal confinement in molecular trajectories is the focus of **Chapter 4**.

Scope of this thesis

The organization of the postsynaptic membrane at excitatory synapses is of great importance for proper synaptic functioning. Therefore, the general aim of this thesis was to unravel the dynamic subsynaptic organization of individual glutamate receptor subtypes and the organization of membrane lipids and their contribution to the complex architecture of the postsynaptic membrane.

In **Chapter 2** we describe the existing literature around the influence of membrane composition on protein organization in the postsynapse. The membrane consists mainly of lipids that exist in hundreds of different types with their own specific biophysical properties. Their heterogeneous organization is hypothesized to influence the nanodomain organization of glutamate receptors and thereby synaptic functioning.

In **Chapter 3** we describe a protocol to perform single-molecule localization microscopy in neurons. This method allows us to visualize the nanoscale organization of proteins within the synaptic membrane. Different methods are described to label endogenous proteins with either an antibody or by directly visualizing their tag.

In **Chapter 4** we dive deeper into the analysis of the diffusion of molecules and more specifically their temporal confinement. Using single-molecule tracking we can track individual molecules and learn more about their dynamic behavior. In this chapter, we were specifically interested in the periods in those tracks where the molecule was stuck in a certain area for a while. Those confinement periods could indicate areas of higher organization. We investigated the different parameters involved in this analysis and their influence on the results.



In **Chapter 5** we focus on AMPA receptors, specifically the GluA3-containing AMPA receptor. This receptor has not been investigated deeply because its role initially appeared to be marginal. However recent research showed that GluA3 could have a specific role in certain forms of synaptic plasticity and brain-related diseases. Therefore, we investigated the nanoscale distribution and dynamics of this AMPA receptor subunit in comparison with GluA1.

In **Chapter 6** the focus is on the metabotropic glutamate receptor mGluR5. This receptor resides in the perisynaptic area surrounding the PSD, however, how this is precisely regulated and why mGluR5 must localize specifically there was unknown. Using super-resolution techniques we investigated both the nanoscale distribution and dynamics of this receptor within the postsynaptic area.

In **Chapter 7** we describe different methods to study the dynamic lipid organization in the postsynaptic membrane. One approach was to directly label the lipids and investigate their diffusion and distribution. The other approach was to modify the lipid composition and study the effect on receptor organization within the postsynaptic membrane.

We end with a general discussion of this thesis in **Chapter 8**. In this chapter, we summarize our findings and discuss the future perspectives after this research.

References

- Azevedo, F. A. C., Carvalho, L. R. B., Grinberg, L. T., Farfel, J. M., Ferretti, R. E. L., Leite, R. E. P., et al. (2009). Equal numbers of neuronal and nonneuronal cells make the human brain an isometrically scaled-up primate brain. *J. Comp. Neurol.* 513, 532–541.
- Banke, T. G., Bowie, D., Lee, H.-K., Huganir, R. L., Schousboe, A., and Traynelis, S. F. (2000). Control of GluR1 AMPA Receptor Function by cAMP-Dependent Protein Kinase. *J. Neurosci.* 20, 89–102.
- Boehm, J., Kang, M.-G., Johnson, R. C., Esteban, J., Huganir, R. L., and Malinow, R. (2006). Synaptic Incorporation of AMPA Receptors during LTP Is Controlled by a PKC Phosphorylation Site on GluR1. *Neuron* 51, 213–225.
- Breckenridge, W. C., Gombos, G., and Morgan, I. G. (1972). The lipid composition of adult rat brain synaptosomal plasma membranes. *Biochim. Biophys. Acta - Biomembr.* 266, 695–707.
- Cao, D., Kevala, K., Kim, J., Moon, H.-S., Jun, S. B., Lovinger, D., et al. (2009). Docosahexaenoic acid promotes hippocampal neuronal development and synaptic function. *J. Neurochem.* 111, 510–521.
- Cotman, C., Blank, M. L., Moehl, A., and Snyder, F. (1969). Lipid Composition of Synaptic Plasma Membranes Isolated from Rat Brain by Zonal Centrifugation. *Biochemistry* 8, 4606–4612.
- Derkach, V., Barria, A., and Soderling, T. R. (1999). Ca²⁺/calmodulin-kinase II enhances channel conductance of α -amino-3-hydroxy-5-methyl-4-isoxazolepropionate type glutamate receptors. *Proc. Natl. Acad. Sci.* 96, 3269–3274.
- Díaz-Alonso, J., Sun, Y. J., Granger, A. J., Levy, J. M., Blankenship, S. M., and Nicoll, R. A. (2017). Subunit-specific role for the amino-terminal domain of AMPA receptors in synaptic targeting. *Proc. Natl. Acad. Sci.* 114, 7136–7141.
- Granger, A. J., Shi, Y., Lu, W., Cerpas, M., and Nicoll, R. A. (2013). LTP requires a reserve pool of glutamate receptors independent of subunit type. *Nature* 493, 495–500.
- Greaves, J., and Chamberlain, L. H. (2007). Palmitoylation-dependent protein sorting. *J. Cell Biol.* 176, 249–254.
- Hayashi, Y., Shi, S.-H., Esteban, J. A., Piccini, A., Poncer, J.-C., and Malinow, R. (2000). Driving AMPA Receptors into Synapses by LTP and CaMKII: Requirement for GluR1 and PDZ Domain Interaction. *Science* 287, 2262–2267.
- Hell, S. W., and Wichmann, J. (1994). Breaking the diffraction resolution limit by stimulated emission: stimulated-emission-depletion fluorescence microscopy. *Opt. Lett.* 19, 780.
- Henley, J. M., and Wilkinson, K. A. (2016). Synaptic AMPA receptor composition in development, plasticity and disease. *Nat. Rev. Neurosci.* 17, 337–350.
- Hering, H., Lin, C., and Sheng, M. (2003). Lipid Rafts in the Maintenance of Synapses, Dendritic Spines, and Surface AMPA Receptor Stability. *J. Neurosci.* 23, 3262–3271.
- Hollmann, M., Hartley, M., and Heinemann, S. (1991). Ca²⁺ + Permeability of KA-AMPA—Gated Glutamate Receptor Channels Depends on Subunit Composition. *Science* 252, 851–853.
- Hume, R., Dingle, R., and Heinemann, S. (1991). Identification of a site in glutamate receptor subunits that controls calcium permeability. *Science* 253, 1028–1031.
- Isaac, J. T. R., Ashby, M. C., and McBain, C. J. (2007). The Role of the GluR2 Subunit in AMPA Receptor Function and Synaptic Plasticity. *Neuron* 54, 859–871.
- Kessels, H. W., Kopec, C. D., Klein, M. E., and Malinow, R. (2009). Roles of stargazin and phosphorylation in the control of AMPA receptor subcellular distribution. *Nat. Neurosci.* 12, 888–896.
- Klar, T. A., and Hell, S. W. (1999). Subdiffraction resolution in far-field fluorescence microscopy. *Opt. Lett.* 24, 954.
- Korinek, M., Gonzalez-Gonzalez, I. M., Smejkalova, T., Hajdukovic, D., Skrenkova, K., Krusek, J., et al. (2020). Cholesterol modulates presynaptic and postsynaptic properties of excitatory synaptic transmission. *Sci. Rep.* 10, 12651.
- Korinek, M., Vyklicky, V., Borovska, J., Lichnerova, K., Kaniakova, M., Krausova, B., et al. (2015). Cholesterol modulates open probability and desensitization of NMDA receptors. *J. Physiol.* 593, 2279–2293.
- Kumari, R., Castillo, C., and Francesconi, A. (2013). Agonist-dependent Signaling by Group I Metabotropic Glutamate Receptors Is Regulated by Association with Lipid Domains. *J. Biol. Chem.* 288, 32004–32019.
- Lelek, M., Gyparaki, M. T., Beliu, G., Schueder, F., Griffié, J., Manley, S., et al. (2021). Single-molecule localization microscopy. *Nat. Rev. Methods Prim.* 1, 39.
- Levental, K. R., Lorent, J. H., Lin, X., Skinkle, A. D., Surma, M. A., Stockenbojer, E. A., et al. (2016). Polyunsaturated Lipids Regulate Membrane Domain Stability by Tuning Membrane Order. *Biophys. J.* 110, 1800–1810.
- Levental, K. R., Surma, M. A., Skinkle, A. D., Lorent, J. H., Zhou, Y., Klose, C., et al. (2017). ω -3 polyunsaturated fatty acids direct differentiation of the membrane phenotype in mesenchymal stem cells to potentiate osteogenesis. *Sci. Adv.* 3, ea01193.
- Lohmann, C., and Kessels, H. W. (2014). The developmental stages of synaptic plasticity. *J. Physiol.* 592, 13–31.
- Lu, W., Shi, Y., Jackson, A. C., Bjorgan, K., During, M. J., Sprengel, R., et al. (2009). Subunit Composition of Synaptic AMPA Receptors Revealed by a Single-Cell Genetic Approach. *Neuron* 62, 254–268.
- Luján, R., Nusser, Z., Roberts, J. D. B., Shigemoto, R., and Somogyi, P. (1996). Perisynaptic Location of Metabotropic Glutamate Receptors mGluR1 and mGluR5 on Dendrites and Dendritic Spines in the Rat Hippocampus. *Eur. J. Neurosci.* 8, 1488–1500.
- MacGillivray, H. D., Song, Y., Raghavachari, S., and Blanpied, T. A. (2013). Nanoscale Scaffolding Domains within the Postsynaptic Density Concentrate Synaptic AMPA Receptors. *Neuron* 78, 615–622.
- Mansour, M., Nagarajan, N., Nehring, R. B., Clements, J. D., and Rosenmund, C. (2001). Heteromeric AMPA Receptors Assemble with a Preferred Subunit Stoichiometry and Spatial Arrangement. *Neuron* 32, 841–853.
- Manzo, C., and Garcia-Parajo, M. F. (2015). A review of progress in single particle tracking: from methods to biophysical insights. *Reports Prog. Phys.* 78, 124601.
- Mouritsen, O. G., and Bloom, M. (1984). Mattress model of lipid-protein interactions in membranes. *Biophys. J.* 46, 141–153.
- Nair, D., Hossy, E., Petersen, J. D., Constals, A., Giannone, G., Choquet, D., et al. (2013). Super-Resolution Imaging Reveals That AMPA Receptors Inside Synapses Are Dynamically Organized in Nanodomains Regulated by PSD95. *J. Neurosci.* 33, 13204–13224.
- Niswender, C. M., and Conn, P. J. (2010). Metabotropic Glutamate Receptors: Physiology, Pharmacology, and Disease. *Annu. Rev. Pharmacol. Toxicol.* 50, 295–322.
- Nusser, Z., Mulvihill, E., Streit, P., and Somogyi, P. (1994). Subsynaptic segregation of metabotropic and ionotropic glutamate receptors as revealed by immunogold localization. *Neuroscience* 61, 421–427.
- Saffman, P. G., and Delbrück, M. (1975). Brownian motion in biological membranes. *Proc. Natl. Acad. Sci.* 72, 3111–3113.



- Scheefhals, N., and MacGillavry, H. D. (2018). Functional organization of postsynaptic glutamate receptors. *Mol. Cell. Neurosci.* 91, 82–94.
- Scheefhals, N., Westra, M., and MacGillavry, H. D. (2023). mGluR5 is transiently confined in perisynaptic nanodomains to shape synaptic function. *Nat. Commun.* 14, 244.
- Schwenk, J., Bachrens, D., Haupt, A., Bildl, W., Boudkkazi, S., Roeper, J., et al. (2014). Regional Diversity and Developmental Dynamics of the AMPA-Receptor Proteome in the Mammalian Brain. *Neuron* 84, 41–54.
- Shi, S.-H., Hayashi, Y., Esteban, J. A., and Malinow, R. (2001). Subunit-Specific Rules Governing AMPA Receptor Trafficking to Synapses in Hippocampal Pyramidal Neurons. *Cell* 105, 331–343.
- Simons, K., and Ikonen, E. (1997). Functional rafts in cell membranes. *Nature* 387, 569–572.
- Singer, S. J., and Nicolson, G. L. (1972). The Fluid Mosaic Model of the Structure of Cell Membranes. *Science* 175, 720–731.
- Tang, A.-H., Chen, H., Li, T. P., Metzbower, S. R., MacGillavry, H. D., and Blanpied, T. A. (2016). A trans-synaptic nanocolumn aligns neurotransmitter release to receptors. *Nature* 536, 210–214.
- Tulodziecka, K., Diaz-Rohrer, B. B., Farley, M. M., Chan, R. B., Di Paolo, G., Levental, K. R., et al. (2016). Remodeling of the postsynaptic plasma membrane during neural development. *Mol. Biol. Cell* 27, 3480–3489.
- Wassall, S. R., and Stillwell, W. (2009). Polyunsaturated fatty acid–cholesterol interactions: Domain formation in membranes. *Biochim. Biophys. Acta - Biomembr.* 1788, 24–32.
- Watson, J. F., Ho, H., and Greger, I. H. (2017). Synaptic transmission and plasticity require AMPA receptor anchoring via its N-terminal domain. *Elife* 6.
- Wenthold, R., Petralia, R., Blahos J, I., and Niedzielski, A. (1996). Evidence for multiple AMPA receptor complexes in hippocampal CA1/CA2 neurons. *J. Neurosci.* 16, 1982–1989.
- Yang, G., Xiong, W., Kojic, L., and Cynader, M. S. (2009). Subunit-selective palmitoylation regulates the intracellular trafficking of AMPA receptor. *Eur. J. Neurosci.* 30, 35–46.
- Zamanillo, D., Sprengel, R., Hvalby, Ø., Jensen, V., Burnashev, N., Rozov, A., et al. (1999). Importance of AMPA Receptors for Hippocampal Synaptic Plasticity But Not for Spatial Learning. *Science* 284, 1805–1811.
- Zhu, J. J., Esteban, J. a, Hayashi, Y., and Malinow, R. (2000). Postnatal synaptic potentiation: Delivery of GluR4-containing AMPA receptors by spontaneous activity. *Nat. Neurosci.* 3, 1098–1106.



2



Contribution of membrane lipids to postsynaptic protein organization

Manon Westra*, Yolanda Gutierrez* and Harold D. MacGillavry

Frontiers in Synaptic Neuroscience (2021), 13:790773

Cell Biology, Neurobiology and Biophysics, Department of Biology,
Faculty of Science, Utrecht University, Utrecht, The Netherlands

* These authors contributed equally to this work

Abstract

The precise subsynaptic organization of proteins at the postsynaptic membrane controls synaptic transmission. In particular, postsynaptic receptor complexes are concentrated in distinct membrane nanodomains to optimize synaptic signaling. However, despite the clear functional relevance of subsynaptic receptor organization to synaptic transmission and plasticity, the mechanisms that underlie the nanoscale organization of the postsynaptic membrane remain elusive. Over the last decades, the field has predominantly focused on the role of protein-protein interactions in receptor trafficking and positioning in the synaptic membrane. In contrast, the contribution of lipids, the principal constituents of the membrane, to receptor positioning at the synapse remains poorly understood. Nevertheless, there is compelling evidence that the synaptic membrane is enriched in specific lipid species and that deregulation of lipid homeostasis in neurons severely affects synaptic functioning. In this review we focus on how lipids are organized at the synaptic membrane, with special emphasis on how current models of membrane organization could contribute to protein distribution at the synapse and synaptic transmission. Finally, we will present an outlook on how novel technical developments could be applied to study the dynamic interplay between lipids and proteins at the postsynaptic membrane.

Introduction

Experience-dependent modulation of synaptic connections in the brain underlies complex cognitive processes such as learning and memory. In particular, activity-dependent changes in the postsynaptic organization are thought to be essential for the expression of the long-term changes in the efficiency of synaptic transmission that underlie memory formation (Martin et al., 2000; Takeuchi et al., 2014). Indeed, recent super-resolution microscopy studies demonstrated that the positioning of synaptic scaffolding molecules and receptors anchored at the postsynaptic density (PSD) is tightly controlled at the nanoscale and is adjusted by synaptic activity (Fukata et al., 2013; MacGillavry et al., 2013; Nair et al., 2013; Tang et al., 2016; Goncalves et al., 2020). Specifically, subsynaptic clusters of receptors, or nanodomains, in the synaptic membrane enriched in AMPA- or NMDA-type glutamate receptors (AMPA and NMDARs) and scaffolding molecules were found to be aligned with the presynaptic glutamate release site to optimize synaptic transmission (Tang et al., 2016; Li et al., 2021). However, how these nanodomains are formed and modulated during synaptic plasticity remains unknown.

Despite synaptic receptors being integral membrane proteins that are embedded in the lipid bilayer, the contribution of lipids to synaptic organization and functioning remains poorly understood. Nevertheless, lipids are the most abundant components of the brain and lipid dysregulation is thought to underlie several cognitive disorders (Kanungo et al., 2013; Martín et al., 2014; Pérez-Cañamás et al., 2017; van der Kant et al., 2019). Interestingly, synapses are enriched in specific lipid species such as cholesterol and sphingolipids (Breckenridge et al., 1972) and other less abundant components, such as phosphoinositides. This unique lipid composition can have various important consequences for synapse organization and functioning. For instance, lipids can control compartmentalization and proper positioning or activation of critical synaptic protein complexes (Haucke and Di Paolo, 2007; Arendt et al., 2010; Dotti et al., 2014; Brachet et al., 2015). Moreover, changes in lipid composition



determine membrane viscosity, thereby directly controlling the mobility and lateral diffusion of membrane molecules. Indeed, the particular composition of the lipid bilayer strongly favors the maintenance of a heterogeneous spatial organization of membrane lipids and associated proteins (Ingólfsson et al., 2017; Fitzner et al., 2020). The unique composition and structure of the synaptic membrane is therefore predicted to directly impact the activity-dependent changes in protein organization at synapses, ultimately controlling synaptic physiology and brain function.

In this review we will focus on the contribution of the postsynaptic plasma membrane to synapse organization and neuronal function. We will discuss our current understanding of the lipid composition of the synaptic membrane, consider intrinsic and extrinsic factors that influence membrane organization and lastly, we will highlight technical advances that can be used to further study the role of the membrane in postsynaptic organization.

The neuronal and synaptic lipidome

The composition of the plasma membrane is significantly different between cell types, is adjusted during developmental stages and can adapt in response to environmental changes. We are only beginning to understand how this dynamic diversity in lipid composition influences cellular functions but it is becoming clear that the heterogeneity in lipid composition directly determines physical properties of the membrane and is important for key cellular processes.

Cellular membrane lipids are amphipathic molecules with a characteristic polar headgroup and long hydrophobic fatty acid tails causing them to spontaneously form a thin lipid bilayer (Figure 1). Lipids can be categorized based on their head groups, fatty acid chain lengths and degree of saturation. The three major classes of membrane lipids are phospholipids, glycolipids, and sterol (Figure 1A). Phospholipids form the vast majority of lipids in plasma membranes (>50%), with a small contribution of glycolipids (<5%). Cholesterol constitutes 25–35% of the membrane lipids and provides rigidity to the plasma membrane. Together, the phospholipids phosphatidylethanolamine (PE), phosphatidylcholine (PC), phosphatidylserine (PS), and sphingomyelin constitute more than half the mass of lipids in most mammalian membranes.

Advances in lipidomic profiling have enabled the precise identification and quantification of lipid species in tissues. These approaches revealed that lipid composition of the brain is highly distinct from other tissues with relatively high levels of cholesterol and polyunsaturated fatty acids (PUFAs; Bozek et al., 2015; Fitzner et al., 2020). Interestingly, comparison between species revealed that this diversity rapidly expanded in primates, linking brain lipidome complexity to the evolution of higher cognitive brain functions (Bozek et al., 2015). Further analysis of cell-type specific lipid profiles revealed that neurons are particularly enriched in cholesterol and ceramide (Fitzner et al., 2020).

Several studies have investigated the lipid composition of synaptic plasma membranes isolated using zonal centrifugation from adult rat brain (Cotman et al., 1969; Breckenridge et al., 1972; Igbavboa et al., 2002; Tulodziecka et al., 2016). The major lipid types in synaptic membranes are cholesterol, phospholipids and gangliosides, with PE and PC as the most abundant phospholipids (Cotman et al., 1969; Igbavboa et al., 2002). Compared to the whole brain, the fraction of glycolipids in synaptic membranes seems lower while sphingomyelin seems more abundant (Cotman et al., 1969). Interestingly, although sphingomyelin is detected at low levels, in contrast to other membranes, in synapses sphingomyelin is composed of

almost exclusively stearic (18:0) acid (Breckenridge et al., 1972). When looking more closely at the fatty acid composition, it was found that the synaptic plasma membrane is particularly enriched in PUFAs (Cotman et al., 1969; Breckenridge et al., 1972; Igbavboa et al., 2002). Particularly high levels of docosahexaenoic acid (DHA) in PE and PS phospholipids were

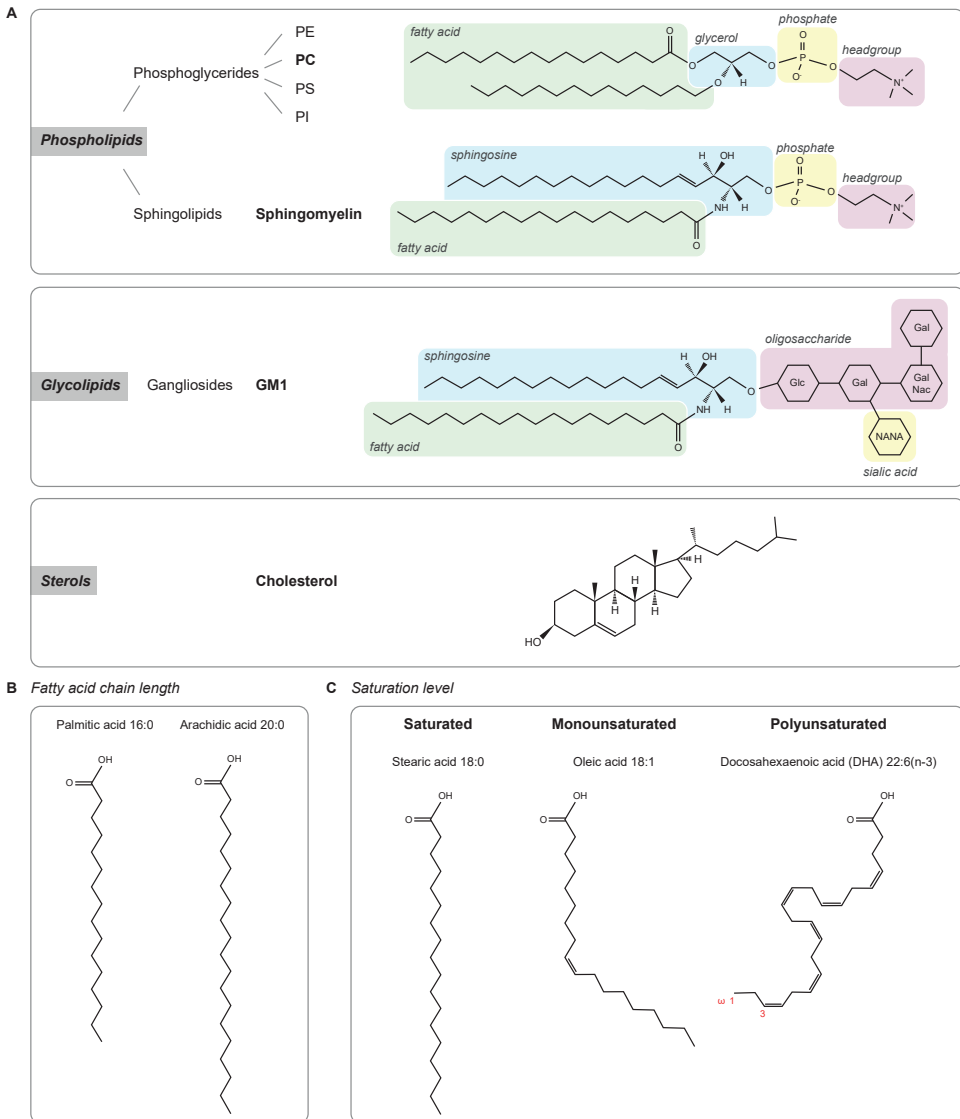


Figure 1. Lipid types

(A) The three major classes of membrane lipids (phospholipids, glycolipids, and sterols) with an example lipid structure (bold) for each. Glc – D-glucose, Gal – D-galactose, NANA – N-acetylneuraminic acid, and GalNac – N-acetyl-D-galactoseamine. (B,C) Acyl chain composition. (B) Fatty acid chain length for palmitic acid and arachidic acid. (C) Lipid structures of lipids with different saturation levels (stearic acid, oleic acid, and docosahexaenoic acid).



detected, which is a striking difference compared to the plasma membrane composition of other tissues. A recent comprehensive lipidomic study showed that the lipid composition of the PSD membrane evolves with development (Tulodziecka et al., 2016), with key species such as cholesterol progressively increasing during development. Additionally, glycosphingolipid levels are developmentally regulated and increase throughout postnatal life (Ngamukote et al., 2007).

It is worth noting, however, that several technical limitations prevent forming a comprehensive characterization of the absolute synaptic plasma membrane lipidome with existing biochemical approaches. Whereas synaptosomal preparations contain a mixture of presynaptic membranes, like synaptic vesicles, and other organellar membranes, isolation of PSD plasma membrane relies on the use of non-ionic detergents that can influence the extracted lipid content. Nevertheless, despite differences in absolute numbers of certain lipid species, namely cholesterol and glycosphingolipids, relative compositional changes in response to specific conditions can reliably be detected (Tulodziecka et al., 2016).

Membrane composition dictates its organization: intrinsic factors

The distinct lipidomic profile of neuronal membranes is likely to influence key neuronal functions. Particularly at synapses, the specific lipid composition could contribute to the heterogeneous nanodomain organization of receptors. However, testing the precise contribution of individual lipids to membrane organization and function in neurons remains technically challenging. Nevertheless, pioneering studies in model membrane systems have characterized the unique biophysical properties of individual lipid species and revealed that these intrinsic properties determine important organizational properties of membranes. We will first provide a brief overview of the general concepts and models of membrane organization and then discuss how these could be incorporated in our current understanding of synapse organization. For more extensive reviews on membrane organization, we refer to a few excellent recent reviews (Sezgin et al., 2017; Jacobson et al., 2019; van Deventer et al., 2021).

Contribution of biophysical properties of lipids to membrane organization

The classic fluid mosaic model (Singer and Nicolson, 1972) was the first to conceptualize and explain experimental observations on the fluidic nature of the plasma membrane. It emphasized that the two-dimensional lipid bilayer is liquid, and that membrane fluidity is the key driver that allows the heterogeneous mixing of lipids and membrane proteins. Almost 50 years later, this model is still valid and has clear relevance for our current thinking on membrane organization. The fluidity of membranes is a key determinant of the diffusion rate of lipids and transmembrane proteins in the membrane as formalized in the hydrodynamic model proposed by Saffman and Delbrück (1975). Membrane fluidity is largely determined by acyl chain composition of membrane lipids (Figures 1B,C). First, longer acyl chains have a larger surface area available for Van der Waals interactions with neighboring acyl chains, reducing membrane fluidity. Second, while straight saturated acyl chains can be efficiently packed closely together, the kink in the hydrocarbon chain of unsaturated acyl chains prevents

efficient packing and thus helps to maintain membrane fluidity. Another important determinant of fluidity is cholesterol, which generally promotes packing of lipids.

Driven by their intrinsic biophysical properties, long saturated acyl chains and cholesterol tend to segregate into tightly packed, liquid-ordered (Lo) phases, whereas unsaturated acyl chains preferentially accumulate in liquid-disordered (Ld) phases. This phase behavior has been studied extensively in synthetic model membranes and has also been observed in giant plasma membrane vesicles (GPMVs) derived from living cells (Baumgart et al., 2007). These observations have greatly influenced the lipid raft theory proposing the existence of ordered lipid domains enriched in cholesterol and glycosphingolipids that facilitate the clustering of specific membrane proteins and associated signaling complexes to form dynamic signaling platforms (Simons and Ikonen, 1997; Figure 2). This theory has been investigated vigorously by biochemical methods that extract detergent-resistant membranes (DRMs) enriched in glycosphingolipids and cholesterol (Brown and Rose, 1992). However, because of technical caveats associated with these biochemical approaches and the absence of direct visualization of lipid rafts in living cells, this theory has gained considerable criticism (Pike, 2009; Levental et al., 2020). Nevertheless, in general, rafts are considered to constitute rather small (20–200 nm) and transient membrane domains (Pike, 2006; Eggeling et al., 2009) and considerable attention has been devoted to characterize raft-promoting lipids such as cholesterol and glycosphingolipids in different cellular systems. In contrast, the role of (poly-) unsaturated fatty acids in membrane organization is less well understood. However, these lipids are increasingly recognized as drivers of membrane domain formation (Wassall and Stillwell, 2009). Particularly, studies using GPMVs indicate that polyunsaturated lipids (especially DHA) promote the formation

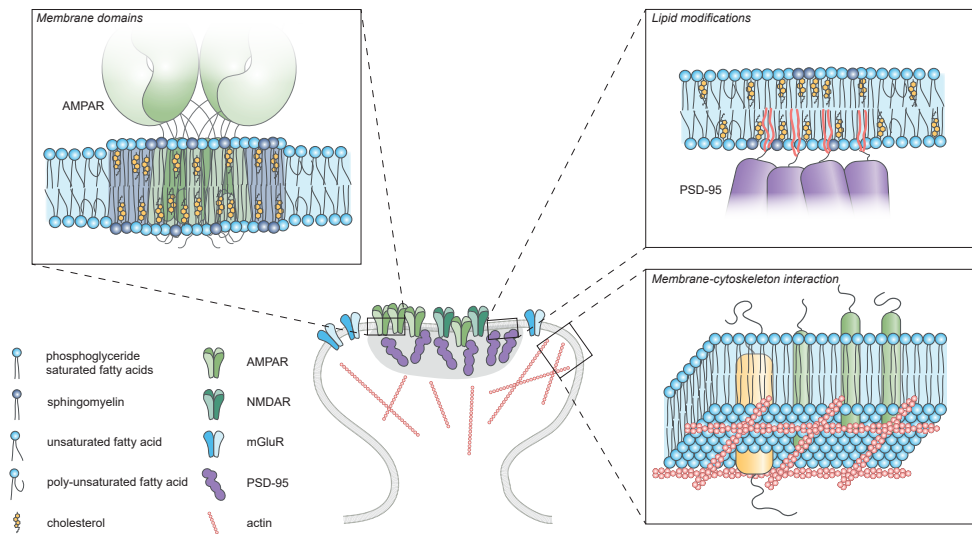


Figure 2. Lipid-protein interactions.

Schematic diagram of the different lipid-protein interactions within the postsynaptic plasma membrane. Membrane domains enriched in cholesterol, glycosphingolipids and saturated lipids can facilitate clustering of membrane proteins by influencing fluidity and thickness of the membrane. Reversible palmitoylation can translocate proteins to the plasma membrane. Actin-linked transmembrane proteins can act as “pickets” and hinder the diffusion of lipids and proteins within the membrane.



and stabilization of ordered membrane domains by increasing the phase difference in ordering (Levental et al., 2016, 2017).

Variations in membrane thickness can also have profound consequences for the organization of transmembrane proteins. The thickness of the membrane is primarily determined by the acyl chain properties of the lipids, with longer, saturated chains forming thicker membranes. When the hydrophobic transmembrane segment of a protein does not match the hydrophobic thickness of the membrane, a so-called hydrophobic mismatch will occur. To compensate for such hydrophobic mismatches, lipids with matching chain lengths will preferentially surround the transmembrane segment causing local variations in the lateral distribution of lipids. Also, the protein can adapt its orientation or conformation to match the thickness (de Planque et al., 2001), or even undergo aggregation to minimize the mismatch. Hydrophobic matching has therefore been proposed as a mechanism that drives self-assembly of domains consisting of transmembrane proteins and lipids with similar hydrophobic length (Mouritsen and Bloom, 1984; Anderson and Jacobson, 2002). Indeed, computational simulations and experimental analysis in model membranes and cells indicate that hydrophobic matching could promote the lateral segregation of proteins and lipids which is further modulated by cholesterol (Kaiser et al., 2011; Diaz-Rohrer et al., 2014). The mattress model by Mouritsen and Bloom (1984) proposes that hydrophobic mismatch promotes lateral segregation in the membrane such that lipids and proteins self-organize in domains of similar hydrophobic thickness. This has for instance been found to underlie the segregation into functionally distinct membrane domains of two related SNARE proteins, Syntaxin-1 and -4 (Milovanovic et al., 2015). Whether such mechanisms underlie the compartmentalization of postsynaptic transmembrane proteins has not been studied yet.

The concepts and models discussed here conceptualized many of the observations on membrane organization in synthetic and cellular membrane models. However, it is becoming increasingly clear that these models are not universal and the factors determining membrane heterogeneity are highly interdependent (Bernardino de la Serna et al., 2016). Both fluidity and membrane thickness can lead to lateral heterogeneity in the membrane. Particularly, in cellular membranes interactions between lipids and membrane proteins seem dominant in determining membrane domain formation. Thus, the nature of membrane domains, i.e., their spatial dimensions and lifetimes are likely to be highly dependent on the specific subcellular composition of the membrane. Indeed, the current goal of the field is to understand how the interplay between the biophysical properties of lipids and membrane proteins orchestrates membrane organization.

Intrinsic determinants of postsynaptic membrane organization

At excitatory synapses, the density of glutamate receptors is a direct determinant of synaptic strength. Mechanisms that control the retention and positioning of receptors have therefore gained tremendous interest. Scaffold proteins in the PSD form a structural platform that anchor receptors via intricate networks of protein-protein interactions. Nevertheless, concepts in membrane biology pose a central role for the intrinsic capacity of lipids to self-organize and form functional membrane domains. In the following sections we discuss how the unique

composition of the postsynaptic membrane suggests that synapses actively maintain and perhaps adjust this composition to instruct the organization and function of synaptic protein components.

Fluidity controls receptor diffusion

Lipidomics studies consistently point out that the brain and particularly synaptic membranes are enriched in both cholesterol and PUFAs. How does this specific composition, with high concentrations of lipids that have opposing effects on lipid ordering and membrane fluidity, influence fluidity at the postsynaptic membrane? Commonly, quantification of the mobility of transmembrane proteins using fluorescence recovery after photobleaching or single-molecule tracking approaches is taken as an estimate of membrane fluidity. However, synaptic membrane proteins are mostly either directly anchored to scaffold proteins or are slowed down in their diffusion due to the relative high density of proteins at the synapse (Li and Blanpied, 2016; Li et al., 2016). In fact, the diffusion of even small transmembrane proteins that are unable to bind synaptic scaffolds is severely influenced by local, subsynaptic variations in cytoplasmic protein density (Li and Blanpied, 2016). Measures of protein mobility do therefore not directly report on the fluidity or ordering of lipids within the membrane itself but are the result of a complex interplay of many different factors. Nevertheless, single-molecule tracking studies showed that even the diffusion rates of fluorescently labeled lipids that are not specifically enriched at synaptic sites are significantly reduced in the postsynaptic membranes compared to extrasynaptic regions (Renner M. L. et al., 2009). However, more direct measures of membrane fluidity using for instance environment-sensitive dyes would be of interest. As an alternative, recently developed computational approaches now allow investigation of the dynamic interplay between lipids and membrane proteins at high spatiotemporal resolution (Ingólfsson et al., 2016). In particular, coarse-grained molecular dynamics simulations allow accurate predictions of how mixtures of lipid species are organized. In a recently developed model of a “brain-like plasma membrane” it was found that while the high concentration of cholesterol leads to an overall increase in acyl chain ordering, the fluidizing effect of high levels of tail unsaturation appears to balance this out (Ingólfsson et al., 2017). Interestingly, however, the extent of ordering in the case of brain membranes was unequally divided over the inner and outer membrane leaflets, with the brain membrane showing distinctively more ordering in the outer leaflet. Also, diffusion rates of lipids were on average 40% lower in brain membranes. Comparable to earlier models of cellular membranes, considerable heterogeneity in the lateral distribution of lipids was found, with more but smaller and more transient cholesterol domains in the brain membrane. These simulations thus provide an unprecedented high-resolution snapshot of how the plasma membrane of neurons could be organized, and it will be of interest to expand these models to test how the high molecular density of integral and membrane-associated proteins at the synapse will influence and interact with this specific composition of lipids.

Synapses have raft properties

The enrichment of cholesterol and sphingolipids at synaptic membranes and the computational simulations suggest that the postsynaptic membrane could have confined regions reminiscent of lipid rafts. Indeed, DRMs isolated from whole brain contain key components of excitatory synapses, most notably PSD-95, as well as glutamate receptors and interacting proteins (Perez and Brecht, 1998; Brückner et al., 1999; Suzuki et al., 2001, 2011; Hering



et al., 2003; Ma et al., 2003; Besshoh et al., 2005; Hou et al., 2008; Delint-Ramirez et al., 2010). Moreover, rafts can be isolated from synaptic membrane fractions (Suzuki et al., 2001, 2011; Besshoh et al., 2005) and ChTx (cholera toxin) labeling overlaps with PSD-95 staining, indicating the presence of raft-like structures at the PSD (Perez and Brecht, 1998; Brückner et al., 1999; Suzuki et al., 2001; Hering et al., 2003; Hou et al., 2008). At the ultrastructural level, electron cryotomography showed that GM1-positive raft-like membranes were frequently found associated, preferentially with adult PSDs (Suzuki et al., 2001; Besshoh et al., 2005; Swulius et al., 2012), consistent with the developmental increase in raft-promoting lipids at synaptic membranes (Tulodziecka et al., 2016). Further, immuno-EM studies demonstrated the presence of raft markers such as flotilins at the PSD (Suzuki, 2002; Hering et al., 2003), that were also shown to interact with NMDAR subunits (Swanwick et al., 2009). All these data thus suggest that raft-like domains exist within the postsynaptic membrane, perhaps compartmentalizing specific receptor complexes (Perez and Brecht, 1998; Brückner et al., 1999; Suzuki et al., 2001; Hering et al., 2003; Allen et al., 2007; Hou et al., 2008). Indeed, PSD-95-NMDAR complexes isolated from raft fractions were enriched in a different complement of signaling molecules than those isolated from PSD or soluble fractions (Delint-Ramirez et al., 2010). The association of NMDARs with raft vs. non-raft domains has been shown to be regulated for instance during spatial memory formation (Delint-Ramirez et al., 2008) and ischemia (Besshoh et al., 2005) indicating that the association of synaptic receptors with specific membrane domains can be dynamic and regulated by synaptic activity.

Thus, although lipid raft characterization relies on biochemical procedures that may occlude investigation of more complex membrane dynamics, evidence gathered through these and other experimental means clearly points toward the existence of a heterogeneous distribution of different components in the postsynaptic membrane. However, it remains difficult to assess how individual lipid types contribute to this heterogeneity. In large part this is difficult because the behavior of individual lipids is highly dependent on the environment. For example, while PUFAs might form disordered membrane domains, they could also contribute to stabilize ordered membrane domains (Wassall and Stillwell, 2009; Levental et al., 2016). Additionally, the interactions of lipids with proteins provide an extra layer of complexity that could underlie the lateral distribution of postsynaptic membrane components.

Lipids modulate synaptic transmission

Consistent with the notion that lipid rafts are important for regulating NMDAR function, interfering with membrane cholesterol levels was shown to perturb NMDAR-dependent calcium responses as well as LTP (Koudinov and Koudinova, 2001; Frank et al., 2004, 2008; Kotti et al., 2006; Maggo and Ashton, 2014; Guo et al., 2021). More specifically, cholesterol depletion was reported to decrease the open probability of NMDARs and reduce the fraction of synaptic immobile NMDARs (Korinek et al., 2015, 2020). Furthermore, cholesterol reduction increased basal internalization of AMPARs (Hering et al., 2003) and the mobility of slow diffusing molecules within the synapse (Renner M. et al., 2009). In addition, treatment with statins (inhibitors of cholesterol synthesis) impaired recognition and working memory (Maggo and Ashton, 2014; Guo et al., 2021). Cholesterol replenishment could rescue impaired LTD resulting from cholesterol loss in aged mice, also improving hippocampal learning and memory (Ledesma et al., 2012; Martin et al., 2014). On the contrary, other studies reported enhancement of LTP and hippocampal-dependent learning and memory after cholesterol reduction, while

adding cholesterol impaired LTP (Li et al., 2006; Mans et al., 2010; Brachet et al., 2015). These conflicting results could be explained by a dose-dependent effect of cholesterol (Baytan et al., 2008; Wang and Zheng, 2015). To untangle these effects, several studies have looked at it from a different perspective: what influence does glutamatergic synaptic transmission have on cholesterol levels? Stimulation of glutamatergic transmission was found to induce a loss of cholesterol from synaptic membranes and recruitment of CYP46A1 — an enzyme responsible for cholesterol removal — to the synaptic plasma membrane (Sodero et al., 2012; Brachet et al., 2015; Mitroi et al., 2019). Taken together, these findings highlight the dynamic interplay between cholesterol levels and glutamatergic transmission.

Long-chain PUFAs, particularly DHA, are also found to be enriched in synapses and could play an important role in compartmentalizing the membrane and thereby influencing synaptic transmission. The addition of exogenous DHA to dissociated neuronal cultures was found to enhance spontaneous glutamatergic synaptic activity and promote NMDAR function (Nishikawa et al., 1994; Cao et al., 2009). Furthermore, the protein levels of both AMPAR and NMDAR subunits were higher in the DHA-supplemented cultures (Cao et al., 2009). However, DHA-treatment has been linked to variable effects on synaptic plasticity on brain slices. Exogenous DHA supplementation leads to facilitated LTP in the corticostriatal pathway (Mazzocchi-Jones, 2015) whereas LTP and LTD in the CA1 region were found to be impaired (Young et al., 1998; Mirnikjoo et al., 2001) or unaffected (Fujita et al., 2001; Mazzocchi-Jones, 2015). Some of the discrepancies might arise from region-dependent effects of DHA on synaptic plasticity. In the CA1 region LTP was inhibited whereas in the dentate gyrus there was no effect on LTP after intracerebroventricular injection of DHA (Itokazu et al., 2000). Interestingly, dietary supplementation or deprivation has proven to be an effective method of manipulating DHA levels. The importance of DHA for synaptic plasticity has been found both in young mice, where maternal dietary deprivation of DHA leads to inhibited induction of LTP (Cao et al., 2009), as well as in old rats, where the age-related impairment of LTP is restored by a DHA-supplemented diet (McGahon et al., 1999). Although the variety of results found could be a result of the different experimental paradigms used, it is apparent that DHA plays an important role in modulating cognitive functions. This is highlighted also from the finding that DHA deficiency results in affected spatial learning whereas the fat-1 transgenic mouse, producing high DHA levels, shows improved spatial learning (Fedorova et al., 2007; He et al., 2009). Lastly, it is important to note that apart from the structural role these lipids can play in membranes, cholesterol (through its metabolites) and PUFAs also have roles as signaling intermediates (Bazinet and Layé, 2014; Petrov et al., 2016). Therefore, although it cannot be concluded from these studies that modulating either cholesterol or PUFA levels solely influences membrane organization, these findings underscore the importance of synaptic membrane composition for neuronal function.

Additional layers contributing to membrane organization: extrinsic factors

The intrinsic properties of lipids are likely to contribute to membrane organization, but in cellular membranes extrinsic factors add an additional layer of complexity. For instance, interactions with the underlying actin cytoskeleton, oligomerization of membrane proteins or immobilized, membrane-associated protein scaffolds can greatly impact domain formation in



the membrane (Kusumi et al., 1993; Fujiwara et al., 2002; Tulodziecka et al., 2016). Particularly at the PSD, that contains a high density of transmembrane and membrane-associated proteins, reciprocal interactions between lipid species and proteins are likely to influence postsynaptic membrane organization.

Post-translational lipid modifications

In addition to hydrophobic structures in proteins, covalent binding of lipidic moieties can mediate the membrane association of proteins (Figure 2). These lipid modifications can be irreversibly added during translation or can be reversibly attached post-translationally by several enzymes [reviewed in detail in Magee and Seabra (2005), Hentschel et al. (2016), Resh (2016)]. Examples of irreversible lipid modifications include myristoylation and prenylation where myristoyl and prenyl groups are attached, respectively. On the other hand, the binding of a GPI anchor or palmitate group are reversible modifications that allow dynamic regulation of protein localization. Many proteins located in the PSD (either transmembrane or membrane-bound) present reversible lipid modifications that can be regulated by activity, incorporating another layer of control of synaptic function. The role of protein palmitoylation in synaptic plasticity is covered more extensively in the following reviews: Fukata et al. (2016), Ji and Skup (2021).

The saturated nature of the lipophilic palmitate group is thought to contribute to the association of palmitoylated proteins with ordered membrane domains. In fact, it has been shown that palmitoylation is essential for partitioning of transmembrane proteins to the ordered domain of GPMVs (Levental et al., 2010; Lorent et al., 2017). Several synaptic receptors are palmitoylated. For instance, different AMPAR subunits are palmitoylated at specific sites (Hayashi et al., 2005). Beyond establishing a quality check-point for protein surface expression, this lipid modification is shown to be a regulated activity-dependent process that controls AMPAR trafficking and recycling (Greaves and Chamberlain, 2007; Yang et al., 2009). Also, NMDAR subunits undergo palmitoylation, influencing their trafficking and stabilization at the synaptic plasma membrane (Hayashi et al., 2009). Nevertheless, it is worth noting that while palmitoylation generally promotes the partitioning of transmembrane proteins into ordered membrane regions, it is not strictly necessary nor sufficient in all cases. For example, the transferrin receptor, a canonical non-raft marker, is palmitoylated at two residues, and the raft reporter caveolin is present in detergent resistant fractions even when its palmitoylation residues are mutated (Alvarez et al., 1990; Dietzen et al., 1995).

For cytosolic proteins, palmitoylation mediates the efficient and dynamic translocation to the membrane. A prominent example is the protein AKAP79, which undergoes dynamic, activity-regulated palmitoylation (Keith et al., 2012; Woolfrey et al., 2015). Interestingly, palmitoylation of AKAP79 is required for its recruitment to dendritic spines and contributes to its stabilization in membranes through association with lipid rafts, which occurs only when it is palmitoylated (Delint-Ramirez et al., 2011; Keith et al., 2012; Purkey et al., 2018). Additionally, the main organizer of PSD architecture, PSD-95, is also anchored to the membrane through palmitoylation of two residues (Topinka and Bredt, 1998; Craven et al., 1999; El-Husseini et al., 2000). Interestingly, Tulodziecka et al. (2016), using biochemical approaches and lipidome analysis of synaptosomal membrane fractions, revealed a developmentally regulated increase in PSD-95 palmitoylation, which is accompanied by an enrichment of domain-promoting lipid species. Thus, while it is clear that palmitoylation controls membrane targeting of key

synaptic components, it is plausible that palmitoylation also serves as a nucleation platform for defined lipids. As such, insertion of palmitoylated proteins such as PSD-95, could facilitate the segregation of protein/lipid nanodomains that contribute to the subsynaptic organization of the PSD. In line with this notion, the use of a specific intrabody recognizing palmitoylated PSD-95 in combination with STED microscopy revealed subsynaptic nanodomains of palmitoylated PSD-95 (Fukata et al., 2013). Additionally, PSD-95 palmitoylation regulates its conformation and orientation at the PSD, subsynaptic organization, as well as AMPAR clustering and surface expression at synapses (El-Husseini et al., 2002; Tsutsumi et al., 2008; Fukata et al., 2013; Jeyifous et al., 2016; Yokoi et al., 2016), ultimately controlling synaptic strength.

Although palmitoylation regulates trafficking and membrane targeting of synaptic proteins, its dynamic nature could thus also contribute to regulate the nanoscale distribution of synaptic proteins. Although further experiments are required to elucidate this point, it is tempting to speculate that palmitoyl residues contribute to this subsynaptic organization through interactions with defined membrane regions.

Protein-lipid interactions

Several models of membrane organization include the role of cortical actin in membrane organization (Kusumi et al., 1993; Fujiwara et al., 2002). In particular, the picket-fence model poses that certain actin-linked transmembrane proteins act as “pickets” and hinder diffusion of phospholipids to the next compartment (Figure 2). Even though the actin cytoskeleton is absent from the PSD, it is still one of the major constituents of spines and greatly influences spine morphogenesis and architecture, having a crucial role in neuronal function (Sidenstein et al., 2016; Basu and Lamprecht, 2018). Using single-molecule tracking of a lipid-bound protein Renner M. L. et al. (2009) revealed that actin depolymerization increases diffusion rates of the probe indicating that the actin cytoskeleton could hinder the diffusion of membrane proteins in spines.

Interestingly, several receptors have been reported to contain specific recognition domains for cholesterol and sphingolipids that could be involved in concentrating these receptors in specific lipid domains (Hanson et al., 2008; Jafurulla et al., 2017). For example, mGluR1 is recruited to lipid rafts through a cholesterol recognition/interaction amino acid consensus (CRAC) motif. This recruitment is enhanced upon agonist activation of the receptor, and mutations that reduce mGluR1 affinity for lipid rafts as well as alterations in cholesterol content have a direct effect in the regulation of the agonist-dependent activation of downstream pathways (Kumari et al., 2013). Nevertheless, it is worth noting that although these motifs are present in integral membrane proteins, there is inconclusive evidence to support their necessity or sufficiency for cholesterol binding. Although later efforts have focused on defining a structure-based cholesterol-binding pocket consensus (Marlow et al., 2021), cholesterol and sphingolipids can also interact with membrane-associated proteins and receptors that lack such specific binding motifs. Such lipid-protein interactions could then form a so-called “lipid shell,” allowing proteins to segregate into defined domains (Anderson and Jacobson, 2002; Fantini and Barrantes, 2009). Interestingly, recent structural studies of AMPARs in complex with CNIH2, but not with CNIH3, presented the acyl chains of two lipids penetrating the CNIH-binding site. Therefore, by extending the hydrophobic network and preventing a closer CNIH2-AMPA interaction, membrane lipids could contribute to regulate receptor function (Zhang et al., 2021). In addition to binding to their specific scaffold proteins, these



receptor-specific properties and their interaction with defined PSD membrane regions could also contribute to the segregation of AMPA- and NMDARs on distinct nanodomains within the PSD (Goncalves et al., 2020; Li et al., 2021).

Technical advances and challenges to study lipid organization in the synaptic plasma membrane

The precise organization of different lipid species within the postsynaptic membrane remains largely elusive. This lack of understanding predominantly arises from the lack of adequate tools to study the integrity and lateral heterogeneity of biological membranes in their native state (Jacobson et al., 2007). Nevertheless, new tools continue to be developed to bridge this knowledge gap (Muro et al., 2014; Sezgin et al., 2017) and it will be exciting to see the application of these tools to study the synaptic membrane.

Recent advances in lipidomics methods allow studying the composition of different neuronal compartments in greater detail, including the synaptic plasma membrane (Iuliano et al., 2021). However, while detailed lipidomic characterization provides a general picture of membrane composition (Aureli et al., 2015; Fitzner et al., 2020), it does not reveal the heterogeneity and dynamics of the lateral order of lipids in the membrane. Nevertheless, these studies provide important insights and can be currently combined with *in silico* analysis and databases to analyze protein-membrane interactions to provide further insights into the molecular dynamics at specific membranes (Ingólfsson et al., 2017; Mohamed et al., 2019; Hernández-Adame et al., 2021).

Major advances and efforts have been developed in recent years to directly visualize different lipid species and determine their precise localization and organization. For an in-depth review and overview of fluorescent lipid probes, we refer to Klymchenko and Kreder (2014). A major difficulty in visualizing lipids with fluorescence microscopy arises from the fact that fluorophores are often almost the size of the lipid molecule itself. The addition of such fluorophores could therefore influence the behavior of the lipid and alter its specific amphiphilic properties thereby changing its dynamics. One strategy to circumvent this caveat is to label the head group of the lipid with a fluorophore through the addition of a linker to prevent interaction with the surrounding headgroups (Kinoshita et al., 2017; Mobarak et al., 2018). Such newly developed fluorescent lipid analogs combined with super-resolution imaging (e.g., STED-FCS), single-molecule tracking, and expansion microscopy allow the study of membrane organization at high spatial resolution (Lenne et al., 2006; Eggeling et al., 2009; Mizuno et al., 2011; Klymchenko and Kreder, 2014; Komura et al., 2016; Götz et al., 2020; Sun et al., 2021). Alternatively, reporters that bind to specific lipids can also be used. However, such probes can influence the native membrane organization. For example ChTx, that can bind up to five GM1 gangliosides and thereby could induce cluster formation (Day and Kenworthy, 2015). In the case of cholesterol, filipin is widely used for visualization, but requires fixation because the dye permeabilizes membranes (Behnke et al., 1984). An alternative solution relies on the use of a single domain (D4) from a cholesterol-binding toxin, being sufficient for the binding of cholesterol and use as a sensor for cholesterol in live cells without perturbing its native behavior (Maekawa, 2017).

Single-molecule tracking studies have proven to be a powerful approach in studying the dynamic behavior of lipids and transmembrane proteins in synapses (Choquet and Triller,

2013) and revealed for instance the dynamic exchange of receptors in and out of synapses. Single-molecule trajectories also provide spatial information on the local, temporal confinement of transmembrane proteins, defined as regions where molecules are retained longer than expected from a Brownian moving molecule (Saxton, 1993; Simson et al., 1995), that could indicate the presence of membrane domains. A particularly powerful approach to study the dynamic behavior of lipids is high-speed (up to 25- μ s intervals) single-molecule tracking of lipids coupled to photostable dyes. This can reveal temporal subdiffusive behavior and confinement of lipids and membrane proteins that are not observed at typical, slower frame rates (20–30-ms intervals; Fujiwara et al., 2002). Such studies revealed for instance that at these time scales most lipid species and transmembrane proteins undergo short-term confinement in nanoscale compartments and longer-term “hop” movements to adjacent compartments, a phenomenon referred to as “hop diffusion” (Fujiwara et al., 2002; Kusumi et al., 2010). These compartments have been related to the picket-fence model where lipids and transmembrane proteins “hop” from compartments fenced by cortical actin segments (Fujiwara et al., 2016).

The use of environment-sensitive dyes (Danylchuk et al., 2020) allows the study of membrane ordering. These lipophilic dyes have a different emission spectrum dependent on their localization in a more ordered or disordered phase of the membrane. Interestingly, a recent study made it even possible to image lipid order at the nanoscale using the photoswitchable solvatochromic probe NR4A in combination with super-resolution microscopy (Danylchuk et al., 2019). However, some of these probes are derived from voltage-sensitive probes, and could thus behave differently in the excitable membranes of neurons (Obaid et al., 2004).

Finally, a direct test of how individual lipids contribute to membrane organization or functioning in living cells is still lacking. Specific modulation of the composition of cellular membranes cannot be achieved with common pharmacological treatments. Therefore, there is still a void in molecular tools to locally and temporally manipulate membrane composition without affecting downstream pathways. Optical manipulation of lipid biosynthesis might be an interesting future direction to manipulate lipid levels with high spatiotemporal precision (Kol et al., 2019).

Altogether, it is increasingly clear that although recent technical developments provide great insight, a combination of tools and approaches is still required to define the precise lipid composition and organization at the nanoscale in the synaptic membrane.

Conclusion and future directions

The lateral distribution of lipids and proteins in the plasma membrane is highly heterogeneous and is organized as a dynamic patchwork with specific components concentrated in domains that vary largely in size and lifetime. The unique intrinsic composition of the synaptic membrane, as well as the specific spatial distribution of lipids, is predicted to contribute to the formation of specialized nanodomains within the postsynaptic membrane. It will thus be important to understand how lipid and protein components of the postsynaptic plasma membrane interact to contribute to the organization and function of synapses.

Different approaches have been used to characterize the lipid composition of the synaptic plasma membrane. Through isolation of enriched synaptic plasma membrane fractions important observations have been made. In particular, it is evident that the synaptic membrane is enriched in cholesterol and PUFAs and that its composition evolves during development.



However, the dynamic nature and lateral heterogeneity of the membrane precludes drawing the complete picture. Therefore, development of new tools is required to provide a better understanding of the organization of the synaptic plasma membrane and how it is modulated by neuronal activity. Importantly, information can be gathered not only on a descriptive level, but also through finer tools to manipulate membrane composition in a spatial and temporally regulated manner.

Another interesting notion is the cooperative nature of protein-lipid interactions. Although synapses have raft properties and general concepts for membrane organization seem to be true for the synaptic membrane, the high abundance of proteins within the synapse makes it a unique structure. Thus, generalizing models of membrane organization and imposing these on how synapses are organized is not straightforward. Nevertheless, while protein-protein domain nucleation undoubtedly plays an important instructive role in shaping the nanoscale architecture of synapses, the interaction of proteins with lipids in the surrounding membrane is likely modulating this nanoarchitecture. This is particularly relevant for proteins containing lipid interacting domains as well as post-translational lipid modifications. The challenge is thus to not only consider protein- and lipid-driven lateral organization as mutually exclusive mechanisms, but to investigate the concerted actions of proteins and lipids in generating the functional heterogeneity of the postsynaptic membrane. However, determining the contribution of lipids to synaptic organization remains a considerable challenge. One important consideration is that lipids can have a dual role, both as structural organizers of membrane domains and as signaling molecules. In fact, lipid signaling greatly contributes to neuronal function (Dotti et al., 2014), directing both intracellular transport of vesicles as well as controlling targeting or activation of key enzymes. For example, lysophospholipid-triggered signaling controls excitatory and inhibitory postsynaptic currents through defined presynaptic and postsynaptic mechanisms, respectively (García-Morales et al., 2015). Thus, altered synaptic function as a result of experimental lipid composition manipulations, could arise from effects on membrane organization, but could also be an indirect effect of disrupted signaling. Designing novel experimental tools to specifically delineate these entangled functions of lipids in synaptic signaling is a formidable task. Nevertheless, the rapid progress in the field of membrane biology and the ongoing efforts in developing novel, specific experimental tools to study membrane organization, are likely to stimulate studies on postsynaptic membrane organization. Such studies are critical to move the field toward a more comprehensive model that integrates both nanoscale protein organization as well as the heterogeneity of the synaptic lipidome.

Author contributions

MW, YG, and HM wrote the manuscript. All authors contributed to the article and approved the submitted version.

Funding

This work was supported by Netherlands Organization for Scientific Research (016.Vidi.171.029 to HM).

Conflict of interest

The authors declare that the research was conducted in the absence of any commercial or financial relationships that could be construed as a potential conflict of interest.

Acknowledgments

We want to thank all members of the MacGillavry Lab for discussions.

References

- Allen, J. A., Halverson-Tamboli, R. A., and Rasenick, M. M. (2007). Lipid raft microdomains and neurotransmitter signalling. *Nat. Rev. Neurosci.* 8, 128–140.
- Alvarez, E., Girones, N., and Davis, R. J. (1990). Inhibition of the receptor-mediated endocytosis of diferric transferrin is associated with the covalent modification of the transferrin receptor with palmitic acid. *J. Biol. Chem.* 265, 16644–16655.
- Anderson, R. G. W., and Jacobson, K. (2002). A role for lipid shells in targeting proteins to caveolae, rafts, and other lipid domains. *Science* 296, 1821–1825.
- Arendt, K. L., Royo, M., Fernández-Monreal, M., Knafo, S., Petrok, C. N., Martens, J. R., et al. (2010). PIP 3 controls synaptic function by maintaining AMPA receptor clustering at the postsynaptic membrane. *Nat. Neurosci.* 13, 36–44.
- Aureli, M., Grassi, S., Prioni, S., Sonnino, S., and Prinetti, A. (2015). Lipid membrane domains in the brain. *Biochim. Biophys. Acta - Mol. Cell Biol. Lipids* 1851, 1006–1016.
- Basu, S., and Lamprecht, R. (2018). The Role of Actin Cytoskeleton in Dendritic Spines in the Maintenance of Long-Term Memory. *Front. Mol. Neurosci.* 11, 143.
- Baumgart, T., Hammond, A. T., Sengupta, P., Hess, S. T., Holowka, D. A., Baird, B. A., et al. (2007). Large-scale fluid/fluid phase separation of proteins and lipids in giant plasma membrane vesicles. *Proc. Natl. Acad. Sci. U. S. A.* 104, 3165–3170.
- Baytan, S. H., Alkanat, M., Okuyan, M., Ekinci, M., Gedikli, E., Ozeren, M., et al. (2008). Simvastatin impairs spatial memory in rats at a specific dose level. *Tohoku J. Exp. Med.* 214, 341–349.
- Bazinet, R. P., and Layé, S. (2014). Polyunsaturated fatty acids and their metabolites in brain function and disease. *Nat. Rev. Neurosci.* 15, 771–785.
- Behnke, O., Tranum-Jensen, J., and Van Deurs, B. (1984). Filipin as a cholesterol probe. II. Filipin-cholesterol interaction in red blood cell membranes. *Eur. J. Cell Biol.* 35, 200–215.
- Bernardino de la Serna, J., Schütz, G. J., Eggeling, C., and Cebecaer, M. (2016). There Is No Simple Model of the Plasma Membrane Organization. *Front. Cell Dev. Biol.* 4, 1–17.
- Besshoh, S., Bawa, D., Teves, L., Wallace, M. C., and Gurd, J. W. (2005). Increased phosphorylation and redistribution of NMDA receptors between synaptic lipid rafts and post-synaptic densities following transient global ischemia in the rat brain. *J. Neurochem.* 93, 186–194.
- Bozek, K., Wei, Y., Yan, Z., Liu, X., Xiong, J., Sugimoto, M., et al. (2015). Organization and Evolution of Brain Lipidome Revealed by Large-Scale Analysis of Human, Chimpanzee, Macaque, and Mouse Tissues. *Neuron* 85, 695–702.
- Brachet, A., Norwood, S., Brouwers, J. F., Palomer, E., Helms, J. B., Dotti, C. G., et al. (2015). LTP-triggered cholesterol redistribution activates Cdc42 and drives AMPA receptor synaptic delivery. *J. Cell Biol.* 208, 791–806.
- Breckenridge, W. C., Gombos, G., and Morgan, I. G. (1972). The lipid composition of adult rat brain synaptosomal plasma membranes. *Biochim. Biophys. Acta - Biomembr.* 266, 695–707.
- Brown, D. A., and Rose, J. K. (1992). Sorting of GPI-anchored proteins to glycolipid-enriched membrane subdomains during transport to the apical cell surface. *Cell* 68, 533–544.
- Brückner, K., Labrador, J. P., Scheiffele, P., Herb, A., Seeburg, P. H., and Klein, R. (1999). EphrinB ligands recruit GRIP family PDZ adaptor proteins into raft membrane microdomains. *Neuron* 22, 511–524.
- Cao, D., Kevala, K., Kim, J., Moon, H.-S. S., Jun, S. B., Lovinger, D., et al. (2009). Docosahexaenoic acid promotes hippocampal neuronal development and synaptic function. *J. Neurochem.* 111, 510–521.
- Choquet, D., and Triller, A. (2013). The Dynamic Synapse. *Neuron* 80, 691–703.
- Cotman, C., Blank, M. L., Moehl, A., and Snyder, F. (1969). Lipid Composition of Synaptic Plasma Membranes Isolated from Rat Brain by Zonal Centrifugation. *Biochemistry* 8, 4606–4612.
- Craven, S. E., El-Husseini, A. E., and Bredt, D. S. (1999). Synaptic targeting of the postsynaptic density protein PSD-95 mediated by lipid and protein motifs. *Neuron* 22, 497–509.
- Danylchuk, D. I., Moon, S., Xu, K., and Klymchenko, A. S. (2019). Switchable Solvatochromic Probes for Live-Cell Super-resolution Imaging of Plasma Membrane Organization. *Angew. Chemie* 131, 15062–15066.
- Danylchuk, D. I., Sezgin, E., Chabert, P., and Klymchenko, A. S. (2020). Redesigning Solvatochromic Probe Laurdan for Imaging Lipid Order Selectively in Cell Plasma Membranes. *Anal. Chem.* 92, 14798–14805.
- Day, C. A., and Kenworthy, A. K. (2015). Functions of cholera toxin B-subunit as a raft cross-linker. *Essays Biochem.* 57, 135–145.
- de Planque, M. R. R., Goormaghtigh, E., Greathouse, D. V., Koeppe, R. E., Kruijtz, J. A. W., Liskamp, R. M. J., et al. (2001). Sensitivity of Single Membrane-Spanning α -Helical Peptides to Hydrophobic Mismatch with a Lipid Bilayer: Effects on Backbone Structure, Orientation, and Extent of Membrane Incorporation. *Biochemistry* 40, 5000–5010.
- Delint-Ramírez, I., Fernández, E., Bayés, A., Kicsi, E., Komiyama, N. H., and Grant, S. G. N. (2010). In vivo composition of NMDA receptor signaling complexes differs between membrane subdomains and is modulated by PSD-95 and PSD-93. *J. Neurosci.* 30, 8162–8170.
- Delint-Ramírez, I., Salcedo-Tello, P., and Bermudez-Rattoni, F. (2008). Spatial memory formation induces recruitment of NMDA receptor and PSD-95 to synaptic lipid rafts. *J. Neurochem.* 106, 1658–1668.
- Delint-Ramírez, I., Willoughby, D., Hammond, G. V. R., Ayling, L. J., and Cooper, D. M. F. (2011). Palmitoylation targets AKAP79 protein to lipid rafts and promotes its regulation of calcium-sensitive adenylyl cyclase type 8. *J. Biol. Chem.* 286, 32962–32975.
- Diaz-Rohrer, B. B., Levental, K. R., Simons, K., and Levental, I. (2014). Membrane raft association is a determinant of plasma membrane localization. *Proc. Natl. Acad. Sci.* 111, 8500–8505.
- Dietzen, D. J., Hastings, W. R., and Lublin, D. M. (1995). Caveolin is palmitoylated on multiple cysteine residues. Palmitoylation is not necessary for localization of caveolin to caveolae. *J. Biol. Chem.* 270, 6838–6842.
- Dotti, C. G., Esteban, J. A., and Ledesma, M. D. (2014). Lipid dynamics at dendritic spines. *Front. Neuroanat.* 8, 1–11.
- Eggeling, C., Ringemann, C., Medda, R., Schwarzmann, G., Sandhoff, K., Polyakova, S., et al. (2009). Direct observation of the nanoscale dynamics of membrane lipids in a living cell. *Nature* 457, 1159–1162.
- El-Husseini, A. E., Craven, S. E., Chetkovich, D. M., Firestein, B. L., Schnell, E., Aoki, C., et al. (2000). Dual palmitoylation of PSD-95 mediates its vesiculotubular sorting, postsynaptic targeting, and ion channel clustering. *J. Cell Biol.* 148, 159–171.
- El-Husseini, A. E. D., Schnell, E., Dakoji, S., Sweeney, N., Zhou, Q., Prange, O., et al. (2002). Synaptic strength regulated by palmitate cycling on PSD-95. *Cell* 108, 849–863.
- Fantini, J., and Barrantes, F. J. (2009). Sphingolipid/cholesterol regulation of neurotransmitter receptor conformation and function. *Biochim. Biophys. Acta - Biomembr.* 1788, 2345–2361.
- Fedorova, I., Hussein, N., Di Martino, C., Moriguchi, T., Hoshida, J., Majchrzak, S., et al. (2007). An n-3 fatty acid deficient diet

- affects mouse spatial learning in the Barnes circular maze. *Prostaglandins Leukot. Essent. Acids* 77, 269–277.
- Fitzner, D., Bader, J. M., Penkert, H., Bergner, C. G., Su, M., Weil, M.-T., et al. (2020). Cell-Type- and Brain-Region-Resolved Mouse Brain Lipidome. *Cell Rep.* 32, 108132.
- Frank, C., Giammaricoli, A. M., Peponi, R., Fiorentini, C., and Rufini, S. (2004). Cholesterol perturbing agents inhibit NMDA-dependent calcium influx in rat hippocampal primary culture. *FEBS Lett.* 566, 25–29.
- Frank, C., Rufini, S., Tancredi, V., Forcina, R., Grossi, D., and D'Arcangelo, G. (2008). Cholesterol depletion inhibits synaptic transmission and synaptic plasticity in rat hippocampus. *Exp. Neurol.* 212, 407–414.
- Fujita, S., Ikegaya, Y., Nishikawa, M., Nishiyama, N., and Matsuki, N. (2001). Docosahexaenoic acid improves long-term potentiation attenuated by phospholipase A2 inhibitor in rat hippocampal slices. *Br. J. Pharmacol.* 132, 1417–1422.
- Fujiwara, T. K., Iwasawa, K., Kalay, Z., Tsunoyama, T. A., Watanabe, Y., Umemura, Y. M., et al. (2016). Confined diffusion of transmembrane proteins and lipids induced by the same actin meshwork lining the plasma membrane. *Mol. Biol. Cell* 27, 1101–1119.
- Fujiwara, T., Ritchie, K., Murakoshi, H., Jacobson, K., and Kusumi, A. (2002). Phospholipids undergo hop diffusion in compartmentalized cell membrane. *J. Cell Biol.* 157, 1071–1081.
- Fukata, Y., Dimitrov, A., Boncompain, G., Vielmeyer, O., Perez, F., and Fukata, M. (2013). Local palmitoylation cycles define activity-regulated postsynaptic subdomains. *J. Cell Biol.* 202, 145–161.
- Fukata, Y., Murakami, T., Yokoi, N., and Fukata, M. (2016). “Local Palmitoylation Cycles and Specialized Membrane Domain Organization,” in *Curr. Top. Membr.* 2016, 97–141.
- García-Morales, V., Montero, F., González-Forero, D., Rodríguez-Bey, G., Gómez-Pérez, L., Medialdea-Wandossell, M. J., et al. (2015). Membrane-Derived Phospholipids Control Synaptic Neurotransmission and Plasticity. *PLoS Biol.* 13:1002153.
- Goncalves, J., Bartol, T. M., Camus, C., Levat, F., Menegolla, A. P., Sejnowski, T. J., et al. (2020). Nanoscale co-organization and coactivation of AMPAR, NMDAR, and mGluR at excitatory synapses. *Proc. Natl. Acad. Sci. U. S. A.* 117, 14503.
- Götz, R., Kunz, T. C., Fink, J., Solger, F., Schlegel, J., Seibel, J., et al. (2020). Nanoscale imaging of bacterial infections by sphingolipid expansion microscopy. *Nat. Commun.* 11, 6173.
- Greaves, J., and Chamberlain, L. H. (2007). Palmitoylation-dependent protein sorting. *J. Cell Biol.* 176, 249–254.
- Guo, Y., Zou, G., Qi, K., Jin, J., Yao, L., Pan, Y., et al. (2021). Simvastatin impairs hippocampal synaptic plasticity and cognitive function in mice. *Mol. Brain* 14, 41.
- Hanson, M. A., Cherezov, V., Griffith, M. T., Roth, C. B., Jaakola, V.-P., Chien, E. Y. T., et al. (2008). A Specific Cholesterol Binding Site Is Established by the 2.8 Å Structure of the Human β 2-Adrenergic Receptor. *Structure* 16, 897–905.
- Haucke, V., and Di Paolo, G. (2007). Lipids and lipid modifications in the regulation of membrane traffic. *Curr. Opin. Cell Biol.* 19, 426–435.
- Hayashi, T., Rumbaugh, G., and Haganir, R. L. (2005). Differential Regulation of AMPA Receptor Subunit Trafficking by Palmitoylation of Two Distinct Sites. *Neuron* 47, 709–723.
- Hayashi, T., Thomas, G. M., and Haganir, R. L. (2009). Dual Palmitoylation of NR2 Subunits Regulates NMDA Receptor Trafficking. *Neuron* 64, 213–226.
- He, C., Qu, X., Cui, L., Wang, J., and Kang, J. X. (2009). Improved spatial learning performance of fat-1 mice is associated with enhanced neurogenesis and neurogenesis by docosahexaenoic acid. *Proc. Natl. Acad. Sci. U. S. A.* 106, 11370–11375.
- Hentschel, A., Zahedi, R. P., and Ahrends, R. (2016). Protein lipid modifications - More than just a greasy ballast. *Proteomics* 16, 759–782.
- Hering, H., Lin, C., and Sheng, M. (2003). Lipid Rafts in the Maintenance of Synapses, Dendritic Spines, and Surface AMPA Receptor Stability. *J. Neurosci.* 23, 3262–3271.
- Hernández-Adame, P. L., Meza, U., Rodríguez-Menchaca, A. A., Sánchez-Armass, S., Ruiz-García, J., and Gomez, E. (2021). Determination of the size of lipid rafts studied through single-molecule FRET simulations. *Biophys. J.* 120, 2287–2295.
- Hou, Q., Huang, Y., Amato, S., Snyder, S. H., Haganir, R. L., and Man, H.-Y. (2008). Regulation of AMPA receptor localization in lipid rafts. *Mol. Cell. Neurosci.* 38, 213–223.
- Igbavboa, U., Hamilton, J., Kim, H. Y., Sun, G. Y., and Wood, W. G. (2002). A new role for apolipoprotein E: Modulating transport of polyunsaturated phospholipid molecular species in synaptic plasma membranes. *J. Neurochem.* 80, 255–261.
- Ingólfsson, H. I., Arnarez, C., Periole, X., and Marrink, S. J. (2016). Computational ‘microscopy’ of cellular membranes. *J. Cell Sci.* 129, 257–268.
- Ingólfsson, H. I., Carpenter, T. S., Bhatia, H., Bremer, P. T., Marrink, S. J., and Lightstone, F. C. (2017). Computational Lipidomics of the Neuronal Plasma Membrane. *Biophys. J.* 113, 2271–2280.
- Itokazu, N., Ikegaya, Y., Nishikawa, M., and Matsuki, N. (2000). Bidirectional actions of docosahexaenoic acid on hippocampal neurotransmissions in vivo. *Brain Res.* 862, 211–216.
- Iuliano, M., Seeley, C., Sapp, E., Jones, E. L., Martin, C., Li, X., et al. (2021). Disposition of Proteins and Lipids in Synaptic Membrane Compartments Is Altered in Q175/Q7 Huntington’s Disease Mouse Striatum. *Front. Synaptic Neurosci.* 13, 618391.
- Jacobson, K., Liu, P., and Lagerholm, B. C. (2019). The Lateral Organization and Mobility of Plasma Membrane Components. *Cell* 177, 806–819.
- Jacobson, K., Mouritsen, O. G., and Anderson, R. G. W. (2007). Lipid rafts: at a crossroad between cell biology and physics. *Nat. Cell Biol.* 9, 7–14.
- Jafurulla, M., Bandari, S., Pucadyil, T. J., and Chattopadhyay, A. (2017). Sphingolipids modulate the function of human serotonin 1A receptors: Insights from sphingolipid-deficient cells. *Biochim. Biophys. Acta - Biomembr.* 1859, 598–604.
- Jeyifous, O., Lin, E. I., Chen, X., Antinone, S. E., Mastro, R., Drisdell, R., et al. (2016). Palmitoylation regulates glutamate receptor distributions in Postsynaptic densities through control of PSD95 conformation and orientation. *Proc. Natl. Acad. Sci. U. S. A.* 113, E8482–E8491.
- Ji, B., and Skup, M. (2021). Roles of palmitoylation in structural long-term synaptic plasticity. *Mol. Brain* 14, 8.
- Kaiser, H. J., Orłowski, A., Róg, T., Nyholm, T. K. M., Chai, W., Feizi, T., et al. (2011). Lateral sorting in model membranes by cholesterol-mediated hydrophobic matching. *Proc. Natl. Acad. Sci. U. S. A.* 108, 16628–16633.
- Kanungo, S., Soares, N., He, M., and Steiner, R. D. (2013). Sterol metabolism disorders and neurodevelopment—an update. *Dev. Disabil. Res. Rev.* 17, 197–210.
- Keith, D. J., Sanderson, J. L., Gibson, E. S., Woolfrey, K. M., Robertson, H. R., Olszewski, K., et al. (2012). Palmitoylation of A-Kinase anchoring protein 79/150 regulates dendritic endosomal targeting and synaptic plasticity mechanisms. *J. Neurosci.* 32, 7119–7136.
- Kinoshita, M., Suzuki, K. G. N., Matsumori, N., Takada, M., Ano, H., Morigaki, K., et al. (2017). Raft-based sphingomyelin interactions revealed by new fluorescent sphingomyelin analogs. *J. Cell Biol.* 216, 1183–1204.

- Klymchenko, A. S., and Kreder, R. (2014). Fluorescent Probes for Lipid Rafts: From Model Membranes to Living Cells. *Chem. Biol.* 21, 97–113.
- Kol, M., Williams, B., Toombs-Ruane, H., Franquelim, H. G., Korneev, S., Schroer, C., et al. (2019). Optical manipulation of sphingolipid biosynthesis using photoswitchable ceramides. *Elife* 8, 43230.
- Komura, N., Suzuki, K. G. N., Ando, H., Konishi, M., Koikeda, M., Imamura, A., et al. (2016). Raft-based interactions of gangliosides with a GPI-anchored receptor. *Nat. Chem. Biol.* 12, 402–410.
- Korinek, M., Gonzalez-Gonzalez, I. M., Smejkalova, T., Hajdukovic, D., Skrenkova, K., Krusek, J., et al. (2020). Cholesterol modulates presynaptic and postsynaptic properties of excitatory synaptic transmission. *Sci. Rep.* 10, 12651.
- Korinek, M., Vyklicky, V., Borovska, J., Lichnerova, K., Kaniakova, M., Krausova, B., et al. (2015). Cholesterol modulates open probability and desensitization of NMDA receptors. *J. Physiol.* 593, 2279–2293.
- Kotti, T. J., Ramirez, D. M. O., Pfeiffer, B. E., Huber, K. M., and Russell, D. W. (2006). Brain cholesterol turnover required for geranylgeraniol production and learning in mice. *Proc. Natl. Acad. Sci. U. S. A.* 103, 3869–3874.
- Koudinov, A. R., and Koudinova, N. V. (2001). Essential role for cholesterol in synaptic plasticity and neuronal degeneration. *FASEB J.* 15, 1858–1860.
- Kumari, R., Castillo, C., and Francesconi, A. (2013). Agonist-dependent signaling by group I metabotropic glutamate receptors is regulated by association with lipid domains. *J. Biol. Chem.* 288, 32004–32019.
- Kusumi, A., Sako, Y., and Yamamoto, M. (1993). Confined lateral diffusion of membrane receptors as studied by single particle tracking (nanovision microscopy). Effects of calcium-induced differentiation in cultured epithelial cells. *Biophys. J.* 65, 2021–2040.
- Kusumi, A., Shirai, Y. M., Koyama-Honda, I., Suzuki, K. G. N., and Fujiwara, T. K. (2010). Hierarchical organization of the plasma membrane: Investigations by single-molecule tracking vs. fluorescence correlation spectroscopy. *FEBS Lett.* 584, 1814–1823.
- Ledesma, M. D., Martin, M. G., and Dotti, C. G. (2012). Lipid changes in the aged brain: Effect on synaptic function and neuronal survival. *Prog. Lipid Res.* 51, 23–35.
- Lenne, P.-F., Wawrzyniec, L., Conchonaud, F., Wurtz, O., Boned, A., Guo, X.-J., et al. (2006). Dynamic molecular confinement in the plasma membrane by microdomains and the cytoskeleton meshwork. *EMBO J.* 25, 3245–3256.
- Levental, I., Levental, K. R., and Heberle, F. A. (2020). Lipid Rafts: Controversies Resolved, Mysteries Remain. *Trends Cell Biol.* 30, 341–353.
- Levental, I., Lingwood, D., Grzybek, M., Coskun, U., and Simons, K. (2010). Palmitoylation regulates raft affinity for the majority of integral raft proteins. *Proc. Natl. Acad. Sci.* 107, 22050–22054.
- Levental, K. R., Lorent, J. H., Lin, X., Skinkle, A. D., Surma, M. A., Stockenbojer, E. A., et al. (2016). Polyunsaturated Lipids Regulate Membrane Domain Stability by Tuning Membrane Order. *Biophys. J.* 110, 1800–1810.
- Levental, K. R., Surma, M. A., Skinkle, A. D., Lorent, J. H., Zhou, Y., Klose, C., et al. (2017). ω -3 polyunsaturated fatty acids direct differentiation of the membrane phenotype in mesenchymal stem cells to potentiate osteogenesis. *Sci. Adv.* 3, eaa01193.
- Li, L., Cao, D., Kim, H., Lester, R., and Fukuchi, K. I. (2006). Simvastatin enhances learning and memory independent of amyloid load in mice. *Ann. Neurol.* 60, 729–739.
- Li, S., Raychaudhuri, S., Lee, S. A., Brockmann, M. M., Wang, J., Kusick, G., et al. (2021). Asynchronous release sites align with NMDA receptors in mouse hippocampal synapses. *Nat. Commun.* 12, 21004.
- Li, T. P., and Blanpied, T. A. (2016). Control of Transmembrane Protein Diffusion within the Postsynaptic Density Assessed by Simultaneous Single-Molecule Tracking and Localization Microscopy. *Front. Synaptic Neurosci.* 8, 1–14.
- Li, T. P., Song, Y., MacGillavry, H. D., Blanpied, T. A., and Raghavachari, S. (2016). Protein Crowding within the Postsynaptic Density Can Impede the Escape of Membrane Proteins. *J. Neurosci.* 36, 4276–4295.
- Lorent, J. H., Diaz-Rohrer, B., Lin, X., Spring, K., Gorf, A. A., Levental, K. R., et al. (2017). Structural determinants and functional consequences of protein affinity for membrane rafts. *Nat. Commun.* 8, 1219.
- Ma, L., Huang, Y. Z., Pitcher, G. M., Valtschanoff, J. G., Ma, Y. H., Feng, L. Y., et al. (2003). Ligand-dependent recruitment of the ErbB4 signaling complex into neuronal lipid rafts. *J. Neurosci.* 23, 3164–3175.
- MacGillavry, H. D., Song, Y., Raghavachari, S., and Blanpied, T. A. (2013). Nanoscale Scaffolding Domains within the Postsynaptic Density Concentrate Synaptic AMPA Receptors. *Neuron* 78, 615–622.
- Mackawa, M. (2017). Domain 4 (D4) of Perfringolysin O to Visualize Cholesterol in Cellular Membranes—The Update. *Sensors* 17, 504.
- Magee, T., and Seabra, M. C. (2005). Fatty acylation and prenylation of proteins: what's hot in fat. *Curr. Opin. Cell Biol.* 17, 190–196.
- Maggo, S., and Ashton, J. C. (2014). Effects of HMG-CoA reductase inhibitors on learning and memory in the guinea pig. *Eur. J. Pharmacol.* 723, 294–304.
- Mans, R. A., Chowdhury, N., Cao, D., McMahon, L. L., and Li, L. (2010). Simvastatin enhances hippocampal long-term potentiation in C57BL/6 mice. *Neuroscience* 166, 435–444.
- Marlow, B., Kuenze, G., Li, B., Sanders, C. R., and Meiler, J. (2021). Structural determinants of cholesterol recognition in helical integral membrane proteins. *Biophys. J.* 120, 1592–1604.
- Martin, M. G., Ahmed, T., Korovaichuk, A., Venero, C., Menchón, S. A., Salas, I., et al. (2014). Constitutive hippocampal cholesterol loss underlies poor cognition in old rodents. *EMBO Mol. Med.* 6, 902–917.
- Martin, M. G., Prieger, F., and Dotti, C. G. (2014). Cholesterol in brain disease: sometimes determinant and frequently implicated. *EMBO Rep.* 15, 1036–1052.
- Martin, S. J., Grimwood, P. D., and Morris, R. G. M. (2000). Synaptic plasticity and memory: an evaluation of the hypothesis. *Neurosci.* 23, 649–711.
- Mazzocchi-Jones, D. (2015). Impaired corticostriatal LTP and depotentiation following iPLA2 inhibition is restored following acute application of DHA. *Brain Res. Bull.* 111, 69–75.
- McGahon, B. M., Martin, D. S. D., Horrobin, D. F., and Lynch, M. A. (1999). Age-related changes in synaptic function: analysis of the effect of dietary supplementation with ω -3 fatty acids. *Neuroscience* 94, 305–314.
- Milovanovic, D., Honigsmann, A., Koike, S., Göttfert, F., Pähler, G., Junius, M., et al. (2015). Hydrophobic mismatch sorts SNARE proteins into distinct membrane domains. *Nat. Commun.* 6, 1–10.
- Mirnikjoo, B., Brown, S. E., Kim, H. F. S., Marangell, L. B., Sweatt, J. D., and Weeber, E. J. (2001). Protein Kinase Inhibition by ω -3 Fatty Acid. *J. Biol. Chem.* 276, 10888–10896.
- Mitroi, D. N., Pereyra-Gómez, G., Soto-Huelin, B., Senovilla, F., Kobayashi, T., Esteban, J. A., et al. (2019). NPC1 enables cholesterol mobilization during long-term potentiation that can be restored in Niemann-Pick disease type C by CYP46A1 activation. *EMBO Rep.* 20, e48143.

- Mizuno, H., Abe, M., Dedecker, P., Makino, A., Rocha, S., Ohno-Iwashita, Y., et al. (2011). Fluorescent probes for super-resolution imaging of lipid domains on the plasma membrane. *Chem. Sci.* 2, 1548.
- Mobarak, E., Javanainen, M., Kulig, W., Honigmann, A., Sezgin, E., Aho, N., et al. (2018). How to minimize dye-induced perturbations while studying biomembrane structure and dynamics: PEG linkers as a rational alternative. *Biochim. Biophys. Acta - Biomembr.* 1860, 2436–2445.
- Mohamed, A., Shah, A. D., Chen, D., and Hill, M. M. (2019). RaftProt V2: understanding membrane microdomain function through lipid raft proteomes. *Nucleic Acids Res.* 47, D459–D463.
- Mouritsen, O. G., and Bloom, M. (1984). Mattress model of lipid-protein interactions in membranes. *Biophys. J.* 46, 141–153.
- Muro, E., Atilla-Gokcumen, G. E., and Eggert, U. S. (2014). Lipids in cell biology: how can we understand them better? *Mol. Biol. Cell* 25, 1819–1823.
- Nair, D., Hossy, E., Petersen, J. D., Constals, A., Giannone, G., Choquet, D., et al. (2013). Super-Resolution Imaging Reveals That AMPA Receptors Inside Synapses Are Dynamically Organized in Nanodomains Regulated by PSD95. *J. Neurosci.* 33, 13204–13224.
- Ngamukote, S., Yanagisawa, M., Ariga, T., Ando, S., and Yu, R. K. (2007). Developmental changes of glycosphingolipids and expression of glycogenes in mouse brains. *J. Neurochem.* 103, 2327–2341.
- Nishikawa, M., Kimura, S., and Akaike, N. (1994). Facilitatory effect of docosahexaenoic acid on N-methyl-D-aspartate response in pyramidal neurones of rat cerebral cortex. *J. Physiol.* 475, 83–93.
- Obaid, A. L., Loew, L. M., Wuskell, J. P., and Salzberg, B. M. (2004). Novel naphthylstyryl-pyridinium potentiometric dyes offer advantages for neural network analysis. *J. Neurosci. Methods* 134, 179–190.
- Pérez-Cañamás, A., Benvegnù, S., Rueda, C. B., Rábano, A., Satrustegui, J., and Ledesma, M. D. (2017). Sphingomyelin-induced inhibition of the plasma membrane calcium ATPase causes neurodegeneration in type A Niemann–Pick disease. *Mol. Psychiatry* 22, 711–723.
- Perez, A.-S., and Bredt, D. S. (1998). The N-terminal PDZ-containing region of postsynaptic density-95 mediates association with caveolar-like lipid domains. *Neurosci. Lett.* 258, 121–123.
- Petrov, A. M., Kasimov, M. R., and Zefirov, A. L. (2016). Brain cholesterol metabolism and its defects: Linkage to neurodegenerative diseases and synaptic dysfunction. *Acta Naturae* 8, 58–73.
- Pike, L. J. (2006). Rafts defined: a report on the Keystone symposium on lipid rafts and cell function. *J. Lipid Res.* 47, 1597–1598.
- Pike, L. J. (2009). The challenge of lipid rafts. *J. Lipid Res.* 50, S323–S328.
- Purkey, A. M., Woolfrey, K. M., Crosby, K. C., Stich, D. G., Chick, W. S., Aoto, J., et al. (2018). AKAP150 Palmitoylation Regulates Synaptic Incorporation of Ca2+-Permeable AMPA Receptors to Control LTP. *Cell Rep.* 25, 974–987.e4.
- Renner, M., Choquet, D., and Triller, A. (2009a). Control of the Postsynaptic Membrane Viscosity. *J. Neurosci.* 29, 2926–2937.
- Renner, M. L., Cognet, L., Lounis, B., Triller, A., and Choquet, D. (2009b). The excitatory postsynaptic density is a size exclusion diffusion environment. *Neuropharmacology* 56, 30–36.
- Resh, M. D. (2016). “Lipid Modification of Proteins,” in *Biochemistry of Lipids, Lipoproteins and Membranes* (Elsevier), 391–414.
- Saffman, P. G., and Delbrück, M. (1975). Brownian motion in biological membranes. *Proc. Natl. Acad. Sci. U. S. A.* 72, 3111–3113.
- Saxton, M. J. (1993). Lateral diffusion in an archipelago. Single-particle diffusion. *Biophys. J.* 64, 1766–1780.
- Sezgin, E., Levental, I., Mayor, S., and Eggeling, C. (2017). The mystery of membrane organization: Composition, regulation and roles of lipid rafts. *Nat. Rev. Mol. Cell Biol.* 18, 361–374.
- Sidestein, S. C., D’Este, E., Böhm, M. J., Danzl, J. G., Belov, V. N., and Hell, S. W. (2016). Multicolour Multilevel STED nanoscopy of Actin/Spectrin Organization at Synapses. *Sci. Rep.* 6, 26725.
- Simons, K., and Ikonen, E. (1997). Functional rafts in cell membranes. *Nature* 387, 569–572.
- Simson, R., Sheets, E. D., and Jacobson, K. (1995). Detection of temporary lateral confinement of membrane proteins using single-particle tracking analysis. *Biophys. J.* 69, 989–993.
- Singer, S. J., and Nicolson, G. L. (1972). The Fluid Mosaic Model of the Structure of Cell Membranes. *Science* 175, 720–731.
- Sodero, A. O., Vriens, J., Ghosh, D., Stegner, D., Brachet, A., Pallotto, M., et al. (2012). Cholesterol loss during glutamate-mediated excitotoxicity. *EMBO J.* 31, 1764–1773.
- Sun, D., Fan, X., Shi, Y., Zhang, H., Huang, Z., Cheng, B., et al. (2021). Click-EXM enables expansion microscopy for all biomolecules. *Nat. Methods* 18, 107–113.
- Suzuki, T. (2002). Lipid rafts at postsynaptic sites: distribution, function and linkage to postsynaptic density. *Neurosci. Res.* 44, 1–9.
- Suzuki, T., Ito, J. I., Takagi, H., Saitoh, F., Nawa, H., and Shimizu, H. (2001). Biochemical evidence for localization of AMPA-type glutamate receptor subunits in the dendritic raft. *Mol. Brain Res.* 89, 20–28.
- Suzuki, T., Zhang, J., Miyazawa, S., Liu, Q., Farzan, M. R., and Yao, W.-D. (2011). Association of membrane rafts and postsynaptic density: proteomics, biochemical, and ultrastructural analyses. *J. Neurochem.* 119, 64–77.
- Swanwick, C. C., Shapiro, M. E., Yi, Z., Chang, K., and Wenthold, R. J. (2009). NMDA receptors interact with flotillin-1 and -2, lipid raft-associated proteins. *FEBS Lett.* 583, 1226–1230.
- Swilius, M. T., Farley, M. M., Bryant, M. A., and Waxham, M. N. (2012). Electron cryotomography of postsynaptic densities during development reveals a mechanism of assembly. *Neuroscience* 212, 19–29.
- Takeuchi, T., Duszkievicz, A. J., and Morris, R. G. M. (2014). The synaptic plasticity and memory hypothesis: Encoding, storage and persistence. *Philos. Trans. R. Soc. B Biol. Sci.* 369, 288.
- Tang, A.-H., Chen, H., Li, T. P., Metzbowler, S. R., MacGillavry, H. D., and Blanpied, T. A. (2016). A trans-synaptic nanocolumn aligns neurotransmitter release to receptors. *Nature* 536, 210–214.
- Topinka, J. R., and Bredt, D. S. (1998). N-terminal palmitoylation of PSD-95 regulates association with cell membranes and interaction with K⁺ channel K(v)1.4. *Neuron* 20, 125–134.
- Tsutsumi, R., Fukata, Y., and Fukata, M. (2008). Discovery of protein-palmitoylating enzymes. *Pflügers Arch. - Eur. J. Physiol.* 456, 1199–1206.
- Tulodziecka, K., Diaz-Rohrer, B. B., Farley, M. M., Chan, R. B., Di Paolo, G., Levental, K. R., et al. (2016). Remodeling of the postsynaptic plasma membrane during neural development. *Mol. Biol. Cell* 27, 3480–3489.
- van der Kant, R., Langness, V. F., Herrera, C. M., Williams, D. A., Fong, L. K., Leestemaker, Y., et al. (2019). Cholesterol Metabolism Is a Druggable Axis that Independently Regulates Tau and Amyloid- β in iPSC-Derived Alzheimer’s Disease Neurons. *Cell Stem Cell* 24, 363–375.e9.
- van Deventer, S., Arp, A. B., and van Spruel, A. B. (2021). Dynamic Plasma Membrane Organization: A Complex Symphony. *Trends Cell Biol.* 31, 119–129.
- Wang, D., and Zheng, W. (2015). Dietary cholesterol concentration affects synaptic plasticity and dendrite spine morphology of rabbit hippocampal neurons. *Brain Res.* 1622, 350–360.

- Wassall, S. R., and Stillwell, W. (2009). Polyunsaturated fatty acid-cholesterol interactions: Domain formation in membranes. *Biochim. Biophys. Acta - Biomembr.* 1788, 24–32.
- Woolfrey, K. M., Sanderson, J. L., and Dell'Acqua, M. L. (2015). The palmitoyl acyltransferase DHHC2 regulates recycling endosome exocytosis and synaptic potentiation through palmitoylation of AKAP79/150. *J. Neurosci.* 35, 442–456.
- Yang, G., Xiong, W., Kojic, L., and Cynader, M. S. (2009). Subunit-selective palmitoylation regulates the intracellular trafficking of AMPA receptor. *Eur. J. Neurosci.* 30, 35–46.
- Yokoi, N., Fukata, Y., Sekiya, A., Murakami, T., Kobayashi, K., and Fukata, M. (2016). Identification of PSD-95 depalmitoylating enzymes. *J. Neurosci.* 36, 6431–6444.
- Young, C., Gean, P. W., Wu, S. P., Lin, C. H., and Shen, Y. Z. (1998). Cancellation of low-frequency stimulation-induced long-term depression by docosahexaenoic acid in the rat hippocampus. *Neurosci. Lett.* 247, 198–200.
- Zhang, D., Watson, J. F., Matthews, P. M., Cais, O., and Greger, I. H. (2021). Gating and modulation of a hetero-octameric AMPA glutamate receptor. *Nature* 594, 454–458.

3



Single-molecule localization microscopy of subcellular protein distribution in neurons

Jelmer Willems*, Manon Westra* and Harold D. MacGillavry

Methods in Molecular Biology (2022), 2440, 271–288

Cell Biology, Neurobiology and Biophysics, Department of Biology,
Faculty of Science, Utrecht University, Utrecht, The Netherlands

* These authors contributed equally to this work

Abstract

Over the past years several forms of superresolution fluorescence microscopy have been developed that offer the possibility to study cellular structures and protein distribution at a resolution well below the diffraction limit of conventional fluorescence microscopy (<200 nm). A particularly powerful superresolution technique is single-molecule localization microscopy (SMLM). SMLM enables the quantitative investigation of subcellular protein distribution at a spatial resolution up to tenfold higher than conventional imaging, even in live cells. Not surprisingly, SMLM has therefore been used in many applications in biology, including neuroscience. This chapter provides a step-by-step SMLM protocol to visualize the nanoscale organization of endogenous proteins in dissociated neurons but can be extended to image other adherent cultured cells. We outline a number of methods to visualize endogenous proteins in neurons for live-cell and fixed application, including immunolabeling, the use of intrabodies for live-cell SMLM, and endogenous tagging using CRISPR/Cas9.

Key words

Superresolution microscopy, Single-molecule localization microscopy, Stochastic optical reconstruction microscopy, Photoactivated localization microscopy, Neuron, Synapse

1. Introduction

Fluorescence microscopy is instrumental for the investigation of subcellular protein organization which is critical to understand cellular function in health and disease. The development of superresolution microscopy techniques such as single-molecule localization microscopy (SMLM) has tremendously increased the ability to resolve protein distribution achieving resolution below 30 nm. SMLM relies on the sequential acquisition of sparse, single emitting fluorophores that label a structure of interest. The spatial isolation of individual fluorescent events allows the accurate localization of the center point of each emission event with nanometer precision. Together, the spatial coordinates of individual localizations accumulated over thousands of frames are used to reconstruct a superresolved image [1] (Fig. 1a). Importantly, in SMLM the resolution of the image is no longer determined by the diffraction limit but relies on the localization precision of fluorophores and the density of localized molecules that label the structure of interest. The localization precision (σ) is determined by a number of factors such as background noise and pixel size [2], but is mostly dependent on the number of photons (N) emitted by the fluorophore as:

$$\sigma = \frac{1}{\sqrt{N}}$$

The localization density equally contributes to the resolving power: too few localizations will result in a poor reconstruction of the structure of interest. This can be formalized based on the Nyquist-Shannon sampling criterium such that to achieve a certain resolution, fluorophores have to be sampled at a density at least twice as high as the desired spatial frequency [3]. It is therefore important to optimize labeling strategies to achieve a high labeling density.

In the recent years, a multitude of SMLM approaches have been developed, including techniques such as photoactivated localization microscopy (PALM) [4, 5], (direct) stochastic

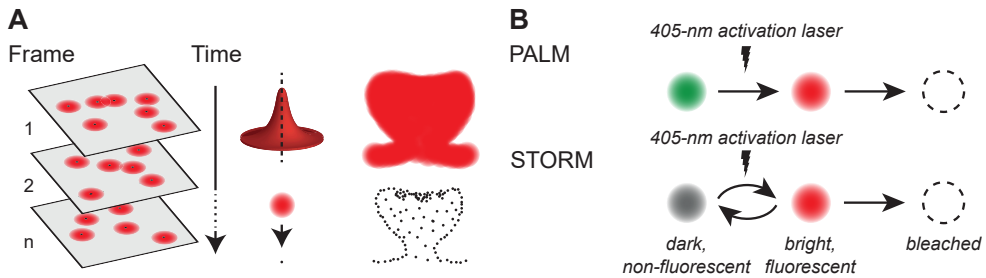


Figure 1. Principle of single-molecule localization microscopy.

(a) Single emitters are recorded over a large number of frames. Each identified event is fitted to localize the centroid position of the fluorophore. Together, these localizations form the reconstructed image, which is no longer diffraction limited. (b) PALM: fluorophores change their emission spectrum upon activation with 405-nm laser. STORM: fluorophores can reversibly switch between dark, nonemissive and bright, emissive states in a stochastic manner

optical reconstruction microscopy (d)STORM) [6, 7], point accumulation for imaging in nanoscale topography (PAINT) [8] and MINIFLUX [9]. Here, we will describe the use of PALM and (d)STORM (Fig. 1b). In PALM, a low-power activation laser is used to stochastically photoactivate or photoconvert subsets of fluorescent proteins in the active state. The most commonly used fluorescent protein is mEos3.2, which switches from green to red fluorescence upon illumination by 405 nm light and yields relatively high photon counts [10]. In (d)STORM reversible blinking of organic dyes is induced by high-intensity laser power under reducing buffer conditions resulting in the reversible transition of the fluorophores into a long-lived dark state [11, 12]. Organic dyes can be coupled to a protein of interest via dye-conjugated antibodies or using self-labeling enzymes like Halo- [13], SNAP- [14], and CLIP-tags [15]. Dyes suitable for dSTORM include but are not limited to Alexa 647 and JF646 (*see Note 1*).

The different SMLM approaches each have their own advantages and disadvantages and the choice for the optimal technique ultimately depends on the goal of the experiment and which type of results would allow for testing the hypothesis [16–18]. This is especially true for SMLM experiments, which often involve extensive postimaging analysis [19]. For example, STORM imaging usually yields more localization events than PALM due to signal amplification by immunolabeling. Also, the organic dyes used for STORM imaging yield a higher photon count, and thus generally result in a higher localization precision [10, 12]. On the other hand, PALM imaging is compatible with live-cell imaging, and does not require fixation and additional labeling steps, and thus effectively preserves ultrastructure.

For every fluorescence imaging technique, but particularly for SMLM, the method used to label a protein of interest is critical, as the quality of the final image depends on the properties of the fluorophore, coupling distance of the fluorophore to the protein of interest and labeling density but is also highly sensitive to experimental alterations that affect protein organization [20, 21]. Ideally, the labeling strategy should thus allow the visualization of endogenously expressed proteins using a small tag or label that yields a high signal to noise ratio, and that preserves the cellular ultrastructure (*also see Note 2*). We recently developed a CRISPR/Cas9-based genome editing toolbox that enables the accurate tagging of endogenous proteins in neurons, allowing the investigation of native protein complexes [22]. Importantly, this approach omits the need for specific antibodies and does not rely on overexpression of proteins that could have adverse effects.

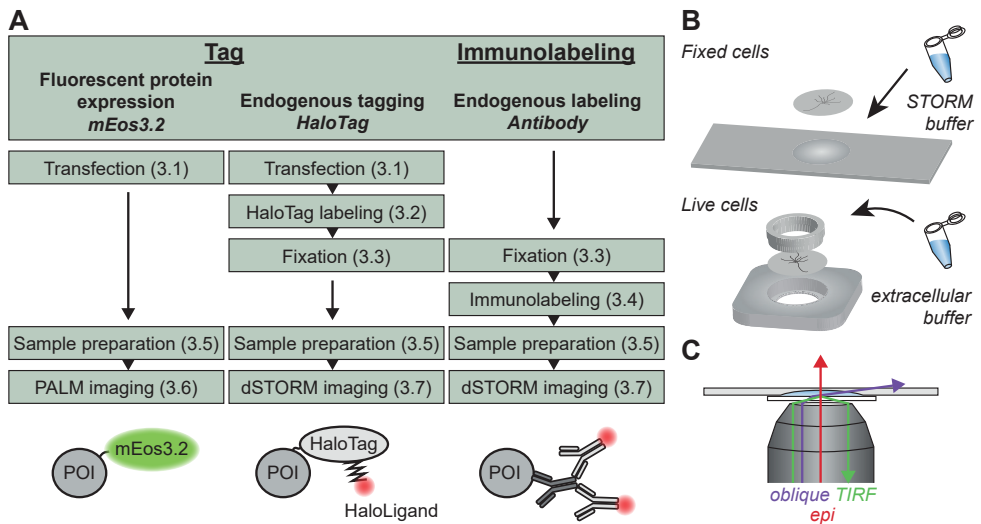


Figure 2. SMLM experimental workflow.

(a) Experimental workflow for 1. PALM imaging of mEos3.2, 2. dSTORM imaging of Halotag on endogenously tagged proteins, and 3. dSTORM imaging of endogenously labeled proteins. (b) Top: mounting of the coverslip upside down on a concave slide filled with STORM buffer. Bottom: mounting of the coverslip with live cells in a Ludin chamber with extracellular buffer on top. (c) Visualizing the different angles of the laser through the sample for epifluorescence, oblique illumination and TIRF imaging. POI, protein of interest

Here we describe a SMLM protocol with three parallel workflows, each using a different labeling strategy (1) live-cell PALM using expression of mEos3.2-fused intrabodies recognizing the synaptic scaffold protein PSD-95 [23], and dSTORM making use of either (2) endogenous tagging with HaloTag [13, 22], or (3) conventional labeling using antibodies (Fig. 2a). This protocol aims to provide a starting point for setting up SMLM experiments and thus elaborates on several important experimental steps in Subheading 4. Additionally, we describe several considerations for data processing and visualization steps. As examples, the approaches are used to superresolve the distribution of endogenous synaptic receptor proteins and their scaffolds in dissociated hippocampal rat neurons, but the described methodologies are, in principle, applicable to other adherent cell types.

2. Materials

2.1 Cell Culture and Transfection

1. Dissociated rat hippocampal cultures on 18-mm coverslips in 1 mL neuronal culture medium.
2. BrainPhys neuronal medium.
3. BP full medium: BrainPhys neuronal medium, 2% (v/v) NeuroCult SM1 neuronal supplement and 1% penicillin-streptomycin.
4. BP incubation medium: BrainPhys neuronal medium, 0.5 mM L-glutamine.



5. Lipofectamine 2000.
6. Water bath 37 °C.
7. Cell culture incubator (37 °C, 5% CO₂).
8. DNA plasmids: pORANGE GluA1-HaloTag knock-in [22] and PSD95.FingR-mEos3.2 [23].

2.2 HaloTag Labeling

1. HaloLigand-JF646 stock: 140 µg/mL in DMSO. Store as 1 µL single-use aliquots at -20 °C. Protect from direct light.
2. Humidified incubation chamber (plastic tray, wrapped in aluminum foil and with some moist tissues).

2.3 Fixation and Immunolabeling

1. PEM buffer: 80 mM PIPES, 2 mM MgCl₂, 5 mM EGTA, pH 6.8. Filter before use (<0.3 µm filter). Store at 4 °C for a maximum of 2 weeks.
2. PFA (EM grade 32% glass ampoule). After opening, store at 4 °C in a closed tube. Warning: PFA is toxic, and quite volatile. Take proper safety precautions.
3. Fixative PEM-PFA: Dilute PFA 1:8 in PEM buffer to obtain a 4% PFA solution. Prepare fresh.
4. Phosphate buffered saline (PBS).
5. PBS-Gly: 0.1 M glycine in PBS.
6. Blocking buffer (prepare fresh): 10% (v/v) normal goat serum (NGS), 0.1% (v/v) Triton X-100 in PBS-Gly.
7. Antibody buffer (prepare fresh): 5% (v/v) normal goat serum (NGS), 0.1% (v/v) Triton X-100 in PBS-Gly.
8. Humidified incubation chamber (plastic tray, wrapped in aluminum foil and with some moist tissues).
9. Primary antibody: mouse anti-Bassoon (Enzo, RRID AB_10618753).
10. Secondary antibody: goat anti-mouse Alexa 647.

2.4 Imaging Buffers and Mounting

1. GLOX: 70 mg/mL glucose oxidase, 4 mg/mL catalase in PBS. Snap-freeze ~10 µL aliquots and store at -80 °C for up to a year. Keep thawed aliquots for maximum 1 week at 4 °C.
2. MEA stock: 1 M cysteamine in 150 mM HCl. Store as ~10 µL single-use aliquots at -80 °C for maximum 1 year. MEA is sensitive to oxygen. Prevent exposure of the powder or dissolved solution to air as much as possible.

3. Tris-glucose buffer: 50 mM Tris, 10 mM NaCl, 10% (w/v) glucose, pH 8.0. Filter through 0.2 μm filter. Store at 4 °C for up to 2 weeks, but check before use as the glucose in this buffer makes it prone to contamination.
4. STORM-buffer (prepare fresh for each coverslip, just before mounting): Add 1 μL GLOX and 0.5–2 μL MEA to 100 μL Tris-glucose buffer. Preferably, prewarm the Tris-glucose buffer.
5. Extracellular buffer: 10 mM HEPES, 120 mM NaCl, 3 mM KCl, 2 mM CaCl_2 , 2 mM MgCl_2 , 10 mM glucose, pH 7.35. Store at 4 °C for up to 2 weeks, but check before use as the glucose in this buffer makes it prone to contamination.
6. Concave mounting slide (for dSTORM) (Fig. 2b).
7. Vacuum pump.
8. Ludin chamber/imaging ring (for PALM) (Fig. 2b).

2.5 Microscope Setup

The imaging system described here is the setup used in our laboratory but can serve as an example to lay out the principal requirements for a suitable microscope setup. We use the commercially available Nanoimager microscope (Oxford Nanoimaging; ONI), equipped with a 100 \times oil-immersion objective (Olympus Plan Apo, NA 1.4) and a XYZ closed-loop piezo stage. Imaging lasers are 561 nm and 640 nm (>200 mW). Activation laser is 405 nm (>50 mW). An adjustable mirror for adjusting the angle of illumination. Camera for fluorescence detection: sCMOS (ORCA Flash 4, Hamamatsu), with an effective pixel size of 117 nm (*see Note 3*). Integrated filters are used to split far-red emission onto the right side of the camera and blue-green-red emission spectra on the left side. The imaging chamber can be temperature controlled. Continuous feedback control over the focus position is critical. This is built into some microscope models (as is the case for the Nanoimager), or can be added with separate accessories.

2.6 Software

Integrated ONI software is used for detection and fitting of single-molecule blinking events. Alternatively, freely available options can be used: 3D-Daostorm [24], Picasso [25], Thunderstorm [26], DoM [27], ZOLA-3D [28], Fit3Dspline (integrated into SMAP) [29], SMAP [30], and Decode [31]. For additional processing steps, we use MATLAB.

3. Methods

All steps are performed at room temperature, unless mentioned otherwise. See Fig. 2a for a flowchart indicating which steps to follow for each individual method.

For direct labeling with antibodies, go to Subheading 3.3.

3.1 Transfection of Dissociated Hippocampal Rat Neurons

Perform all steps in a sterile flow hood. DNA plasmids for the generation of a Halo knock-in are transfected on day in vitro (DIV) 3, and those expressing an intrabody on DIV 14 (*see Note 4*).



1. Prepare fresh 300 μL BP incubation medium and 500 μL BP full medium for each coverslip to be transfected. Warm to 37 $^{\circ}\text{C}$.
2. Prepare the lipofectamine mix by diluting 3.3 μL Lipofectamine 2000 in 100 μL BrainPhys neuronal medium (without supplements) per coverslip to be transfected. Incubate for 5 min at room temperature.
3. For each coverslip, prepare a 1.5 mL microtube with 1 μg of DNA and add 100 μL BrainPhys neuronal medium (without supplements).
4. Add the lipofectamine mix to the DNA mix, gently mix using a pipette and incubate 30 min. DNA-Lipofectamine complex is stable for several hours at room temperature.
5. Transfer 50% (500 μL) of the conditioned medium from each well to a new 12-wells plate. Add 500 μL fresh BP full medium to each well of this new plate. Place this 'new plate' in the incubator.
6. Add 300 μL BP incubation medium to each coverslip with neurons.
7. Using a pipette, gently drop the DNA-Lipofectamine mix onto the cells and place the plate in the incubator for 1–2 h.
8. Transfer the coverslips to the 'new plate'.
9. Grow the neurons until DIV 21. Refresh half the medium with new BP full medium once a week.

For HaloTag labeling, go to Subheading 3.2. For PALM imaging, go to Subheading 3.5.

3.2 Live-Cell HaloTag Labeling

See **Note 5** for more information about self-labeling enzymes.

During the labeling procedure, prevent exposure to direct light as much as possible.

1. Prepare an incubation chamber with a piece of parafilm.
2. Dilute the HaloLigand (JF646) 1:1000 in conditioned medium (1 mL medium is enough for 12 coverslips). Mix well by pipetting up and down.
3. Place drops of ~ 80 μL on the parafilm and gently place the coverslips upside down on these drops. Place the incubation chamber in the incubator (37 $^{\circ}\text{C}$, 5% CO_2) for 15 min.
4. Transfer the coverslips back to the conditioned medium and continue with fixation (Subheading 3.3) (see **Note 5**).

3.3 Fixation

See **Note 6** for more information about the importance of fixation and other methods.

1. Freshly prepare and prewarm PEM-PFA mixture at 37 $^{\circ}\text{C}$.
2. Remove medium from cells using a vacuum pump and add 500 μL fixative to the coverslip. Perform this step according to the PFA MSDS and handling protocols.
3. Incubate for 5–10 min with PEM-PFA.
4. Wash 3 times 5 min with PBS-Gly (1 mL). Samples can be stored and kept stable for several days at 4 $^{\circ}\text{C}$ in PBS.

In case of no antibody staining, go to Subheading 3.5.

3.4 Immunolabeling

1. Incubate coverslips with ~250 μL blocking buffer and incubate for 1 h at 37 °C (*see Note 7*).
2. Prepare primary antibody dilutions in antibody buffer (50 μL per coverslip).
3. Prepare an incubation chamber with parafilm. Place drops (~50 μL) with the antibody mixture on the parafilm and gently place the coverslips upside down on the drops.
4. Incubate for 2 h at room temperature or overnight at 4 °C (*see Note 7*).
5. Wash three times 5 min with PBS-Gly.
6. Dilute secondary Alexa 647-conjugated antibodies 1:400 in antibody buffer (50 μL per coverslip).
7. Incubate the coverslips as in **step 3** for 1 h (at room temperature).
8. Wash three times 5 min with PBS-Gly.
9. Postfixation (optional): Wash once with PBS (no glycine) and perform another fixation with PEM-PFA for 5 min, and wash three times with PBS-Gly (*see Note 8*).
10. Store the coverslips in PBS until mounting. Samples remain stable for several days if kept at 4 °C and protected from light.

3.5 Sample Preparation and Mounting

3.5.1 Live-Cell PALM

1. Preheat the microscope chamber to 37 °C.
2. Preheat extracellular buffer to 37 °C and filter (<0.3 μm filter).
3. Mount the coverslip in an imaging ring or Ludin chamber (Fig. 2b). Gently wash the coverslip once with extracellular buffer before adding up to 500 μL of extracellular buffer as final volume. Handle cells with care, try to avoid cells from drying and pipette slowly.
4. Continue at Subheading 3.6.

3.5.2 dSTORM

1. Preheat the microscope chamber to 30 °C (*see Note 9*).
2. Prepare fresh STORM buffer (prepare just before mounting to prevent too much exposure to air).
3. Put 100 μL STORM buffer on the concave slide and place the coverslip upside down, with the cells facing the buffer (Fig. 2b).
4. Use tweezers or a pipette tip to stabilize the coverslip. Using a vacuum pump, remove excess buffer surrounding the coverslip. Next, gently apply some pressure on top of the coverslip and remove excess buffer. Relieve the pressure slowly. Try to prevent



air bubbles from entering the buffer. The coverslip should now be stably fixed to the microscope slide.

5. Continue at Subheading 3.7.

3.6 PALM Imaging

1. Locate the transfected mEos3.2-positive cell using low laser powers or light source (488-nm wavelength). Avoid long exposures, as mEos3.2 is prone to photobleaching and will be converted by 488-nm light.
2. Set acquisition parameters: The number of frames depends largely on the number of blinking events that can be detected over time. Usually, this is somewhere between 5000 and 20,000 frames. The exposure time and frame rate are of major importance for the quality of the acquisitions. For PALM imaging, we usually take a 50-ms (20 Hz) frame rate (*see Note 10*).
3. Set the angle of the laser to obtain oblique illumination (Fig. 2c) (*see Note 11*).
4. Optional: Make a snapshot of the mEos3.2 using the 488-nm laser (at low laser power). We do not recommend this for low-expressing proteins for the same reason as mentioned at **step 1** in Subheading 3.6. Alternatively, use a cotransfected marker in the far-red channel. Obtaining a diffraction-limited image can be useful for comparison with the superresolution image later on.
5. Turn on the 561-nm laser. At first, single-molecule switching events will occur without usage of the 405-nm activation laser. Suitable 561 nm laser intensity should be balanced based on the sample, with the goal being the observation of clear single-molecule events. When this is the case, start the acquisition.
6. Gradually increase 405-nm laser intensity to enhance the conversion of green to red fluorescence, but make sure the blinking events do not become too dense and start to overlap.
7. Export the acquisition as a multilayer TIF file. Continue at Subheading 3.8.

3.7 dSTORM Imaging (on Alexa 647 or HaloLigand JF646)

1. Locate cells using low laser power light source.
2. Set acquisition parameters: The number of frames depends largely on the number of blinking events that can be detected over time. Usually, this is somewhere between 5000 and 20,000 frames. The exposure time and frame rate are of major importance for the quality of the acquisitions. For STORM, we usually take a 50-ms (20 Hz) frame rate (*see Note 10*).
3. Set the angle of the laser to obtain oblique illumination (Fig. 2c) (*see Note 11*).
4. Optional: Make a snapshot using the 640-nm laser (at low laser power). Alternatively, use a cotransfected marker in the green or red channel. Obtaining a diffraction-limited image can be useful for comparison with the superresolution image later on.

5. Turn on 640-nm laser. With high laser power, try to get most fluorophores to the dark state. Initially, and especially for samples with high labeling density, this might require slightly higher laser powers than required for imaging (*see* **Note 12**).
6. Start the acquisition as soon as blinking events can be clearly identified as individual emission events.
7. Gradually increase 405-nm laser intensity to increase the number of blinking events per frame, but make sure the blinking events do not become too dense and start to overlap.
8. When finished, export the acquisition as multilayer TIF file.

3.8 Data Processing

1. Detection and fitting of single molecules can be performed using a broad range of freely available software packages. We use ONI software integrated as part of the Nanoimager system. The software detects single emission events and uses fitting routines to estimate the coordinates of the molecules (Fig. 1a). The output is usually a results table, containing the coordinates of each fitted localization, together with parameters like the frame number, photon count and localization precision. Alternative and freely available software options are provided in Subheading 2.5.
2. Drift correction: As SMLM acquisitions take minutes to acquire, lateral drift can occur. Drift correction is a feature integrated in most processing software tools.
3. Filtering recurrent localizations (optional but strongly advised): Although many single-molecule emission events are short-lived, they can still be in the 'on state' for consecutive frames. To correct for this, these localizations can be filtered out, or merged. This feature is integrated in most processing software. If this step results in a significant reduction in the number of localizations, consider imaging with longer exposure time and higher laser power (*see* **Note 10**).
4. Filtering on localization precision: Considered one of the most important filtering steps, filtering on localization precision allows for the removal of localization events that are either the result of noise or overlapping localizations. Alternatively, or in addition to, filtering on the shape of the Gaussian can be performed. The latter being helpful in removing overlapping emission events. We usually filter out all localizations with a localization precision of >15 nm for STORM and >25 nm for PALM imaging. This difference has to do with the fact that organic dyes provide more photons per emission event compared to fluorescent proteins, and thus a better average localization precision.
5. Filtering on photon count: Additional filtering on photon count might help to reduce the amount of noise in the dataset due to localizations derived from nonemission events. Note that localizations with a low photon count often have a low localization precision as well and most are probably filtered out when filtering just on the localization precision.

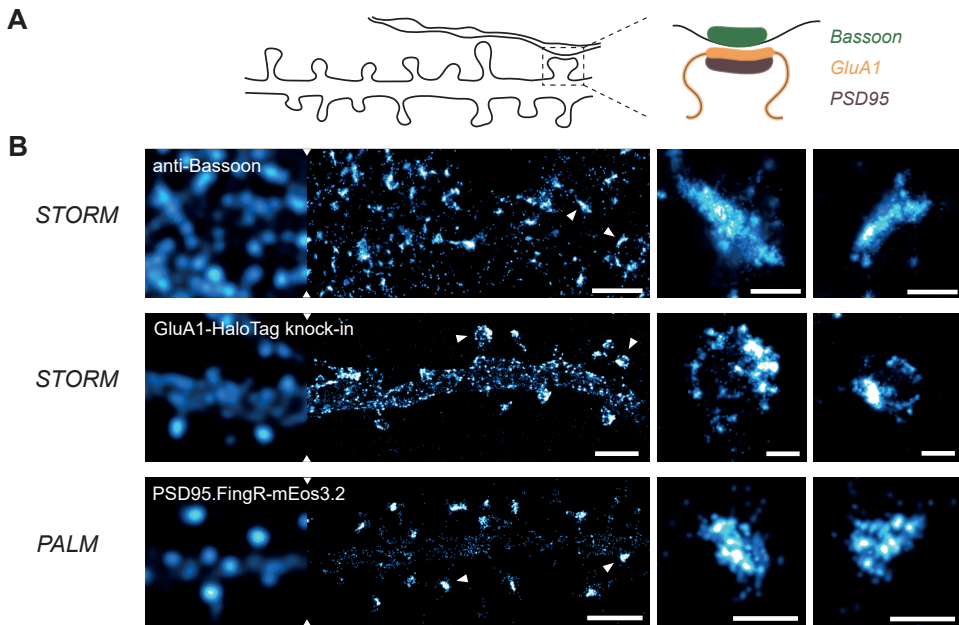


Figure 3. SMLM of synaptic proteins.

(a) Illustration of the expected localization of different synaptic proteins in the dendrite or axon. Scaffolding protein Bassoon localizes in the active zone of the presynaptic bouton, glutamate receptor GluA1 is localized on the dendritic membrane with an enrichment on the postsynaptic membrane, and PSD95 is a postsynaptic scaffolding protein. (b) Examples of dSTORM acquisitions of Bassoon using immunolabeling, endogenously tagged GluA1 with HaloTag, and live-cell PALM of PSD95 using expression of mEos3.2-fused intrabodies. Comparing the diffraction-limited image on the left part with the SMLM acquisition. Scale bars: 2 μm , zooms: 300 nm

3.9 Visualization and Data Analysis

1. **Rendering/Binning:** The most common method of visualizing SMLM datasets is by binning the localizations into pixels. The localizations are converted to pixels and plotted as a Gaussian distribution with the standard deviation adjusted by the localization precision. Figure 3 shows examples of rendered superresolution plots with their diffraction-limited images, for both PALM imaging of mEos3.2-tagged intrabodies targeting PSD95 and dSTORM imaging of HaloTag-GluA1 and antibody-tagged Bassoon. Commonly used pixel sizes for rendering are in the range of 10–50 nm or half the average localization precision. Combining a rendered image with a diffraction-limited snapshot of the same region, allows for visualization of the improvement in resolution and judgement of image quality as much can be learned by “just looking at the thing” [32].
2. **Analyzing SMLM datasets:** Extracting information about protein distribution in SMLM datasets can be challenging, and highly depends on your research question. A good way to start is exploring the heterogeneity in protein density using the molecular coordinates of the localizations instead of rendered images (Fig. 4). Density can thus not only be determined from pixel intensity but can be calculated directly from the

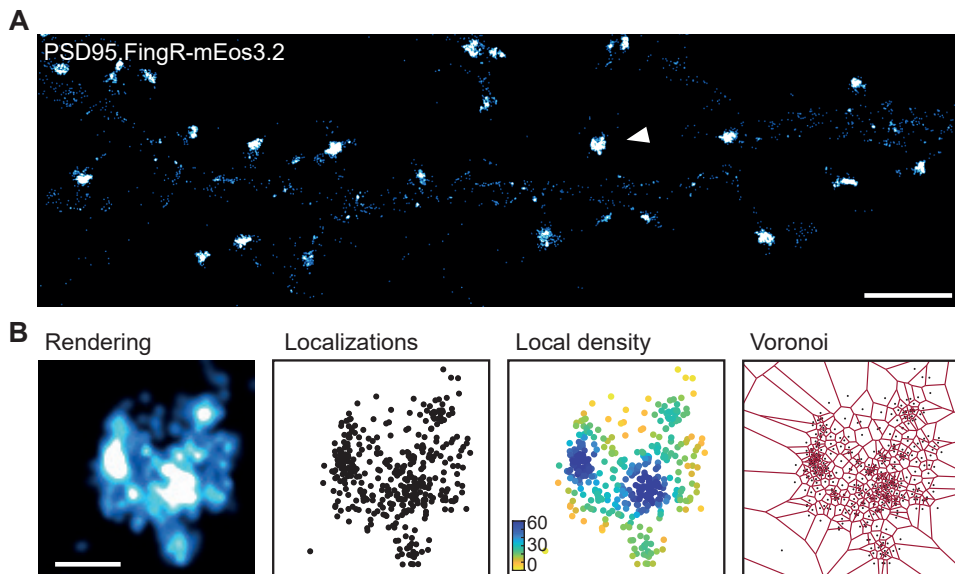


Figure 4. Data visualization and evaluation.

(a) Rendered image from a SMLM acquisition of PSD95.FingR-mEos3.2. (b) Examples of different visualization and evaluation options. Rendering: localizations are converted to pixels by plotting them as Gaussians with integrated density 1 and the localization precision as standard deviation. Localizations: Plotting the centroids of the fluorophores. Local density: Each localization is color-coded for the number of localizations within a given radius. Voronoi: Boundaries can be drawn that assign each localization to their own area that includes all points closer to that localization than any other localization. This area reflects its density relative to the overall density. Scale bar: 2 μm , zoom: 200 nm

molecular coordinates. Examples of these are the so-called local density values and Voronoi diagrams. See Fig. 4b for a comparison of these different plotting methods.

3. The local density value is calculated as the number of localizations in a given radius (in this case 5 times the mean nearest neighbor distance (MNND)) [33]. To calculate the local density, we use the MATLAB functions *knnsearch* (for determining the NND) and *rangeseach* (for the local density). The outcome can be used as color-code for plotting, as well as being used for further analysis. We use 5 times the MNND as this normalizes for differences in overall localization density across the field of view and between datasets.
4. Voronoi diagrams are aimed to segment localizations into areas, reflecting the density based on the distance of each localization to its neighbors. Thus, the area of each so-called Voronoi cell reflects its density relative to the overall density of the acquisition. Voronoi diagrams can be generated using the MATLAB function *voronoi*. The area of individual Voronoi cells can be calculated from the output vertices.
5. Statistical analysis: Both the local density and Voronoi diagrams can yield important information about protein density. Further image analysis including cluster detection is often very specific to distinct biological questions. Therefore, we would like to

refer to other sources for more information regarding SMLM postimaging analysis options including cluster detection, segmentation, protein counting, and colocalization [19, 34, 35].

4. Notes

1. *Dye selection for dSTORM.* Alexa 647 is considered as the best dye for dSTORM, but other dyes work as well and new dyes suitable for dSTORM are constantly being developed, mostly in the far-red emission spectrum. Besides Alexa 647 and JF646, another dye that works well in our hands is CF568. CF568 is a bit more difficult to get into the dark state (also see **Note 12**), and thus not advised for very dense protein structures or proteins with high expression levels. Note that imaging CF568 requires a different laser for excitation than described in the protocol (where Alexa 647 and JF646 are used).
2. *Choice of labeling method.* In our experience, protein abundance and the availability of specific antibodies are the main challenges that impact the quality of labeling, and thus the choice of method. For example, PALM on endogenous proteins is only feasible for medium to highly expressed proteins. For STORM, endogenous tagging of a protein with HaloTag can be used, but with the note that the dye to protein ratio is much lower than labeling with antibodies. Alternatively, and not described here, proteins can be tagged with other fluorescent proteins like GFP or small epitope tags like HA, FLAG, and ALFA-tag, which can be subsequently labeled with organic dyes using antibodies or nanobodies, significantly amplifying the signal and making it possible to perform dSTORM.
3. *Pixel size.* The optimal pixel size for a given experiment depends on the number of expected photons and background. Usually, a pixel size in the range of 100–160 nm is used, based on the point spread function [2].
4. *Optimal DIV for transfection of hippocampal rat neurons.* For genomic tagging of a gene (coding for a protein of interest) we advise to transfect at a relatively young age (DIV2–5). As neurons mature, the transfection efficiency drops quite significantly. Also, and especially for proteins with a low turnover, a longer window between transfection and imaging allows for more of the protein pool to be replaced with the tagged version [22]. For exogenous expression of a fusion protein or intrabody, the optimal window between transfection and imaging day has to be optimized for individual constructs, but we usually use 3–7 days between transfection and imaging. If exogenous expression of a recombinant fusion protein is used, it is critical to make sure the level of overexpression does not alter the localization of the protein.
5. *HaloTag Ligand labeling.* HaloTag is a haloalkane dehalogenase enzyme which is designed to covalently bind to synthetic ligands (HaloLigand) [13] (Fig. 2a). The HaloTag can be coupled to the protein of interest, for example via genomic tagging (as used in this protocol), or through exogenous expression of HaloTag fusion proteins. The HaloLigand is commercially available conjugated to organic dyes. As the HaloTag–HaloLigand binding is enzymatic, live-cell labeling is preferred over labeling of already fixed samples. In addition to the protocol described here, always check the protocol of the supplier and adjust if needed. The HaloTag Ligand-JF646 used in this

protocol is membrane permeable. Thus, both intracellular and extracellular HaloTag-fused proteins are labeled. The optimal length of labeling has to be determined experimentally. Extensive washing of the HaloLigand before fixation is not needed. Besides the potential harmful effects of washing on living cells, most fixatives do not react with the HaloLigand as it is not a protein. The washing steps after fixation will remove any unbound HaloLigand.

6. *Type and length of fixation.* A good fixation protocol is considered one of the most important steps of any superresolution imaging technique as it is key to the preservation of the cell's ultrastructure. Sometimes, glutaraldehyde is used as a fixative in addition to or to replace PFA. When used, additional quenching steps (to reduce autofluorescence) using fresh NaBH_4 are advised. Alternatively, fixation using ice-cold methanol is sometimes used, but this is not compatible with all antibodies and might negatively influence the ultrastructure, particularly membrane-associated complexes, more than PFA. Therefore, we do not recommend this for SMLM. Although 10 min of PEM-PFA fixation is the standard, staining quality can benefit from optimizing the duration of fixation.
7. *Blocking and immunolabeling.* The protocol described here is a general protocol for immunolabeling that is used in our lab. Other blocking reagents like bovine serum albumin (BSA) can be used instead of NGS. Also, the duration and temperature of the antibody incubation step, as well as antibody concentration have to be optimized experimentally for each protein labeling.
8. *Postfixation.* Although not a must, postfixation allows for better preservation of the staining if imaging is not performed directly after labeling. Postfixed cells can be stored for several days in PBS at 4 °C.
9. *Temperature control of microscope.* Preheating and controlling the temperature of the microscope system is also advised for fixed samples. During an acquisition, heat is produced which might cause some drift, which in our hands is reduced if the temperature is already stable at around 30 °C. Therefore, we also advise to keep the STORM buffer and glass slides at least at room temperature.
10. *Exposure time, frame rate, and laser power.* Longer exposure time/lower frame rate allows for more photons to be collected from single emission events, which positively influences the localization precision. However, a long exposure time can also increase the chance of overlapping single-molecules, and when performing PALM in live cells, the movement of molecules within the exposure time of a single frame reduces the localization precision due to motion blurring. Depending on the camera, imaging smaller ROIs can allow for a higher frame rate. Alternatively, higher laser power can be used, but this reduces the lifetime of an emission event.
11. *Illumination angle.* SMLM experiments are generally performed with near TIRF illumination or so-called oblique illumination. Oblique illumination can be achieved by changing the angle of illumination toward full TIRF. Adjust the angle so that in-focus fluorescence events are mostly retained, but that out-of-focus events are not excited.
12. *Induction of dark state.* In the presence of the reducing STORM buffer, high laser power will turn molecules into the dark state. The most common issue faced, is the inability of reducing the number of blinks per frame causing individual emission events to overlap.

Using a higher concentration of MEA in the STORM buffer can help. Alternatively, 2-betamercaptoethanol (BME) is sometimes used instead of MEA, depending on the organic dye used for imaging. In our hands, using a few short pulses of the 488 nm or 561 nm laser can help to bring more far-red emitting dyes to the dark state, but with the risk of irreversible photobleaching.

Acknowledgments

This work was supported by the Netherlands Organization for Scientific Research (ALW-VIDI 171.029 to H.D.M.) and the European Research Council (ERC-StG 716011 to H.D.M.).

References

- Vangindertael J, Camacho R, Sempels W, Mizuno H, Dedecker P, Janssen KPF (2018) An introduction to optical super-resolution microscopy for the adventurous biologist. *Methods Appl Fluoresc* 6(2):022003.
- Thompson RE, Larson DR, Webb WW (2002) Precise nanometer localization analysis for individual fluorescent probes. *Biophys J* 82(5): 2775–2783.
- Gould TJ, Verkhusa VV, Hess ST (2009) Imaging biological structures with fluorescence photoactivation localization microscopy. *Nat Protoc* 4(3):291–308.
- Betzig E, Patterson GH, Sougrat R, Lindwasser OW, Olenych S, Bonifacino JS, Davidson MW, Lippincott-Schwartz J, Hess HF (2006) Imaging intracellular fluorescent proteins at nanometer resolution. *Science* 313(5793): 1642–1645.
- Hess ST, Girirajan TP, Mason MD (2006) Ultra-high resolution imaging by fluorescence photoactivation localization microscopy. *Biophys J* 91(11):4258–4272.
- Rust MJ, Bates M, Zhuang X (2006) Subdiffraction-limit imaging by stochastic optical reconstruction microscopy (STORM). *Nat Methods* 3(10):793–795.
- Heilemann M, van de Linde S, Schüttelz M, Kasper R, Seefeldt B, Mukherjee A, Tinnefeld P, Sauer M (2008) Subdiffraction-resolution fluorescence imaging with conventional fluorescent probes. *Angew Chem Int Ed Engl* 47(33):6172–6176.
- Jungmann R, Avendano MS, Woehrstein JB, Dai M, Shih WM, Yin P (2014) Multiplexed 3D cellular super-resolution imaging with DNA-PAINT and exchange-PAINT. *Nat Methods* 11(3):313–318.
- Balzarotti F, Eilers Y, Gwosch KC, Gynna AH, Westphal V, Stefani FD, Elf J, Hell SW (2017) Nanometer resolution imaging and tracking of fluorescent molecules with minimal photon fluxes. *Science* 355(6325):606–612.
- Li H, Vaughan JC (2018) Switchable fluorophores for single-molecule localization microscopy. *Chem Rev* 118(18):9412–9454.
- Dempsey GT, Vaughan JC, Chen KH, Bates M, Zhuang X (2011) Evaluation of fluorophores for optimal performance in localization-based super-resolution imaging. *Nat Methods* 8(12):1027–1036.
- Samanta S, Gong W, Li W, Sharma A, Shim I, Zhang W, Das P, Pan W, Liu L, Yang Z, Qu J, Kim JS (2019) Organic fluorescent probes for stochastic optical reconstruction microscopy (STORM): recent highlights and future possibilities. *Coord Chem Rev* 380:17–34.
- Los GV, Encell LP, McDougall MG, Hartzell DD, Karassina N, Zimprich C, Wood MG, Learish R, Ohana RF, Urh M, Simpson D, Mendez J, Zimmerman K, Otto P, Vidugiris G, Zhu J, Darzins A, Klauert DH, Bulleit RF, Wood KV (2008) HaloTag: a novel protein labeling technology for cell imaging and protein analysis. *ACS Chem Biol* 3(6): 373–382.
- Keppeler A, Gendreizig S, Gronemeyer T, Pick H, Vogel H, Johnsson K (2003) A general method for the covalent labeling of fusion proteins with small molecules in vivo. *Nat Biotechnol* 21(1):86–89.
- Gautier A, Juillerat A, Heinis C, Correa IR Jr, Kindermann M, Beaufls F, Johnsson K (2008) An engineered protein tag for multiprotein labeling in living cells. *Chem Biol* 15(2): 128–136.
- Jacquemet G, Carisey AF, Hamidi H, Henriques R, Leterrier C (2020) The cell biologist's guide to super-resolution microscopy. *J Cell Sci* 133(11).
- Schermelleh L, Ferrand A, Huser T, Eggeling C, Sauer M, Bielemaier O, Drummen GPC (2019) Super-resolution microscopy demystified. *Nat Cell Biol* 21(1):72–84.
- Wait EC, Reiche MA, Chew TL (2020) Hypothesis-driven quantitative fluorescence microscopy- the importance of reverse-thinking in experimental design. *J Cell Sci* 133(21).
- Wu YL, Tschanz A, Krupnik L, Ries J (2020) Quantitative data analysis in single-molecule localization microscopy. *Trends Cell Biol* 30(11):837–851.
- Jimenez A, Friedl K, Leterrier C (2020) About samples, giving examples: optimized single molecule localization microscopy. *Methods* 174:100–114.
- Yang X, Specht CG (2020) Practical guidelines for two-color SMLM of synaptic proteins in cultured neurons. In: Yamamoto N, Okada Y (eds) *Single molecule microscopy in neurobiology*. Neuromethods Humana, New York, NY.
- Willems J, de Jong APH, Scheefhals N, Mertens E, Catsburg LAE, Poorthuis RB, de Winter F, Verhaagen J, Meye FJ, MacGillivray HD (2020) ORANGE: a CRISPR/Cas9based genome editing toolbox for epitope tagging of endogenous proteins in neurons. *PLoS Biol* 18(4):e3000665.
- Gross GG, Junge JA, Mora RJ, Kwon HB, Olson CA, Takahashi TT, Liman ER, Ellis-Davies GC, McGee AW, Sabatini BL, Roberts RW, Arnold DB (2013) Recombinant probes for visualizing endogenous synaptic proteins in living neurons. *Neuron* 78(6):971–985.
- Babcock H, Sigal YM, Zhuang X (2012) A high-density 3D localization algorithm for stochastic optical reconstruction microscopy. *Opt Nanoscopy* 1(6).
- Schnitzbauer J, Strauss MT, Schlichthaerle T, Schueder F, Jungmann R (2017) Superresolution microscopy with DNA-PAINT. *Nat Protoc* 12(6):1198–1228.
- Ovesny M, Krizek P, Borkovec J, Svindrych Z, Hagen GM (2014) ThunderSTORM: a comprehensive ImageJ plug-in for PALM and STORM data analysis and super-resolution imaging. *Bioinformatics* 30(16):2389–2390.
- Chazeau A, Katrukha EA, Hoogenraad CC, Kapitein LC (2016) Studying neuronal microtubule organization and microtubule-associated proteins using single molecule localization microscopy. *Methods Cell Biol* 131: 127–149.
- Aristov A, Lelandais B, Rensen E, Zimmer C (2018) ZOLA-3D allows flexible 3D localization microscopy over an adjustable axial range. *Nat Commun* 9(1):2409.
- Li Y, Mund M, Hoess P, Deschamps J, Matti U, Nijmeijer B, Sabinina VJ, Ellenberg J, Schoen I, Ries J (2018) Real-time 3D single-molecule localization using experimental point spread functions. *Nat Methods* 15(5):367–369.
- Ries J (2020) SMAP: a modular super-resolution microscopy analysis platform for SMLM data. *Nat Methods* 17(9):870–872.
- Speiser A, Muller L-R, Matti U, Obara CJ, Legant WR, Kreshuk A, Macke JH, Ries J, Turaga SC (2020) Deep learning enables fast and dense single-molecule localization with high accuracy. *BioRxiv*.
- Mund M, Ries J (2020) How good are my data? Reference standards in superresolution microscopy. *Mol Biol Cell* 31(19): 2093–2096.
- MacGillivray HD, Song Y, Raghavachari S, Blanpied TA (2013) Nanoscale scaffolding domains within the postsynaptic density concentrate synaptic AMPA receptors. *Neuron* 78(4):615–622.
- Khater IM, Nabi IR, Hamarneh G (2020) A review of super-resolution single-molecule localization microscopy cluster analysis and quantification methods. *Patterns (NY)* 1(3): 100038.



35. Baddeley D, Bewersdorf J (2018) Biological insight from super-resolution microscopy: what we can learn from localization-based images. *Annu Rev Biochem* 87:965–989.



A large, white, sans-serif number '4' is centered on a blue background. The background features a marbled, ink-like pattern with various shades of blue and teal, creating a textured, organic appearance. The number '4' is the primary focus, standing out sharply against the complex, swirling patterns of the background.

4



Precise detection and visualization of nanoscale temporal confinement in single-molecule tracking analysis

Manon Westra and Harold D. MacGillavry

Membranes (2022), 12(7), 650

Cell Biology, Neurobiology and Biophysics, Department of Biology,
Faculty of Science, Utrecht University, Utrecht, The Netherlands

Abstract

The plasma membrane consists of a diverse mixture of molecules that dynamically assemble into a highly non-random organization. The formation of nanoscale domains in the membrane is of particular interest as these domains underlie critical cellular functions. Single-molecule tracking is a powerful method to detect and quantify molecular motion at high temporal and spatial resolution and has therefore been instrumental in understanding mechanisms that underlie membrane organization. In single-molecule trajectories, regions of temporal confinement can be determined that might reveal interesting biophysical interactions important for domain formation. However, analytical methods for the detection of temporal confinement in single-molecule trajectories depend on a variety of parameters that heavily depend on experimental factors and the influence of these factors on the performance of confinement detection are not well understood. Here, we present elaborate confinement analyses on simulated random walks and trajectories that display transient confined behavior to optimize the parameters for different experimental conditions. Furthermore, we demonstrate a heatmap visualization tool that allows spatial mapping of confinement hotspots relative to subcellular markers. Using these optimized tools, we reliably detected subdiffusive behavior of different membrane components and observed differences in the confinement behavior of two types of glutamate receptors in neurons. This study will help in further understanding the dynamic behavior of the complex membrane and its role in cellular functioning.

Keywords: single-molecule tracking; confinement; plasma membrane

1. Introduction

The plasma membrane is a highly complex and dynamic environment where a vast variety of transmembrane proteins are embedded in a mixture of over a hundred different types of lipids. Key to understanding membrane organization is determining how components are organized and move within the lateral plane of the membrane [1]. The development of single-molecule tracking techniques has been instrumental in quantifying the diffusion of membrane components in living cells and has provided important new insights into how the dynamic nanoscale organization of membrane components contributes to cellular functions. In contrast to other techniques, single-molecule tracking experiments provide trajectories that describe the motion of individual molecules, rather than the average, ‘ensemble’ behavior of a population of molecules. Careful analysis of single-molecule trajectories can therefore reveal a wealth of information on the dynamic behavior of molecules, the biophysical properties of the cellular environment, and the compartmentalization of molecules. Single-molecule trajectories can be described as directed, random (Brownian), or confined motion. Confinement zones, regions where a molecule remains longer than expected from a Brownian diffusant, are of particular biological interest. Confinement zones could indicate organizational hotspots where proteins undergo transient binding to intracellular scaffold molecules or are trapped by the underlying membrane cytoskeleton. Examples of such organizational hotspots that are relevant for biological processes are lipid domains [2,3], neurotransmitter receptor nanodomains [4–7], G-protein-coupled receptor hotspots [8] and ion channel nanoclusters [9,10]. There is thus a need for analytical tools that reliably detect, measure, and visualize confinement zones.



Several studies have reported on strategies to analyze and detect confined behavior in single-molecule trajectories [11–18]. In fact, Einstein formulated a theory about Brownian diffusants already in 1905, where he argued that the displacement of a Brownian particle is proportional to the square root of the elapsed time [19]. Confinement is defined as the portion of a trajectory that deviates from what a random walk would look like. Therefore, it is essential to know how long a Brownian diffusant would stay in a certain region. Saxton defined the probability that a molecule will stay in a region by the following equation: $\log \psi = 0.2048 - 2.5117(D \times t/R^2)$ where D is the diffusion coefficient, t the period of time, and R the radius of the region [20]. Simson et al. translated this probability into the confinement index, which is inversely related to the probability that a Brownian molecule will stay in a certain area [11]. When this probability during the trajectory becomes lower, the confinement index will increase, indicating a period of transient confinement within the trajectory. This confinement analysis has been used extensively by many labs to detect temporal confinement in single-molecule trajectories [21–33].

This confinement analysis depends on different manually defined parameters that need to be optimized to reliably detect confinement. These parameters include for instance the window of frames to analyze, threshold for the confinement index, and the minimal time a molecule should be in this state to be considered confined. Determining the optimal values for each of these parameters, however, is not trivial and varying individual parameters can have a large impact on the detection power of the analysis. Therefore, in this study, we set out to understand the influence of individual parameters on the performance of the confinement analysis and tested the robustness of this analysis on simulated random walks and trajectories that display transient confined behavior. This allowed us to optimize parameters and balance the detection of false-negatives and false-positives. Furthermore, we developed a tool to visualize confinement areas in heatmaps that allows spatial mapping of confinement hotspots relative to subcellular markers. To test the performance of this analysis, we applied our analysis on experimental data and reliably detected subdiffusive behavior for a variety of membrane components. Lastly, we found that two neuronal glutamate receptors, mGluR5 (metabotropic glutamate receptor 5) and AMPA-type glutamate receptors, reveal different confinement properties. This study will help in further understanding the dynamic behavior of membrane components and their role in membrane organization.

2. Materials and Methods

2.1. Simulations

To simulate 2D random walks, we tested two different simulation methods (Figure S1, see Supplementary Materials). In the first model (model 1), every consecutive coordinate is drawn from a Gaussian distribution based on the diffusion coefficient and the interval time between the steps: $step = \sqrt{2 \times D \times \Delta t} \times [x \ y]$ where x and y are normally distributed numbers, generated by the MATLAB function *randn*. In the second model (model 2), every step has the same step size derived from the set diffusion coefficient and interval time, however the angle and thus the direction of the step is random: $step = \sqrt{4 \times D \times \Delta t} \times [\cos(\theta) \ \sin(\theta)]$ where θ is a random angle between 0 and 2π , generated using MATLAB (MathWorks, Natick, MA, USA, R2021B) function *rand* (Figure S1A). The MSD curve of model 2 showed less variation in the curve, however the estimated diffusion coefficient is for both models highly similar to the

set diffusion coefficient for the simulation. We applied subsampling to the simulated tracks so that every 100 steps the coordinates were saved in the trajectory. After subsampling, the distributions of the diffusion coefficients were almost identical for both models (Figure S1B) and for the rest of the simulations, we used model 2.

We also tested two different approaches for simulating transient confined trajectories. The principal idea behind the simulations is that the molecule cannot escape a simulated circle for as long as it is simulated to be confined. The first approach is the ‘reflect’ model, where the molecule bounces back from the simulated, circular confinement zone if the next step would be outside the circle (Figure S1C, left panel). The second approach is the ‘stick’ model, where the molecule sticks at the border at the place where it would otherwise escape the circle (Figure S1C, right panel). The ‘reflective’ model appeared to be more stable when varying the step sizes in comparison to the ‘stick’ model. When increasing the step size in the simulations, the plateau in the MSD curve reached higher values for the ‘stick’ model, while it remained the same for the ‘reflect’ model (Figure S1D). Therefore, we used the reflective model for the rest of the confinement simulations.

2.2. Measure Power of Detection

The power of detection was measured as the percentage of confined displacements, meaning all steps in all trajectories simulated that are in a period of detected confinement, i.e., above threshold L_c for period of time longer than T_c .

2.3. Parameters Used in Simulations

Simulations were performed to generate trajectories of 100 frames and confinement periods of 0, 15, or 50 frames, with diffusion coefficient of $0.05 \mu\text{m}^2/\text{s}$ and interval time of 0.02 s unless reported otherwise. Basic simulation settings: $D = 0.05 \mu\text{m}^2/\text{s}$, $N_{\text{steps}} = 10,000$, subsampling = 100, $dt = 0.02 \text{ s}$, $dt_{\text{sim}} = 0.0002 \text{ s}$. Basic confinement parameters: $L_{\text{cm}} = 5.5$, $S_m = 15$, $S_{\text{min}} = 4$, $T_c = 0.2 \text{ s}$, $\alpha = 0.5$, $n_{\text{pointsMSDset}} = 10$, $R_{\text{conf}} = 0.04 \mu\text{m}$ (Table S1).

2.4. Animals

All animal experiments were performed in compliance with the guidelines for the welfare of experimental animals issued by the Government of the Netherlands (Wet op de Dierproeven, 1996) and European regulations (Guideline 86/609/EEC). All animal experiments were approved by the Dutch Animal Experiments Review Committee (Dier Experimenten Commissie; DEC), performed in line with the institutional guidelines of Utrecht University.

2.5. Primary Neuron Cultures and Transfections

Dissociated hippocampal cultures were prepared from embryonic day 18 (E18) Janvier Wistar rat brains of both genders [34]. Dissociated neurons were plated on $\text{Ø}18\text{-mm}$ coverslips coated with poly-L-lysine ($37.5 \mu\text{g}/\text{mL}$, Sigma-Aldrich, St. Louis, MO, USA) and laminin ($1.25 \mu\text{g}/\text{mL}$, Roche Diagnostics, Mannheim, Germany) at a density of 100,000 neurons per well. Neurons were grown in Neurobasal medium (NB) supplemented with 1% penicillin/streptomycin (Gibco), 2% B27 (Gibco), and 0.5 mM L-glutamine (Gibco, Grand Island, NY, USA) at $37 \text{ }^\circ\text{C}$ in 5% CO_2 . From days in vitro (DIV) 1 onward, medium was refreshed weekly by replacing half of the medium with BrainPhys Neuronal Medium (BP, STEMCELL

Technologies, Vancouver, Canada) supplemented with 2% NeuroCult SM1 (STEMCELL Technologies, Vancouver, Canada) and 1% penicillin/streptomycin. At DIV14, neurons were transfected with indicated constructs using Lipofectamine 2000 (Invitrogen, Carlsbad, CA, USA). For each well, 1.8 μg DNA was mixed with 3.3 μL Lipofectamine 2000 in 200 μL BP, incubated for 30 min at room temperature (RT). Then, 400 μL conditioned medium was transferred to a new culture plate and replaced by 260 μL BP supplemented with 0.5 mM L-glutamine. The DNA mix was added to the neurons and incubated at 37 °C in 5% CO₂. After 1 to 2 h, neurons were briefly washed with BP and transferred to the new culture plate with conditioned medium supplemented with an additional 400 μL BP with SM1 and penicillin/streptomycin and kept at 37 °C in 5% CO₂. All experiments were performed using neurons at DIV18–22.

2.6. DNA Plasmids

All plasmids have been described before in previous studies: Homer1c-mCherry [35], SEP-GluA2 [4], SEP-mGluR5 [35]. The GFP-GPI and mHD-GT46 constructs are kind gifts from Dr. Ewers (Institute for Chemistry and Biochemistry, Free University Berlin, Germany; [36]).

2.7. Single-Molecule Tracking

Single-molecule tracking was performed on the Nanoimager S from ONI (Oxford Nanoimaging; ONI, Oxford, UK), equipped with a 100 \times /NA 1.4 oil immersion objective (Olympus Plan Apo, Hamburg, Germany), an XYZ closed-loop piezo stage, and with 471-, 561-, and 640-nm wavelength excitation lasers. Fluorescence emission was detected using a sCMOS camera (ORCA Flash 4, Hamamatsu, Hamamatsu City, Japan). Stacks of 5000 frames were acquired at 50 or 100 Hz with oblique illumination using the 640-nm laser. NimOS software (version 1.18.3) from ONI was used for localization and drift correction was performed. Neurons were imaged in extracellular imaging buffer containing 120 mM NaCl, 3 mM KCl, 10 mM HEPES, 2 mM CaCl₂, 2 mM MgCl₂, and 10 mM glucose, pH adjusted to 7.35 with NaOH. The GFP/RFP-booster Atto647N (Chromotek, Martinsried, Germany) was added before image acquisition in a concentration of 1:200,000 in extracellular imaging buffer while blocking with 1% BSA. For the tracking of DOPE, we added Atto647N-DOPE (ATTO-TEC, Siegen, Germany) in complex with defatted BSA [37] before image acquisition at a final concentration of 6.5 nM. We used a minimum track length of 30 frames (10- or 20-ms interval) for visualization and quantification. Postsynaptic density (PSD) masks were created from a stack of 30 frames obtained for Homer1c-mCherry using the 561 nm excitation laser as described in [38].

2.8. Single-Molecule Tracking Analysis

Using MATLAB (version 2021b), molecules with a localization precision <50 nm were selected for analysis. Tracking was achieved using custom algorithms in MATLAB described previously with a tracking radius of <500 nm [39]. The first three points of the MSD with the addition of the value 0 at MSD(0) were used to fit the slope using a linear fit. Tracks with a negative slope were not used for further analysis. The diffusion coefficient was estimated based on the fit using the formula: $MSD = 4 \times D \times \Delta t$. Only tracks of at least 30 frames were selected for further analysis. Tracks were classified as immobile when the ratio between the radius of gyration and mean step size ($\frac{\sqrt{\pi/2} \times \text{radius of gyration}}{\text{mean stepsize}}$) was smaller than 2.11 [40]. The PSD mask was

created based on the maximum intensity projection of Homer1c-mCherry. Peaks in intensity were detected, after which a FWHM-like boundary was defined for each PSD.

Transient confinement analysis on mobile trajectories was done in MATLAB using slightly modified scripts from a previously published MATLAB implementation [21]. As modifications, we included the last segments of the trajectory shorter than Sm in the averaging to improve confinement detection at the end of a trajectory (Figure S2A). Furthermore, the point in the trajectory is the middle of the sliding window of the D over time instead of the beginning of the sliding window, for a better correlation with L over time (Figure S2B). Lastly, we corrected the \ln into the \log_{10} for defining confinement index L . As D , the maximum D_{inst} was used, estimated for each sub-trajectory of Δt . Parameters used in the analysis are: $Lc = 5.5$, $Sm = 15$, $\alpha = 0.5$, $Tc = 0.2$ s (Table S1). The confinement zones are further analyzed for size and duration of confinement and diffusion coefficient in and outside confinement zones. Confinement maps were created based on the detected confinement radius for each confinement zone. Each confinement zone was stored as a two-dimensional Gaussian distribution with the radius as FWHM. The final matrix was plotted with a color-code, where higher values indicate confinement hotspots because there are multiple Gaussians on top of each other.

2.9. Statistical Analysis

Statistical significance was tested using a Student's t -test when comparing two groups. Statistical tests with a p -value below 0.05 were considered significant. Significance is indicated as follows: $p < 0.05$ is indicated by *, $p < 0.01$ by **, and $p < 0.001$ by ***. Analysis was performed on neurons originating from three individual preparations of hippocampal neurons. The number of neurons used for analysis is indicated as n . Statistical analysis and graphs were prepared in GraphPad Prism (version 9, Graphpad Software, San Diego, CA, USA) and figures were generated in Adobe Illustrator 2022 (Adobe Systems, San Jose, CA, USA).

3. Results

3.1. Detection of Transient Confinement within Single-Molecule Trajectories

To detect transient confinement within single-molecule trajectories, Simson et al. [11] developed a statistical framework defining areas where a diffusing molecule remains significantly longer than expected if it would undergo Brownian motion. The probability ψ that a molecule stays within a bounded region for a set period of time has been defined by Saxton as:

$$\log \psi = 0.2048 - 2.5117(Dt/R^2) \quad (1)$$

with D being the diffusion coefficient, t the period of time, and R the radius of the region [20]. Simson et al. [11] used this probability to derive the confinement index L , which is inversely related to ψ :

$$L = \begin{cases} -\log(\psi) - 1 & \psi \leq 0.1 \\ 0 & \psi > 0.1 \end{cases} \quad (2)$$

High values of L are thus indicative of non-random confinement and $L = 0$ in cases of random diffusion. The calculation of L is inherently based on a number of variables that will influence the detection power of the confinement analysis. To correctly interpret the results of this analysis, here we aimed to understand the influence of these different variables on the detection power of the analysis. The analysis in this study is based on the MATLAB

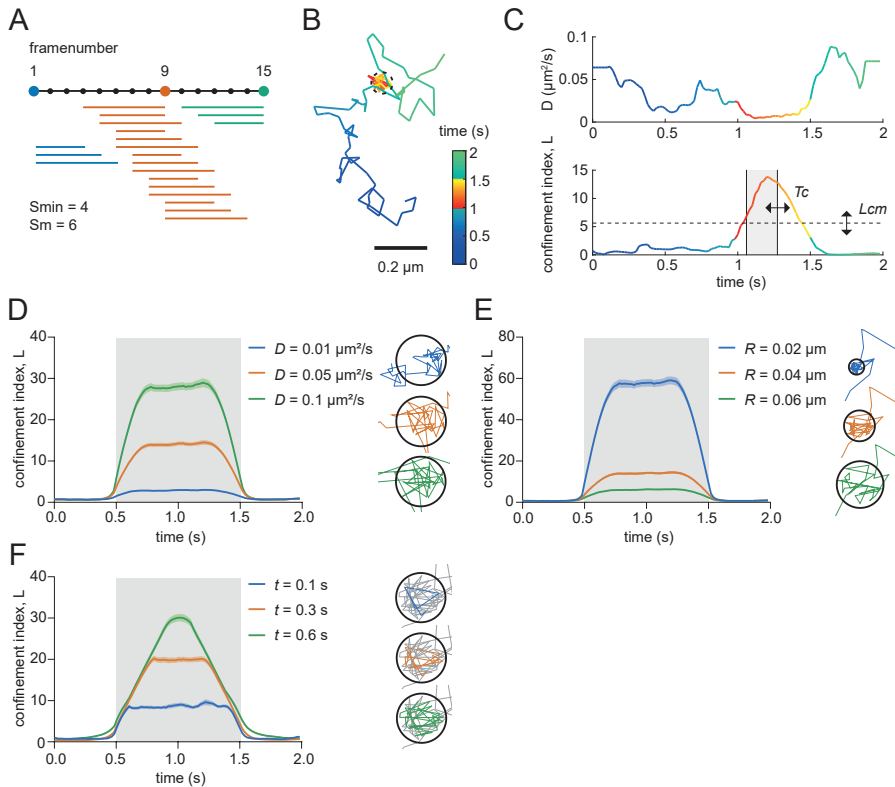


Figure 1. Influence of variables in confinement index formula.

(A) Schematic diagram of how trajectories are divided into segments with different lengths. In this simplified example, the minimal segment length (S_{min}) is 4 frames and the maximum segment (S_m) is 6. All the segments are displayed that will be included in the confinement index of frame 1 (blue), 9 (orange), and 15 (green). (B) Simulated trajectory with a confinement zone with radius of 40 nm. Color-coded for time and confined period. Scale bar, 0.2 μm . (C) Diffusion coefficient (top) and confinement index (bottom) over time of the simulated trajectory in (B). Color-coded for time and confined period. T_c and L_{cm} indicate the critical time period and critical L threshold used to detect confinement periods. (D) Average confinement index over time for 100 simulated trajectories with three different diffusion coefficients. Simulated confined period is indicated with the gray box. Illustrations display for each condition one example segment of the track in the corresponding color. Simulated confinement radius (R_{conf}) is 0.04 μm and S_m is 15 frames. (E) Average confinement index over time for 100 simulated trajectories with three different simulated confinement radii. Simulated confined period is indicated with the gray box. Illustrations display for each condition one example segment of the track in the corresponding color. Diffusion coefficient is 0.05 $\mu\text{m}^2/\text{s}$ and S_m is 15 frames. (F) Average confinement index over time for 100 simulated trajectories with 3 different segment lengths ($S_m = S_{min}$). Simulated confined period is indicated with the gray box. Illustrations display for each condition one example segment of the track in the corresponding color. Diffusion coefficient is 0.05 $\mu\text{m}^2/\text{s}$ and R_{conf} is 0.04 μm . Data are represented as means \pm SEM.

implementation from Ménchon et al. [21] with some modifications (see Section 2.8; Figure S2). To define the confinement index over time for individual trajectories, a trajectory is first divided into segments with minimum length S_{min} and maximum length S_m (Figure 1A) and for each individual segment, L is calculated as described above. As such, these parameters are thus expected to determine the spatial and temporal sensitivity of the analysis. The radius R of the segment is defined by the maximum distance between one of the points and the starting point of the segment. The diffusion coefficient D used in the formula is the same for all the segments in the trajectory and should represent the diffusion coefficient of the molecule if it would move freely. Then, for each point in the trajectory, L is averaged over all the segments that include that point. Note, that as a consequence, the averaged L for points at the beginning and the end of the track is averaged over fewer segments than points in the middle. As can be seen for a simulated trajectory with a short period of transient confinement (Figure 1B), L values are higher during the confined period, which is accompanied by a temporal decrease in the diffusion coefficient (Figure 1C). Confined periods within a trajectory can then be defined by selecting periods in which all points are above the critical minimum L (L_{cm}) for a duration longer than a critical period of time (T_c) (Figure 1C).

When increasing the diffusion coefficient D of simulated molecules, it can be seen that because for a molecule with a higher D it is less likely that it would stay in the same area for the same time, relatively higher L values are calculated (Figure 1D and Figure S3A). On the other hand, when D remains constant but the region in which the molecule is observed is larger, the calculated confinement index becomes lower, because it is more likely that a freely moving molecule would stay in a larger area (Figure 1E and Figure S3B). Lastly, if we only increase the observed time window (t) — which is represented by S_{min} and S_m — while keeping the other variables the same, a higher confinement index will be detected because it is less likely that a Brownian molecule with that diffusion coefficient would stay in the same area for a longer time (Figure 1F).

3.2. Optimizing Input Parameters for Accurate Transient Confinement Zone Detection in Single-Molecule Trajectories

After considering the influence of the different variables in the confinement index calculation, we aimed to optimize the user-defined parameters for the confinement detection to minimize the false positive rate while maximizing the true detection rate. False positives can be detected because L is not zero: even in random walks fluctuations in L could be inadvertently interpreted as confinement.

First, we wanted to define what effect the input parameters would have on incorrectly detecting confinement in random walks, therefore we simulated random walks with parameters comparable to experimental situations ($D = 0.05 \mu\text{m}^2/\text{s}$, $dt = 0.02 \text{ s}$, 100 frames) and started off with a maximum window size (S_m) of 15 frames. Lowering the minimum L threshold (L_{cm}) increased the percentage of false positives detected in random walks, similar to decreasing the critical period of time (T_c) (Figure 2A). Changing the maximum window size (S_m) did not lead to a large change in the detection of false positives (Figure 2B). Thus, to achieve the lowest number of false positives, L_{cm} and T_c should be set relatively high, whereas the value of S_m is of less significance.

Next, we investigated the effect of the input parameters on the detection of true confinement. Therefore, we simulated trajectories with confined periods and parameters comparable to

experimental situations ($D = 0.05 \mu\text{m}^2/\text{s}$, $dt = 0.02 \text{ s}$, 100 frames, confined period of 15 or 50 frames and simulated confinement radius (R_{conf}) of 0.04–0.06 μm). Increasing L_{cm} lowered the detection power of true confinement (Figure 2C). Furthermore, in contrast to the effect

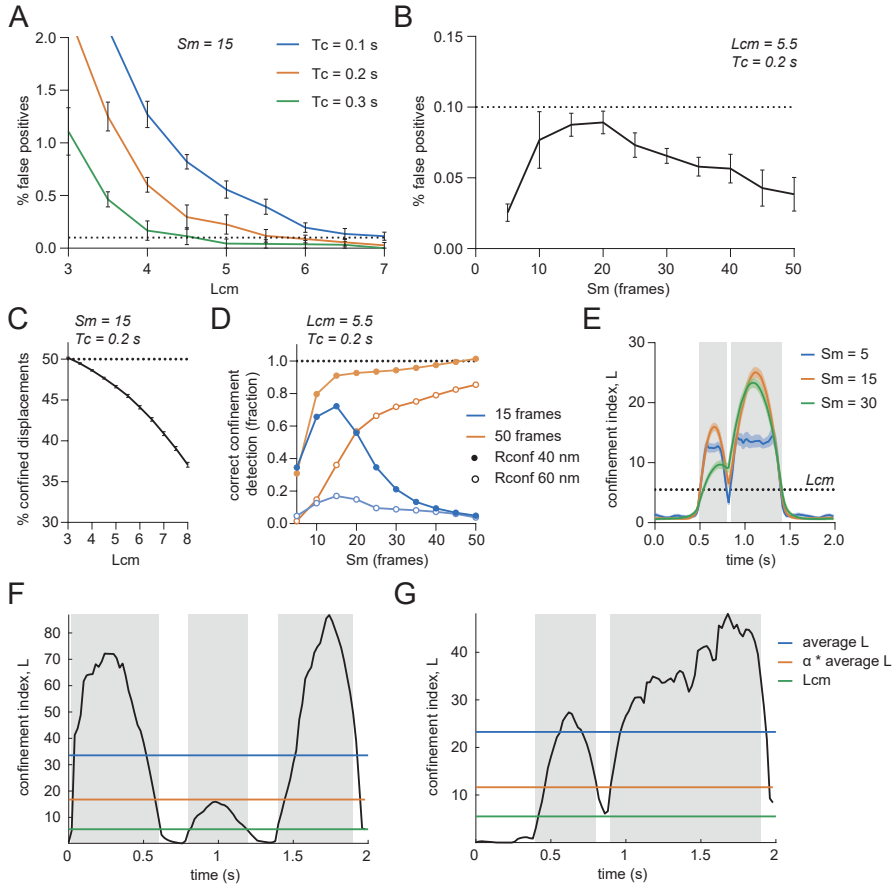


Figure 2. Influence of user-defined parameters on the confinement analysis.

(A) Effect of minimal critical L (L_{cm}) and critical time (T_c) on percentage of false positives in simulated random walks. Dotted line indicates 0.1% false positives. Sm is 15. Five independent simulations of 100 trajectories. Data are represented as means \pm SEM. (B) Effect of Sm on percentage of false positives in simulated random walks. Dotted line indicates 0.1% false positives. L_{cm} is 5.5 and T_c is 0.2 s. Five independent simulations of 1000 trajectories. Data are represented as means \pm SEM. (C) Effect of L_{cm} on the percentage of detected confined displacements in trajectories simulated to be confined for 50 of the 100 frames. $Sm = 15$, $T_c = 0.2 \text{ s}$, $R_{\text{conf}} = 0.04 \mu\text{m}$. Five independent simulations of 1000 trajectories. Data are represented as means \pm SD. (D) Effect of Sm on correct confinement detection in trajectories simulated to be confined 15 or 50 of the 100 frames. $L_{\text{cm}} = 5.5$ and $T_c = 0.2 \text{ s}$. 100 simulated trajectories per condition. (E) Effect of Sm on the ability to discriminate between multiple confinement zones shortly after each other. $L_{\text{cm}} = 5.5$ and $R_{\text{conf}} = 0.03 \mu\text{m}$, 100 trajectories. Simulated confined periods are indicated with the gray boxes. Data are represented as means \pm SEM. (F) Negative effect of ' $\alpha \times$ average L ' as L_c . Single simulated trajectory with three confinement zones. The middle confinement zone does not reach the threshold. $R_{\text{conf}} = 0.015 \mu\text{m}$ and $0.03 \mu\text{m}$ and $\alpha = 0.5$. Simulated confined periods are indicated with the gray boxes. (G) Positive effect of ' $\alpha \times$ average L ' as L_c . Single simulated trajectory with two confinement zones. With L_{cm} as threshold, both confinement zones would have been merged into one. $R_{\text{conf}} = 0.03 \mu\text{m}$ and $\alpha = 0.5$. Simulated confined periods are indicated with the gray boxes.

on random walks, the time window plays an important role in the correct detection of true confinement. The power of detection increased with larger Sm when the confinement period was equally long, whereas the power of detection decreased if the confinement period was shorter than Sm (Figure 2D). Choosing this maximum time window will also affect the power of detecting multiple confinement zones after each other. Increasing the Sm to achieve increased power of detection could lead to combining multiple confinement zones because L will not go below the threshold in between the zones (Figure 2E, orange and green traces). Taken together, to achieve high power of detection, Lcm should not be too high and the value for Sm will affect the resolution at which confinement zones can be detected. While higher Sm values increase detection of confinement, it reduces the power to detect shorter periods of confinement that, at high Sm values, will be averaged out or combined with other confinement zones.

Because the diffusion coefficient can change over the course of a trajectory, M enchon et al. introduced another L threshold where the threshold is defined by the average L of a trajectory multiplied by a factor α that ranges from 0 to 1 [21]. It is important to consider the effect of using this threshold definition as it can both increase and decrease the power of detection. For example, when the average L is high because of two highly confined regions, Lc will be higher than Lcm , resulting in not detecting a less confined third region (Figure 2F). On the other hand, when there are highly confined zones — possibly caused by a lower diffusion coefficient — shortly after each other, using the threshold Lc will separate the two zones, whereas Lcm would be too low (Figure 2G).

3.3. Estimated Diffusion Coefficient Can Be Influenced by Track Length

One important parameter in the confinement index formula is the diffusion coefficient. This is the diffusion coefficient of the molecule if it could move freely. However, setting this diffusion coefficient is not trivial. One approach is to use the maximum instantaneous diffusion coefficient (D_{inst}) per trajectory, assuming that the molecule undergoes Brownian diffusion during at least part of the trajectory [21]. To calculate the maximum D_{inst} of a trajectory, we need to determine how the diffusion coefficient changes along the trajectory. Therefore, the D_{inst} was estimated based on the linear part of the MSD versus time lag curve for each window of ten steps over the complete trajectory and the maximum D_{inst} was used as the D of that trajectory. For this short window, the uncertainty in estimating the diffusion coefficient could be relatively high, but it allows for the detection of changes in the diffusion coefficient within individual trajectories. Another approach would be to test against a set diffusion coefficient chosen a priori that would resemble the Brownian diffusion of the molecule of interest. This value could for instance be deduced from independent tracking experiments, taking the diffusion coefficient of a freely moving population of trajectories as a reference value [22,28,29].

We investigated the effect of the different approaches in defining the Brownian diffusion coefficient on the false positive rate and confinement detection. For simulations, it is possible to test against a set diffusion coefficient and we compared this approach (Dset) to using the maximum instantaneous diffusion coefficient (Dmax). An interesting observation was that the false positive rate depended on the length of the simulated tracks for the Dmax approach whereas this was stable with Dset (Figure 3A,B). This was caused by a higher Dmax for the longer tracks, probably because there is a higher chance that there is a peak in the diffusion coefficient over time when there are more steps in the trajectory (Figure 3C). Similarly, in

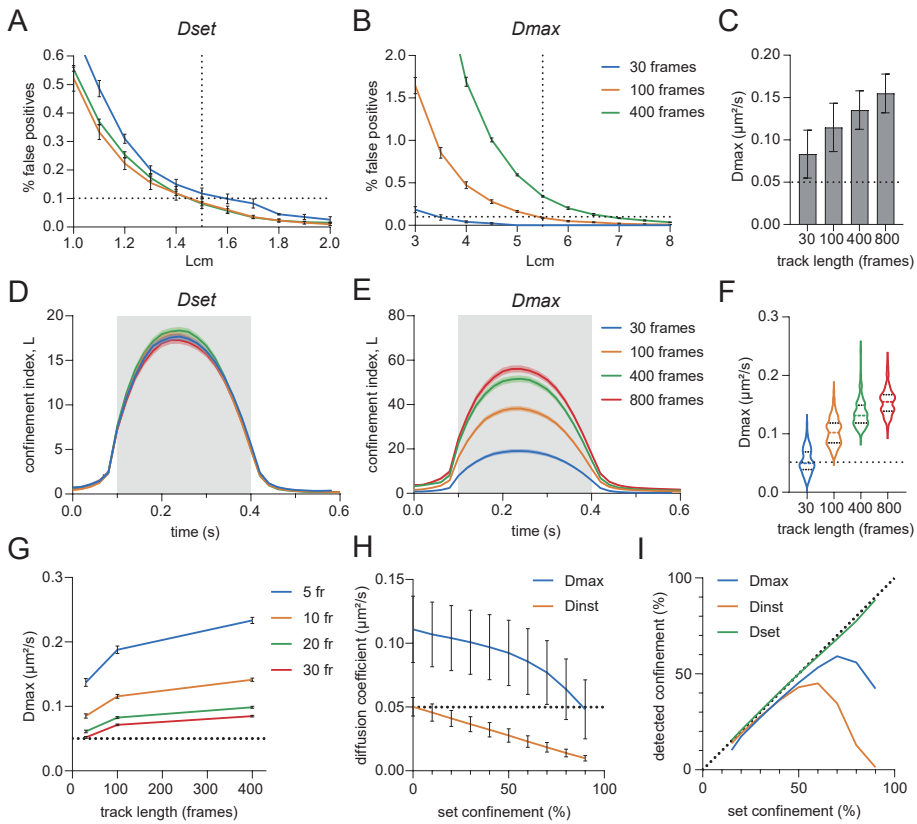


Figure 3. Effect of diffusion coefficient in the confinement index formula on confinement detection. (A,B) Effect of track length on the percentage of false positives in random walks using Dset (A) or Dmax (B) as diffusion coefficient in the confinement index formula. Five independent simulations of 1000 trajectories per condition. Data are represented as means \pm SEM. (C) Effect of track length on Dmax. 100 simulated random walks per condition. Data are represented as means \pm SD. (D,E) Effect of track length on the confinement index over time using Dset (D) or Dmax (E) as diffusion coefficient in the confinement index formula. 100 confined trajectories per condition, $Rconf = 0.02 \mu\text{m}$. Data are represented as means \pm SEM. (F) Violin plots of Dmax values from (E). (G) Effect of the length of the segments used for estimating D_{inst} within trajectories on Dmax. (H) Effect of the percentage of confinement within a trajectory on the estimated diffusion coefficient of the whole trajectory (Dinst) or the Dmax. 1000 trajectories per condition, $Rconf = 0.04 \mu\text{m}$. Data are represented as means \pm SD. (I) Effect of the percentage of confinement within a trajectory on the detected confinement within the trajectory using Dmax, Dinst or Dset. Dotted line indicates set confinement = detected confinement. 1000 trajectories per condition, $Rconf = 0.04 \mu\text{m}$.

confined tracks with the same confinement zone but a longer total length, the confinement index during the period of confinement was higher with the Dmax method, whereas with Dset, the confinement index was similar for all track lengths (Figure 3D,E). This difference could also be explained by the higher Dmax values for the longer tracks (Figure 3F). To improve the Dmax method, we tested the effect of including more steps in the sliding window for the estimation of D_{inst} . That resulted in a lower Dmax because the peaks are averaged out. However, Dmax still increases with longer track lengths (Figure 3G). A third option (Dinst)

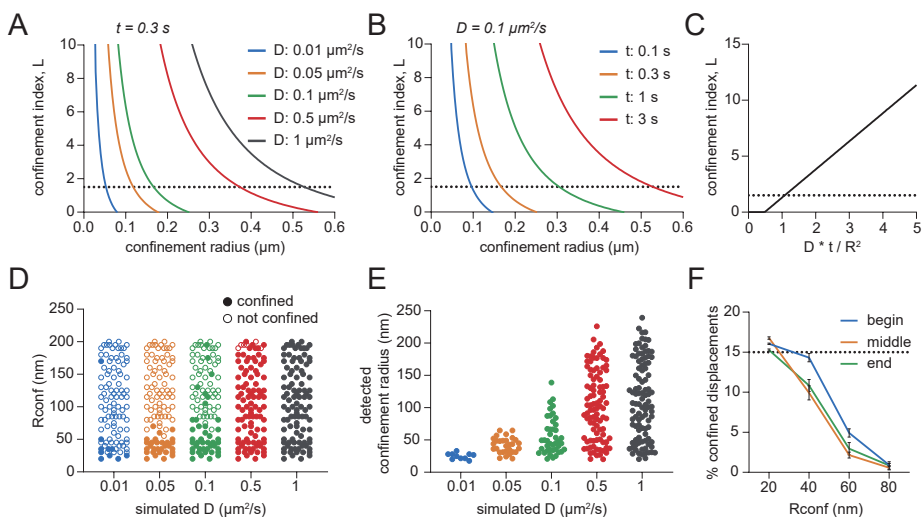


Figure 4. Detection limits of the confinement analysis.

(A) Theoretical effect of the confinement radius and diffusion coefficient on the confinement index that can be detected. Observing time = 16 frames or 0.3 s. Dotted line indicates L_{cm} of 1.5 as used with Dset. (B) Theoretical effect of the confinement radius and observing time on the confinement index that can be detected. $D = 0.1 \mu\text{m}^2/\text{s}$. (C) Theoretical relation between $D \times t / R^2$ and the confinement index. (D) Effect of the diffusion coefficient in trajectories on the ability to detect a range of different simulated confinement radii (R_{conf}). (E) Effect of the diffusion coefficient in trajectories on the detected confinement radius given the same range of confinement radii in (D) as input for the simulations. (F) Effect of the timing of simulated confinement periods and R_{conf} on the correct detection of confinement. Fifteen frames confined of total 100 frames per simulated track. Five independent simulations of 100 trajectories per condition. Dotted line indicates correct confinement detection. Data are represented as means \pm SD.

would be to use the estimated instantaneous diffusion coefficient per track as the D in the confinement formula as used by Simson et al. [11]. However, although based on only the first three points of the MSD versus time lag curve, D_{inst} is heavily influenced by confinement in the trajectory, whereas D_{max} only declined when the largest part of the trajectory is confined (Figure 3H). Thus, using D_{inst} per trajectory negatively affects the ability to detect transient confinement. Particularly, when a track was confined for more than 50% of the time, the power of detection dropped dramatically (Figure 3I). To conclude, using a set diffusion coefficient as D in the confinement formula appears to be the most reliable method, however this is under the assumption that the Brownian diffusion coefficient of the molecule is known. The alternative method would be using the D_{max} , where the diffusion of the whole trajectory is tested against the fastest segment in the trajectory, thus investigating changes in diffusion behavior over the course of the trajectory.

3.4. Detection Limits in the Confinement Analysis

Next, we wanted to understand the detection limits of the confinement analysis to interpret the results correctly. Can similarly sized confinement zones still be detected for molecules with different diffusion coefficients? Purely based on the theoretical formula behind the confinement analysis, it is only possible to detect a large confinement zone if the diffusion

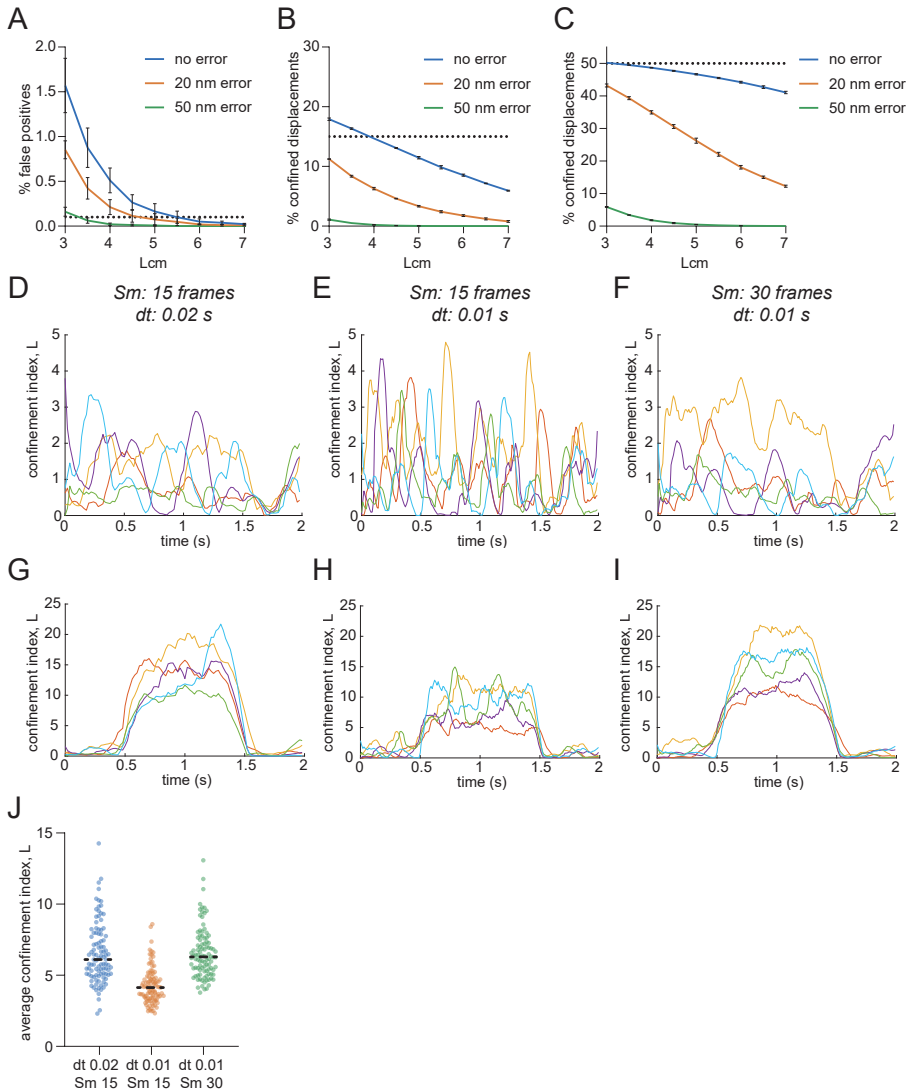


Figure 5. Influence of experimental parameters on confinement detection.

(A) Effect of localization error on the percentage of false positives detected in random walks. Three independent simulations of 1000 trajectories per condition. Data are represented as means \pm SD. (B,C) Effect of localization error on the percentage of detected confined displacements in tracks simulated to be confined for 15 (B) or 50 (C) of the 100 frames. $R_{conf} = 0.04 \mu\text{m}$. Three independent simulations of 1000 trajectories. Data are represented as means \pm SD. (D–F) Confinement index of 5 random trajectories over time with (D) $Sm = 15$, $dt = 0.02$ s and 100 frames, (E) $Sm = 15$, $dt = 0.01$ s and 200 frames, (F) $Sm = 30$, $dt = 0.01$ s and 200 frames. (G–I) Confinement index of 5 confined trajectories over time with (G) $Sm = 15$, $dt = 0.02$ s and 100 frames, (H) $Sm = 15$, $dt = 0.01$ s and 200 frames, (I) $Sm = 30$, $dt = 0.01$ s and 200 frames. $R_{conf} = 0.04 \mu\text{m}$. (J) Corresponding average confinement index values of (G–I).

coefficient is high enough and the time is long enough (Figure 4A,B). Only then will the confinement index L still reach the threshold when the confinement radius is large. In other words, the ratio between the possible explored area of a random diffusing molecule ($D \times t$) — with given diffusion coefficient and time — and the observed explored area (R^2) should be high enough to be considered confined (Figure 4C). To study the limits of the confinement analysis in detecting confinement zones of specific sizes, we simulated confined tracks with varying diffusion coefficients ($0.01\text{--}1 \mu\text{m}^2/\text{s}$) and confinement radii (R_{conf} , $20\text{--}200 \text{ nm}$). Next, we ran the transient confinement analysis on these simulations and found the fraction of confinement zones that were detected and their detected confinement radius (Figure 4D,E). It is clear from the results that the larger confinement zones cannot be detected in tracks with low diffusion coefficients. Such a molecule with a low diffusion coefficient could reside in a larger area without deviating from a Brownian molecule in their behavior.

Additionally, the first and last points in the confinement profile of a track are averaged over a lower number of segments. Therefore, we tested whether the timing of a confinement zone would affect the power of detection. We simulated confinement zones with varying radii and duration of 15 or 50 frames at the beginning, middle, and end of the track, and observed no considerable differences in the detected confined displacements (Figure 4F and Figure S4). Thus, the detection of confinement in this analysis is not limited by the timing of the confinement periods.

3.5. Influence of Localization Error and Frame Rate on Confinement Detection Accuracy

In single-molecule tracking analysis, the first step is to localize the sub-pixel position of fluorescence emission events of single molecules. Generally, the point spread function of single-molecule emission spots can be fitted with a two-dimensional Gaussian function. The uncertainty inherent to the fitting routine, or localization error, influences the accuracy of the detected single-molecule trajectories. To investigate the effect of the localization error on the performance of the confinement detection, we simulated random walks and confined tracks with no error, 20 nm, and 50 nm localization error. We found that in random walks, a larger localization error resulted in fewer false positives (Figure 5A and Figure S5A). Thus, the L_{cm} threshold could be lowered to achieve the same detection precision. This can be explained by R^2 being, on average, larger with a higher localization error. However, a higher localization error also resulted in a dramatic decrease in the detection of both short and longer confinement periods, even with the lowered L_{cm} threshold (Figure 5B,C and Figure S5B,C).

Another experimental parameter we considered is the frame rate of the acquisition that determines the time resolution in the single-molecule trajectories. It is important to adjust the parameters of the analysis accordingly, especially when comparing different experiments with different experimental parameters. Using the same maximum segment window with a smaller interval time will lead to narrower peaks in random walks (Figure 5D,E). Moreover, for a similar long period of confinement, the average confinement index will be lower with a smaller interval time and the same segment window (Figure 5G,H). Changing the interval time can be corrected by adjusting the maximum segment window (S_m) accordingly to obtain a more similar confinement index over time profile (Figure 5F,I,J).

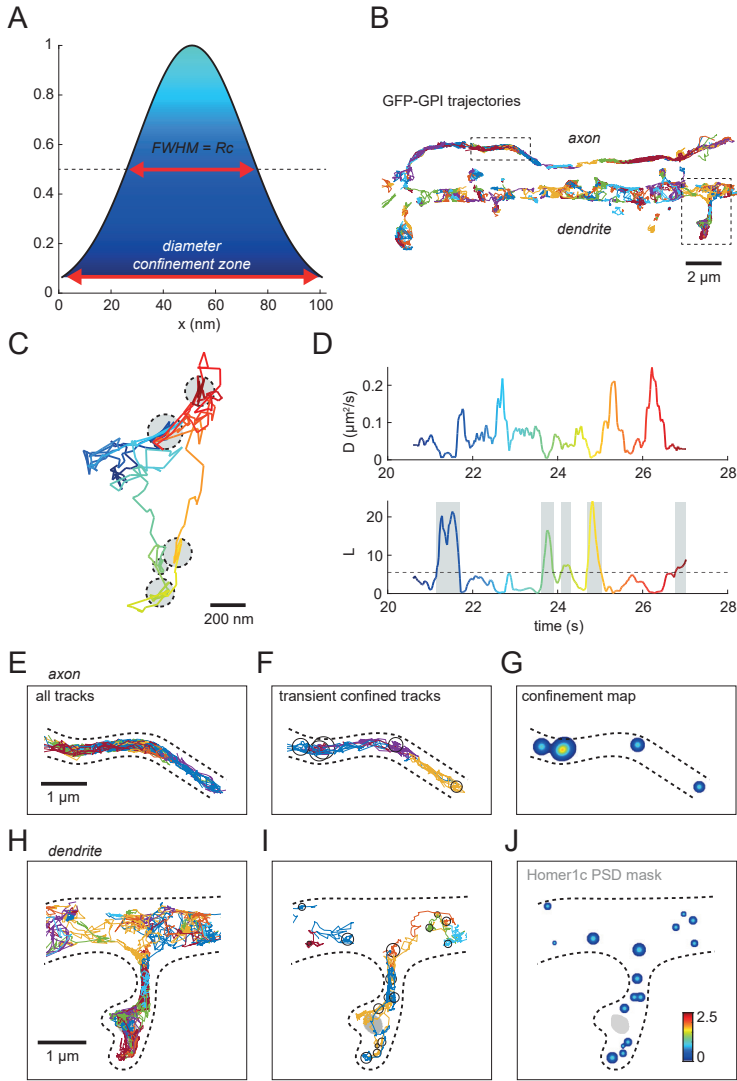


Figure 6. Spatial visualization of confinement.

(A) Gaussian function used in confinement map with amplitude 1. FWHM is the confinement radius. Color-coded for amplitude. (B) GFP-GPI anti-GFP nanobody Atto647N trajectories in axon and dendrite. Boxes mark location of zooms in (E–J). Scale bar, 2 μm . (C) Example experimental GPI trajectory with 5 confinement zones indicated with the gray circles. Color-coded for time. Scale bar, 200 nm. (D) Diffusion coefficient (top) and confinement index (bottom) over time of the experimental trajectory in (C). Color-coded for time and the detected confined periods are indicated with the gray boxes. (E–J) Zoom of trajectories in the axon (E–G) and dendrite (H–J). (E, H) All trajectories displayed in different colors. (F, I) Trajectories with confined periods. Confinement zones are indicated with the black circles. (G, J) Confinement map indicating areas with multiple confinement zones close to or on top of each other. Homer1c PSD mask is indicated in gray in the dendrite. Scale bar, 1 μm .

3.6. Spatial Mapping of Transient Confinement of Membrane Probes

Next, we wanted to test the robustness of the confinement analysis on experimental single-molecule tracking data. We therefore focused on the neuronal membrane, where the dynamic behavior of individual membrane components collectively contributes to the efficient transfer of synaptic signals [41]. Subsynaptic domains enriched in glutamate receptors and scaffolding molecules were found to be aligned with the presynaptic glutamate release to optimize synaptic transmission, which emphasizes the importance of the heterogeneous organization of the neuronal membrane [42,43]. First, we developed a visualization tool to map the detected confinement zones resulting in a spatial heatmap of confinement hotspots. Such a heatmap can be displayed together with other cellular markers to locate confinement hotspots relative to specific subcellular domains. To create such a heatmap, we plotted every confinement zone as a Gaussian with amplitude 1 and the radius of the confinement zone as the FWHM (Figure 6A). Overlapping confinement zones would result in higher amplitude values, resulting in a heatmap that is color-coded for the amplitude values. Neurons were transfected with GFP-GPI, and we performed single-molecule tracking experiments using an anti-GFP nanobody coupled to Atto647N (Figure 6B). After tracking the molecules, we performed the transient confinement analysis on the mobile trajectories to obtain information on the location and timing of confinement zones in experimental trajectories (Figure 6C,D). Finally, we plotted the trajectories and confinement heatmap in combination with a marker of excitatory synapses (Homer1c-mCherry) (Figure 6E–J). We observed confinement of GFP-GPI in the axon, dendrite, and spines, where confinement does not seem to be specifically enriched at synaptic locations. Overall, this visualization tool allows for the detection of areas with high levels of transient confinement in a cellular context, by mapping the confinement zones relative to cellular markers.

To address the effect of changing parameters in the confinement analysis on the resulting confinement measures in experimental datasets, we applied the confinement analysis on a single-molecule tracking acquisition of GFP-GPI in the neuronal membrane. Lowering the Lcm increased the detected confinement radius, the diffusion coefficient inside confinement zones, and resulted in more trajectories with detected confinement (number of tracks with confinement for Lcm 3: 381, Lcm 4: 309, Lcm 5.5: 219, Figure 7A and Figure S6A). On the other hand, varying Tc did not affect the average detected confinement radius or the diffusion coefficient inside confinement zones, although with higher Tc , fewer trajectories with detected confinement were found because of the stricter thresholds (Tc 0.1: 311, Tc 0.2: 219, Tc 0.3: 139, Figure 7B and Figure S6B). Lastly, a longer time window resulted in the detection of larger confinement zones and a higher diffusion coefficient inside confinement zones, but did not noticeably affect the number of trajectories with detected confinement (Sm 5: 181, Sm 15: 219, Sm 30: 177, Figure 7C and Figure S6C).

Furthermore, we wanted to investigate the possibility to compare confinement of different membrane probes with different diffusional properties. Therefore, we compared the confinement behavior of (1) the AMPAR subunit GluA2 with (2) an artificial protein with single-spanning transmembrane domain (GT46), (3) GFP-GPI, and (4) the phospholipid DOPE in neurons. We detected transient confinement in the trajectories of all four membrane probes, but considerably larger confinement zones were detected for DOPE in comparison to GluA2 (Figure 7D). This difference could be explained by their difference in diffusion as DOPE has a higher diffusion coefficient (Figure 4, Figure 7E,F, and Figure S6D). The difference in

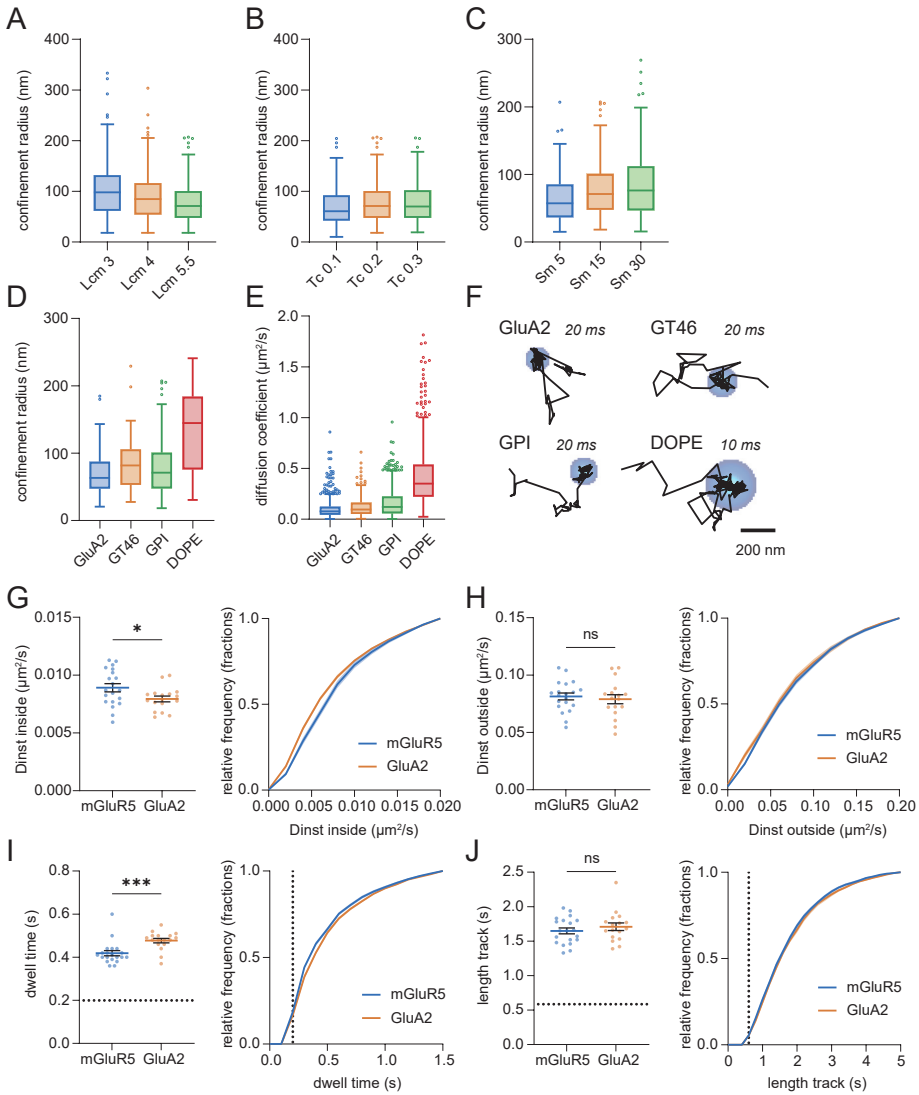


Figure 7. Confinement analysis on experimental trajectories.

(A–C) Effect of user-defined parameters on the detected confinement radius. (A) Vary critical L , L_{cm} . Number of trajectories with confinement: L_{cm} 3: 381, L_{cm} 4: 309, L_{cm} 5.5: 219. (B) Vary critical time, T_c . Number of trajectories with confinement: T_c 0.1: 311, T_c 0.2: 219, T_c 0.3: 139. (C) Vary maximum segment length, S_m . Number of trajectories with confinement: S_m 5: 181, S_m 15: 219, S_m 30: 177. (D–F) Confinement zones detected for membrane probes: GluA1, GT46, GPI, and DOPE. (D) Detected confinement radius for each probe. (E) Estimated diffusion coefficients for each probe. (F) Example trajectories with their detected confinement zone. Interval times during the acquisition are indicated. Scale bar, 200 nm. (G–J) (G) Average estimated diffusion coefficient inside confinement zones, (H) average estimated diffusion coefficient outside confinement zones, (I) average dwell time, (J) average total track length for mGluR5 ($n = 20$) and GluA2 ($n = 17$; unpaired t -test) (left), and corresponding cumulative frequency distribution (right). (I) Dotted line indicates dwell time threshold. (J) Dotted line indicates minimum track length threshold. Data are represented as means \pm SEM. * $p < 0.05$, *** $p < 0.001$, ns, $p > 0.05$.

size of the confinement zones related to their difference in diffusion coefficient for all probes, except GPI which diffused slightly faster than GT46 but revealed slightly smaller confinement zones. In conclusion, comparison of confinement zone properties should be approached with caution when the diffusion coefficients of the probes differ considerably.

Lastly, we aimed to compare the transient confinement properties of two glutamate receptors that have comparable diffusion coefficients: the metabotropic glutamate receptor 5 (mGluR5) and the AMPA receptor subunit GluA2 (Figure S6E). These receptors both reside in the postsynaptic membrane, but GluA2 is found to be more enriched in the synapse whereas mGluR5 is concentrated in an area around the synapse [44,45]. We found that the diffusion coefficient of GluA2 inside confinement zones was lower than for mGluR5 (mGluR5: $0.00891 \pm 0.00035 \mu\text{m}^2/\text{s}$ and GluA2: $0.00793 \pm 0.00025 \mu\text{m}^2/\text{s}$; Figure 7G), while the diffusion coefficient outside confinement zones was not significantly different (mGluR5: $0.0813 \pm 0.0030 \mu\text{m}^2/\text{s}$ and GluA2: $0.0789 \pm 0.0040 \mu\text{m}^2/\text{s}$; Figure 7H). In addition, the time GluA2 resided in confinement zones was longer than mGluR5 (mGluR5: $0.419 \pm 0.012 \text{ s}$ and GluA2: $0.477 \pm 0.010 \text{ s}$; Figure 7I), while the total track length was not significantly different (mGluR5: $1.65 \pm 0.043 \text{ s}$ and GluA2: $1.71 \pm 0.054 \text{ s}$; Figure 7J). These results suggest that there are different mechanisms responsible for the confinement of mGluR5 and GluA2.

4. Discussion

Single-molecule tracking is a powerful approach to investigate the heterogeneous organization of cellular membranes. However, precise and reliable analysis of single-molecule tracking data remains challenging. This study set out to gain a better understanding of the detection of transient confinement in single-molecule trajectories.

We found that a considerable factor in the confinement analysis is the diffusion coefficient that is used in the formula to define the diffusion coefficient of the molecule when it would move freely. However, defining this free diffusion coefficient a priori is not straightforward. We therefore compared three different methods: using the maximum instantaneous diffusion coefficient per trajectory based on shorter segments [21], the instantaneous diffusion coefficient per trajectory [11], and defining a constant diffusion coefficient for the molecule of interest considered to be the free diffusion coefficient [22,25,26]. It is important to note the limitations of all these methods and their consequences on the results. The D_{max} could be an overestimation of the free diffusion coefficient and therefore lead to an overestimation of the detected confinement in that trajectory and in addition, the value of D_{max} seems to depend on the length of the track. However, it does allow for detecting changes in diffusion behavior over the trajectory. Estimating the instantaneous diffusion coefficient per trajectory could be heavily influenced by the percentage of confinement in the trajectory and therefore lead to reduced power of detection. Using a set diffusion coefficient is another approach of using the confinement analysis as with this method not only transient confinement would be detected but also completely confined tracks, as all the tracks are tested against the same diffusion coefficient and thus no longer for a temporal deviation within the trajectory. This heavily depends on choosing the free diffusion coefficient in a correct way. Previous studies used this approach, but this was under the assumption that the diffusion of these molecules was mainly Brownian [22,25,26]. This should be done with caution as we showed that the percentage of confinement in a track could influence the D_{inst} . It is important to note that when



using this approach in the case of comparing confinement after, for instance, an experimental treatment, that the difference may solely come from a change in the diffusion coefficient and does not necessarily reflect a true difference in the confinement behavior.

One of the interesting quantitative outcomes of the confinement analysis is the size of a confinement zone. We found, however, that the maximal size that can be detected, depends on the diffusion coefficient of the molecule. Thus, comparing confinement of molecules with varying diffusion coefficients could lead to erroneous conclusions about differences in their confinement zone sizes. It is also not directly evident from the data which biological mechanism underlies these confined periods, and different mechanisms might also result in different confinement measures. Phase separation into liquid-ordered and liquid-disordered phases in model membranes arises mainly from the combination of lipid composition and temperature. Biological membranes are even more complex, both in the heterogeneity of lipids and involvement of membrane-associated proteins that affect the thermodynamics. Neurons and more specifically synapses are enriched in cholesterol and sphingolipids [46,47]. These lipids comprise the more ordered phase in the membrane and especially add up to the heterogeneous organization of biological membranes [48–50]. Furthermore, characteristics of confinement zones could be explained by compartmentalization by the actin-based membrane skeleton, molecular crowding, or binding to scaffold proteins [37–39].

Interestingly, we detected differences in the confinement behavior of glutamate receptors mGluR5 and GluA2, which suggests that different mechanisms are responsible for their confinement. It is known that these glutamate receptors show different distribution patterns within the postsynaptic membrane, GluA2 is concentrated in the postsynaptic density (PSD) whereas mGluR5 seems to be surrounding the PSD [51]. As our results reveal that GluA2 is trapped for longer time and moves slower, this could be an indication that GluA2 is trapped at a specific location mainly by scaffold molecules, supported by the finding that the actin cytoskeleton is absent from the PSD [52]. On the other hand, mGluR5 might be slowed down in its diffusion by other mechanisms such as steric hindrance or interactions with the cytoskeleton. Other methods for confinement analysis might help in detecting specific underlying mechanisms. For example, Meilhac et al. modified the method from Simson et al. to be able to detect jumps between compartments in the membrane [11,12]. Another way to characterize confinement are potential wells, describing a field of force resulting from molecular interactions, which has been suggested for synaptic receptors [18,40,41]. Lastly, this method could also be applied to less complex membranes to get a better estimate of the mechanism behind detected confinement behavior. For example, to study the effect of temperature on confined behavior and thus membrane organization.

5. Conclusions

This study provides a systematic analysis of the influence of the different parameters that are used for detecting temporal confinement in single-molecule trajectories and proposes a visualization tool to map confinement zones in the cellular context. To demonstrate the validity of the presented approach, we studied the diffusion of two glutamate receptor types in neurons and found that mGluR5 and GluA2 differ in their confinement behavior. We believe the presented results can guide future studies in the correct detection and interpretation

of confinement analysis. As such, this study will help in better understanding the complex organization of the membrane by reliably detecting and spatially mapping confinement.

Supplementary Materials

The following supporting information can be downloaded at: <https://www.mdpi.com/article/10.3390/membranes12070650/s1>, Table S1: Confinement parameters and their effect on the power of detection; Figure S1: Random walk and confinement simulations; Figure S2: Improvements in the confinement analysis; Figure S3: Raw simulated transient confined trajectories from Figure 1; Figure S4: Effect of timing confinement on power of detection; Figure S5: Effect of localization error on confinement detection using Dset; Figure S6: Confinement analysis on experimental trajectories. Reference [21] is cited in Supplementary Materials.

Author Contributions

Conceptualization, M.W. and H.D.M.; methodology, M.W. and H.D.M.; software, M.W. and H.D.M.; validation, M.W. and H.D.M.; formal analysis, M.W. and H.D.M.; investigation, M.W. and H.D.M.; resources, H.D.M.; data curation, M.W. and H.D.M.; writing – original draft preparation, M.W. and H.D.M.; writing – review and editing, M.W. and H.D.M.; visualization, M.W. and H.D.M.; supervision, H.D.M.; project administration, H.D.M.; funding acquisition, H.D.M. All authors have read and agreed to the published version of the manuscript.

Funding

This work was funded by the Netherlands Organization for Scientific Research (ALW-VIDI 171.029 to H.D.M.).

Institutional Review Board Statement

All experiments were approved by the Dutch Animal Experiments Committee (Dier Experimenten Commissie (DEC), work protocol project number: AVD1080020173404), performed in line with institutional guidelines of Utrecht University, and conducted in agreement with Dutch law (Wet op de Dierproeven, 1996) and European regulations (Directive 2010/63/EU).

Data Availability Statement

The data that support the findings of this study are available on request from the corresponding author, H.D.M.

Acknowledgments

We would like to thank Marijn Siemons for his help with the simulations and all members of the MacGillavry lab for helpful discussions.

Conflicts of Interest

The authors declare no conflict of interest.

References

- Jacobson, K.; Liu, P.; Lagerholm, B.C. The Lateral Organization and Mobility of Plasma Membrane Components. *Cell* **2019**, *177*, 806–819.
- Pike, L.J. Rafts defined: A report on the Keystone symposium on lipid rafts and cell function. *J. Lipid Res.* **2006**, *47*, 1597–1598.
- Kusumi, A.; Fujiwara, T.K.; Tsunoyama, T.A.; Kasai, R.S.; Liu, A.; Hirokawa, K.M.; Kinoshita, M.; Matsumori, N.; Komura, N.; Ando, H.; et al. Defining raft domains in the plasma membrane. *Traffic* **2020**, *21*, 106–137.
- MacGillavry, H.D.; Song, Y.; Raghavachari, S.; Blanpied, T.A. Nanoscale Scaffolding Domains within the Postsynaptic Density Concentrate Synaptic AMPA Receptors. *Neuron* **2013**, *78*, 615–622.
- Nair, D.; Hossy, E.; Petersen, J.D.; Constals, A.; Giannone, G.; Choquet, D.; Sibarita, J.-B. Super-Resolution Imaging Reveals That AMPA Receptors Inside Synapses Are Dynamically Organized in Nanodomains Regulated by PSD95. *J. Neurosci.* **2013**, *33*, 13204–13224.
- Crosby, K.C.; Gookin, S.E.; Garcia, J.D.; Hahm, K.M.; Dell'Acqua, M.L.; Smith, K.R. Nanoscale Subsynaptic Domains Underlie the Organization of the Inhibitory Synapse. *Cell Rep.* **2019**, *26*, 3284–3297.e3.
- Specht, C.G.; Izeddin, I.; Rodriguez, P.C.; ElBeheiry, M.; Rostaing, P.; Darzacq, X.; Dahan, M.; Triller, A. Quantitative nanoscopy of inhibitory synapses: Counting gephyrin molecules and receptor binding sites. *Neuron* **2013**, *79*, 308–321.
- Sungkaworn, T.; Jobin, M.-L.; Burneck, K.; Weron, A.; Lohse, M.J.; Calebiro, D. Single-molecule imaging reveals receptor-G protein interactions at cell surface hot spots. *Nature* **2017**, *550*, 543–547.
- Akin, E.J.; Solé, L.; Johnson, B.; El Beheiry, M.; Masson, J.-B.; Krapf, D.; Tamkun, M.M. Single-Molecule Imaging of Nav1.6 on the Surface of Hippocampal Neurons Reveals Somatic Nanoclusters. *Biophys. J.* **2016**, *111*, 1235–1247.
- Heck, J.; Parutto, P.; Ciurazkiewicz, A.; Bikbaev, A.; Freund, R.; Mitlöchner, J.; Andres-Alonso, M.; Fejtova, A.; Holcman, D.; Heine, M. Transient Confinement of CaV2.1 Ca²⁺-Channel Splice Variants Shapes Synaptic Short-Term Plasticity. *Neuron* **2019**, *103*, 66–79.e12.
- Simson, R.; Sheets, E.D.; Jacobson, K. Detection of temporary lateral confinement of membrane proteins using single-particle tracking analysis. *Biophys. J.* **1995**, *69*, 989–993.
- Meilhac, N.; Le Guyader, L.; Salomé, L.; Destainville, N. Detection of confinement and jumps in single-molecule membrane trajectories. *Phys. Rev. E* **2006**, *73*, 011915.
- Renner, M.; Wang, L.; Levi, S.; Hennekinne, L.; Triller, A. A Simple and Powerful Analysis of Lateral Subdiffusion Using Single Particle Tracking. *Biophys. J.* **2017**, *113*, 2452–2463.
- Wehs, D.; Gilad, D.; Seon, M.; Cohen, I. Image-based algorithm for analysis of transient trapping in single-particle trajectories. *Microfluid. Nanofluidics* **2012**, *12*, 337–344.
- Rajani, V.; Carrero, G.; Golan, D.E.; de Vries, G.; Cairo, C.W. Analysis of Molecular Diffusion by First-Passage Time Variance Identifies the Size of Confinement Zones. *Biophys. J.* **2011**, *100*, 1463–1472.
- Sikora, G.; Wytomańska, A.; Gajda, J.; Solé, L.; Akin, E.J.; Tamkun, M.M.; Krapf, D. Elucidating distinct ion channel populations on the surface of hippocampal neurons via single-particle tracking recurrence analysis. *Phys. Rev. E* **2017**, *96*, 062404.
- Lanoiselée, Y.; Grimes, J.; Koszegi, Z.; Calebiro, D. Detecting Transient Trapping from a Single Trajectory: A Structural Approach. *Entropy* **2021**, *23*, 1044.
- Hoze, N.; Nair, D.; Hossy, E.; Sieben, C.; Manley, S.; Herrmann, A.; Sibarita, J.-B.; Choquet, D.; Holcman, D. Heterogeneity of AMPA receptor trafficking and molecular interactions revealed by superresolution analysis of live cell imaging. *Proc. Natl. Acad. Sci.* **2012**, *109*, 17052–17057.
- Einstein, A. Über die von der molekularkinetischen Theorie der Wärme geforderte Bewegung von in ruhenden Flüssigkeiten suspendierten Teilchen. *Ann. Phys.* **1905**, *322*, 549–560.
- Saxton, M.J. Lateral diffusion in an archipelago. Single-particle diffusion. *Biophys. J.* **1993**, *64*, 1766–1780.
- Menchón, S.A.; Martín, M.G.; Doti, C.G. APM_GUI: Analyzing particle movement on the cell membrane and determining confinement. *BMC Biophys.* **2012**, *5*, 4.
- Sergé, A.; Fourgeaud, L.; Hémar, A.; Choquet, D. Receptor Activation and Homer Differentially Control the Lateral Mobility of Metabotropic Glutamate Receptor 5 in the Neuronal Membrane. *J. Neurosci.* **2002**, *22*, 3910–3920.
- Orr, G.; Hu, D.; Özçelik, S.; Opreško, L.K.; Wiley, H.S.; Colson, S.D. Cholesterol Dictates the Freedom of EGF Receptors and HER2 in the Plane of the Membrane. *Biophys. J.* **2005**, *89*, 1362–1373.
- Wu, H.M.; Lin, Y.H.; Yen, T.C.; Hsieh, C.L. Nanoscopic substructures of raft-mimetic liquid-ordered membrane domains revealed by high-speed single-particle tracking. *Sci. Rep.* **2016**, *6*, 20542.
- Kovtun, O.; Torres, R.; Ferguson, R.S.; Josephs, T.; Rosenthal, S.J. Single Quantum Dot Tracking Unravels Agonist Effects on the Dopamine Receptor Dynamics. *Biochemistry* **2021**, *60*, 1031–1043.
- Neupert, C.; Schneider, R.; Klatt, O.; Reissner, C.; Repetto, D.; Biermann, B.; Niesmann, K.; Missler, M.; Heine, M. Regulated dynamic trafficking of neuroligins inside and outside of synaptic terminals. *J. Neurosci.* **2015**, *35*, 13629–13647.
- Dietrich, C.; Yang, B.; Fujiwara, T.; Kusumi, A.; Jacobson, K. Relationship of Lipid Rafts to Transient Confinement Zones Detected by Single Particle Tracking. *Biophys. J.* **2002**, *82*, 274–284.
- Notelaers, K.; Rocha, S.; Paesen, R.; Smisdom, N.; De Clercq, B.; Meier, J.C.; Rigo, J.M.; Hofkens, J.; Ameloot, M. Analysis of $\alpha 3$ GlyR single particle tracking in the cell membrane. *Biochim. Biophys. Acta-Mol. Cell Res.* **2014**, *1843*, 544–553.
- Meier, J.; Vannier, C.; Sergé, A.; Triller, A.; Choquet, D. Fast and reversible trapping of surface glycine receptors by gephyrin. *Nat. Neurosci.* **2001**, *4*, 253–260.
- Bürli, T.; Baer, K.; Ewers, H.; Sidler, C.; Fuhrer, C.; Fritschy, J.M. Single Particle Tracking of $\alpha 7$ Nicotinic AChR in Hippocampal Neurons Reveals Regulated Confinement at Glutamatergic and GABAergic Perisynaptic Sites. *PLoS ONE* **2010**, *5*, e11507.
- Syed, A.; Zhu, Q.; Smith, E.A. Ligand binding affinity and changes in the lateral diffusion of receptor for advanced glycation endproducts (RAGE). *Biochim. Biophys. Acta-Biomembr.* **2016**, *1858*, 3141–3149.
- Borgdorff, A.J.; Choquet, D. Regulation of AMPA receptor lateral movements. *Nature* **2002**, *417*, 649–653.
- Wong, W.C.; Juo, J.-Y.; Lin, C.-H.; Liao, Y.-H.; Cheng, C.-Y.; Hsieh, C.-L. Characterization of Single-Protein Dynamics in Polymer-Cushioned Lipid Bilayers Derived from Cell Plasma Membranes. *J. Phys. Chem. B* **2019**, *123*, 6492–6504.

34. Kapitein, L.C.; Yau, K.W.; Hoogenraad, C.C. *Microtubule Dynamics in Dendritic Spines. Methods in Cell Biology*, 1st ed; Elsevier Inc.: Amsterdam, The Netherlands, 2010; Volume 97, pp. 111-132. ISBN 9780123813497.
35. Scheefhals, N.; Catsburg, L.A.E.; Westerveld, M.L.; Blanpied, T.A.; Hoogenraad, C.C.; MacGillavry, H.D. Shank Proteins Couple the Endocytic Zone to the Postsynaptic Density to Control Trafficking and Signaling of Metabotropic Glutamate Receptor 5. *Cell Rep.* **2019**, *29*, 258–269.e8.
36. Albrecht, D.; Winterlood, C.M.; Ewers, H. Dual color single particle tracking via nanobodies. *Methods Appl. Fluoresc.* **2015**, *3*, 024001.
37. Eggeling, C.; Ringemann, C.; Medda, R.; Schwarzmann, G.; Sandhoff, K.; Polyakova, S.; Belov, V.N.; Hein, B.; Von Middendorff, C.; Schönle, A.; et al. Direct observation of the nanoscale dynamics of membrane lipids in a living cell. *Nature* **2009**, *457*, 1159–1162.
38. Willems, J.; de Jong, A.P.H.; Scheefhals, N.; Mertens, E.; Catsburg, L.A.E.; Poorthuis, R.B.; de Winter, F.; Verhaagen, J.; Meye, F.J.; MacGillavry, H.D. Orange: A Crispr/Cas9-based genome editing toolbox for epitope tagging of endogenous proteins in neurons. *PLOS Biol.* **2020**, *18*, e3000665.
39. Lu, H.E.; MacGillavry, H.D.; Frost, N.A.; Blanpied, T.A. Multiple Spatial and Kinetic Subpopulations of CaMKII in Spines and Dendrites as Resolved by Single-Molecule Tracking PALM. *J. Neurosci.* **2014**, *34*, 7600–7610.
40. Golan, Y.; Sherman, E. Resolving mixed mechanisms of protein subdiffusion at the T cell plasma membrane. *Nat. Commun.* **2017**, *8*, 15851.
41. Westra, M.; Gutierrez, Y.; MacGillavry, H.D. Contribution of Membrane Lipids to Postsynaptic Protein Organization. *Front. Synaptic Neurosci.* **2021**, *13*, 790773.
42. Tang, A.H.; Chen, H.; Li, T.P.; Metzbower, S.R.; MacGillavry, H.D.; Blanpied, T.A. A trans-synaptic nanocolumn aligns neurotransmitter release to receptors. *Nature* **2016**, *536*, 210–214.
43. Li, S.; Raychaudhuri, S.; Lee, S.A.; Brockmann, M.M.; Wang, J.; Kusick, G.; Prater, C.; Syed, S.; Falahati, H.; Ramos, R.; et al. Asynchronous release sites align with NMDA receptors in mouse hippocampal synapses. *Nat. Commun.* **2021**, *12*, 677.
44. Luján, R.; Nusser, Z.; Roberts, J.D.B.; Shigemoto, R.; Somogyi, P. Perisynaptic location of metabotropic glutamate receptors mGluR1 and mGluR5 on dendrites and dendritic spines in the rat hippocampus. *Eur. J. Neurosci.* **1996**, *8*, 1488–1500.
45. Nusser, Z.; Mulvihill, E.; Streit, P.; Somogyi, P. Subsynaptic segregation of metabotropic and ionotropic glutamate receptors as revealed by immunogold localization. *Neuroscience* **1994**, *61*, 421–427.
46. Fitzner, D.; Bader, J.M.; Penkert, H.; Bergner, C.G.; Su, M.; Weil, M.-T.; Surma, M.A.; Mann, M.; Klose, C.; Simons, M. Cell-Type- and Brain-Region-Resolved Mouse Brain Lipidome. *Cell Rep.* **2020**, *32*, 108132.
47. Breckenridge, W.C.; Gombos, G.; Morgan, I.G. The lipid composition of adult rat brain synaptosomal plasma membranes. *Biochim. Biophys. Acta-Biomembr.* **1972**, *266*, 695–707.
48. Valsecchi, M.; Mauri, L.; Casellato, R.; Prioni, S.; Loberto, N.; Prinetti, A.; Chigorno, V.; Sonnino, S. Ceramide and sphingomyelin species of fibroblasts and neurons in culture. *J. Lipid Res.* **2007**, *48*, 417–424.
49. Mainali, L.; Raguz, M.; Subczynski, W.K. Phase-Separation and Domain-Formation in Cholesterol-Sphingomyelin Mixture: Pulse-EPR Oxygen Probing. *Biophys. J.* **2011**, *101*, 837–846.
50. Balleza, D.; Mescola, A.; Marín-Medina, N.; Ragazzini, G.; Pieruccini, M.; Facci, P.; Alessandrini, A. Complex Phase Behavior of GUVs Containing Different Sphingomyelins. *Biophys. J.* **2019**, *116*, 503–517.
51. Scheefhals, N.; MacGillavry, H.D. Functional organization of postsynaptic glutamate receptors. *Mol. Cell. Neurosci.* **2018**, *91*, 82–94.
52. Sidenstein, S.C.; D'Este, E.; Böhm, M.J.; Danzl, J.G.; Belov, V.N.; Hell, S.W. Multicolour multilevel STED nanoscopy of actin/spectrin organization at synapses. *Sci. Rep.* **2016**, *6*, 26725.

Table S1. Confinement parameters and their effect on the power of detection.

Parameter	Definition	Value in this study	Effect on confinement detection
L_c	Critical L ; threshold for confinement detection	$\alpha \times$ average L	
L_{cm}	Minimum critical L ; L below this value will be random diffusion	5.5	Lower L_{cm} will increase false positives, higher L_{cm} will decrease true positives
T_c	Critical time; minimal time period L should be above L_c	0.2 s	Lower T_c will increase false positives, higher T_c will decrease true positives
S_m	Maximum segment length for confinement detection	15 frames	Larger S_m will increase power of detection, but reduces the temporal resolution
S_{min}	Minimum segment length for confinement detection	4 frames	No large effect on confinement detection
α	Average L of a trajectory is multiplied by this factor in the range of 0–1 resulting in L_c	0.5	Low value will lead to L_c close to L_{cm} , high value could increase power of detection when there are highly confined zones but could also merge multiple confinement zones

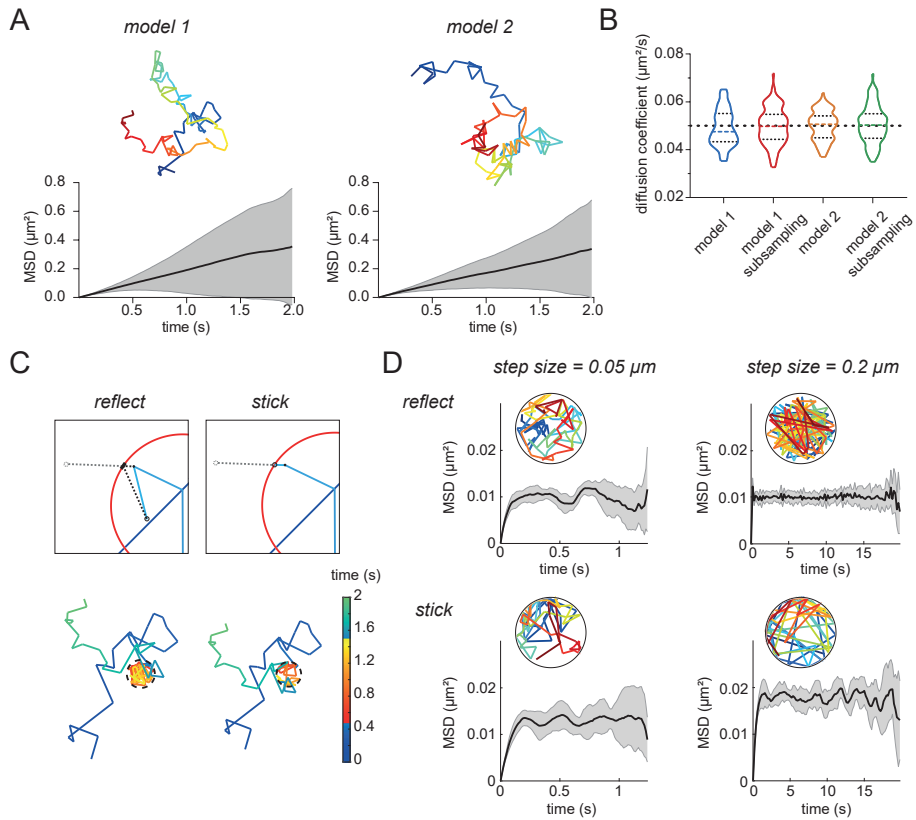


Figure S1. Random walk and confinement simulations.

(**A**) Model 1: random walk simulation where every consecutive coordinate is drawn from a Gaussian distribution based on diffusion coefficient and time step (left). Model 2: random walk simulation where step length is the same for every step, but the direction of the step is random (right). MSD versus time lag curves of 100 random walks (bottom). (**B**) Distribution of diffusion coefficients for the different random walk simulation models and after applying subsampling: only including the coordinate after every 100 simulation steps. (**C**) Principle of the ‘reflect’ confinement model (left). Principle of the ‘stick’ confinement model (right). Example trajectory for both models color-coded for time (bottom). $R_{conf} = 0.05 \mu\text{m}$. (**D**) MSD curves for 10 completely confined tracks simulated with the ‘reflect’ model (top) and the ‘stick’ model. Comparing a step size of $0.05 \mu\text{m}$ (left) and $0.2 \mu\text{m}$ (right). Gray area represents the weighted standard deviation over all MSD curves. $R_{conf} = 0.1 \mu\text{m}$.

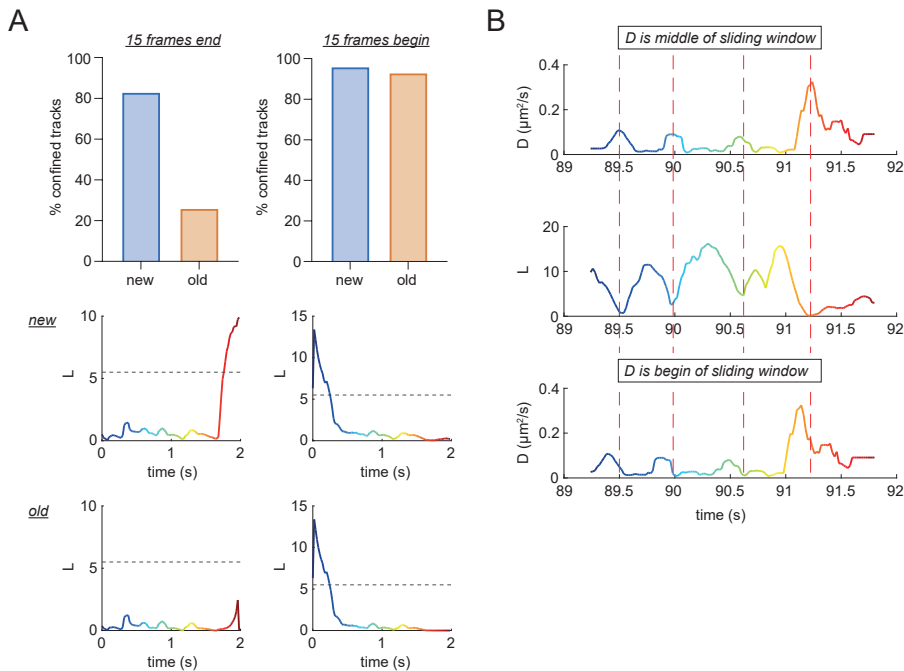


Figure S2. Improvements in the confinement analysis.

(A) Including the last points of a trajectory in the confinement index averaging, 100 trajectories were simulated with the last 15 frames of 100 frames confined. Comparison of the analysis from [1] (old) and our updated analysis (new). Our analysis achieves better detection of confinement periods at the end of the trajectory (left). There is no large difference in the detection of confinement at the beginning of trajectories (right). 100 simulated trajectories with the first 15 frames of 100 frames confined. $R_{conf} = 0.04 \mu\text{m}$. Confinement index (L) over time is shown for example trajectories analyzed with the updated method (middle) and the method from [1] (bottom). (B) Use D as the middle of the sliding window instead of the beginning. Peaks in the diffusion coefficient over time are indicated with the dashed red lines and correspond with valleys in the confinement index over time graph, as expected. This correlation of peaks and valleys is not as prominent when D is used as the beginning of the sliding window (bottom).

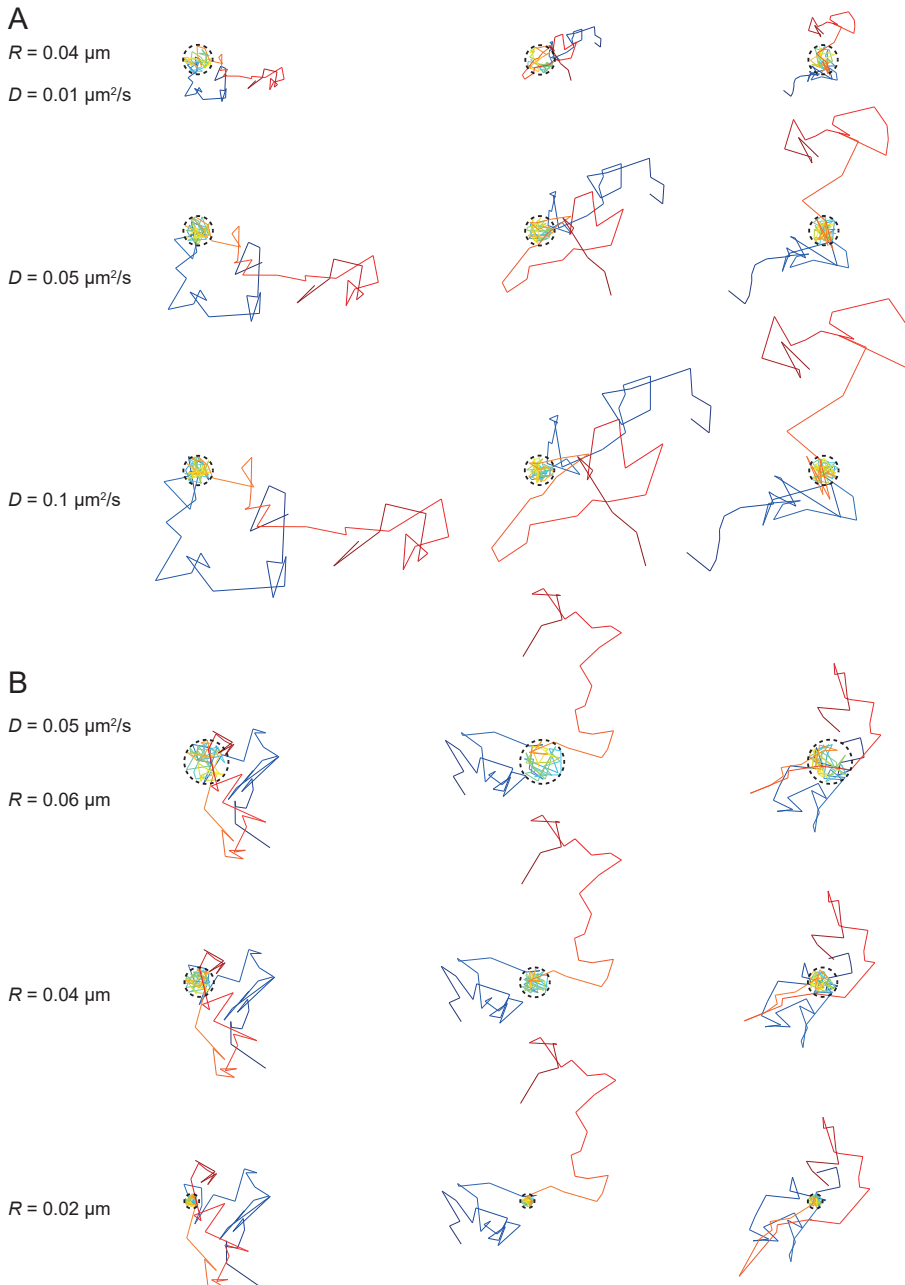


Figure S3. Raw simulated transient confined trajectories from Figure 1.

(A) Three different simulated trajectories varied in the diffusion coefficient of the simulation. $R_{conf} = 0.04 \mu\text{m}$.
(B) Three different simulated trajectories varied in their confinement radius size. $D = 0.05 \mu\text{m}^2/\text{s}$.

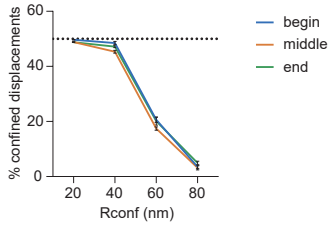


Figure S4. Effect of timing confinement on power of detection.

Effect of the timing of simulated confinement periods and R_{conf} on the correct detection of that confinement. 50 frames confined of total 100 frames per simulated track. Five independent simulations of 100 trajectories per condition. Dotted line indicates correct confinement detection. Data are represented as means \pm SD.

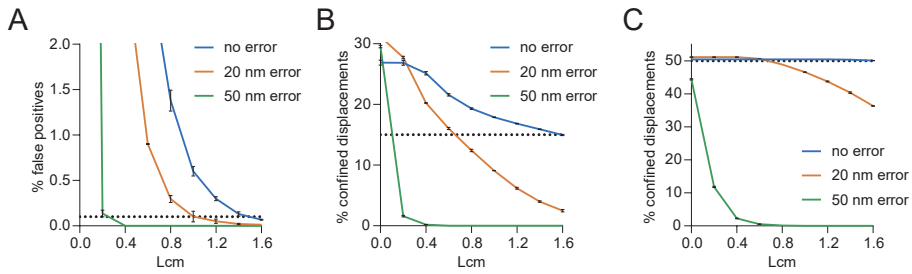


Figure S5. Effect of localization error on confinement detection using Dset.

(A) Effect of localization error on the percentage of false positives detected in random walks using Dset instead of Dmax. 3 independent simulations of 1000 trajectories per condition. Data are represented as means \pm SD. (B, C) Effect of localization error on the percentage of detected confined displacements in tracks simulated to be confined for 15 (B) or 50 (C) of the 100 frames. $R_{conf} = 0.04 \mu\text{m}$. 3 independent simulations of 1000 trajectories. Data are represented as means \pm SD.

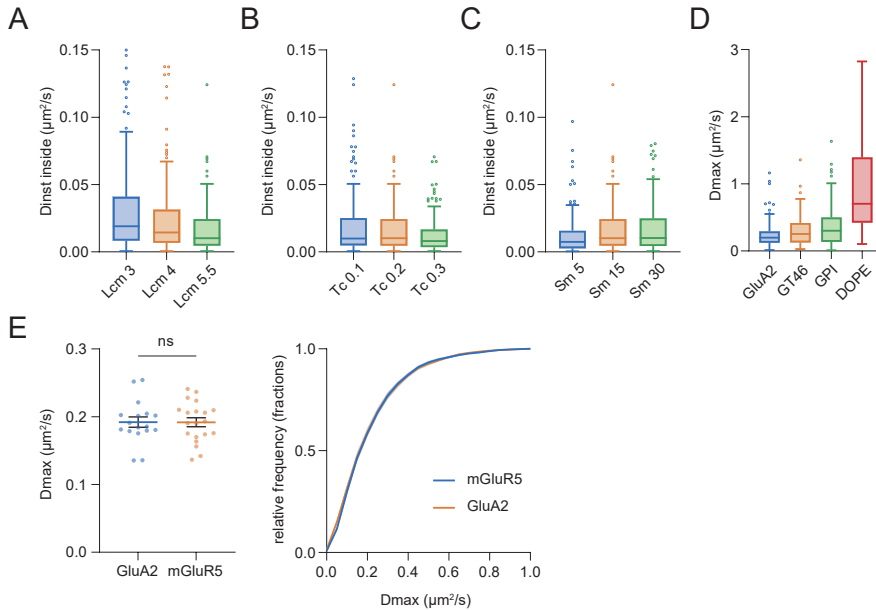



Figure S6. Confinement analysis on experimental trajectories.

(A–C) Effect of user-defined parameters on the estimated diffusion coefficient inside confinement zones. (A) Vary critical L , L_{cm} . Number of trajectories with confinement: $L_{cm} 3$: 381, $L_{cm} 4$: 309, $L_{cm} 5.5$: 219. (B) Vary critical time, T_c . Number of trajectories with confinement: $T_c 0.1$: 311, $T_c 0.2$: 219, $T_c 0.3$: 139. (C) Vary maximum segment length, S_m . Number of trajectories with confinement: $S_m 5$: 181, $S_m 15$: 219, $S_m 30$: 177. (D) Estimated D_{max} for membrane probes: GluA1, GT46, GPI and DOPE. (E) Average estimated D_{max} for mGluR5 ($n = 20$) and GluA2 ($n = 17$; unpaired t-test) (left), and corresponding cumulative frequency distribution (right). Data are represented as means \pm SEM.

References

1. Menchón, S.A.; Martín, M.G.; Dotti, C.G. APM_GUI: Analyzing particle movement on the cell membrane and determining confinement. *BMC Biophys.* **2012**, *5*, 4. <https://doi.org/10.1186/2046-1682-5-4>.

5



Resolving the dynamic subsynaptic distribution of GluA1- and GluA3-containing AMPA receptors

Manon Westra, Nicky Scheefhals and Harold D. MacGillavry

Cell Biology, Neurobiology and Biophysics, Department of Biology,
Faculty of Science, Utrecht University, Utrecht, The Netherlands

Abstract

AMPA-type glutamate receptors (AMPA_s) mediate the majority of fast excitatory transmission in the brain. In the hippocampus, most AMPARs are hetero-tetramers composed of GluA1/GluA2 or GluA2/GluA3 subunits. The subunit-specific addition and removal of AMPARs to and from the synapse are thought to control the long-term alterations in synaptic strength associated with learning and memory. It is becoming clear however that not just the number of receptors, but also their subsynaptic positioning relative to the presynaptic release machinery determines synaptic strength. Yet, we know surprisingly little about the subsynaptic organization of different AMPAR subunits, and even less about how this organization is controlled by synaptic activity. Here, we mapped the subsynaptic distribution of GluA1/2 and GluA2/3 AMPAR subtypes relative to PSD95 at excitatory synapses in hippocampal neurons using dual-color single-molecule localization microscopy. Using this technique we found that the different subunits accumulate in nanodomains and are enriched in PSD95 nanodomains. Furthermore, single-molecule tracking studies revealed that the different subunits are immobilized within the postsynaptic density. Lastly, we compared the subsynaptic organization and dynamics of the different AMPAR subtypes, both under basal conditions and after increasing cAMP levels to investigate potential differences during cAMP-mediated potentiation. We show that both AMPAR subtypes are recruited to the PSD after synaptic activation, but we observed no effect on the subsynaptic distribution. Together, these experiments revealed novel aspects of the dynamic subsynaptic organization of AMPAR subtypes that is relevant for a better understanding of synaptic transmission and plasticity.

Introduction

The vast majority of fast excitatory synaptic transmission in the brain is mediated by the neurotransmitter glutamate. The main ionotropic glutamate receptor is the α -amino-3-hydroxy-5-methyl-4-isoxazolepropionic acid receptor (AMPA), located on the postsynaptic terminal of a dendritic spine. AMPARs mediate fast synaptic transmission and play crucial roles in activity-dependent synaptic plasticity, including long-term potentiation (LTP) and long-term depression (LTD) (Huganir and Nicoll, 2013). The potentiation of synapses during LTP requires an increase in the number of AMPARs at the synaptic membrane, mediated by both exocytosis and lateral diffusion, whereas the weakening of synapses relies on the removal of AMPARs from the synaptic membrane via lateral diffusion and endocytosis. Thus, the dynamic trafficking of AMPARs leads to long-term alterations in synaptic strength, which is important for learning and memory processes.

AMPARs are composed of four subunits (GluA1–4) forming a tetramer. In the hippocampus, the most prevalent subunit combinations are GluA1/2 and GluA2/3 with a small proportion of GluA1 homomers (Wenthold et al., 1996; Mansour et al., 2001; Kessels et al., 2009; Lu et al., 2009). The AMPAR subunit composition has implications for its ion channel function. GluA2-lacking receptors are calcium permeable, whereas most GluA2-containing receptors are calcium impermeable, only GluA2 without Q607R RNA-editing is still calcium permeable (Hollmann et al., 1991; Hume et al., 1991; Isaac et al., 2007). The four AMPAR subunits differ in their C-terminal domains and this sequence determines their specific interactions with scaffold molecules and contains numerous regulatory elements subjected to phosphorylation

and other post-translational modifications (Anggono and Huganir, 2012) that can regulate the conductance and open probability of the AMPAR (Derkach et al., 1999; Banke et al., 2000).

To closely regulate AMPAR trafficking from the ER to the synaptic membrane, the AMPAR subunits also display different trafficking properties (Shi et al., 2001). GluA1 is easily transported from the endoplasmic reticulum (ER), through the Golgi, and finally to the synaptic membrane. However, GluA2 is retained in the ER and requires tetramerization with GluA1 to leave the ER and be transported to the synaptic membrane (Greger et al., 2002). It is proposed that the GluA1-containing receptors play a role in activity-dependent plasticity (Malinow et al., 2000). The synapse would first be populated by GluA1 homomers after the induction of LTP whereafter they are replaced by GluA1/2 heteromers to maintain LTP (Plant et al., 2006). On the other hand, GluA2/3 receptors are thought to be involved in the constitutive recycling of AMPARs at the synapse. Nevertheless, the role of the GluA3 subunit in synaptic trafficking has not been extensively investigated, and for a long time, the main perception has been that the GluA3 subunit was virtually dispensable. The GluA3 knockout (KO) mouse for instance shows normal basal synaptic transmission and normal pathway-specific LTP, in contrast to GluA1 and GluA2 KO mice (Meng et al., 2003; Reinders et al., 2016). However, recent studies revealed a specific role for the GluA3 subunit. Under basal conditions GluA3-containing AMPARs are in a low-conductance state, however, upon rising levels of intracellular cyclic AMP (cAMP) the open-channel probability of GluA3-containing AMPARs changes to a high-conductance state leading to synaptic potentiation (Gutierrez-Castellanos et al., 2017; Renner et al., 2017). Furthermore, GluA3-containing AMPARs are critical for A β -mediated synaptic depression and subsequent spine loss (Reinders et al., 2016). Altogether, it is evident that individual AMPAR subunits have unique contributions to the synaptic trafficking rules of AMPARs and play different roles in plasticity, but the exact mechanisms are still not completely understood.

Once arrived at the synaptic membrane, the surface AMPARs are concentrated at the postsynaptic density (PSD), a dense organization of postsynaptic scaffold molecules (Kharazia and Weinberg, 1997). The AMPARs are anchored and positioned by numerous scaffold molecules in the PSD, also forming a connection to the actin cytoskeleton (Sheng and Hoogenraad, 2007). The lateral organization of the PSD including the AMPARs is found to be of great importance for synaptic strength (MacGillavry et al., 2011). Because the affinity of AMPARs for glutamate is low, only postsynaptic receptors close to the presynaptic release site of glutamate will be activated (Liu et al., 1999; Compans et al., 2016). Therefore, alignment of the postsynaptic AMPARs with the presynaptic site of neurotransmitter release is crucial for efficient synaptic transmission (Franks et al., 2003; Tarusawa et al., 2009). Previous studies revealed that this organization of AMPARs is established through the formation of nanodomains: small areas (~70–80 nm) within the PSD that contain high densities of receptors (MacGillavry et al., 2013; Nair et al., 2013). It was found that these AMPAR nanodomains are directly opposed to the presynaptic sites of neurotransmitter release (Tang et al., 2016). Not surprisingly, the subsynaptic organization of AMPARs is suggested to have a functional effect on synaptic transmission, as simulations of receptor activation revealed that proper alignment of postsynaptic receptors with the presynaptic release site will result in larger synaptic responses (MacGillavry et al., 2013; Nair et al., 2013). Taken together, AMPARs are organized in subsynaptic domains which leads to improved synaptic functioning. However, it is unknown how different subunit compositions are organized in these nanodomains. Because of the proposed difference in the contribution of the subunits to synaptic trafficking and

plasticity, it is of great importance to elucidate the subsynaptic organization of the different AMPAR subtypes.

Here we investigated the dynamic subsynaptic distribution of the two AMPAR subtypes GluA1/2 and GluA2/3 at the excitatory postsynapse during basal conditions and after increasing cAMP levels. How are the different AMPAR subtypes distributed over the synapse and are there differences in their dynamic behavior? To study AMPAR organization within the small confines of the synapse we made use of super-resolution microscopy techniques. We found that the different AMPAR subunits are organized in subsynaptic domains that are on average the same size. Furthermore, using single-molecule tracking we found that AMPARs are immobilized within the synapse, and observed that GluA3 is less mobile and more confined within the PSD compared to GluA1. Increasing cAMP levels resulted in the recruitment of both GluA1 and GluA3 to the PSD, however, we observed no differences in their subsynaptic distribution.

Results

AMPA subunits are organized in subsynaptic domains

To investigate the organization of different AMPAR subtypes at the synapse, we first studied the expression and targeting of AMPAR subunits using confocal microscopy. We co-expressed the different SEP-tagged AMPAR subunits with Homer1c-mCherry, a marker for the PSD. For the subunits GluA1, GluA2 and GluA3 we observed expression at dendritic spines, with synaptic enrichment as the labeling signal overlapped with Homer1c-mCherry and there was low expression in the dendritic shaft (Supplementary Figure 1A). Studying endogenously-tagged AMPAR subunits using CRISPR/Cas9 revealed a similar expression pattern, with all three subunits being enriched at synapses (Supplementary Figure 1B). However, the GFP tags are integrated at the C-terminus of the AMPAR subtypes, which excludes the possibility of only investigating the surface pool of receptors. Therefore, the rest of the experiments are completed using overexpression constructs.

To resolve the subsynaptic distribution of AMPARs at high resolution, we used stimulated emission depletion (STED) microscopy. We labeled neurons expressing SEP-GluA1–3 with an anti-GFP nanobody coupled to the dye ATTO647N. Whereas with confocal microscopy the synaptic distribution of the AMPAR subunits appeared homogeneous, using STED we observed that the subunits are organized in distinct subsynaptic domains (Figure 1A). These domains are defined by clearly separated peaks in intensity as shown by the line profile. Because of the subsynaptic resolving potential of STED, we investigated the subsynaptic organization of AMPAR subunits GluA1–3 individually (Figure 1B). We observed different patterns of receptor distribution within synapses. In a large fraction of the synapses, the receptors form domains (~60%) whereas in other synapses the distribution of the synapse appeared more homogeneous (~40%). The subunits formed up to four domains per synapse (Figure 1C). Interestingly, we found a positive correlation between the number of domains per synapse and the size of the PSD ($0.55 \pm 0.2 \mu\text{m}$, mean \pm SD), measured by confocal resolved Homer1c-mCherry (Spearman $r = 0.50$, $p < 0.001$, $n = 123$ PSDs from 7 neurons, Figure 1D). On the other hand, domain size ($0.30 \pm 0.1 \mu\text{m}$, mean \pm SD) did not correlate to the size of the PSD (Pearson $r = 0.089$, $p = 0.18$, $n = 227$ domains from 7 neurons, Figure 1E). Both the average length and width of the domains did not differ

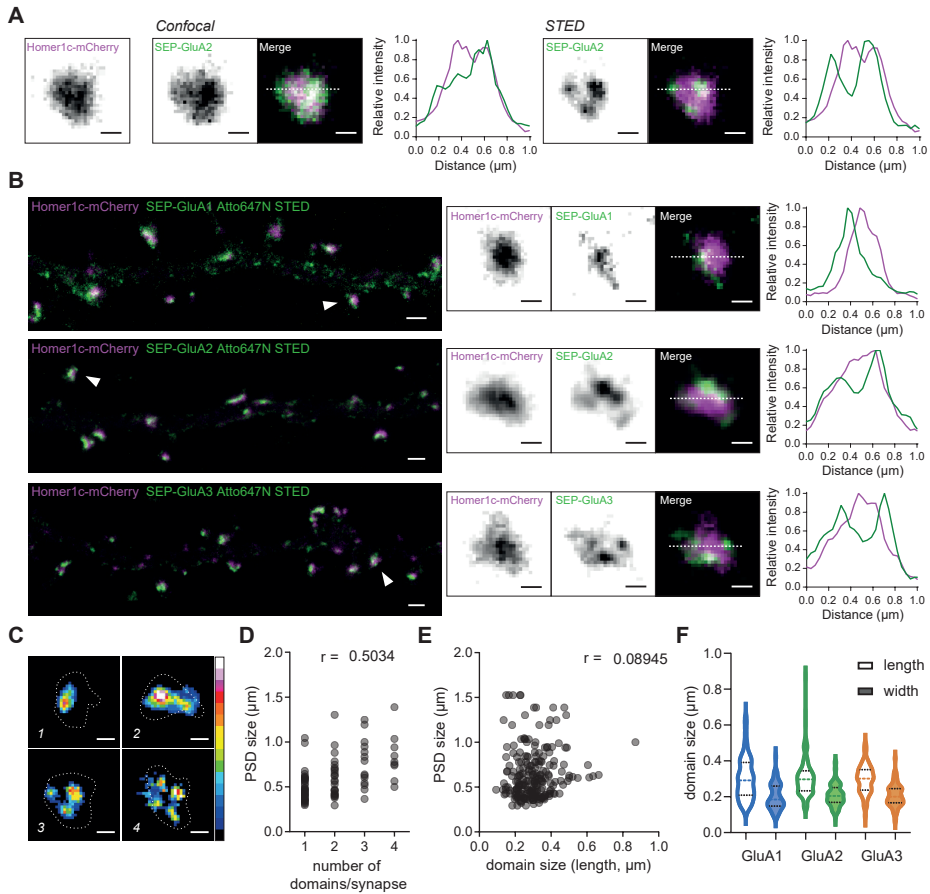


Figure 1. AMPAR subunits are organized in subsynaptic domains

(A) (left) Z_{max} projections of a confocal image of a synapse co-expressing Homer1c mCherry and SEP-GluA2 labeled with GFP booster Atto647N. Line indicates profile along which intensity was measured plotted in the graph. (right) Z_{max} projection of the corresponding STED image of SEP GluA2 with the line profile graph. (B) Z_{max} projections of STED images of dendrites expressing Homer1c-mCherry (confocal) together with SEP-GluA1/2/3 labeled with GFP booster Atto647N. Zooms show subsynaptic distribution of the different AMPAR subunits on Homer1c-mCherry as a PSD marker. Line indicates profile along which intensity was measured plotted in the graph. (C) 1–4 subsynaptic domains per synapse detected by STED microscopy. Color scale based on intensity, dotted line shows outline of confocal Homer1c-mCherry. (D) The number of domains per synapse is related to the size of the PSD, $p < 0.001$. (E) The size of the domains is not related to the size of the PSD, $p = 0.18$ (F) Violin plots showing the length and width of the domains formed by GluA1–3. Scale bars are 1 μm and 300 nm in the zooms.

significantly for the different AMPAR subunits (GluA1: l (length) $0.30 \pm 0.1 \mu\text{m}$, mean \pm SD, w (width) $0.20 \pm 0.07 \mu\text{m}$, $n = 61$; GluA2: l $0.31 \pm 0.1 \mu\text{m}$, w $0.21 \pm 0.06 \mu\text{m}$, $n = 103$; GluA3: l $0.30 \pm 0.08 \mu\text{m}$, w $0.21 \pm 0.06 \mu\text{m}$, $n = 63$) (Figure 1F). To summarize, we found that all AMPAR subunits are organized in subsynaptic domains with similar characteristics and that the size of the PSD is correlated with the number, but not the size of these domains.

Single-molecule localization microscopy reveals the subsynaptic distribution of GluA1 and GluA3

To further resolve the organization of subsynaptic AMPARs, we adopted another super-resolution microscopy technique, single-molecule localization microscopy (SMLM) and more specifically direct stochastic optical reconstruction microscopy (dSTORM). Since GluA2 forms AMPARs with both GluA1 and GluA3, for the remaining experiments we only studied GluA1 and GluA3 to investigate the two main AMPAR subtypes, GluA1/2 and GluA2/3. We surface-labeled SEP-GluA1 and SEP-GluA3 with an anti-GFP nanobody conjugated to the STORM-suitable dye Alexa647. We co-transfected PSD95.FingR-mEos3.2 to do two-color SMLM and combine STORM and photoactivated localization microscopy (PALM). Here we also found that both GluA1 and GluA3 localizations are overlapping with the PSD95 localizations (Figure 2A). Local-density-based plots reveal the nanodomain organization of PSD95, GluA1, and GluA3 (Figure 2B). The PSD area was identified using density-based spatial clustering of applications with noise (DBSCAN) on the PSD95 localizations. Both GluA1 and GluA3 are enriched within the PSD (Supplementary Figure 2A). We quantified the overlap of GluA1 and GluA3 with the PSD by calculating the fraction of AMPAR localizations within the spine that overlapped with the PSD area. This fraction of overlap with the PSD was higher for GluA3 compared to GluA1 (Figure 2C). In agreement with this result, when investigating the distance of the AMPAR localizations to the PSD border, we found that the relative fraction of localizations inside the PSD was higher for GluA3 than for GluA1 (Figure 2D). Within the PSD and closely surrounding the PSD we did not observe different relative distributions of GluA1 and GluA3 (Supplementary Figure 2B). Using a custom local-density-based cluster analysis, we identified nanodomains of PSD95, GluA1, and GluA3. The local density of both GluA1 and GluA3 is higher inside PSD95 nanodomains compared to the rest of the PSD, showing that GluA1 and GluA3 are enriched in PSD95 nanodomains (Figure 2E). The area and number of AMPAR nanodomains were not significantly different between GluA1 and GluA3 (Figure 2F–H).

cAMP stimulates recruitment of GluA1 and GluA3 to the PSD

In addition to studying AMPAR organization during basal conditions, we aimed to investigate a possible change in organization during synaptic potentiation. Therefore, we performed the same experiments after increasing the levels of cAMP by adding forskolin and IBMX. As previous research showed that the contribution of GluA3-containing AMPARs to synaptic transmission is potentiated upon increased cAMP levels (Renner et al., 2017), we hypothesized that GluA3 would become more enriched in PSD95 nanodomains or that GluA3 domains would increase in size and number. However, we did not observe any significant difference in nanodomain organization or co-localization of AMPARs with PSD95 between the control and cAMP conditions (Figure 2C–H, Supplementary Figure 2A, C–F).

Because this synaptic plasticity paradigm did not seem to affect the subsynaptic organization of GluA1 or GluA3, we wondered if there would be synaptic recruitment of AMPARs during increased cAMP levels. To visualize the surface pool of AMPARs during live-cell imaging, we made use of super-ecliptic pHluorin (SEP), a pH-sensitive GFP variant (Supplementary Figure 3A, B). We indeed observed a modest, but significant increase in relative intensity of both GluA1 and GluA3, specifically in spines, of approximately 5% that plateaued after 5–15 minutes (Figure 3A–C). A similar increase in intensity was not found in the shaft, thus

there was not a general increase in surface expression in the whole neuron (Supplementary Figure 3C, D). Thus, cAMP stimulates the increase in AMPAR surface expression in spines but seems to not affect the subsynaptic organization of GluA1 or GluA3.

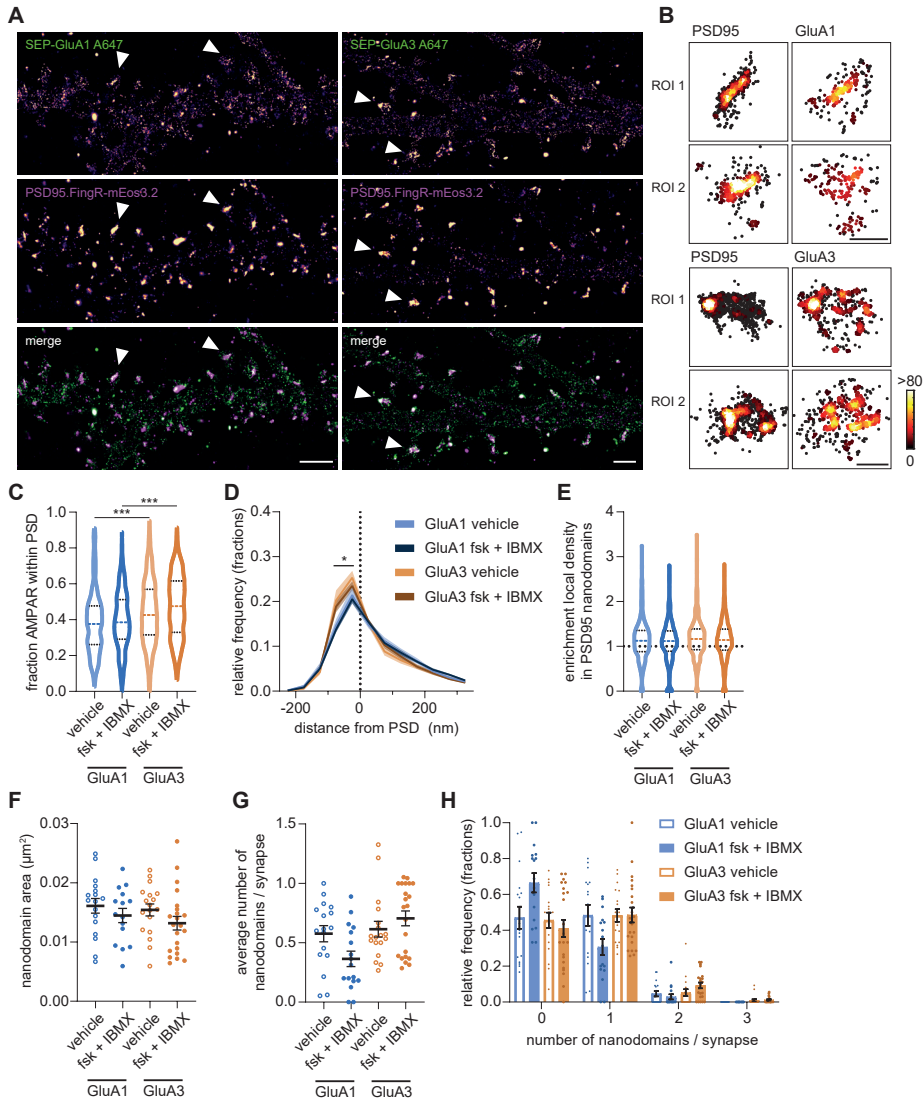


Figure 2. SMLM reveals subsynaptic distribution of AMPAR subunits

(A) Two-color single-molecule localization microscopy images of SEP-GluA1 and SEP-GluA3 labeled with anti-GFP nanobody Alexa647 and PSD95.FingR-mEos3.2. Scale bars, 2 μm . (B) Zooms show local density plots of the four indicated synapses. Scale bars, 500 nm. (C) Fraction of AMPAR localizations within the spine that overlap with the PSD. (D) Relative frequency distribution of the distance of AMPAR localizations to the PSD border. (E) Enrichment of the local density of AMPARs inside PSD95 nanodomains. (F) Average nanodomain area per synapse for each neuron. (G) Average number of nanodomains per synapse for each neuron. (H) Relative frequency distribution of number of nanodomains per synapse. * $p < 0.05$, *** $p < 0.001$.

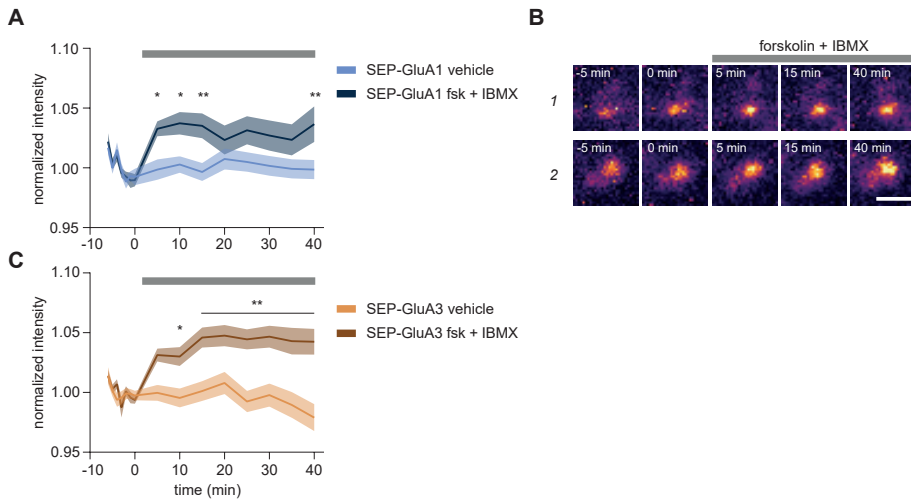


Figure 3. Recruitment of GluA1 and GluA3 to the PSD after increase in cAMP levels

(A) Spine intensity of SEP-GluA1 over time, with and without the addition of forskolin and IBMX at timepoint 0 to increase cAMP levels, indicated by the grey bar. (B) Two GluA3 spines over time after the addition of forskolin and IBMX. Scale bar, 1 μm . (C) Spine intensity of SEP-GluA3 over time, with and without the addition of forskolin and IBMX at timepoint 0 to increase cAMP levels, indicated by the grey bar. $*p < 0.05$, $**p < 0.01$.

AMPA receptors are immobilized within the synapse

To learn more about the diffusion and confinement of AMPAR subunits in and around synapses, we studied the dynamics of the AMPAR subtypes in living neurons using single-molecule tracking (SMT). We co-expressed SEP-GluA1 or SEP-GluA3 with Homer1c-mCherry to mark the PSD and obtained single-molecule localizations that were visualized by the anti-GFP nanobody coupled to ATTO647N that transiently binds to the SEP-tagged subunits. Using single-molecule tracking algorithms we could track localized molecules that appeared in consecutive frames. This resulted in many single-molecule trajectories with associated mean squared displacement (MSD) versus time curves. We plotted the trajectories of GluA1 and GluA3 on the corresponding PSD mask made from the widefield image of Homer1c-mCherry. To estimate the diffusion coefficient for each trajectory, we used the relation between the MSD and the diffusion coefficient ($MSD = 4 \times D \times \Delta t$). The frequency distributions of the diffusion coefficient for both GluA1 and GluA3 showed two peaks where the less mobile peak was higher for GluA3. This shows that GluA3 diffuses at a slower rate compared to GluA1, which is also shown by the lower median diffusion coefficient (GluA1: $0.028 \pm 0.002 \mu\text{m}^2/\text{s}$, GluA3: $0.021 \pm 0.001 \mu\text{m}^2/\text{s}$, $p = 0.016$) and the smaller mobile fraction (Figure 4A–C, Supplementary Figure 4A). Here we also compared the basal condition with the condition in which we increased cAMP levels. Although not significant, we do see a trend towards lower diffusion coefficients for both GluA1 and GluA3 after the addition of forskolin and IBMX (Figure 4B–E, Supplementary Figure 4B, C).

Next, we created a PSD mask based on the widefield image of Homer1c-mCherry. Trajectories were divided into synaptic tracks and extrasynaptic tracks: the synaptic tracks are the trajectories that overlap with the PSD for 75% of the time and the extrasynaptic tracks

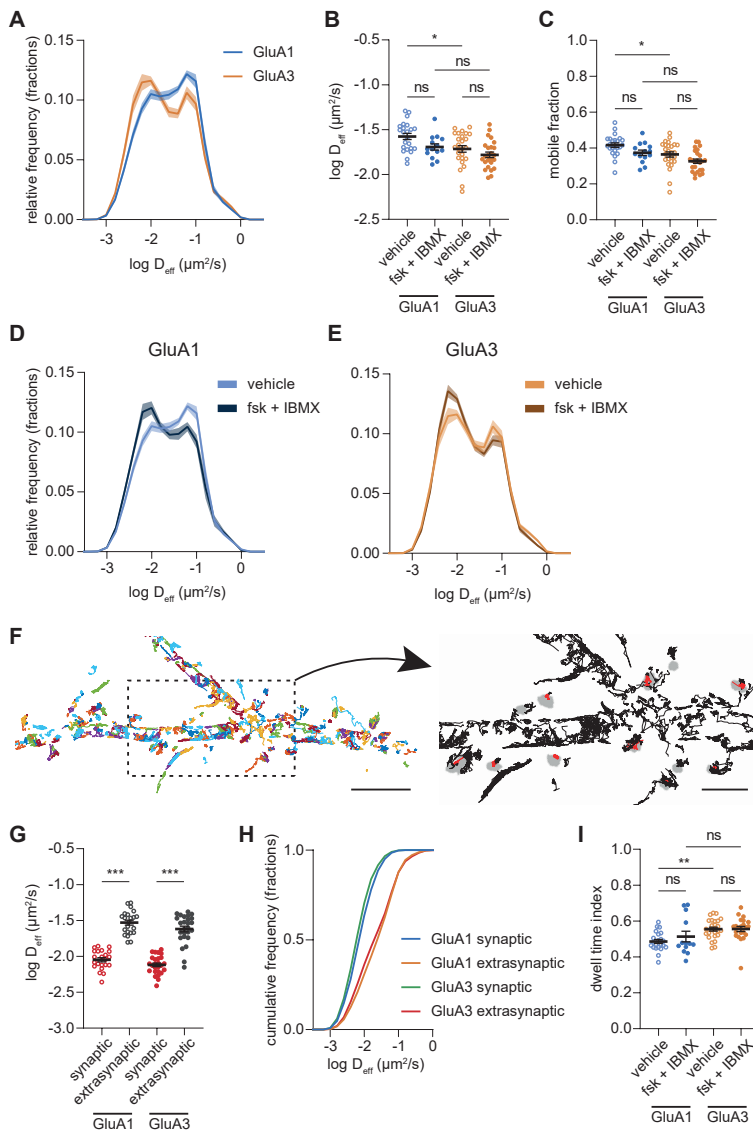


Figure 4. AMPARs are immobilized within the synapse

(A) Relative frequency distributions of the diffusion coefficient of SEP-GluA1 and SEP-GluA3. (B) The corresponding comparison of the median diffusion coefficient per neuron of SEP-GluA1 and SEP-GluA3 with and without forskolin and IBMX. (C) The corresponding comparison of the fraction of mobile trajectories per neuron of SEP-GluA1 and SEP-GluA3 with and without forskolin and IBMX. (D) Relative frequency distributions of the diffusion coefficient of SEP-GluA1 with and without forskolin and IBMX. (E) Relative frequency distributions of the diffusion coefficient of SEP-GluA3 with and without forskolin and IBMX. (F) Single-molecule trajectories of SEP-GluA3, every track assigned a random color. Zoom shows synaptic tracks in red and synaptic marker Homer1c in grey. Scale bar is 5 μm and 2 μm in the zoom. (G) Comparison of the median diffusion coefficient per neuron for synaptic and extrasynaptic tracks of GluA1 and GluA3. (H) The corresponding cumulative frequency distribution of the diffusion coefficient of the synaptic and extrasynaptic tracks of GluA1 and GluA3. (I) Comparison of the dwell time index per neuron for GluA1 and GluA3 with and without forskolin and IBMX. Dwell time index is the fraction of a track that overlaps with the PSD. * $p < 0.05$, ** $p < 0.01$, *** $p < 0.001$, ns $p > 0.05$.

are the remaining tracks (Figure 4F). Quantification revealed that the synaptic tracks are immobilized in contrast to the extrasynaptic tracks that are mobile. The median diffusion coefficient of synaptic GluA1 tracks ($0.0093 \pm 0.0006 \mu\text{m}^2/\text{s}$) differed significantly from extrasynaptic tracks ($0.031 \pm 0.003 \mu\text{m}^2/\text{s}$). The same difference was observed between the median diffusion coefficient of synaptic ($0.0079 \pm 0.0005 \mu\text{m}^2/\text{s}$) and extrasynaptic GluA3 tracks ($0.026 \pm 0.002 \mu\text{m}^2/\text{s}$) (Figure 4G, H). Furthermore, the dwell time index — the fraction of time that a trajectory overlaps with the PSD — was higher for GluA3 compared to GluA1, but was not affected by increased cAMP levels (Figure 4I).

Lastly, we categorized the trajectories into a mobile and an immobile pool based on the ratio between the radius of gyration and the mean step size (Golan and Sherman, 2017). We analyzed the mobile pool of trajectories for periods of transient confinement (Westra and MacGillavry, 2022). The detected confinement zones had a radius of around 60 nm and were on average confined for 33% of the trajectory, these measures did not change after increasing cAMP levels (Figure 5A, B). There was a higher degree of overlap of the transient confinement zones with the PSD for GluA3 than for GluA1 (Figure 5C). Similarly, the centers of the immobile GluA3 trajectories overlapped more with the PSD compared to GluA1 (Figure 5D). The frequency distributions of the distance of transient confinement zones or immobile trajectories to the border of the PSD revealed that GluA3 is relatively more confined within or at the border of the PSD than GluA1 (Figure 5E, F). These relative distributions did not change after increasing cAMP levels (Supplementary Figure 5A–D).

Discussion

The proper alignment of the presynaptic release site of glutamate with the postsynaptic AMPARs has been found to be important for efficient synaptic transmission. Thus, not only the trafficking of AMPARs to and from the synapse plays a role in synaptic functioning, but also their location within the synaptic membrane can make a difference. It has previously been reported that AMPARs are organized in distinct nanodomains within the PSD, however, information is lacking on the relative distribution of the different AMPAR subtypes. Using super-resolution techniques, we investigated the dynamic subsynaptic distribution of the different AMPAR subunits. Both with STED microscopy and SMLM, we were able to resolve subsynaptic domains of GluA1–3 within the PSD, but we found no striking differences in the subsynaptic distribution of different AMPAR subunits. We did find that GluA3 is less mobile than GluA1 and is more confined within the PSD. The distribution and dynamics of GluA1 and GluA3 under basal conditions and after increased cAMP levels were seemingly similar, but both receptor types were recruited to the PSD during this synaptic activation paradigm.

Previous studies reported on the organization of AMPARs in nanodomains (MacGillavry et al., 2013; Nair et al., 2013). However, it is unknown which AMPAR subtypes these nanodomains comprise. In this study, we investigated the subsynaptic organization of the GluA1 and GluA3 AMPAR subunits. With STED microscopy we found an average domain size of 200–300 nm for each subunit, which is consistent with the domain size reported for PSD nanodomains resolved with STED (Fukata et al., 2013). As a logical result of better resolution, the observed size of nanodomains resolved with SMLM is smaller with an area of around $0.015 \mu\text{m}^2$, but slightly larger than the size of PSD95 and AMPAR nanodomains reported in previous studies (MacGillavry et al., 2013; Nair et al., 2013). However, we did observe a

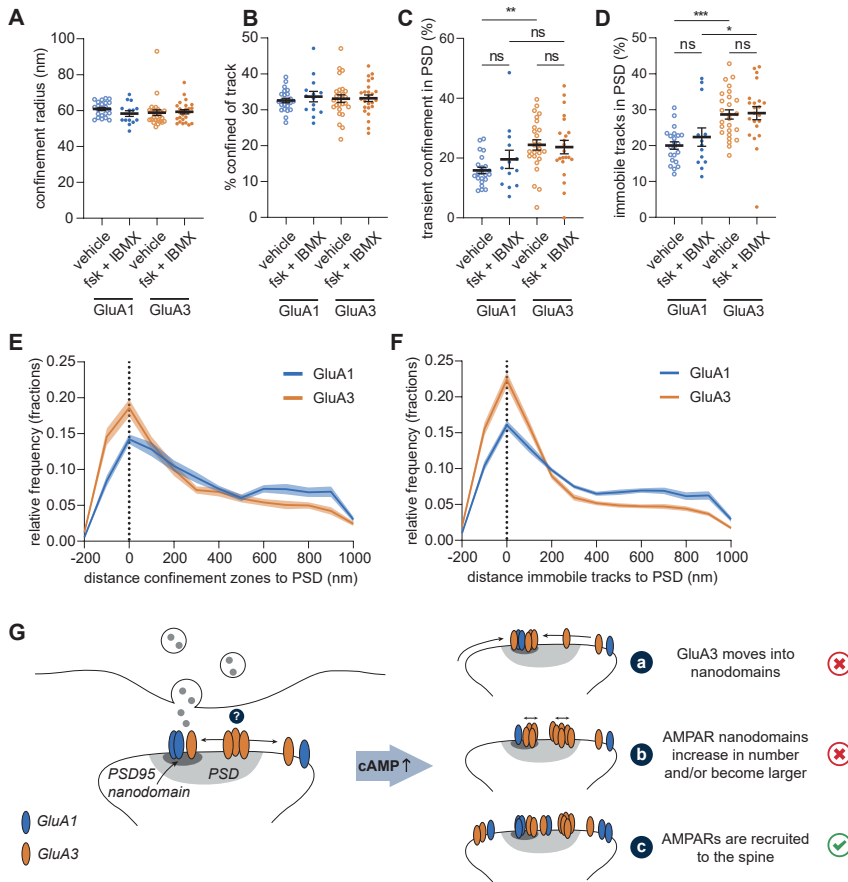


Figure 5. GluA3 is more confined within the PSD than GluA1

(A) Median confinement radius per neuron for GluA1 and GluA3 with and without forskolin and IBMX. (B) Median percentage of confinement per trajectory per neuron for GluA1 and GluA3 with and without forskolin and IBMX. (C) Percentage of transient confinement zones from which the center is inside the PSD for GluA1 and GluA3 with and without forskolin and IBMX. (D) Percentage of immobile trajectories from which the center is inside the PSD for GluA1 and GluA3 with and without forskolin and IBMX. (E) Relative frequency distribution of the distance of the center of transient confined areas to the border of the PSD. (F) Relative frequency distribution of the distance of the center of immobile trajectories to the border of the PSD. (G) Schematic representation of the different hypotheses about the effect of an increase in cAMP levels on the subsynaptic organization of AMPAR subunits at the postsynaptic membrane. The results of this study do not unveil evidence for hypotheses a and b, only for hypothesis c. * $p < 0.05$, ** $p < 0.01$, *** $p < 0.001$, ns $p > 0.05$.

positive correlation between the size of the PSD and the number of domains we resolved, as also previously described for AMPAR nanodomains (Nair et al., 2013). A larger spine with a larger PSD can contain more AMPARs (Matsuzaki et al., 2001), which we show are likely to be organized in multiple subsynaptic domains.

As the localization of AMPAR subunits is a consequence of their mobility, we studied the dynamics of the different subunits using single-molecule tracking. We found that the synaptic

trajectories are significantly less mobile than the extrasynaptic trajectories. This conclusion is consistent with previous studies that reported on diffusion coefficients of AMPARs and looked at the difference between the dynamics of synaptic and extrasynaptic receptors (Bats et al., 2007). The diffusion coefficients we found, fall within the range of diffusion coefficients found for GluA1-containing AMPARs inside and outside PSD95 clusters (Bats et al., 2007). Furthermore, we show that GluA3 has a lower diffusion coefficient than GluA1 and resides longer within the PSD. The longer confinement of GluA3 within the PSD combined with the result that AMPARs are less mobile within the PSD could explain the lower mobility of GluA3.

Perhaps most interesting to investigate is the role of the dynamic subsynaptic distribution of the different subunits in synaptic transmission. What happens to the subsynaptic organization of the subunits in response to activity? Do the different subunits respond differently? Recent studies reported that GluA3 seems to be ‘silent’ under normal conditions, but becomes involved in specific situations like cAMP-mediated potentiation or A β -mediated memory impairment. Genetic deletion of GluA3 does not influence synaptic transmission under basal conditions, however, A β cannot exert its effects on synapses and memory in GluA3 knockout mice (Reinders et al., 2016). Furthermore, a rise in cAMP was shown to lead to GluA3-dependent potentiation (Gutierrez-Castellanos et al., 2017; Renner et al., 2017). More specifically, Renner et al. showed that under basal conditions the GluA2/3 receptors are in a low-conductance state, whereas they shift towards a high-conductance state upon a rise in intracellular cAMP (Renner et al., 2017). Thus, a change in conductance of GluA2/3 is suggested to be responsible for the GluA3-dependent potentiation. However, we hypothesized that the subsynaptic distribution of AMPARs during these specific circumstances could be different from basal conditions and could also contribute to the GluA3-dependent potentiation (Figure 5G). One of the hypotheses was that under basal conditions the GluA2/3 AMPARs are not incorporated in subsynaptic domains that enable efficient synaptic transmission. But that upon synaptic potentiation these receptors would move inside these subsynaptic domains, allowing the receptors to become activated. However, we did not observe an increased enrichment of GluA3 within the PSD upon the increase in cAMP levels. Another hypothesis was that the AMPAR nanodomains increase in size or number after potentiation, for which we found no proof. We only observed recruitment of GluA3 to the PSD after the addition of forskolin and IBMX, however, this cannot explain the specific effect of cAMP-driven synaptic potentiation via GluA3 because a similar increase was observed for GluA1. These recruitment results were in contrast to the previous study, where no recruitment of GluA3 was observed after forskolin and IBMX (Renner et al., 2017). A possible explanation could be that our experiments were performed in dissociated cultures instead of organotypic slices, which perhaps allowed us to identify more subtle differences in synaptic enrichment.

To conclude, the objective of this study was to resolve the dynamic subsynaptic distribution of the different AMPAR subtypes. Our findings indicate that the different AMPAR subunits are organized in subsynaptic domains and are enriched in PSD95 nanodomains. However, even though individual AMPAR subunits have been reported to have unique contributions to the synaptic trafficking rules of AMPARs and play distinct roles in plasticity, we observed surprisingly little difference in their dynamics and subsynaptic distribution. Further research is required to determine the specific relative distributions and contributions of the different AMPAR subtypes, particularly during different synaptic activation paradigms. It is possible that posttranslational modifications and auxiliary subunits play a more significant role in the diversification of AMPAR subtypes than the subunit composition itself. A deeper understanding

of these mechanisms will aid in comprehending how the subsynaptic organization of AMPARs contributes to glutamatergic signaling.

Methods

Animals

All animal experiments were performed in compliance with the guidelines for the welfare of experimental animals issued by the Government of the Netherlands (Wet op de Dierproeven, 1996) and European regulations (Guideline 86/609/EEC). All animal experiments were approved by the Dutch Animal Experiments Review Committee (Dier Experimenten Commissie; DEC), performed in line with the institutional guidelines of Utrecht University.

Primary neuron cultures and transfections

Dissociated hippocampal cultures were prepared from mixed-sex embryonic day 18 (E18) pups from Wistar rats (Janvier Labs) (Kapitein et al., 2010). Dissociated neurons were plated on Ø18-mm coverslips coated with poly-L-lysine (37.5 µg/mL, Sigma-Aldrich) and laminin (1.25 µg/mL, Roche Diagnostics) at a density of 100,000 neurons per well. Neurons were grown in Neurobasal medium (NB) supplemented with 1% penicillin/streptomycin (Gibco), 2% B27 (Gibco), and 0.5 mM L-glutamine (Gibco) at 37 °C in 5% CO₂. From days in vitro (DIV) 1 onward, medium was refreshed weekly by replacing half of the medium with BrainPhys Neuronal Medium (BP, STEMCELL Technologies) supplemented with 2% NeuroCult SM1 (STEMCELL Technologies) and 1% penicillin/streptomycin. At DIV3 (knock-ins) or DIV14–18 (overexpression), neurons were transfected with indicated constructs using Lipofectamine 2000 (Invitrogen). For each well, 1–2 µg DNA was mixed with 3.3 µL Lipofectamine 2000 in 200 µL BP, incubated for 30 min at room temperature (RT). Then, 400 µL conditioned medium was transferred to a new culture plate and replaced by 260 µL BP supplemented with 0.5 mM L-glutamine. The DNA mix was added to the neurons and incubated at 37 °C in 5% CO₂. After 1 to 2 h, neurons were briefly washed with BP and transferred to the new culture plate with conditioned medium supplemented with an additional 400 µL BP with SM1 and penicillin/streptomycin and kept at 37 °C in 5% CO₂. All experiments were performed using neurons at DIV18–22.

DNA plasmids

The following plasmids have been described before in previous studies: Homer1c-mCherry (Scheefhals et al., 2019), PSD95.FingR-mEos3.2 (Gross et al., 2013), and the ORANGE knock-ins for GluA1-GFP, GluA2-GFP, and GluA3-GFP (Willems et al., 2020). The GluA1 (flop), GluA2 (flip, Q/R edited), and GluA3 (flop) receptor sequences were subcloned into a pRK5 vector between the MluI and XbaI restriction sites. SEP- or SNAP-tags were located at the N-terminus of the receptors and therefore these PCR-amplified cDNAs were subcloned between the AgeI and MluI restriction sites immediately after the signal sequence in pRK5-GluA1/2/3. All constructs were verified by sequencing.

Immunocytochemistry of dissociated hippocampal cultures

Hippocampal neurons were fixed using 4% paraformaldehyde (PFA) with 4% sucrose in PBS or with 4% EM-grade PFA in PEM80 buffer (80 mM PIPES, 2 mM MgCl₂, 5mM EGTA, pH 6.8) for 10 minutes at 37 °C and washed three times in PBS containing 0.1 M glycine (PBS/Gly). Neurons were blocked in blocking buffer (10% normal goat serum (NGS) (Abcam) in PBS/Gly) and if indicated permeabilized with 0.1% Triton X100 for 1 hour at 37 °C. Next, to enhance the GFP signal of the knock-ins, coverslips were incubated with rabbit anti-GFP (MBL Sanbio, 598, RRID AB_591819) diluted 1:2000 in incubation buffer (5% NGS in PBS/Gly with 0.1% Triton X100 (only if permeabilization necessary)) overnight at 4 °C or 2 hours at RT. Coverslips were washed three times with PBS/Gly and incubated with anti-rabbit Alexa488 (Life Technologies) diluted 1:250 in incubation buffer for 1 hour at RT. Labeling with nanobodies was similar except the primary antibody step is removed from the protocol. Neurons were incubated with FluorTag-X4 anti-GFP Alexa647 (Nanotag) diluted 1:500 in 3% NGS in PBS/Gly for 1 hour at RT or with GFP-booster Atto647N (Chromotek) 1:200 in 1% BSA in PBS/Gly for 2 hours at RT. For confocal microscopy, coverslips were washed three times in PBS/Gly, dipped in Milli-Q water (MQ), and mounted in Mowiol mounting medium (Sigma). For dSTORM, the coverslips were kept in PBS until mounting for imaging.

Confocal imaging

Confocal images of the GluA knock-ins were acquired with a Zeiss LSM 700 microscope and imaging was performed with a Plan-Apochromat 63× oil (NA 1.40) objective. A Z-stack containing 7–12 planes at a 0.56- μm interval was acquired and maximum intensity projections were made for analysis and display.

STED imaging

STED imaging was performed with a Leica TCS SP8 STED 3X microscope using an HC PL APO 100×/NA1.4 oil-immersion STED WHITE objective. mCherry and Atto647N were excited with 516-nm and 633-nm pulsed laser light (white light laser, 80 MHz), respectively. Atto647N was depleted with a 775-nm pulsed depletion laser. Fluorescence emission was detected using a Leica HyD hybrid detector with a gating time from 0.5 to 6 ns. Images were acquired as Z-stack using the 100× objective. Maximum intensity projections were obtained for image display and analysis. Hippocampal neurons were transfected with SEP-GluA1/2/3 and Homer1c-mCherry and labeled with GFP-booster Atto647N. Line profiles were made in ImageJ, normalized to the maximum intensity.

Subsynaptic domains were defined by plotting intensity profiles along the synapses and observing separate peaks. The size of domains (length and width) was indicated by the full width at half maximum (FWHM) of a subsynaptic domain determined from the standard deviation of the Gaussian fit.

Single-molecule localization microscopy

SMLM experiments were performed on the Nanoimager S from ONI (Oxford Nanoimaging) equipped with a 100× oil immersion objective (Olympus Plan Apo, NA 1.4) and an XYZ closed-loop piezo stage. Imaging was performed using a 640 nm laser. Fluorescence was detected using an sCMOS camera (ORCA Flash 4, Hamamatsu). Integrated filters were used to split far-red emission onto the right side of the camera and blue-green-red emission spectra on the left side, enabling simultaneous dual-color imaging.

The imaging chamber was temperature-controlled at 30 °C to prevent fluctuations in temperature during the time course of an experiment that might affect the alignment of the channels. Channel alignment was performed before each imaging session using 100-nm TetraSpeck beads (Invitrogen). Imaging was performed with oblique illumination using a motorized mirror and all images were acquired at 20 Hz (50 ms exposure time).

Hippocampal neurons were transfected with SEP-GluA1 or SEP-GluA3 with PSD95.FingR-mEos3.2 and fixed at DIV18–22. Neurons were stained with anti-GFP nanobody conjugated to Alexa647. Coverslips were mounted on concave slides in dSTORM-buffer (50 mM Tris, 10 mM NaCl, 10% glucose at pH 8.0, supplemented with 5 mM MEA, 700 $\mu\text{g}/\text{mL}$ glucose oxidase, and 40 $\mu\text{g}/\text{mL}$ catalase). Transfected neurons were localized using low laser powers. At low laser powers, a snapshot was acquired to create a mask from for the analysis. dSTORM was performed for Alexa647 simultaneously with PALM for mEos3.2. While laser power of 640-nm and 561-nm was high, the 405-nm laser was gradually increased to let Alexa647 blink and mEos3.2 photoswitch from green to red fluorescence, at the level that there were no overlapping blinking events. Imaging was continued for 15,000 frames or till no more blinking events could be observed.

Single-molecule localization microscopy analysis

NimOS software from ONI (version 1.18) was used for detection of single-molecule localization events and drift correction. Resulting localization tables were additionally drift-corrected using Detection of Molecules (DoM) plugin v.1.2.1 for ImageJ (https://github.com/ekatrakha/DoM_Utrecht) if required. Further analysis was performed in MATLAB. Localizations were filtered out if the localization precision was >50 nm, next, localizations were tracked to filter on localizations occurring in consecutive frames. If localizations occurred within a radius of 60 nm in consecutive frames, only the localization with the best precision was saved. If localizations occurred in more than 10 consecutive frames, all those localizations were filtered out. Datasets were further filtered, removing all localizations with a localization error >25 nm. ROIs outlining spine heads were defined based on the rendered AMPAR image and drawn by hand. DBSCAN analysis within the manual drawn ROI was used to define the border of the PSD for the PSD_{FingR}-mEos3.2 localizations. For each localization in an ROI, the localization density was calculated as the number of localizations within a radius of $5 \times$ the mean nearest neighbor distance (MNND) (MacGillavry et al., 2013). Localizations were considered part of a nanodomain if the local density was >40 . Nanodomains were isolated using the MATLAB functions *linkage()* and *cluster()*. The nanodomain boundary was constructed using the Voronoi diagrams circumventing the localizations.

For the enrichment analysis the nearest neighbor distance (NND) is calculated for all AMPAR localizations within an ROI, MNND is the mean of all those NNDs. Local density is the number of localizations found within a range of $5 \times \text{MNND}$ for every. Enrichment for in PSD vs outside PSD (but within the ROI) is then calculated by

averaging all local density values for localizations inside and dividing that by the mean of all local density values of localizations outside. Finally, the median of all these ROI values is taken as a measure of enrichment for that neuron. For the enrichment in nanodomains something similar is done. Only now it is the comparison between the local density inside nanodomains versus the local density outside nanodomains and both are only within the PSD.

For the ring analysis, rings were defined as a fraction of the PSD border. Per ring, the number of localizations was calculated resulting in the fraction of localizations per ring. To correct for the variable sizes of the rings, for each ring the fraction of the area was calculated. Next, for each ring, the fraction of localizations was divided by the fraction of ring area and normalized to 1.

Co-localization analysis of GluA1/3 and PSD95 was performed as described in (Willems and MacGillavry, 2022). The co-localization indices calculated for each localization individually are averaged to obtain a mean co-localization index per synapse for both channels.

Live-cell spinning disk confocal imaging

Live-cell experiments were carried out in an environmental chamber at 37 °C (TokaHit) on an inverted Nikon Ti Eclipse microscope equipped with a confocal spinning disk unit (Yokogawa CSU-X1-A1) and a 491-nm laser (Cobolt Calypso). Fluorescence emission was detected using a 100× oil-immersion objective (Nikon, Plan Apo VC, NA 1.4) together with an EMCCD camera (Photometrics Evolve 512) controlled by MetaMorph 7.7 software (Molecular Devices). During the image acquisition neurons were in extracellular buffer (10 mM HEPES, 120 mM NaCl, 3 mM KCl, 2 mM CaCl₂, 2 mM MgCl₂, 10 mM glucose (pH 7.35)).

Neurons were transfected with SEP-GluA1 or SEP-GluA3 and co-transfected with SNAP-GluA2 with the aim to prevent the formation of homomers. 2 hours before imaging the neurons were incubated with 0.5 μM TTX (Tocris). During imaging, neurons were incubated in extracellular buffer with 1 μM TTX. After 6 minutes baseline imaging of 1 image per minute, forskolin (50 μM; Sigma-Aldrich) and IBMX (50 μM; Tocris) or DMSO (vehicle) diluted in conditioned medium was added to the incubation chamber. Imaging was continued for another 40 minutes with 1 image per 5 minutes after addition. All images were a z-stack with a range of 3 μm with a step size of 0.5 μm. For analysis, acquisitions were corrected for drift using the stack reg (rigid body) plugin in ImageJ and maximum intensity projections were obtained. For each neuron, 20 ROIs of variable sizes containing one spine each or a piece of the shaft were drawn. For each ROI, mean intensities were measured for every time point and corrected for background using the average intensity of a background ROI. For each ROI, intensities were normalized to 1 based on the averaged intensities of the baseline frames. Normalized intensities were plotted over time. For each condition, measurements from 20 ROIs from 36 neurons divided over 3 independent neuronal cultures were used in the analysis.

To test the pH-sensitivity of SEP, transfected neurons were imaged in extracellular buffer containing 120 mM NaCl, 3 mM KCl, 10 mM HEPES, 2 mM CaCl₂, 2 mM MgCl₂ and 10 mM glucose, pH adjusted to 7.35 with NaOH. After three minutes, the buffer was replaced by an acidic buffer containing 120 mM NaCl, 3 mM KCl, 16.4 mM MES, 2 mM CaCl₂, 2 mM MgCl₂, and 15 mM glucose, pH adjusted to 5.5 with NaOH to quench the SEP signal. To deacidify the intracellular compartments, after another three minutes, the buffer was replaced by extracellular buffer with NH₄Cl containing 70 mM NaCl, 50 mM NH₄Cl, 3 mM KCl, 15 mM HEPES, 2 mM CaCl₂, 2 mM MgCl₂, 15 mM glucose and 2 mM NaHCO₃, pH adjusted to 7.35 with NaOH. To determine the change in intensity in the time-lapses acquired on the spinning disk microscope, Fiji was used to manually draw regions of interest (ROIs) along the dendrites. From the ROI, the mean intensity was measured from which the background was subtracted. The intensity was normalized to the first time point to get the relative intensity.

Single-molecule tracking

Single-molecule tracking was performed on the Nanoimager S from ONI (Oxford Nanoimaging; ONI), equipped with a 100×/NA 1.4 oil immersion objective (Olympus Plan Apo), an XYZ closed-loop piezo stage, and with 471-, 561-, and 640-nm wavelength excitation lasers. Fluorescence emission was detected using an sCMOS camera (ORCA Flash 4, Hamamatsu). NimOS software (version 1.18.3) from ONI was used for localization and drift correction was performed.

Neurons were transfected with SEP tagged GluA1 or GluA3 and Homer1c-mCherry as described before. Imaging was performed in extracellular buffer supplemented with 1% bovine serum albumin (Sigma) for blocking. Atto647N-conjugated anti-GFP nanobody (GFP booster Atto647N, Chromotek) was bath applied to a final dilution of 1:200,000 to 1:100,000. Imaging was performed at 50-Hz (20 ms exposure time) with 640-nm excitation laser oblique illumination. Imaging was continued for 5,000 frames. Localizations were detected using NimOS software.

Single-molecule tracking analysis

Using MATLAB (version 2021b), molecules with a localization precision of <50 nm were selected for analysis. A cell mask was drawn manually to filter out localizations outside neurons due to nonspecifically bound nanobodies. Tracking was achieved using custom algorithms in MATLAB described previously with a tracking radius of <500 nm (Lu et al., 2014). The first three points of the MSD with the addition of the value 0 at MSD(0) were used to fit the slope using a linear fit. Tracks with a negative slope were not used for further analysis. The diffusion coefficient was estimated based on the fit using the formula: $MSD = 4 \times D \times \Delta t$. Only tracks of at least 30 frames were selected for further analysis. Tracks were classified as immobile when the ratio between the radius of gyration and mean step size $\left(\frac{\sqrt{n/2} \times \text{radius of gyration}}{\text{mean step size}}\right)$ was smaller than 2.11 (Golan and Sherman, 2017).

A PSD mask was made based on the maximum intensity projection of Homer1c-mCherry. Peaks in intensity were detected after which an FWHM-like boundary was defined for each PSD. Synaptic tracks were tracks that were localized for at least 75% of the time within the border of the PSD mask. The remaining tracks were considered extrasynaptic. Diffusion coefficients of all tracks were plotted in (cumulative) frequency distributions. In addition, the medians per neuron of diffusion coefficient averages of synaptic and extrasynaptic tracks were plotted in scatter bar plots.

Transient confinement analysis on mobile trajectories was done in MATLAB as described in (Westra and MacGillavry, 2022). Parameters used in the analysis are: $Lc = 5.5$, $Sm = 15$, $\alpha = 0.5$, $Tc = 0.2$ s. The confinement zones are further analyzed for size and duration of confinement. The distance between a confinement zone and the closest PSD was defined as the shortest distance between the center of the confinement zone to the nearest PSD border. The distance between immobile tracks and PSDs was calculated similarly except here it was the distance from the center of the immobile track to the border of the PSD.

Statistical analysis

Statistical significance was tested with a Student's *t*-test when comparing two groups. A *p*-value below 0.05 was considered significant. If multiple groups were compared, statistical significance was tested with a one-way ANOVA followed by Sidak's multiple comparisons. If groups were not normally distributed, the non-parametric Mann-Whitney test was used. Correlation was performed with Spearman's rank correlation and Pearson's *r* correlation. Treatment over time was fitted by a mixed-effects model followed by Sidak's multiple comparisons. Data is represented by mean \pm SEM unless stated otherwise. In all figures, * was used to indicate a *p*-value < 0.05, ** for *p* < 0.01, and *** for *p* < 0.001. Data are shown as average values, error bars represent standard error of the mean (SEM). Statistical analysis and graphs were prepared in GraphPad Prism 9, and figures were generated in Adobe Illustrator CC.

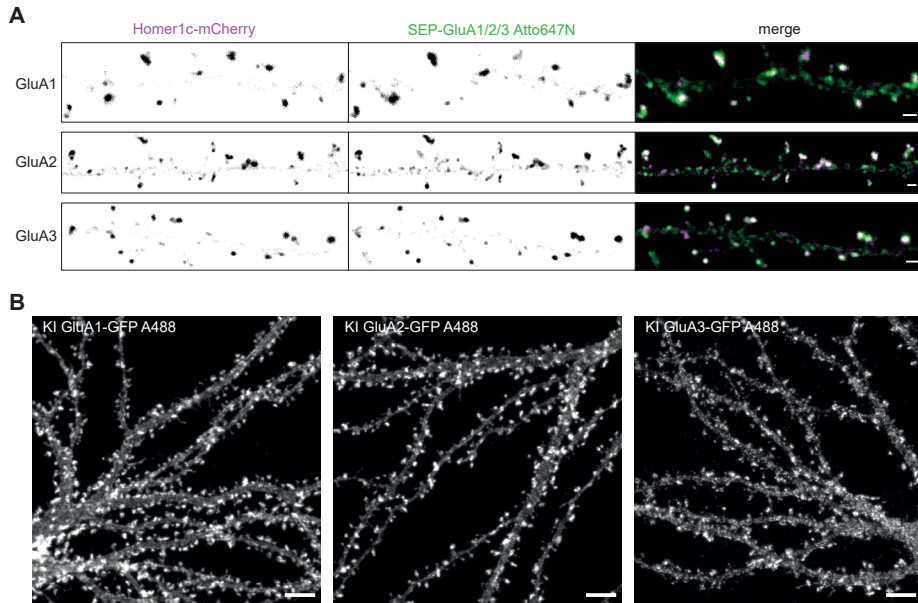
Acknowledgements

We would like to thank Jelmer Willems and Wouter Droogers for their contribution to the SMLM analysis scripts and all members of the MacGillavry lab for helpful discussions. This work was supported by the Netherlands Organization for Scientific Research (ALW-VIDI 171.029 to H.D.M.).

References

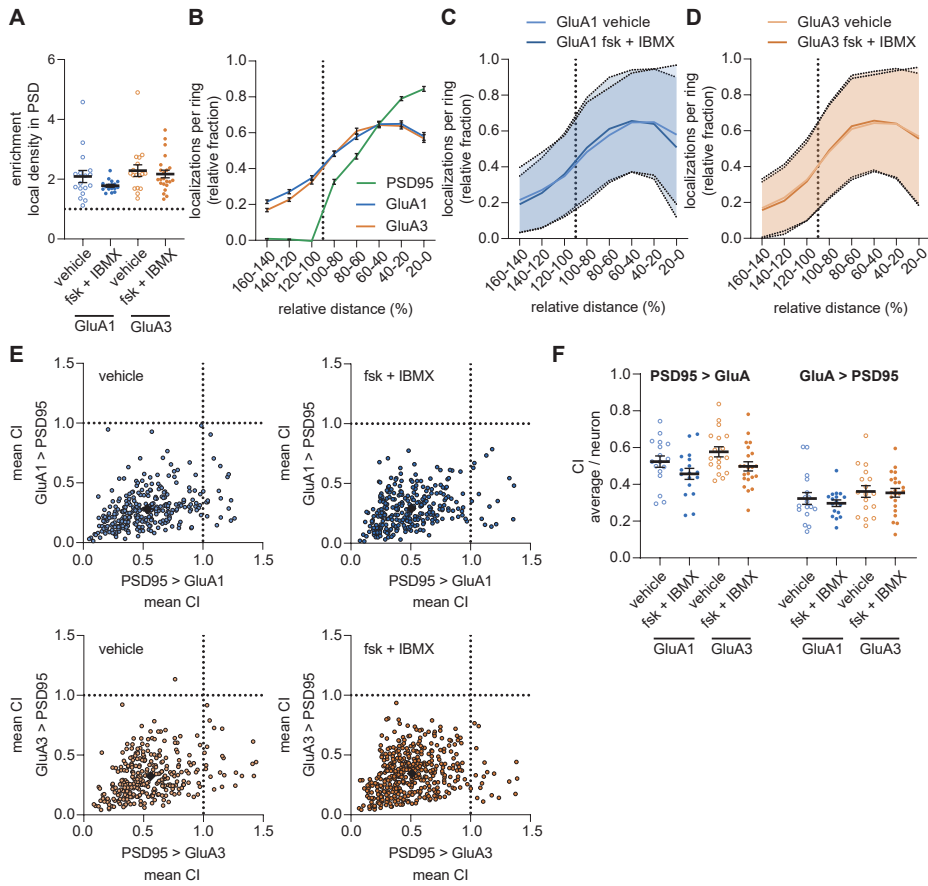
- Anggono, V., and Huganir, R. L. (2012). Regulation of AMPA receptor trafficking and synaptic plasticity. *Curr. Opin. Neurobiol.* 22, 461–469.
- Banke, T. G., Bowie, D., Lee, H.-K., Huganir, R. L., Schousboe, A., and Traynelis, S. F. (2000). Control of GluR1 AMPA Receptor Function by cAMP-Dependent Protein Kinase. *J. Neurosci.* 20, 89–102.
- Bats, C., Groc, L., and Choquet, D. (2007). The Interaction between Stargazin and PSD-95 Regulates AMPA Receptor Surface Trafficking. *Neuron* 53, 719–734.
- Compans, B., Choquet, D., and Hossy, E. (2016). Review on the role of AMPA receptor nano-organization and dynamic in the properties of synaptic transmission. *Neurophotonics* 3, 041811.
- Derkach, V., Barria, A., and Soderling, T. R. (1999). Ca²⁺/calmodulin-kinase II enhances channel conductance of α -amino-3-hydroxy-5-methyl-4-isoxazolepropionate type glutamate receptors. *Proc. Natl. Acad. Sci.* 96, 3269–3274.
- Franks, K. M., Stevens, C. F., and Sejnowski, T. J. (2003). Independent Sources of Quantal Variability at Single Glutamatergic Synapses. *J. Neurosci.* 23, 3186–3195.
- Fukata, Y., Dimitrov, A., Boncompain, G., Vielmeyer, O., Perez, F., and Fukata, M. (2013). Local palmitoylation cycles define activity-regulated postsynaptic subdomains. *J. Cell Biol.* 202, 145–161.
- Golan, Y., and Sherman, E. (2017). Resolving mixed mechanisms of protein subdiffusion at the T cell plasma membrane. *Nat. Commun.* 8, 15851.
- Greger, I. H., Khatri, L., and Ziff, E. B. (2002). RNA Editing at Arg607 Controls AMPA Receptor Exit from the Endoplasmic Reticulum. *Neuron* 34, 759–772.
- Gross, G. G., Junge, J. A., Mora, R. J., Kwon, H.-B., Olson, C. A., Takahashi, T. T., et al. (2013). Recombinant Probes for Visualizing Endogenous Synaptic Proteins in Living Neurons. *Neuron* 78, 971–985.
- Gutierrez-Castellanos, N., Da Silva-Matos, C. M., Zhou, K., Canto, C. B., Renner, M. C., Koene, L. M. C., et al. (2017). Motor Learning Requires Purkinje Cell Synaptic Potentiation through Activation of AMPA-Receptor Subunit GluA3. *Neuron* 93, 409–424.
- Hollmann, M., Hartley, M., and Heinemann, S. (1991). Ca²⁺ + Permeability of KA-AMPA—Gated Glutamate Receptor Channels Depends on Subunit Composition. *Science* 252, 851–853.
- Huganir, R. L., and Nicoll, R. A. (2013). AMPARs and Synaptic Plasticity: The Last 25 Years. *Neuron* 80, 704–717.
- Hume, R., Dingleline, R., and Heinemann, S. (1991). Identification of a site in glutamate receptor subunits that controls calcium permeability. *Science* 253, 1028–1031.
- Isaac, J. T. R., Ashby, M. C., and McBain, C. J. (2007). The Role of the GluR2 Subunit in AMPA Receptor Function and Synaptic Plasticity. *Neuron* 54, 859–871.
- Kapitein, L. C., Yau, K. W., and Hoogenraad, C. C. (2010). “Microtubule Dynamics in Dendritic Spines,” in *Methods in Cell Biology* (Amsterdam, The Netherlands: Elsevier Inc.), 111–132.
- Kessels, H. W., Koepce, C. D., Klein, M. E., and Malinow, R. (2009). Roles of stargazin and phosphorylation in the control of AMPA receptor subcellular distribution. *Nat. Neurosci.* 12, 888–896.
- Kharazia, V., and Weinberg, R. (1997). Tangential synaptic distribution of NMDA and AMPA receptors in rat neocortex. *Neurosci. Lett.* 238, 41–44.
- Liu, G., Choi, S., and Tsien, R. W. (1999). Variability of Neurotransmitter Concentration and Nonsaturation of Postsynaptic AMPA Receptors at Synapses in Hippocampal Cultures and Slices. *Neuron* 22, 395–409.
- Lu, H. E., MacGillavry, H. D., Frost, N. A., and Blanpied, T. A. (2014). Multiple Spatial and Kinetic Subpopulations of CaMKII in Spines and Dendrites as Resolved by Single-Molecule Tracking PALM. *J. Neurosci.* 34, 7600–7610.
- Lu, W., Shi, Y., Jackson, A. C., Bjorgan, K., During, M. J., Sprengel, R., et al. (2009). Subunit Composition of Synaptic AMPA Receptors Revealed by a Single-Cell Genetic Approach. *Neuron* 62, 254–268.
- MacGillavry, H. D., Kerr, J. M., and Blanpied, T. A. (2011). Lateral organization of the postsynaptic density. *Mol. Cell. Neurosci.* 48, 321–331.
- MacGillavry, H. D., Song, Y., Raghavachari, S., and Blanpied, T. A. (2013). Nanoscale Scaffolding Domains within the Postsynaptic Density Concentrate Synaptic AMPA Receptors. *Neuron* 78, 615–622.
- Malinow, R., Mainen, Z. F., and Hayashi, Y. (2000). LTP mechanisms: from silence to four-lane traffic. *Curr. Opin. Neurobiol.* 10, 352–357.
- Mansour, M., Nagarajan, N., Nehring, R. B., Clements, J. D., and Rosenmund, C. (2001). Heteromeric AMPA Receptors Assemble with a Preferred Subunit Stoichiometry and Spatial Arrangement. *Neuron* 32, 841–853.
- Matsuzaki, M., Ellis-Davies, G. C. R., Nemoto, T., Miyashita, Y., Iino, M., and Kasai, H. (2001). Dendritic spine geometry is critical for AMPA receptor expression in hippocampal CA1 pyramidal neurons. *Nat. Neurosci.* 4, 1086–1092.
- Meng, Y., Zhang, Y., and Jia, Z. (2003). Synaptic Transmission and Plasticity in the Absence of AMPA Glutamate Receptor GluR2 and GluR3. *Neuron* 39, 163–176.
- Nair, D., Hossy, E., Petersen, J. D., Constals, A., Giannone, G., Choquet, D., et al. (2013). Super-Resolution Imaging Reveals That AMPA Receptors Inside Synapses Are Dynamically Organized in Nanodomains Regulated by PSD95. *J. Neurosci.* 33, 13204–13224.
- Plant, K., Pelkey, K. A., Bortolotto, Z. A., Morita, D., Terashima, A., McBain, C. J., et al. (2006). Transient incorporation of native GluR2-lacking AMPA receptors during hippocampal long-term potentiation. *Nat. Neurosci.* 9, 602–604.
- Reinders, N. R., Pao, Y., Renner, M. C., da Silva-Matos, C. M., Lodder, T. R., Malinow, R., et al. (2016). Amyloid- β effects on synapses and memory require AMPA receptor subunit GluA3. *Proc. Natl. Acad. Sci.* 113, E6526–E6534.
- Renner, M. C., Albers, E. H., Gutierrez-Castellanos, N., Reinders, N. R., van Huijstee, A. N., Xiong, H., et al. (2017). Synaptic plasticity through activation of GluA3-containing AMPA receptors. *Elife* 6, e25462.
- Scheefhals, N., Catsburg, L. A. E., Westerveld, M. L., Blanpied, T. A., Hoogenraad, C. C., and MacGillavry, H. D. (2019). Shank Proteins Couple the Endocytic Zone to the Postsynaptic Density to Control Trafficking and Signaling of Metabotropic Glutamate Receptor 5. *Cell Rep.* 29, 258–269.e8.
- Sheng, M., and Hoogenraad, C. C. (2007). The Postsynaptic Architecture of Excitatory Synapses: A More Quantitative View. *Annu. Rev. Biochem.* 76, 823–847.
- Shi, S.-H., Hayashi, Y., Esteban, J. A., and Malinow, R. (2001). Subunit-Specific Rules Governing AMPA Receptor Trafficking to Synapses in Hippocampal Pyramidal Neurons. *Cell* 105, 331–343.
- Tang, A.-H., Chen, H., Li, T. P., Metzbowler, S. R., MacGillavry, H. D., and Blanpied, T. A. (2016). A trans-synaptic nanocolumn aligns neurotransmitter release to receptors. *Nature* 536, 210–214.

- Tarusawa, E., Matsui, K., Budisantoso, T., Molnar, E., Watanabe, M., Matsui, M., et al. (2009). Input-Specific Intrasynaptic Arrangements of Ionotropic Glutamate Receptors and Their Impact on Postsynaptic Responses. *J. Neurosci.* 29, 12896–12908.
- Wenthold, R., Petralia, R., Blahos J, I., and Niedzielski, A. (1996). Evidence for multiple AMPA receptor complexes in hippocampal CA1/CA2 neurons. *J. Neurosci.* 16, 1982–1989.
- Westra, M., and MacGillavry, H. D. (2022). Precise Detection and Visualization of Nanoscale Temporal Confinement in Single-Molecule Tracking Analysis. *Membranes (Basel)*. 12, 650.
- Willems, J., de Jong, A. P. H., Scheefhals, N., Mertens, E., Catsburg, L. A. E., Poorthuis, R. B., et al. (2020). Orange: A CRISPR/Cas9-based genome editing toolbox for epitope tagging of endogenous proteins in neurons. *PLoS Biol.* 18, e3000665.
- Willems, J., and MacGillavry, H. D. (2022). A coordinate-based co-localization index to quantify and visualize spatial associations in single-molecule localization microscopy. *Sci. Rep.* 12, 4676.



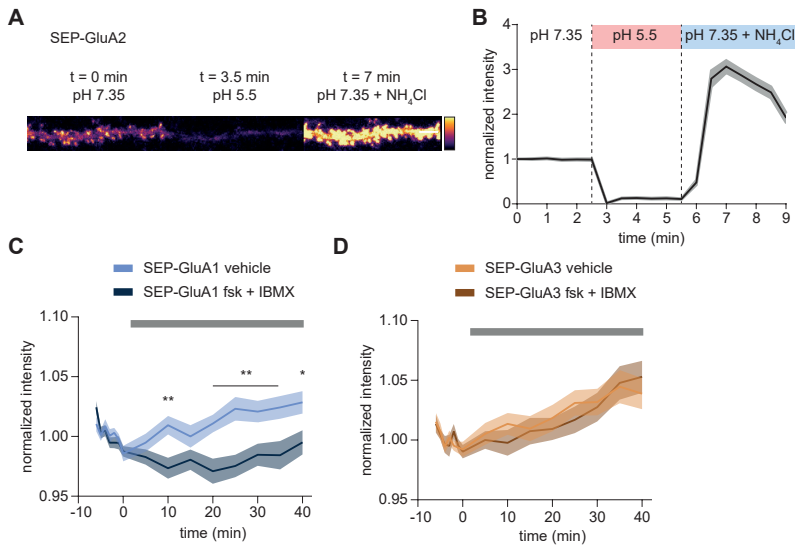
Supplementary Figure 1. Overexpression and endogenous expression of AMPAR subunits

(A) Z_{max} projections of confocal images of dendrites expressing Homer1c-mCherry together with SEP-GluA1/2/3 labeled with GFP booster Atto647N. Scale bars, 1 μm . (B) Z_{max} projections of confocal images of dendrites expressing ORANGE knock-ins of GluA1/2/3-GFP, enhanced with anti-GFP Alexa488 labeling. Scale bars, 5 μm .



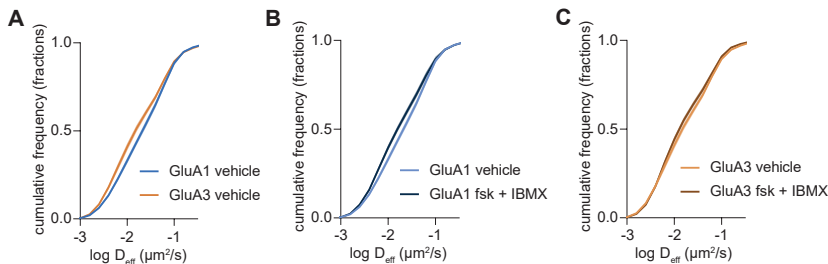
Supplementary Figure 2. SMLM reveals subsynaptic distribution of GluA1 and GluA3

(A) Median enrichment of local density inside the PSD per neuron for GluA1 and GluA3 with and without forskolin and IBMX. (B) Distribution of the fraction of PSD95, GluA1, and GluA3 localizations in 8 rings, proportionally scaled based on the PSD border. For each PSD, the number of localizations was normalized to the maximum number per ring and corrected for the area per ring. (C) The ring distribution analysis for GluA1 with and without forskolin and IBMX with the SD as error instead of SEM to show the amount of variation. (D) The ring distribution analysis for GluA3 with and without forskolin and IBMX with the SD as error instead of SEM to show the amount of variation. (E) Correlation plots of the mean co-localization index for PSD95 with GluA1 and GluA3 with and without forskolin and IBMX, where every point is a different PSD. The average mean co-localization index per plot is indicated with the black diamonds. (F) Mean co-localization index averaged per neuron for PSD95 with GluA1 and GluA3 with and without forskolin and IBMX.



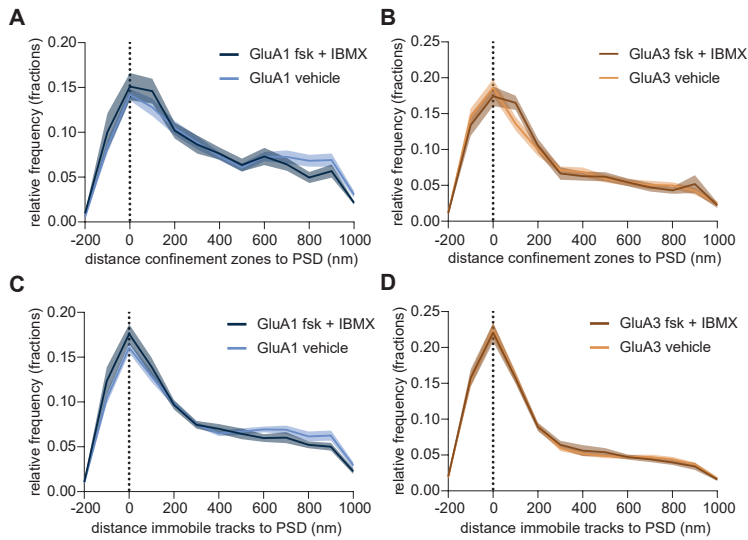
Supplementary Figure 3. No rise of AMPAR levels in the shaft after increase in cAMP levels

(A) pH sensitivity of super-ecliptic pHluorin (SEP). Z_{max} projections from a confocal time-lapse recording of a dendrite expressing SEP-GluA2. Pictures are stills from a dendrite (left) in buffer with pH 7.35, (middle) in buffer with pH 5.5, and (right) in buffer with pH 7.35 and NH₄Cl. Scale bar, 5 μm. (B) Quantification of time-lapses of three SEP-GluA2 transfected dendrites in the different buffers, showing the relative intensity over time. This quantification shows that SEP is not visible in compartments with low pH and thus visualizes the surface levels. (C) Shaft intensity of SEP-GluA1 over time, with and without the addition of forskolin and IBMX at timepoint 0 to increase cAMP levels, indicated by the grey bar. (D) Shaft intensity of SEP-GluA3 over time, with and without the addition of forskolin and IBMX at timepoint 0 to increase cAMP levels, indicated by the grey bar. * $p < 0.05$, ** $p < 0.01$.



Supplementary Figure 4. Diffusion coefficient of GluA1 and GluA3 after increase in cAMP levels

(A) Cumulative frequency distributions of the diffusion coefficient of SEP-GluA1 and SEP-GluA3. (B) Cumulative frequency distributions of the diffusion coefficient of SEP-GluA1 with and without forskolin and IBMX. (C) Cumulative frequency distributions of the diffusion coefficient of SEP-GluA3 with and without forskolin and IBMX.



Supplementary Figure 5. Confinement distance to the PSD after increase in cAMP levels

(A) Relative frequency distribution of the distance of the center of transient confined areas of GluA1 to the border of the PSD with and without forskolin and IBMX. (B) Relative frequency distribution of the distance of the center of transient confined areas of GluA3 to the border of the PSD with and without forskolin and IBMX. (C) Relative frequency distribution of the distance of the center of immobile trajectories of GluA1 to the border of the PSD with and without forskolin and IBMX. (D) Relative frequency distribution of the distance of the center of immobile trajectories of GluA3 to the border of the PSD with and without forskolin and IBMX.

Resolving the dynamic subsynaptic distribution of GluA1- and GluA3-containing AMPA receptors



mGluR5 is transiently confined in perisynaptic nanodomains to shape synaptic function

Nicky Scheefhals, Manon Westra and Harold D. MacGillavry

Nature Communications (2023), 14:244

Cell Biology, Neurobiology and Biophysics, Department of Biology,
Faculty of Science, Utrecht University, Utrecht, The Netherlands

Abstract

The unique perisynaptic distribution of postsynaptic metabotropic glutamate receptors (mGluRs) at excitatory synapses is predicted to directly shape synaptic function, but mechanistic insight into how this distribution is regulated and impacts synaptic signaling is lacking. We used live-cell and super-resolution imaging approaches, and developed molecular tools to resolve and acutely manipulate the dynamic nanoscale distribution of mGluR5. Here we show that mGluR5 is dynamically organized in perisynaptic nanodomains that localize close to, but not in the synapse. The C-terminal domain of mGluR5 critically controlled perisynaptic confinement and prevented synaptic entry. We developed an inducible interaction system to overcome synaptic exclusion of mGluR5 and investigate the impact on synaptic function. We found that mGluR5 recruitment to the synapse acutely increased synaptic calcium responses. Altogether, we propose that transient confinement of mGluR5 in perisynaptic nanodomains allows flexible modulation of synaptic function.

Introduction

Precise modulation of glutamatergic synaptic transmission is critical for the execution of cognitive processes. Glutamatergic transmission is mediated by two types of postsynaptic glutamate receptors: the ionotropic glutamate receptors (iGluRs), including the AMPA and NMDA-type receptors, and the group I metabotropic glutamate receptors (mGluRs), mGluR1 and mGluR5. While iGluRs carry the majority of fast signal transmission across synapses, mGluRs modulate the efficacy of synaptic signaling on longer time scales by coupling to a variety of effector systems that collectively modulate synaptic transmission and plasticity^{1,2}. Postsynaptic group I mGluRs canonically signal through IP₃-mediated calcium release from internal stores, but also through modulation of NMDA receptors³. The contribution of mGluRs to glutamatergic signaling has been found to be critical for cognitive functions such as attention and learning and memory, and disrupted mGluR signaling has been implicated in diverse neurological disorders⁴. Yet, the precise organization of mGluRs within the perisynaptic zone and the underlying mechanisms, critical to efficiently modulate synaptic transmission, are still poorly understood.

Key to the modulation of receptor activation is their subsynaptic organization and alignment with presynaptic vesicle release sites. iGluRs organize in nanodomains within the postsynaptic density (PSD), aligned with vesicle release sites within the presynaptic active zone, increasing the strength of a synaptic response^{5–10}. In contrast, group I mGluRs are enriched in the perisynaptic zone, an annular ring of ~200 nm surrounding the PSD, considerably further away from vesicle release events^{11–13}. A single vesicle release event induces a very local and transient glutamate gradient only activating the opposing iGluRs due to the low affinity of AMPARs and mGluRs for glutamate (0.5–2 mM) and the slow glutamate binding rate of NMDARs^{14–16}. Kinetic profiling of mGluR activation predicts that high frequency or repetitive stimulation is required for glutamate to reach sufficient concentrations in the synaptic cleft to also activate the perisynaptic mGluRs^{17–19}. Hence, the spatial segregation of these functionally distinct receptor types allows for the precise temporal control of synaptic transmission and plasticity. The synaptic density and organization of receptors are not static, but highly dynamic, governed by processes that affect receptor mobility, such as lateral diffusion, endocytosis and

exocytosis, and immobilization to synaptic structures^{20,21}. Disrupted mGluR mobility has been implicated in neurological and neurodegenerative disorders^{22–24}. Thus, an understanding of the dynamic organization of mGluRs is critical to provide new insights into the mechanisms underlying synaptic transmission in both physiological and pathophysiological conditions.

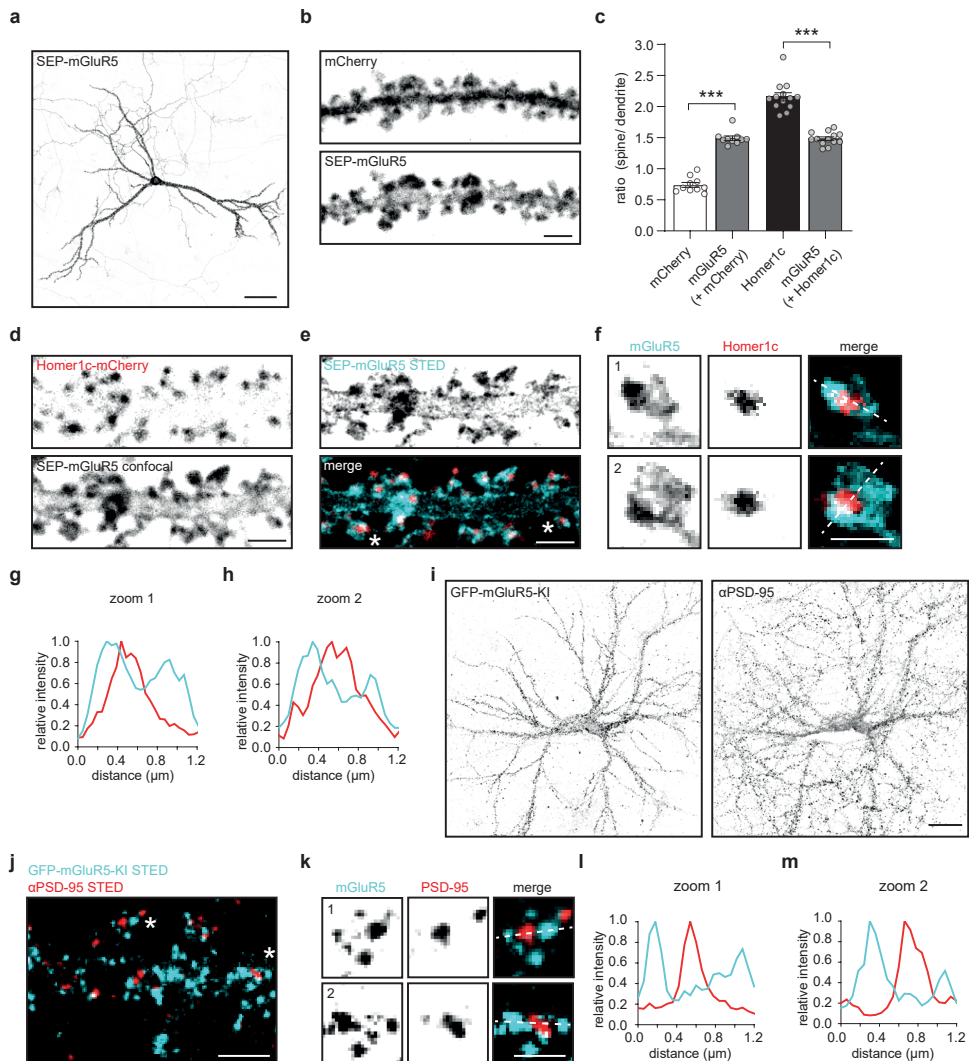
Here, we use complementary super-resolution imaging approaches and show that mGluR5 is largely excluded from the core of the PSD and is preferentially confined in perisynaptic nanodomains. We demonstrate that the C-terminal domain of mGluR5 mediates perisynaptic confinement, but also prevents synaptic entry of mGluR5, even when forced to interact with synaptic scaffolds. We furthermore show that acute disruption of the perisynaptic organization of mGluR5 deregulates calcium signaling in spines.

Results

mGluR5 is enriched in spines but largely excluded from the synapse

To study the distribution of surface-expressed mGluR5 in neurons, we transfected hippocampal neurons with mGluR5 coupled to an extracellular super-ecliptic pHluorin (SEP) tag, additionally labeled with a cell-impermeable GFP nanobody conjugated to Atto647N. The expression of mGluR5 was observed throughout neurons, but was most prominent in the dendritic shaft and spines (Fig. 1a). mGluR5 was significantly enriched in spines compared to a mCherry fill (mGluR5: 1.49 ± 0.035 and mCherry: 0.74 ± 0.04 , Fig. 1b, c), but significantly less enriched compared to the PSD scaffolding protein Homer1c (mGluR5: 1.49 ± 0.029 and Homer1c: 2.16 ± 0.066 ; Fig. 1c, d). Homer1c overexpression to mark the PSD did not affect mGluR5 enrichment in spines (Fig. 1c, light gray bars). Next, we used gated stimulated emission depletion (gSTED) microscopy to assess mGluR5 localization relative to the PSD. Foremost, we found that mGluR5 is largely excluded from the PSD, confirming early EM studies^{11–13} (Fig. 1e, f). Also, two-color gSTED imaging of mGluR5 and the PSD, labeled with a PSD-95 antibody, revealed minimal co-localization between mGluR5 and the PSD (Fig. S1a–d).

We always selected neurons with moderate overexpression levels of mGluR5 (Fig. S1e), and found that the median mGluR5 overexpression was ~ 2 times higher compared to endogenous mGluR5 levels (Fig. S1e–g). Endogenous mGluR5 labeled with an mGluR5 antibody was similarly excluded from PSD-95 immunolabelled synapses compared to overexpressed mGluR5 (Fig. S1h–k), and rather localized close to phalloidin staining F-actin, known to be enriched in the perisynaptic zone²⁵ (Fig. S1l–n). Furthermore, we endogenously tagged mGluR5 with an extracellular GFP-tag using the ORANGE CRISPR/Cas9-based knock-in toolbox⁹ (Fig. 1i). gSTED imaging of the surface-labeled mGluR5 knock-in also revealed mGluR5 distribution throughout the dendrite, with preferential perisynaptic localization in spines (Fig. 1j–m). Notably, the localization observed for mGluR5 is markedly different from other glutamate receptors, including AMPA receptors. The AMPA receptor subunit GluA2 co-localized with the PSD marked by Homer1c (Fig. S1o–r) and localized in subsynaptic domains spatially segregated from mGluR5 shown with two-color gSTED microscopy (Fig. S1s–v).



mGluR5 is organized in perisynaptic nanodomains

To resolve the nanoscale perisynaptic distribution of mGluR5 we used two-color single-molecule localization microscopy (SMLM) on neurons transfected with SEP-mGluR5, labeled with an anti-GFP nanobody coupled to Alexa647, and mEos3.2-tagged PSD_{FingR} to label the PSD²⁶ (Figs. 2a, b and S2a). PSDs were identified using density-based spatial clustering of applications with noise (DBScan)²⁷ on the PSD_{FingR}-mEos3.2 localizations (Fig. 2c). Consistent with our previous observations, we found that most mGluR5 localizations are within 200 nm from the PSD border (Fig. 2d). To investigate this more closely, we mapped the localizations of mGluR5 and PSD_{FingR} in eight incremental rings proportionally scaled to the PSD border to normalize for PSD size (Figs. 2e and S2b)²⁸. As expected, almost all PSD_{FingR} molecules were

Figure 1. mGluR5 is enriched in spines but largely excluded from synapses in hippocampal neurons

a Hippocampal neuron expressing SEP-mGluR5. Scale bar, 50 μm . **b** Representative confocal image of dendrite expressing mCherry and SEP-mGluR5, surface-labeled with an anti-GFP nanobody Atto647N. Scale bar, 2 μm . **c** Quantification of the ratio of spine over dendrite intensity of mCherry, surface SEP-mGluR5 co-expressing mCherry ($n = 10$, $p < 0.0001$; two-sided paired t test), Homer1c-mCherry and surface SEP-mGluR5 co-expressing Homer1c-mCherry ($n = 13$, $p < 0.0001$; two-sided paired t test). **d** Representative confocal image of dendrite expressing Homer1c-mCherry and SEP-mGluR5, surface-labeled with an anti-GFP nanobody Atto647N. Scale bar, 2 μm . **e** gSTED imaging of SEP-mGluR5 surface-labeled with an anti-GFP nanobody Atto647N (cyan) and the merged image showing the relative localization to confocal-resolved Homer1c-mCherry (red), shown in **d**. Scale bar, 2 μm . This experiment was replicated in cultures from more than three independent preparations of hippocampal neurons. **f** Zooms of dendritic spines indicated in **e** with asterisks. Scale bar, 1 μm . **g** Line profiles of spine 1 and **h** spine 2, indicated with dotted line in **f**. **i** Hippocampal neuron with an ORANGE GFP knock-in (KI) endogenously tagging mGluR5 at the N-terminus, enhanced with anti-GFP Alexa488 labeling (left), co-stained for anti-PSD-95 Alexa594 (right). Scale bar, 20 μm . **j** Representative two-color gSTED image of dendrite with GFP-mGluR5 KI stained with anti-GFP Alexa488 to label surface-expressed receptors (cyan) and anti-PSD-95 Alexa594 (red). Scale bar, 2 μm . This experiment was replicated in cultures from three independent preparations of hippocampal neurons. **k** Zooms of dendritic spines indicated in **j** with asterisks. Scale bar, 1 μm . **l** Line profiles of spine 1 and **m** spine 2, indicated with dotted line in **k**. Data are represented as means \pm SEM. *** $p < 0.001$. Source data are provided as a Source Data file.

found within the two inner synaptic rings and were almost absent from the surrounding rings. In contrast, we found that mGluR5 localizations were enriched in the three perisynaptic rings, compared to the synaptic and extrasynaptic rings (Fig. 2f, also see Fig. S2c for absolute number of localizations).

In these two-color SMLM experiments we observed that mGluR5 was not homogeneously distributed in the perisynaptic region. Indeed, using DBScan we found that mGluR5 is concentrated in subsynaptic nanodomains. These nanodomains were most frequently found within the perisynaptic region, with a median border-to-centroid distance from PSD to mGluR5 nanodomains of 240 nm (Fig. 2g, h). The median area of individual mGluR5 nanodomains was $6.0 \times 10^3 \text{ nm}^2$ (95% CI [5.2 7.2] $\times 10^3$; Fig. 2i) and 115 nm in length and 83 nm in width (length: 95% CI [111 120] and width: (95% CI [81 88], full width tenth maximum (FWTM); Fig. 2j). The total mGluR5 nanodomain area per PSD slightly correlated with PSD area (Fig. S2d). Using SR-Tesseler, another quantitative approach based on Voronoi diagrams to segment and quantify protein organization (Fig. S2e, f)²⁹, we confirmed the perisynaptic mGluR5 nanodomains observed using DBScan (Fig. S2g). The SR-Tesseler approach detected more and significantly smaller clusters compared to DBScan (median clusters area: DBScan: $6.3 \times 10^3 \text{ nm}^2$ and SR-Tesseler: $2.1 \times 10^3 \text{ nm}^2$; Fig. S2h), however, this is inherent to the method used to outline the clusters and the different input parameters (see M&M for details). Even though we used stringent criteria to ensure that nanodomains consisted of a considerable amount of receptors, we set out to exclude the possibility that the nanodomains represent dimeric receptors. We used SR-Tesseler without set cluster criteria to detect nano-objects to discriminate between dimeric and clustered receptors in the dendritic shaft and spines. In both the dendritic shaft and spines we found many objects otherwise excluded from the analysis, with the smallest objects likely representing mGluR dimers. In addition, the objects detected in spines were distinct from those on the dendrite as the spine objects were significantly larger in area (median object area: spines: $0.39 \times 10^3 \text{ nm}^2$ and dendrites: $0.18 \times 10^3 \text{ nm}^2$; Fig. S2i, j). Thus, our two-color SMLM experiments revealed a high degree of organization of mGluR5, demonstrating that mGluR5 is enriched in distinct nanodomains that preferentially localize in the perisynaptic zone.

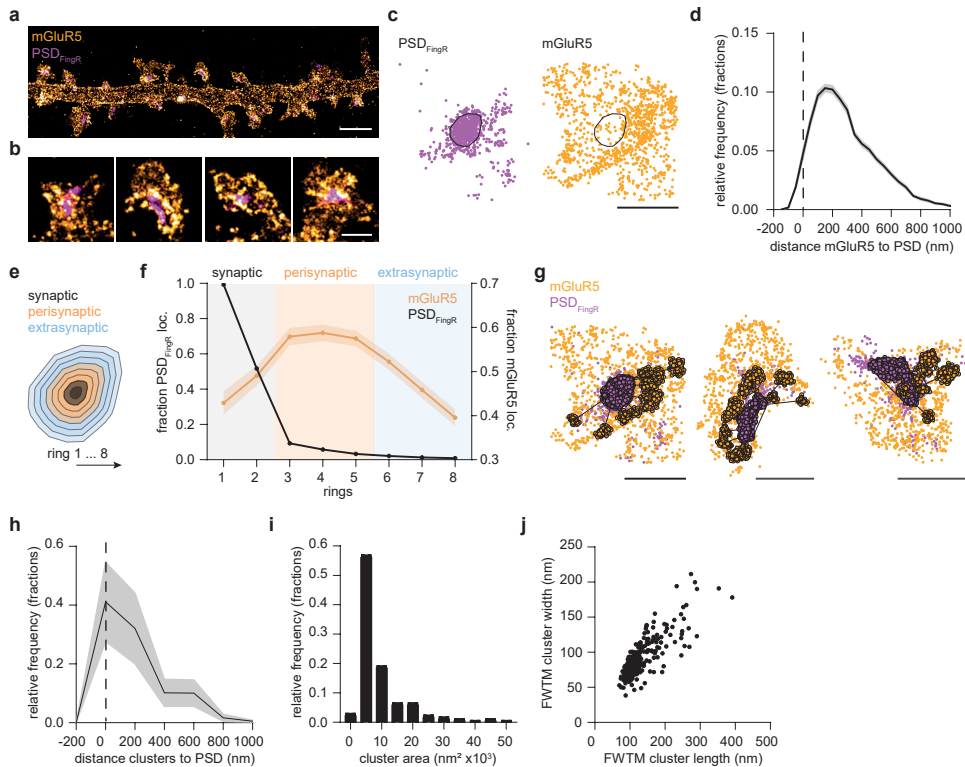


Figure 2. mGluR5 is organized in perisynaptic nanodomains

a Reconstruction of single-molecule localizations obtained for SEP-mGluR5 anti-GFP nanobody Alexa647 using dSTORM (orange hot) and PSD_{FingR}-mEos3.2 using PALM (cyan hot). Same dendritic region is shown in Fig. S2a. Scale bar, 2 μm . **b** Zooms of spines shown in **a**. Scale bar, 500 nm. **c** Representative spine with single-molecule localizations of PSD_{FingR} (cyan) and mGluR5 (orange) with indicated PSD border (black line) determined using DBScan. Scale bar, 500 nm. **d** Relative frequency distribution (fractions) of the distance of individual mGluR5 localizations to the PSD border ($n = 13$ neurons, 253 PSDs). **e** For each PSD, eight rings, proportionally scaled based on its PSD border, defined the synapse (ring 1 and 2; black), perisynaptic zone (ring 3–5; orange), and extrasynaptic region (ring 6–8; blue). **f** Fraction of PSD_{FingR} (black; plotted on left y-axis) and mGluR5 (orange; plotted on right y-axis) localizations in rings 1–8. For each PSD, the number of localizations was normalized to the maximum number per ring, and the area per ring was calculated and corrected for. **g** Example spines with mGluR5 localizations (orange) belonging to clusters (black outline) as determined using DBScan, relative to PSD_{FingR} localizations (magenta). Scale bars, 500 nm. **h** Relative frequency distribution (fractions) of the distance from the center of mGluR5 clusters to the border of the PSD (as indicated in **g** by the black lines) ($n = 273$ clusters). **i** Relative frequency distribution (fractions) of the mGluR5 cluster area. **j** FWTM analysis comparing the width and length (in nm) of individual mGluR5 clusters. Data are represented as means \pm SEM. Source data are provided as a Source Data file.

The spatial distribution of mGluR5 diffusion at and around the synapse is highly heterogeneous

We observed a remarkable heterogeneous perisynaptic distribution of mGluR5, however, we have little insight into whether mGluR5 is stably anchored at perisynaptic sites or only transiently visits these perisynaptic nanodomains. Nevertheless, such information is critical

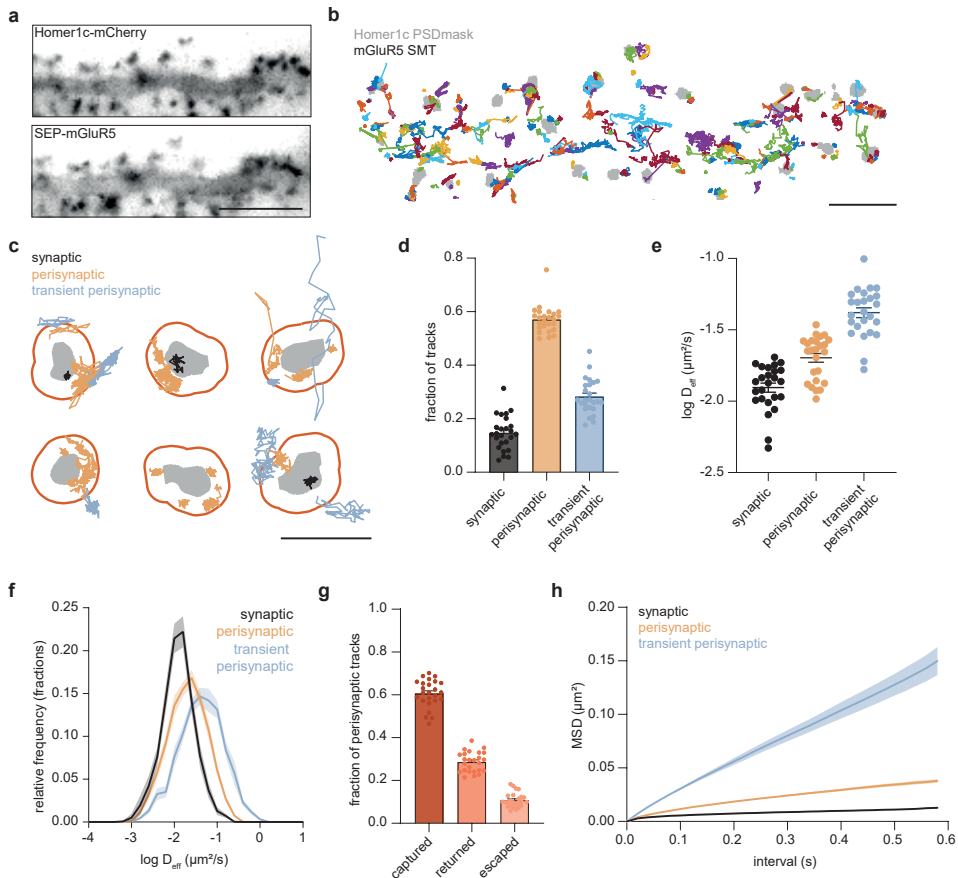


Figure 3. Distribution of mGluR5 diffusion in spines is heterogeneous

a Widefield of dendrite expressing Homer1c-mCherry and SEP-mGluR5. Scale bar, 5 μm . **b** Single-molecule trajectories (SMTs) of mGluR5 (each trajectory is assigned a random color) relative to the Homer1c PSD mask (gray) in the same dendrite as shown in a. Scale bar, 2 μm . **c** Example PSDs (gray) with their perisynaptic zone (orange ring) and mGluR5 SMTs color-coded for their subsynaptic localization. Scale bar, 1 μm . **d** Fraction of synaptic, perisynaptic, and transient perisynaptic mGluR5 SMTs ($n = 25$ neurons). **e** Mean $\log D_{\text{eff}}$ per neuron of synaptic, perisynaptic, and transient perisynaptic mGluR5 SMTs ($n = 25$ neurons). **f** Relative frequency distributions of D_{eff} s of individual synaptic, perisynaptic, and transient perisynaptic mGluR5 SMTs. **g** Fraction of perisynaptic SMTs that stay within perisynaptic/synaptic region once entered (captured), exited at least once, but end up staying inside the perisynaptic/synaptic region (returned) and perisynaptic tracks that escaped the perisynaptic/synaptic region (escaped) ($n = 25$ neurons). **h** Mean MSD curve over time of synaptic, perisynaptic, and transient perisynaptic mGluR5 SMTs. Data are represented as means \pm SEM. Source data are provided as a Source Data file.

to better understand how mGluR5 contributes to synaptic signaling. To address this, we used a single-molecule tracking (SMT) approach called universal point accumulation in nanoscale topography (uPAINT)³⁰ to study the subsynaptic mobility of mGluR5. Neurons were co-transfected with SEP-mGluR5 and Homer1c-mCherry to mark the PSD (Fig. 3a). SMT was performed using an anti-GFP nanobody coupled to Atto647N that stochastically labeled individual SEP-tagged receptors, providing a map of mGluR5 mobility (Fig. 3b). The

diffusion coefficients of mGluR5 trajectories in spines were significantly lower than in dendrites (median D_{eff} spines: $0.022 \mu\text{m}^2/\text{s}$, dendrites: $0.036 \mu\text{m}^2/\text{s}$; Fig. S3c, d). To further differentiate between mGluR5 diffusion at different synaptic subregions, we used the Homer1c-mCherry channel to mark the synaptic region (PSD mask), as well as an annulus surrounding the PSD by expanding the PSD mask with 200 nm to mark the perisynaptic zone. Importantly, we found that mGluR5 diffusion was similar in neurons expressing mCherry and Homer1c, indicating that Homer1c overexpression does not alter mGluR5 diffusion (Fig. S3a–f). Trajectories were categorized as synaptic, perisynaptic, or transient perisynaptic, all associating with the synapse and/or perisynaptic zone but to different extents (see M&M for details) (Fig. S3g). The transient perisynaptic trajectories are largely extrasynaptic and only shortly overlap with the perisynaptic zone to capture the extrasynaptic spine population. Since we were interested in mGluR5 dynamics within spines, trajectories without overlap with the synapse and/or perisynaptic zone were not included for further analysis. We found a large fraction of perisynaptic mGluR5 trajectories and a significantly smaller fraction of mGluR5 trajectories within the synapse (synaptic: 0.15 ± 0.01 , perisynaptic: 0.57 ± 0.01 , transient perisynaptic: 0.28 ± 0.01 ; Figs. 3c, s and S3h), consistent with the mGluR5 distribution found using SMLM and gSTED microscopy. We hypothesized that mechanisms underlying the perisynaptic mGluR5 nanodomains likely influence receptor diffusion. Indeed, the large pool of perisynaptic mGluR5 diffused much slower compared to the mGluR5 trajectories that only transiently associated with the perisynaptic zone (median D_{eff} : synaptic: $0.014 \mu\text{m}^2/\text{s}$, perisynaptic: $0.023 \mu\text{m}^2/\text{s}$, transient perisynaptic: $0.042 \mu\text{m}^2/\text{s}$; Fig. 3e, f), suggesting that mGluR5 surface mobility is specifically regulated at perisynaptic sites. The small fraction of mGluR5 within the synapse diffused at even lower rates, suggesting that although a small fraction of mGluR5 enters the PSD, these receptors are severely hindered in their diffusion. Notably, most receptors that entered the perisynaptic zone remained there for the full duration of the observation time (here termed ‘captured’: 0.61 ± 0.01), or left the perisynaptic zone but returned to the perisynaptic zone (‘returned’: 0.29 ± 0.009). Only a very small fraction of perisynaptic tracks escaped the perisynaptic zone (‘escaped’: 0.11 ± 0.007 ; Fig. 3g). Thus, corroborating our SMLM data, these observations suggest that there is an underlying mechanism that hinders free diffusion of mGluR5 specifically in the perisynaptic zone, effectively containing mGluR5 within the perisynaptic zone. Indeed, the MSD plots indicate that perisynaptic mGluR5 receptors undergo anomalous diffusion, in contrast to the transient perisynaptic mGluR5 trajectories that seem to undergo Brownian diffusion (Fig. 3h).

mGluR5 is transiently confined in perisynaptic nanodomains

To further delineate how mGluR5 diffusion is locally controlled at perisynaptic sites, we next investigated the spatial distribution of mGluR5 immobilization and confinement. First, we classified mGluR5 trajectories as either mobile or immobile based on the ratio between the radius of gyration and the mean displacement per time step of individual trajectories³¹. We then mapped the immobile and mobile trajectories relative to the Homer1c PSD mask (Figs. 4a, b and S4a, b). We found that the majority of mGluR5 trajectories was immobile (fraction of tracks: immobile: 0.65 and mobile: 0.35; Fig. S4c), with an expected diffusion coefficient slower than the mobile trajectories (median D_{eff} immobile trajectories: $0.016 \mu\text{m}^2/\text{s}$ and mobile trajectories: $0.050 \mu\text{m}^2/\text{s}$; Fig. S4d, e). Next, we sought to investigate whether the mobile mGluR5 trajectories undergo transient periods of confinement. We therefore

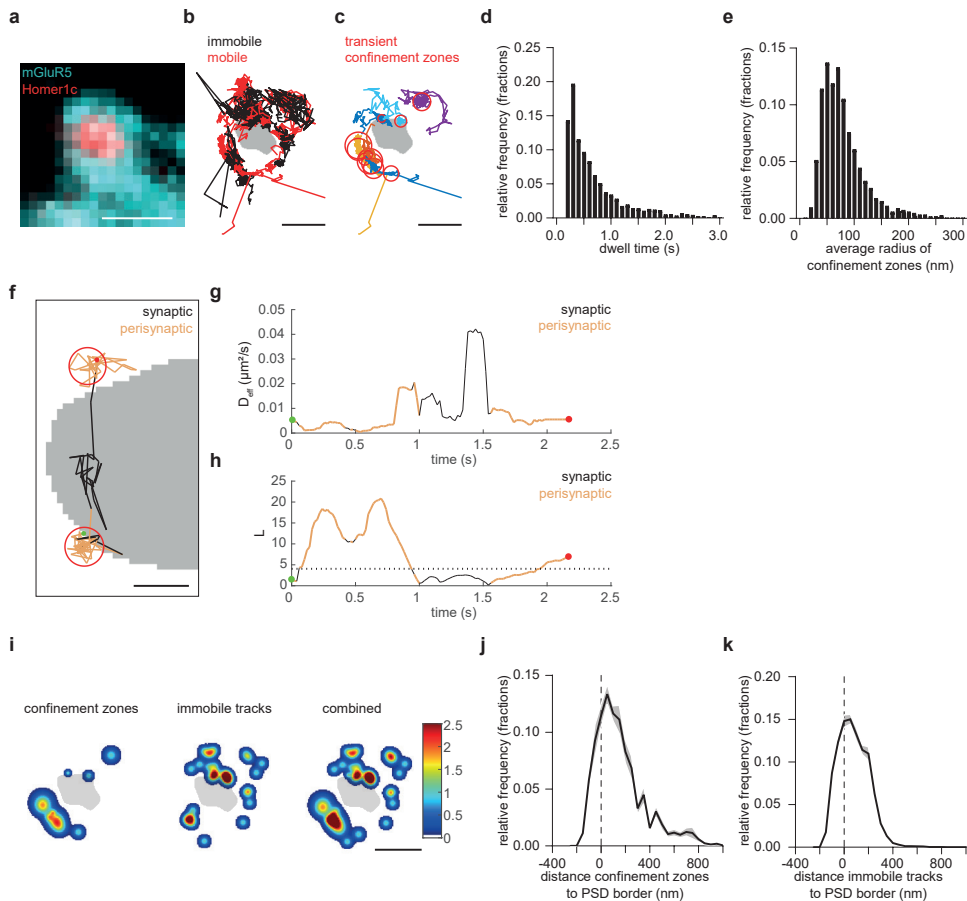


Figure 4. mGluR5 is transiently confined, but also immobilized at the perisynaptic zone

a Widefield image of a dendritic spine expressing SEP-mGluR5 (cyan) and Homer1c-mCherry (red). (larger ROI shown in Fig. S4a). Scale bar, 1 μm . **b** The same spine as in **a** showing immobile (black) and mobile (red) SMTs of mGluR5 relative to the Homer1c PSD mask (larger ROI shown in Fig. S4b). Scale bar, 500 nm. **c** Transient confinement zones (red circles) of the mobile trajectories (random colors) shown in **B** (larger ROI shown in Fig. S4f). Scale bar, 500 nm. **d** Relative frequency plots of the dwell time (s) and **e** average radius of confinement zones for mGluR5 SMTs. **f** Example trajectory (assigned to perisynaptic fraction) that undergoes transient confinement in the perisynaptic zone, color-coded for entering the synapse (black) and perisynaptic zone (orange) and the confinement zones (red). The trajectory starts (green dot) and ends (red dot) in perisynaptic transient confinement zones. Scale bar, 100 nm. **g** The diffusion coefficient and **h** confinement index L over time for the trajectory shown in **f**, using the same color-coding. **i** The same example synapse as in **a–c** with hotspots of transient confinement zones, immobile tracks, and both images combined, color-coded for the frequency of confinement zones and/or immobile tracks (larger ROI shown in Fig. S4i). Scale bar, 500 nm. **j** Relative frequency distribution of the distance of confinement zones of mGluR5 and **k** center of immobile mGluR5 trajectories to the border of the PSD ($= 0$ and indicated by dashed line). Data in this figure is the same dataset as used in Fig. 3, as these figures show different aspects of the same experiment. Data are represented as means \pm SEM. Source data are provided as a Source Data file.

estimated the confinement index L , which relates to the probability that a molecule undergoes confined diffusion in a region of radius R for a period of time t ^{32–34}. This analysis revealed

that a substantial fraction of the mobile mGluR5 trajectories (~40%) undergoes transient confinement with single trajectories displaying alternating periods of free and confined diffusion. Using a critical threshold of confinement L_c we defined regions of confined diffusion, or confinement zones (Figs. 4c and S4f). mGluR5 mobility was strongly reduced inside these confinement zones (median D_{eff} inside: $0.01 \mu\text{m}^2/\text{s}$ and outside: $0.068 \mu\text{m}^2/\text{s}$; Fig. S4g, h). The average radius of confinement zones was $79.8 \pm 0.97 \text{ nm}$, and receptors remained confined for $0.85 \pm 0.03 \text{ s}$ (Fig. 4d, e). Interestingly, we frequently observed that trajectories undergo confinement specifically in the perisynaptic zone (Fig. 4f–h). Indeed, when we mapped the peaks of confinement zones and centers of the immobile trajectories, we detected clear hotspots of reduced mGluR5 mobility around synapses (Figs. 4i and S4i). To quantify this, we determined the distance of the confinement zones to the PSD border. Strikingly we found that the vast majority of confinement zones were located within the perisynaptic zone, <100 nm from the PSD (Fig. 4j). Similarly, immobile tracks were also enriched in the perisynaptic zone (Fig. 4k). Together, these experiment reveal that the diffusion of mGluR5 around PSDs is highly heterogeneous and that mGluR5 is transiently confined primarily at perisynaptic zones, close to the border of the PSD.

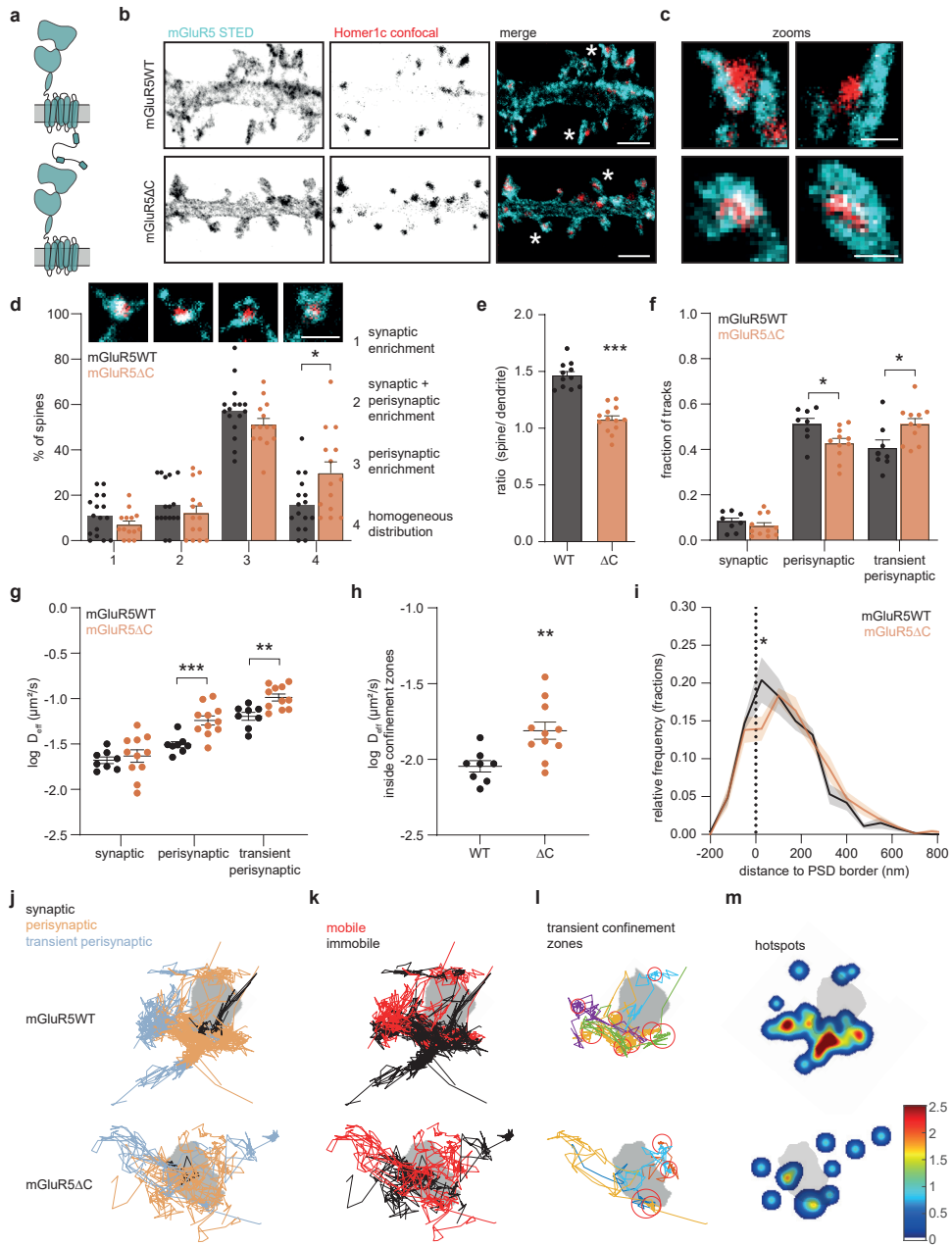
The C-terminal domain of mGluR5 mediates perisynaptic confinement

The particular heterogeneous organization of mGluR5 dynamics suggests that specific mechanisms retain the receptor in the perisynaptic zone. The large intracellular C-terminal domain (CTD) of mGluR5a contains many protein interaction motifs and phosphorylation sites involved in surface expression and trafficking³⁵. However, whether the CTD of mGluR5 contributes to the spatial heterogeneity of surface mobility remains unknown. To test this, we generated a mutant lacking the last 314 C-terminal amino acids (SEP-mGluR5 Δ C) (Fig. 5a).

Figure 5. The C-terminal domain of mGluR5 mediates perisynaptic confinement

a Schematic of monomeric full-length mGluR5WT (top) and mGluR5 Δ C (bottom) lacking its C-terminal tail. **b** Representative gSTED images of dendrite expressing SEP-mGluR5WT and SEP-mGluR5 Δ C, additionally labeled with an anti-GFP nanobody Atto647N (cyan), and Homer1c-mCherry (red; confocal). Scale bar, 2 μm . **c** Zooms of spines indicated in **b** with asterisks. Scale bar, 500 nm. **d** Quantification of mGluR5WT (black; $n = 16$) and mGluR5 Δ C (orange; $n = 14$) localization in spines: (1) synaptic enrichment ($p = 0.1565$), (2) synaptic + perisynaptic enrichment ($p = 0.1488$), (3) perisynaptic enrichment ($p = 0.3696$) and (4) homogeneous distribution ($p = 0.0204$; two-sided unpaired t test for each category). On top are representative images of the different categories of mGluR5 localization (cyan), relative to Homer1c (red), at spines. Scale bar, 1 μm . **e** Quantification of the ratio of spine over dendrite intensity of mGluR5WT ($n = 11$) and mGluR5 Δ C ($n = 13$, $p < 0.0001$; unpaired t test). **f** Fraction of synaptic ($p = 0.3529$), perisynaptic ($p = 0.0218$), and transient perisynaptic trajectories ($p = 0.0254$) of mGluR5WT ($n = 8$) and mGluR5 Δ C ($n = 11$; two-sided unpaired t test for each category). **g** Mean log D_{eff} per neuron of synaptic ($p = 0.5923$), perisynaptic ($p = 0.0008$), and transient perisynaptic ($p = 0.0025$) trajectories of mGluR5WT ($n = 8$) and mGluR5 Δ C ($n = 11$; two-sided unpaired t test for each category). **h** Mean log D_{eff} per neuron of trajectories inside confinement zones of mGluR5WT ($n = 8$) and mGluR5 Δ C ($n = 11$, $p = 0.0053$; two-sided unpaired t test). **i** Relative frequency distribution of the distance of confinement zones of mGluR5WT ($n = 8$) and mGluR5 Δ C ($n = 11$) to the border of the PSD (= 0 and indicated by dashed line) (two-way repeated measures ANOVA with Bonferroni's multiple comparisons test, at 25 nm distance from PSD border: $p = 0.0003$). **j** Example synapses of mGluR5WT and mGluR5 Δ C with trajectories color-coded for being synaptic (black), perisynaptic (orange), and transient perisynaptic (blue), **k** for being mobile (red) and immobile (black), **l** for being transiently confined trajectories (random colors) with corresponding confinement zones (red circles), and **m** hotspots of immobile tracks (shown in **k**) and confinement zones (shown in **l**), color-coded for their frequency. Scale bars, 500 nm. Data are represented as means \pm SEM. * $p < 0.05$, ** $p < 0.01$ and *** $p < 0.001$. Source data are provided as a Source Data file.

Truncation of the mGluR5 CTD did not impact surface expression (Fig. S5a), as has been previously shown³⁶. We first used gSTED microscopy to assess the localization of surface-expressed mGluR5 Δ C relative to the PSD. Compared to mGluR5 wild-type (mGluR5WT), mGluR5 Δ C showed a similar exclusion from the PSD (Fig. 5b–d). However, we found a



significantly increased fraction of spines with a homogeneous distribution of mGluR5 Δ C (synaptic enrichment: WT: $11 \pm 2\%$ and Δ C: $7.1 \pm 2\%$, synaptic + perisynaptic enrichment: WT: $16 \pm 3\%$ and Δ C: $12 \pm 3\%$, perisynaptic enrichment: WT: $57 \pm 3\%$ and Δ C: $51 \pm 3\%$ and homogeneous distribution: WT: $16\% \pm 3$ and Δ C: $30\% \pm 5\%$; Fig. 5d). Furthermore, the loss of the CTD resulted in the loss of mGluR5 enrichment in spines (WT: 1.47 ± 0.045 ; Δ C: 1.08 ± 0.032 ; Figs. 5e and S5a).

To further investigate whether the CTD is involved in mediating mGluR5 confinement in the perisynaptic zone, we performed SMT. Significantly fewer mGluR5 Δ C trajectories were found to be perisynaptic, and more tracks were only transiently associated with the perisynaptic zone (Fig. 5f). We also observed that mGluR5 Δ C tracks were more homogeneously distributed (Fig. 5j). The diffusion coefficient was significantly increased for both perisynaptic and transient perisynaptic trajectories of mGluR5 Δ C (median D_{eff} perisynaptic: WT: $0.031 \mu\text{m}^2/\text{s}$ and Δ C: $0.056 \mu\text{m}^2/\text{s}$, median D_{eff} transient perisynaptic: WT: $0.069 \mu\text{m}^2/\text{s}$ and Δ C: $0.096 \mu\text{m}^2/\text{s}$), but not of synaptic mGluR5 Δ C trajectories (median D_{eff} synaptic: WT: $0.020 \mu\text{m}^2/\text{s}$ and Δ C: $0.026 \mu\text{m}^2/\text{s}$), compared to mGluR5WT (Fig. 5g, j). Consistently, the fraction of immobile trajectories was significantly reduced for mGluR5 Δ C (WT: 0.64 ± 0.03 and Δ C: 0.44 ± 0.03 ; Figs. 5k and S5b), as well as the fraction of mobile mGluR5 Δ C trajectories with transient confinement zones (WT: 0.43 ± 0.03 and Δ C: 0.25 ± 0.02 ; Figs. 5l and S5c). Even when mGluR5 Δ C was transiently confined, diffusion inside the confinement zones was significantly faster compared to mGluR5WT (median D_{eff} WT: $0.0094 \mu\text{m}^2/\text{s}$ and Δ C: $0.015 \mu\text{m}^2/\text{s}$; Figs. 5h and S5d) and mGluR5 Δ C confinement zones were on average larger (radius WT: $76.7 \pm 2.3 \text{ nm}$ and Δ C: $99.4 \pm 2.3 \text{ nm}$; Fig. S5e). We found that the mGluR5 Δ C confinement zones were more homogeneously distributed and particularly showed less enrichment immediately adjacent to the PSD compared to mGluR5WT confinement zones (fraction confinement zones at 25 nm distance from PSD: WT: 0.20 ± 0.03 and Δ C: 0.14 ± 0.03 ; Fig. 5i). Consistently, the map of mGluR5 Δ C confinement and immobility hotspots also revealed less pronounced areas of restricted mGluR5 diffusion in the perisynaptic zone (Fig. 5m). These results further indicate that the mGluR5 CTD contributes to the transient confinement of mGluR5 in perisynaptic nanodomains.

The C-terminal domain of mGluR5 prevents synaptic entry

In stark contrast to AMPARs, mGluR5 seems to be transiently enriched in perisynaptic nanodomains, and almost completely excluded from the PSD. We, therefore, hypothesized that apart from mechanisms that confer perisynaptic retention of mGluR5, specific mechanisms prevent the synaptic entry of mGluR5. To begin to test this, we reasoned that we could target mGluR5 to the PSD by fusing mGluR5 to the CTD of Stargazin (STGtail), the AMPAR auxiliary protein that associates with PSD-95 to concentrate AMPARs in the PSD (Fig. 6a)^{37,38}. When we coupled the STGtail to a single transmembrane domain with an N-terminal SEP-tag (SEP-pDisp-STGtail), this construct was efficiently targeted to synapses marked by Homer1c-mCherry (Fig. S6a–c). Surprisingly, however, when mGluR5 was directly fused to the STGtail (mGluR5-STGtail), the receptor was still largely excluded from the PSD (Fig. 6b–d). For mGluR5-STGtail we observed a modest but significant increase in the number of spines with synaptic and perisynaptic enrichments (mGluR5WT: $16 \pm 3\%$ and mGluR5-STGtail: $29 \pm 3\%$; Fig. 6d), showing that the attempt to recruit mGluR5 to the PSD by the addition of the STGtail was only successful in a few spines. This also resulted in a reduction of spines

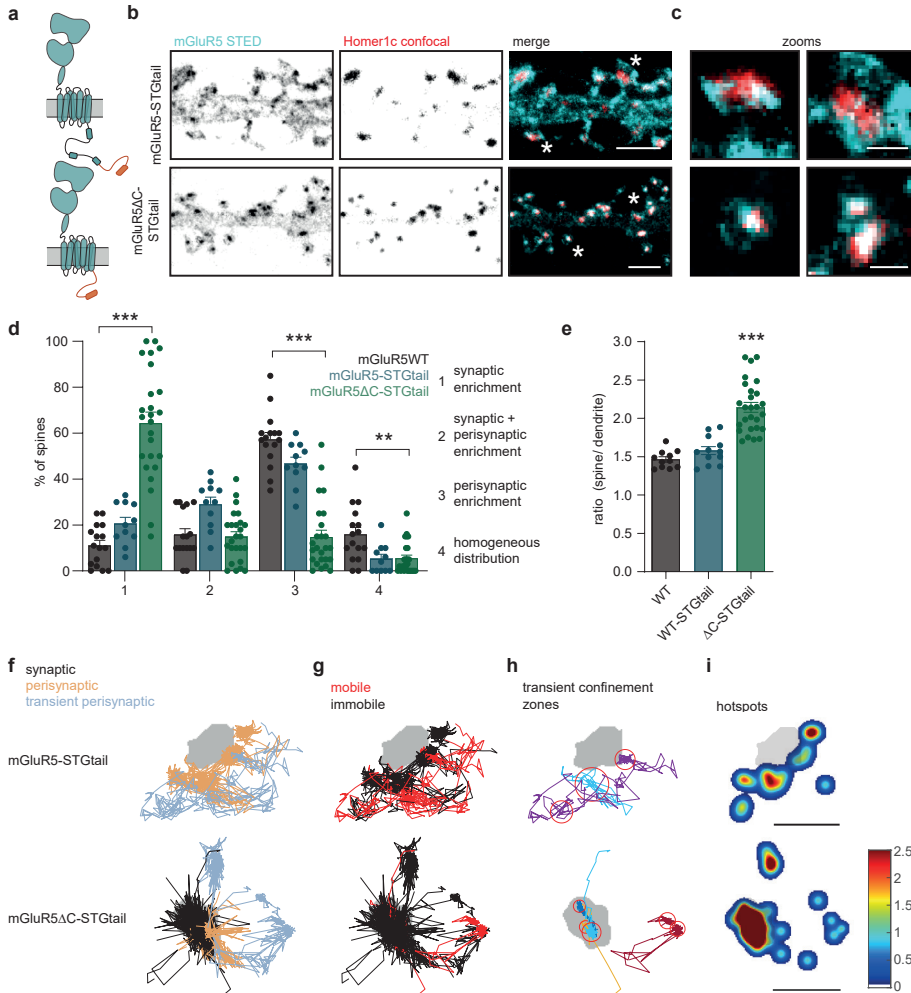


Figure 6. The C-terminal domain of mGluR5 prevents synaptic entry

a Schematic of mGluR5-STGtail (top) and mGluR5ΔC-STGtail (bottom). **b** Representative gSTED images of dendrite expressing SEP-mGluR5-STGtail and SEP-mGluR5ΔC-STGtail, additionally labeled with an anti-GFP nanobody Atto647N (cyan), and Homer1c-mCherry (red; confocal). Scale bar, 2 μm. **c** Zooms of spines indicated in **b** with asterisks. Scale bar, 500 nm. **d** Quantification of mGluR5WT (black; $n = 16$), mGluR5-STGtail (blue; $n = 11$) and mGluR5ΔC-STGtail (green; $n = 25$) localization in spines: (1) synaptic enrichment, (2) synaptic + perisynaptic enrichment, (3) perisynaptic enrichment and (4) homogeneous distribution ($p < 0.0001$, Kruskal-Wallis test for each category with Dunn's multiple comparisons test: $p = 0.5398$ for mGluR5WT vs. mGluR5-STGtail, $p < 0.0001$ for mGluR5WT vs. mGluR5ΔC-STGtail and $p = 0.0011$ for mGluR5-STGtail vs. mGluR5ΔC-STGtail). **e** Quantification of the ratio of spine over dendrite intensity of mGluR5WT ($n = 11$), mGluR5-STGtail ($n = 12$) and mGluR5ΔC-STGtail ($n = 27$; $p < 0.0001$, one-way ANOVA with Dunnett's multiple comparisons test: compared to mGluR5WT $p = 0.4700$ for mGluR5-STGtail and $p < 0.0001$ for mGluR5ΔC-STGtail). **f** Example synapses of mGluR5-STGtail and mGluR5ΔC-STGtail with trajectories color-coded for being synaptic (black), perisynaptic (orange), and transient perisynaptic (blue), **g** for being mobile (red) and immobile (black), **h** for being transiently confined trajectories (random colors) with corresponding confinement zones (red circles), and **i** hotspots of immobile tracks (shown in **g**) and confinement zones (shown in **h**), color-coded for their frequency. Scale bar, 500 nm. The mGluR5WT dataset shown in **d** and **e** is also shown in Fig. 5d, e, as these figures show different aspects of the same experiment. Data are represented as means \pm SEM. * $p < 0.05$, ** $p < 0.01$ and *** $p < 0.001$. Source data are provided as a Source Data file.

with a homogeneous distribution (mGluR5WT: $16 \pm 3\%$ and mGluR5-STGtail: $5.3 \pm 2\%$; Fig. 6d). Overall, however, the distribution of mGluR5-STGtail was similar to mGluR5WT (Figs. 6b–d and 5b–d), corroborated by the unchanged enrichment in spines (mGluR5WT: 1.47 ± 0.035 and mGluR5-STGtail: 1.58 ± 0.053 ; Figs. 6e and S6d).

Considering that the mGluR5 CTD mediates perisynaptic confinement (Fig. 5), we predicted that it may also play a critical role in preventing the synaptic entry of mGluR5. To test this idea we made a chimera construct replacing the CTD of mGluR5 for the STGtail: SEP-mGluR5 Δ C-STGtail (mGluR5 Δ C-STGtail) (Fig. 6a). Interestingly, this mGluR5-Stargazin chimera was very efficiently recruited to the PSD, marked by Homer1c (Fig. 6b, c). We found a 5-fold increase in the percentage of spines with synaptic enrichment, compared to mGluR5WT, and a decrease in spines with a perisynaptic distribution (mGluR5 Δ C-STGtail: synaptic enrichment: $64 \pm 5\%$, synaptic + perisynaptic enrichment: $15 \pm 2\%$, perisynaptic enrichment: $15 \pm 3\%$ and homogeneous distribution: $5.5 \pm 1\%$; Fig. 6d). Furthermore, we observed a significant increase in spine enrichment of mGluR5 Δ C-STGtail (mGluR5 Δ C-STGtail: 2.14 ± 0.064 ; Fig. 6e). Similarly, SMT of mGluR5-STGtail showed that the addition of the STGtail did not affect the distribution of receptor diffusion (Figs. 6f and 5j). However, in the few instances that mGluR5-STGtail entered the PSD, it was more immobile compared to mGluR5WT (median synaptic D_{eff} mGluR5WT: $0.020 \mu\text{m}^2/\text{s}$, mGluR5-STGtail: $0.015 \mu\text{m}^2/\text{s}$ and mGluR5 Δ C-STGtail: $0.014 \mu\text{m}^2/\text{s}$; Fig. S6e). In contrast, the confinement zones and immobile trajectories of mGluR5 Δ C-STGtail were strongly enriched within the PSD (Fig. 6g–i). To ensure that the STGtail is properly exposed in the mGluR5-STGtail construct, we designed mGluR5-STGtail_{split} where we positioned the mGluR5 CTD at amino acid position 302 in the STGtail, just upstream of the PDZ-binding motif (Fig. S6f). It has previously been validated that insertion of a fluorophore (GFP or mCherry), similar in size to the mGluR5 CTD, at position 302 in Stargazin results in a synaptically localized protein shown by co-localization with PSD-95³⁹. In this construct, the putative membrane-bound RS domain (a stretch of seven arginines interleaved by nine serines) at the start of the STGtail is able to attach to the plasma membrane, without masking the PDZ-binding motif at the end. Interestingly, lengthening of the STGtail by an artificial linker after the RS domain (in addition to the fluorophore) has even been shown to potentiate binding to the lower PDZ domains of PSD-95 which is oriented perpendicularly to the plasma membrane³⁹ (Fig. S6f). mGluR5-STGtail_{split} showed the mGluR5-typical perisynaptic localization in spines as shown with STED microscopy (Fig. S6g, h) and we observed no differences in spine enrichment compared to mGluR5-STGtail (1 – mGluR5-STGtail_{split}: 1.77 ± 0.11 , 2 – mGluR5-STGtail: 1.72 ± 0.10 and 3 – mGluR5 Δ C-STGtail: 3.29 ± 0.23 ; Fig. S6l). To assess whether the mGluR5 CTD is sufficient for the synaptic exclusion of the STGtail, we coupled the mGluR5 CTD and STGtail_{split} to a single transmembrane domain (pDisp-CTD-STGtail_{split}; Fig. S6i). Indeed, we observed that the spine enrichment was significantly reduced in pDisp-CTD-STGtail_{split} compared to pDisp-STGtail (pDisp-CTD-STGtail_{split}: 1.87 ± 0.25 and pDisp-STGtail: 7.6 ± 0.67 ; Fig. S6i) with preferential perisynaptic localization in spines (Fig. S6j, k). However, even though pDisp-CTD-STGtail_{split} was significantly less enriched in spines compared to mGluR5 Δ C-STGtail, some neurons displayed a similar spine enrichment. These results show that removing the mGluR5 CTD and increasing the affinity of mGluR5 for the PSD allow the entry and retention of mGluR5 in synapses, indicating that the mGluR5 CTD regulates both the retention and synaptic exclusion of mGluR5.

Inducible heterodimerization system allows robust and rapid recruitment of mGluR5 to the synapse

We hypothesized that the distinct segregation of ionotropic and metabotropic glutamate receptor types in different subsynaptic domains optimizes synaptic signaling. To better understand the functional relevance of mGluR5 nanodomains in the perisynaptic zone, we set out to develop a system to acutely control mGluR5 distribution to study the effect of mGluR5 positioning on

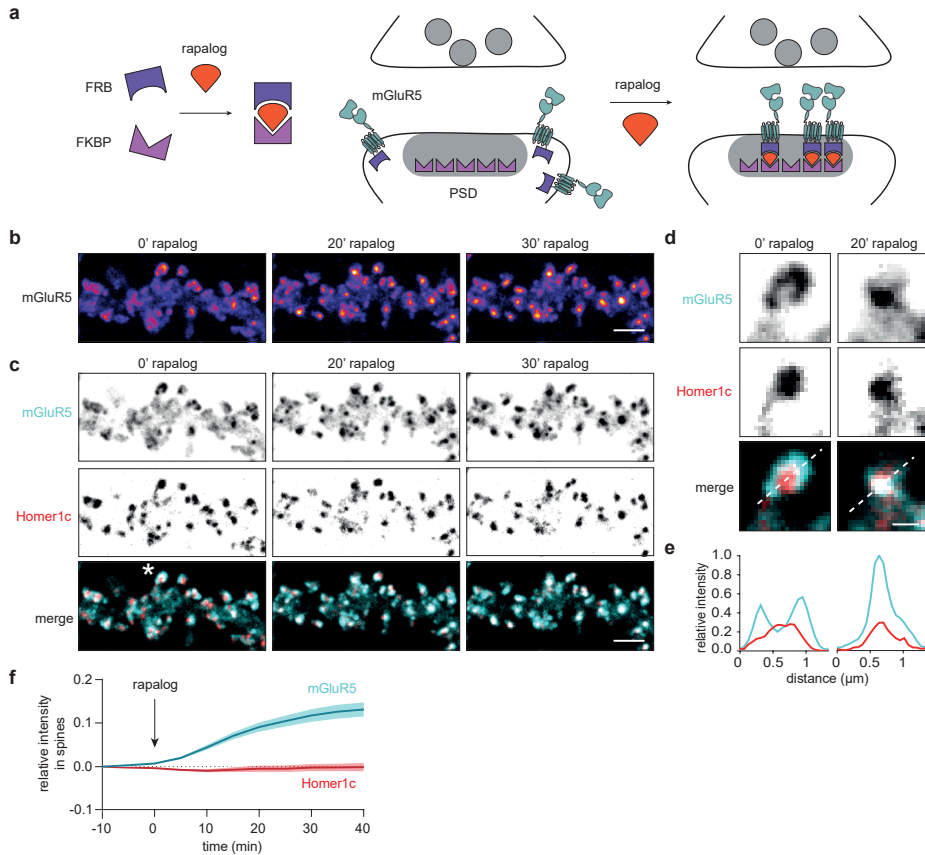


Figure 7. mGluR5 is efficiently recruited to the synapse using the inducible FKBP-ralpalog-FRB heterodimerization system

a Schematic of the FKBP-ralpalog-FRB heterodimerization system (left) and how this system is used to recruit mGluR5 to the PSD (right). **b** Live-cell time-lapse images of SEP-mGluR5-FRB before (0') and 20 and 30 min after rapallog application. The dendrites are color-coded for the fluorescence intensity of SEP-mGluR5-FRB. Scale bar, 2 μ m. **c** Live-cell time-lapse images of the same dendrite as shown in **b** showing the relative localization SEP-mGluR5-FRB (cyan) and 2xFKBP-Homer1c-mCherry (red) before (0') and 20 and 30 min after rapallog application. Scale bar, 500 nm. **d** Zoom of spine indicated in **c** with asterisk before (0') and 20 min after rapallog application. Scale bar, 500 nm. **e** Line profile of the spine in **d**, indicated with dotted line, showing the localization of mGluR5 (cyan) relative to Homer1c (red) before (0') and 20 min after rapallog application. **f** Quantification of SEP-mGluR5-FRB (cyan) and 2xFKBP-Homer1c-mCherry (red) intensity in spines over time upon rapallog application at $t = 0$ ($n = 17$). Data are represented as means \pm SEM. Source data are provided as a Source Data file.

synaptic signaling. To do so, we used the inducible FKBP-rapalog-FRB heterodimerization system, a reliable and robust tool to induce interactions between two proteins by the addition of rapalog⁴⁰. To allow controlled recruitment of mGluR5 to the synaptic scaffold Homer1c we developed FRB-tagged mGluR5 and FKBP-tagged Homer1c constructs (Fig. 7a). Indeed, the enrichment of mGluR5 in spines significantly increased upon the addition of rapalog (before: 1.5 ± 0.08 and 50 min after: 2.7 ± 0.2 ; Fig. S7a–c). Importantly, Homer1c spine enrichment was not different between neurons incubated with rapalog and control neurons where a vehicle was added, indicating unidirectional recruitment of mGluR5 towards Homer1c which is stably retained in the PSD. Live-cell imaging further demonstrated that mGluR5 accumulated within synapses over the time course of 40 min and we observed a clear re-distribution of mGluR5 into the PSD (Fig. 7b–f). Together, these data show that this rapalog-inducible system can be employed to acutely and robustly re-locate mGluR5 to postsynaptic sites.

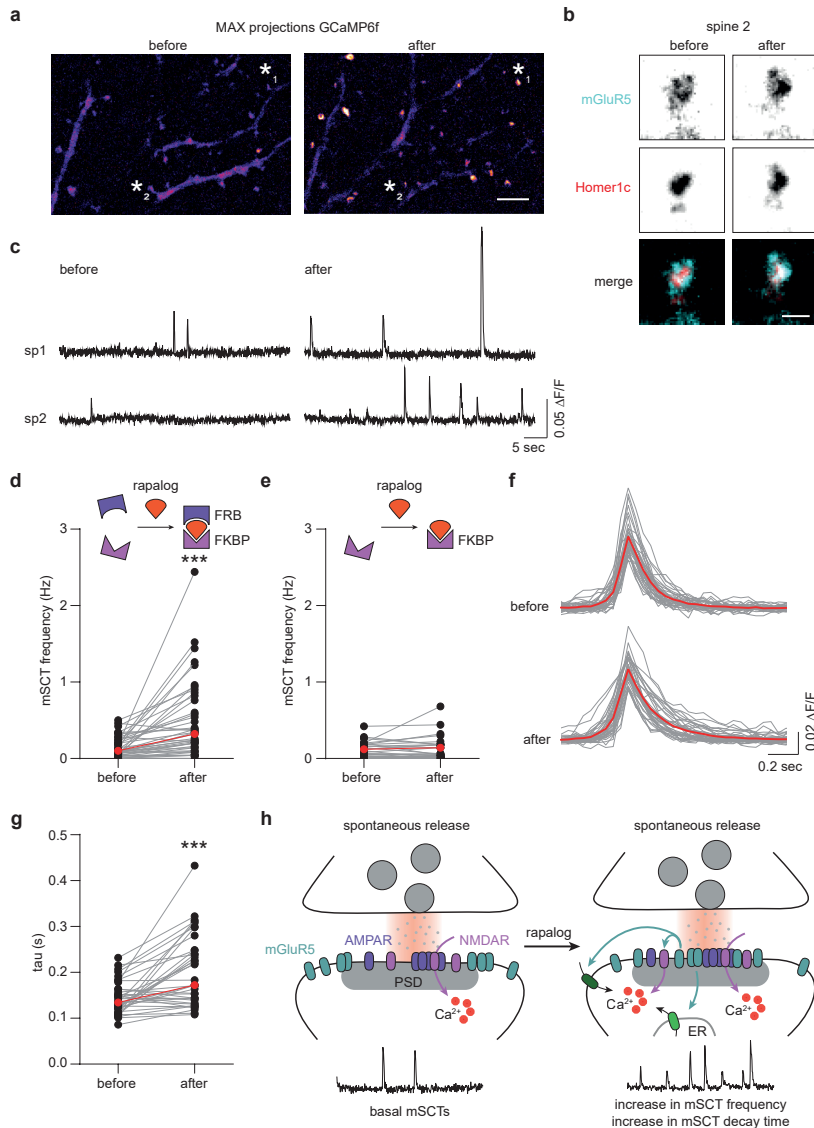
Synaptic recruitment of mGluR5 alters synaptic signaling

Activation of postsynaptic mGluRs modulates spine Ca^{2+} levels via several routes: via IP3-sensitive intracellular stores¹⁴, modulation of voltage-gated calcium channels (VGCCs), NMDA receptors, or Ca^{2+} -induced Ca^{2+} release (CICR)^{41–44}. However, direct measurements of the contribution of perisynaptic mGluR5 to synaptic calcium signaling at the level of a single synapse is difficult, and conclusions thus far rely on biophysical models¹⁷. Nevertheless, it has been generally assumed that spontaneous glutamate release events would not activate mGluR5. If the contribution of mGluR5 to synaptic calcium levels are minimal during spontaneous release events due to its perisynaptic localization, the calcium events should drastically change upon recruiting mGluR5 to the center of synapses, also experimentally revealing the significance of its perisynaptic localization during spontaneous release. To study the dynamic changes in spine calcium concentrations we used the optical Ca^{2+} sensor GCaMP6f⁴⁵. We expressed GCaMP6f and imaged neurons at DIV21–23 in extracellular buffer containing 3 μM TTX and 0 mM Mg^{2+} to block action potentials and relieve the NMDA receptor pore block. GCaMP6f robustly reported miniature spontaneous Ca^{2+} transients (mSCTs) that were detected in individual dendritic spines without detected Ca^{2+} increases in the dendritic shaft or neighboring spines (Fig. S8a–c), consistent with previous studies^{46, 47}. We found a broad range of event frequencies per neuron, ranging from 0 to 25 events/50 seconds,

Figure 8. Synaptic recruitment of mGluR5 increases the frequency of spontaneous synaptic Ca^{2+} transients

a Maximum projections of the GCaMP6f stream (50 s) in a representative dendrite before (baseline) and after 30 min rapalog application. Scale bar, 5 μm . **b** Zoom of spine 2 indicated in **a** with asterisk, expressing SNAP-mGluR5-FRB labeled with the cell-impermeable SNAPdye JF646 (cyan) and 2xFKBP-Homer1c-mCherry (red) before and 30 min after rapalog-induced recruitment. Scale bar, 1 μm . **c** $\Delta\text{F}/\text{F}_0$ traces of GCaMP6f signal from two spines indicated in **a** with asterisks before and after 30 min of rapalog-induced recruitment of mGluR5 to Homer1c. **d** Quantification of mSCT frequencies upon application of rapalog in neurons expressing SNAP-mGluR5-FRB and 2xFKBP-Homer1c-mCherry ($n = 43$ neurons, $p < 0.0001$, two-sided Wilcoxon matched-pairs signed rank test) and **e** in neurons expressing SNAP-mGluR5 and 2xFKBP-Homer1c-mCherry (control; $n = 37$ neurons, $p = 0.5819$, two-sided Wilcoxon matched-pairs signed rank test). **f** Average traces of all mSCTs per neuron (gray) and average mSCT trace of all neurons (red) before and after 30 min of rapalog. **g** Quantification of mSCT decay tau times (s) upon application of rapalog ($n = 37$ neurons, $p < 0.0001$, two-sided Wilcoxon matched-pairs signed rank test). **h** Model of deregulated calcium signaling upon mGluR5 recruitment to the synapse during spontaneous synaptic activity. Medians are indicated by the red lines. Source data are provided as a Source Data file.

with 90.6% of neurons exhibiting at least one event per 50 seconds. Moreover, the mSCT frequency was significantly increased by a 5-min application of the group I mGluR specific agonist DHPG (median mSCT frequency: basal: 0.30 Hz, 95% CI [0.14 0.68], DHPG: 0.78 Hz, 95% CI [0.40 1.86] and AP5: 0.06 Hz, 95% CI [0.00 0.10]; Fig. S8d–f), confirming that endogenous mGluR5 contributes to synaptic calcium signaling. Treatment with the NMDAR antagonist AP5 eliminated most events, indicating that activation of mGluR5, at least in part, induces spine mSCTs by potentiating NMDARs (Fig. S8d–f).



Next, to investigate the spatiotemporal effects of mGluR distribution on synaptic function at individual synapses, we combined the inducible FKBP-rapalog-FRB heterodimerization system and GCaMP6f and determined the effect of mGluR5 recruitment to the synapse on synaptic calcium signaling. We co-expressed GCaMP6f with SNAP-mGluR5-FRB and FKBP-Homer1c-mCherry and imaged GCaMP6f before and 30 min after the application of rapalog. In the maximum intensity projections of the obtained GCaMP6f streams (50 ms) we observed a clear increase in peak intensities at individual spines after a 30-min rapalog incubation (Fig. 8a–c). Indeed, quantification consistently showed that rapalog application caused a dramatic threefold increase in mSCT frequency (median mSCT frequency: before: 0.10 Hz, 95% CI [0.06 0.18] and after: 0.32 Hz, 95% CI [0.20 0.48]; Fig. 8d and S8h), also when corrected for spine density (Fig. S8g). The mSCT amplitude was not changed after the addition of rapalog (median $\Delta F/F_0$: before: 0.057, 95% CI [0.052 0.066] and after: 0.059, 95% CI [0.055 0.064]; Fig. S8i), but we did find significantly larger decay tau times (before: 0.13 s, 95% CI [0.12 0.15] and after 0.17 s, 95% CI [0.14 0.23]; Fig. 8f, g). To control for possible undesired side effects of rapalog on mSCT frequency and amplitude we performed the same experiment but with mGluR5 lacking the FRB domain. In this experiment, we observed no differences in mSCT frequency (median mSCT frequency: before: 0.06 Hz, 95% CI [0.02 0.12] and after: 0.04 Hz, 95% CI [0.02 0.14]; Figs. 8e and S8h) and amplitude (median $\Delta F/F_0$: before: 0.054, 95% CI [0.045 0.064] and after: 0.054, 95% CI [0.048 0.062]; Fig. S8j) before and after rapalog application. Altogether, these data support the model that positioning mGluR5 at perisynaptic sites is critical to restrict mGluR5 overactivation during spontaneous release events as the acute recruitment of mGluR5 to the synapse results in aberrant synaptic calcium signaling (Fig. 8h).

Discussion

The subsynaptic organization of group I mGluRs modulates their activation and subsequent downstream signaling, essential for proper synaptic transmission and plasticity. However, fundamental aspects of mGluR distribution and dynamics at excitatory synapses are still poorly understood. Here, we present a mechanistic understanding of how the CTD of mGluR5 controls its dynamic organization in perisynaptic nanodomains, as well as prevents mGluR5 from entering the synapse, allowing mGluR5 to finely tune synaptic calcium signaling.

Our localization and SMT data show that mGluR5 is enriched in the perisynaptic zone and largely absent from the PSD, consistent with early EM studies^{11–13} and recent super-resolution microscopy studies⁴⁸. Importantly, we observed that the organization of mGluR5 is much more heterogeneous than suggested before. We found that mGluR5 assembles in distinct perisynaptic nanodomains, suggesting that specific mechanisms hinder mGluR5 diffusion at the perisynaptic zone. Consistently, our SMT data revealed that mGluR5 trajectories were enriched in the perisynaptic zone and were confined to domains with radii ranging from 40 up to 200 nm. Interestingly, however, mGluR5 was only transiently trapped in these perisynaptic nanodomains, and rapidly exchanged between diffusive and confined states. Only a small fraction of mGluR5 seemed to be retained in the PSD, possibly by indirect steric hindrance, or molecular crowding mechanisms^{49, 50}. Thus, the enrichment of mGluR5 in perisynaptic nanodomains is the result of a highly dynamic equilibrium of diffusion states.

The transient confinement of mGluR5 may represent either binding and unbinding to an interaction partner or hindrance of movement of mGluRs due to other mechanisms. We found that the perisynaptic retention of mGluR5, but also the exclusion from the synapse is largely controlled by its CTD. Most importantly, the removal of the mGluR5 CTD resulted in a higher mobility in the perisynaptic zone and less transient confinement in perisynaptic nanodomains. Based on these data, we propose that the mGluR5 CTD is critical for the transient confinement of mGluR5 in perisynaptic nanodomains, possibly through stabilizing interactions at the perisynaptic zone. The CTD of mGluRs can interact with a variety of intracellular proteins, including the scaffolding protein Homer1b/c that links mGluRs to a larger synaptic complex^{35,51-54}. Numerous studies have proposed Homer1b/c as the protein regulating the subsynaptic positioning of mGluRs⁵⁵⁻⁵⁸. We found however that Homer1c overexpression did not affect mGluR5 enrichment in spines nor did it affect mGluR5 diffusion. In fact, we found that mGluR5 localizes away from Homer1c, being present in the core of the PSD⁵⁹, and that forced recruitment of mGluR5 to Homer1c using the FKBP-heterodimerization-FRB system is required to recruit mGluR5 to the PSD. This might suggest that mGluR5 only interacts with Homer1c molecules present at the periphery of the PSD. The mGluR5 CTD also contains many other binding motifs and phosphorylation sites that might underlie the dynamic positioning of mGluRs^{3,35}. Also, other mechanisms such as phase separation, molecular crowding, lipid organization, or cytoskeletal hindrance might mediate the organizational properties of the mGluR5 CTD^{2,60}. Furthermore, we cannot exclude the possibility that other mGluR5 domains, including the extracellular N-terminal domain, are involved in receptor positioning^{19,61}. For example, the enrichment of AMPARs at synaptic sites has been ascribed both to the CTD⁶²⁻⁶⁴, as well as the NTD⁶⁵⁻⁶⁷. Based on these findings we propose that at excitatory synapses functionally distinct glutamate receptor types are spatially segregated in subsynaptic domains, in part via intracellular interactions that can either promote or hinder the entry of receptors into the PSD. Our findings reveal that postsynaptic mGluR positioning is regulated by conceptually novel mechanisms that effectively retain mGluR5 close to the synapse, but segregated away from the core synaptic membrane, to efficiently modulate synaptic function.

The preferential perisynaptic organization we observed for mGluR5 is likely to affect receptor activation and function. The perisynaptic mGluRs are perfectly situated to detect glutamate spillover from the synaptic cleft during sustained or high-frequency stimulation and initiate downstream signaling. Furthermore, the perisynaptic nanodomains may function to concentrate signaling machineries optimizing the ability of mGluRs to connect to downstream signaling effectors. Such local accumulations of receptors and their effectors, in so-called signalosomes, have been shown to contribute to the efficiency and fidelity of signal transmission^{68,69}. In support of this concept of perisynaptic signalosomes, the mGluR5 downstream signaling partners Gαq/Gα11, PLCβ, DGL-α, and Norbin were found to closely parallel the organization of mGluR5 as they were either enriched in the perisynaptic zone or found to colocalize with mGluR5⁷⁰⁻⁷⁴. In general, we observed that mGluR5 was not limited to one perisynaptic nanodomain, but formed multiple distinct domains in the perisynaptic zone. This opens the intriguing possibility that mGluRs assemble into distinct signalosomes that each consist of a specific subset of signaling molecules. The compartmentalization of downstream effectors of mGluRs might be of critical importance to regulate the initiation of downstream signaling and warrant the functional selectivity of mGluR1 and mGluR5. The perisynaptic zone also contains a stable endocytic zone (EZ) that functions to locally

internalize and recycle synaptic receptors^{28, 75–77}. In particular, the tight coupling of the PSD to the EZ has been shown to govern the efficient trafficking of mGluR5, regulating mGluR5 surface expression and signaling⁷⁸. mGluR5 organized in perisynaptic nanodomains that localize in close vicinity of the EZ might be particularly well-suited for fast desensitization and local endocytosis and recycling after activation to rapidly respond to sustained synaptic activity. Interestingly, mGluR5 is not exclusively present at perisynaptic sites. A small fraction of mGluR5 does localize to the PSD, which has been shown to be an activity-driven process to remodel mGluR5-scaffold interactions and modulate downstream signaling^{79, 80}. Also, mGluR5 broadly localizes throughout the dendritic shaft and, in contrast to excitatory synapses, localizes inside inhibitory synapses^{81, 82}. This heterogeneous localization suggests that mGluR5 dynamics are regulated by different processes in space and time to specify and support different mGluR5 functions. We found that recruiting mGluR5 from the perisynaptic zone to the core of the PSD strikingly increased calcium events at synapses. These results indicate that increasing the availability of mGluR5 in the PSD for activation during spontaneous synaptic activity strongly deregulates synaptic calcium signaling. The increased mSCT frequency upon recruitment of mGluR5 to the synapse argues for a direct (Ca^{2+} influx through NMDARs) or indirect (downstream activation of Ca^{2+} release) contribution of mGluR5 to mSCTs. Even though increased mSCT frequency is expected to increase NMDA current magnitudes, our results revealed no significant difference in mSCT amplitude indicating that mSCTs measured by GCaMP6f were not solely dependent on NMDA receptor activity. The increased mSCT frequency and decay times might reflect increased Ca^{2+} release from intracellular stores further shaping the mSCTs. Also, the number of mSCTs that were detectable and met by our detection criteria might be increased by Ca^{2+} release from internal stores (see M&M for details). Moreover, even though we performed the experiments in the absence of Mg^{2+} , the Ca^{2+} influx through NMDARs might not always be sufficient to generate mSCTs and further relies on activation of Ca^{2+} release from internal stores to amplify NMDA-mediated Ca^{2+} transients⁴⁶. We can also not exclude the possibility that other sources of Ca^{2+} entry, such as via VGCCs, also play a role here. It is nevertheless tempting to speculate that the induced synaptic enrichment of mGluR5 might to some extent induce the reported physical association between NMDA and mGluR5 initiated upon the activity-induced increase in Homer1a expression^{24, 80, 83}.

Altogether, our data provide an unforeseen level of mechanistic understanding of how postsynaptic mGluRs are transiently retained in distinct perisynaptic nanodomains to control synaptic signaling. Further delineation of these mechanisms will shed new light on how glutamatergic signaling is regulated by the cooperative actions of different glutamate receptor subtypes. The functional implications of erroneous mGluR positioning further underlines the relevance of understanding the relation between mGluR trafficking and signaling in the context of cognitive functioning.

Methods

Animals

All animal (male and female) experiments were performed in compliance with the guidelines for the welfare of experimental animals issued by the Government of the Netherlands (Wet op de Dierproeven, 1996) and European regulations (Guideline 86/609/EEC). All animal experiments were approved by the Dutch Animal Experiments

Review Committee (Dier Experimenten Commissie; DEC), and performed in line with the institutional guidelines of Utrecht University.

Primary neuronal cultures and transfections

Hippocampal cultures were prepared from embryonic day 18 (E18) Janvier Wistar rat brains (both genders)⁸⁴. Dissociated neurons were plated on coverslips coated with poly-L-lysine (37.5 µg/ml, Sigma-Aldrich) and laminin (1.25 µg/ml, Roche Diagnostics) at a density of 100,000 neurons per well in a 12-well plate. Neurons were grown in Neurobasal medium (NB) supplemented with 2% B27 (GIBCO), 0.5 mM glutamine (GIBCO), 15.6 µM glutamate (Sigma-Aldrich), and 1% penicillin/streptomycin (GIBCO) at 37 °C in 5% CO₂. Once per week, starting at 1 day in vitro (DIV1), half of the medium was refreshed with BrainPhys Neuronal Medium (BP, STEMCELL Technologies), supplemented with 2% NeuroCult SMI (STEMCELL Technologies) and 1% penicillin/streptomycin (GIBCO). At DIV3 (knock-in construct) or DIV11–16 neurons were transfected with indicated constructs using Lipofectamine 2000 (Invitrogen). Before transfection 300 µl conditioned medium was transferred to a new culture plate. For each well, 1.8 µg DNA was mixed with 3.3 µl Lipofectamine 2000 in 200 µl BP, incubated for 30 min at room temperature (RT), and added to the neurons. After 1–2 h, neurons were briefly washed with BP and transferred to the new culture plate with conditioned medium supplemented with an additional 400 µl BP with SMI and penicillin/streptomycin and kept at 37 °C in 5% CO₂. All experiments were performed using neurons at DIV18–22. If neurons were kept longer than 6 days, medium was refreshed as described above.

DNA constructs

The pRK5-SEP-mGluR5a and pRK5-myc-mGluR5a are previously described⁷⁸ and used as a template to make pRK5-SNAP-mGluR5a. To make pRK5-SEP-mGluR5aΔC, primers were designed using Gibson Assembly (NEBuilder HiFi DNA assembly cloning kit) to remove the last 314 C-terminal amino acids of mGluR5a. The pDisp-SEP-TM-STGtail construct was a gift from Dr. Thomas A. Blanpied⁵⁰ and the STGtail sequence was used to add to the C-terminal part of mGluR5a and mGluR5aΔC (before the stop codon) to make pRK5-SEP-mGluR5a-STGtail and pRK5-SEP-mGluR5aΔC-STGtail. Primers were designed to split the STGtail into two parts, STGtail203–302 and STGtail303–323, to make the pRK5-SEP-mGluR5-STGtail_{split} and pRK5-SEP-pDisp-CTD-STGtail_{split} constructs (as shown in Fig. S6f and i). The FKBP and FRB containing expression plasmids were a gift from Lukas C. Kapitein⁸⁵ and used to make pRK5-SNAP-mGluR5a-FRB, pRK5-SEP-mGluR5a-FRB, and 2xFKBP-Homer1c-mCherry using Gibson Assembly. Homer1c-mCherry and pSM155-mCherry have been described before⁷⁸. The pRK5-SEP-mGluR5a was used as a template to replace mGluR5a with GluA2 (flip, Q/R edited), previously described in ref. ⁵. GCaMP6f was a gift from Adam Cohen (Addgene plasmid # 58514) and PSD_{FingR}-mEos3.2 was a gift from Matthew J. Kennedy⁸⁶ and is based on (Dr. Don Arnold, Addgene plasmid # 46295)²⁶. The pAAV-GFP-mGluR5 CRISPR/Cas9 ORANGE knock-in construct was designed as described in ref. ⁹. The GFP-tag was inserted into the *Gm5* gene using the following target sequence: 5' – GTGCACAGTCCAGTGAGAGG – 3', resulting in the N-terminal tagging of mGluR5.

Antibody and nanobody labeling

Neurons were fixed between DIV18–21 with 4% paraformaldehyde (PFA) and 4% sucrose in PBS for 10 min at RT, washed three times with PBS supplemented with 100 mM glycine (PBS/Gly), and blocked in 1–2% BSA in PBS/Gly for 30 min at RT. To label the surface-expressed pool of receptors, neurons were labeled with the GFP-booster Atto647N (Chromotek) diluted 1:200 in 1% BSA in PBS/Gly for 2 h at RT or Fluotag-X4 anti-GFP Atto647N (Nanotag) diluted 1:250 in 1% BSA in PBS/Gly for 1 h at RT. Neurons were then washed three times with PBS/Gly, mounted in Mowiol mounting medium (Sigma), and imaged on the Leica SP8 microscope as described below.

For the GFP-mGluR5 knock-in experiments (Fig. 1i–m) neurons were fixed as described above and blocked with 10% NGS in PBS/Gly for 30 min at RT. To label the surface-expressed receptors, neurons were incubated with rabbit anti-GFP (MBL) diluted 1:2000 in 5% NGS in PBS/Gly for 2 h at RT and washed three times with PBS/Gly. Then, to label intracellular PSD-95, neurons were permeabilized in 0.25% Triton X-100 and 5% NGS in PBS/Gly for 10 min at RT, and incubated with mouse anti-PSD-95 (Neuromab) diluted 1:300 in 0.1% Triton X-100 and 5% NGS in PBS/Gly for 2 h at RT or overnight (O/N) at 4 °C. Neurons were washed three times and incubated with anti-rabbit Alexa488 and anti-mouse Alexa594 (Thermo Fisher Scientific) diluted 1:250 in 0.1% Triton X-100 and 5% NGS in PBS/Gly for 1 h at RT. Neurons were washed three times with PBS/Gly, mounted in Mowiol mounting medium (Sigma), and imaged on the Leica SP8 microscope as described below.

For two-color gSTED of SEP-mGluR5 and endogenous PSD-95 (Fig. S1a–d), neurons were fixed and labeled as described above, except for the secondary antibodies used. Rabbit anti-GFP and mouse anti-PSD-95 were visualized with anti-rabbit Atto647N (Sigma-Aldrich) and anti-mouse (Thermo Fisher Scientific) diluted 1:250.

For confocal imaging of mGluR5 expression levels in SEP-mGluR5 transfected and untransfected neurons (Fig. S1e–g), neurons were fixed as described above. Then neurons were blocked in 10% NGS and 0.1% Triton X-100 in PBS/Gly for 30 min at RT, incubated with rabbit anti-mGluR5 (Millipore) diluted 1:500 in 0.1% Triton X-100 and 5% NGS in PBS/Gly O/N at 4 °C. Neurons were washed three times and incubated with anti-rabbit Alexa594 (Thermo Fisher Scientific) diluted 1:250 in 0.1% Triton X-100 and 5% NGS in PBS/Gly for 1 h at RT.

For two-color gSTED of endogenous mGluR5 and PSD-95 (Fig. S1h–k) neurons were fixed and blocked as described above. Then neurons were, incubated with rabbit anti-mGluR5 (Millipore) diluted 1:500 and mouse anti-PSD-95 (Neuromab) diluted 1:300 in 0.1% Triton X-100 and 5% NGS in PBS/Gly O/N at 4 °C. Neurons were washed three times and incubated with anti-rabbit Atto647N (Sigma Aldrich) and anti-mouse Alexa594 (Thermo Fisher Scientific) diluted 1:250 in 0.1% Triton X-100 and 5% NGS in PBS/Gly for 1 h at RT.

For three-color gSTED of endogenous mGluR5, PSD-95 and actin (Fig. S1l–n) neurons were fixed and blocked as described above. Then neurons were incubated with rabbit anti-mGluR5 (Alomone Labs) diluted 1:50 and mouse anti-PSD-95 (Neuromab) diluted 1:300 in 0.1% Triton X-100 and 5% NGS in PBS/Gly for 2 h at RT. Neurons were washed three times and incubated with anti-rabbit Atto647N (Sigma Aldrich), anti-mouse Alexa488 (Thermo Fisher Scientific) diluted 1:250 and Phalloidin Alexa594 (Thermo Fisher Scientific) diluted 1:100 in 0.1% Triton X-100 and 5% NGS in PBS/Gly for 1 h at RT. Note that we visualized the total pool of endogenous mGluR5 using both mGluR5 antibodies.

For two-color STED of myc-mGluR5 and SEP-GluA2 (Fig. S1s–v) neurons were fixed as described above and blocked in 10% NGS in PBS/Gly for 30 min at RT. To label the surface-expressed receptors, neurons were incubated with rabbit anti-GFP (MBL) diluted 1:2000 and mouse anti-myc (Santa Cruz Biotechnology) diluted 1:500 in 5% NGS in PBS/Gly O/N at 4 °C. Neurons were washed three times and incubated with anti-rabbit Atto647N (Sigma Aldrich) and anti-mouse Alexa594 (Thermo Fisher Scientific) diluted 1:250 in 5% NGS in PBS/Gly for 1 h at RT. All neurons were washed three times with PBS/Gly after the incubation with secondary antibodies, mounted in Mowiol mounting medium (Sigma), and imaged on the Leica SP8 microscope as described below.

Confocal and STED microscopy

Imaging was performed with a Leica TCS SP8 STED 3× microscope using an HC PL APO x100/NA 1.4 oil immersion STED WHITE objective. The 488, 590, and 647 nm wavelengths of pulsed white laser (80 MHz) were used to excite Alexa488, Alexa594, and Atto647N, respectively. To obtain gSTED images, Alexa488 was depleted with the 592 nm continuous wave depletion laser, and Alexa594 and Atto647N were depleted with the 775 nm pulsed depletion laser. We used an internal Leica HyD hybrid detector (set at 100% gain) with a time gate of $0.3 \leq t_g \leq 6$ ns. Images were acquired as Z stacks using the x100 objective. Data was collected using the Leica Application Suite X (LAS-X software). Maximum intensity projections were obtained for image display and analysis. For the FKBP-rapalog-FRB heterodimerization assay DIV18–21 neurons transfected with SEP-mGluR5-FRB and 2xFKBP-Homer1c-mCherry were incubated with 1 μM rapalog diluted in extracellular imaging buffer or extracellular imaging buffer only (vehicle) for 50 min before fixation. For the quantification of mGluR5 overexpression, DIV18–21 neurons transfected with SEP-mGluR5 and stained with anti-mGluR5, confocal images were taken with a Zeiss LSM 510 with 63× 1.40 oil objective. Images consist of a z stack of 7–9 planes at 0.39 μm interval, and maximum intensity projections were generated for analysis and display.

Single-molecule localization microscopy using dSTORM and PALM

Neurons were fixed at DIV21 with 4% PFA/sucrose in PBS for 10 min at RT, washed three times with PBS/Gly and blocked with 10% NGS in PBS/Gly for 15 min at RT. To label the surface-expressed pool of receptors, neurons were incubated with Fluotag-X4 anti-GFP Alexa647 (Nanotag) diluted 1:250 in PBS/Gly. Neurons were washed three times in PBS/Gly and stored in PBS at 4 °C (dark) until use. Neurons were imaged in PBS containing 5 mM MEA, 5% w/v glucose, 700 μg/ml glucose oxidase, and 40 μg/ml catalase.

Dual-color SMLM data was acquired on the Nanoimager S from ONI (Oxford Nanoimaging; ONI), equipped with a x100/NA 1.4 oil immersion objective (Olympus Plan Apo), with an effective pixel size of 117 nm, an XYZ closed-loop piezo stage, and with 405, 473, 561 and 640 nm wavelength excitation lasers. Fluorescence emission was detected using a sCMOS camera (ORCA Flash 4, Hamamatsu). Integrated filters were used to split far-red emission from blue-green-red emission, allowing simultaneous dual-color imaging. dSTORM and PALM were simultaneously performed using the 640 nm laser to bring Alexa647 to the dark state along with increasing power of the 405 nm laser to stochastically reactivate Alexa647 fluorophores and stochastically photoconvert

PSD_{FingR}-mEos3.2 from green to red, combined with excitation of the photoconverted molecules by the 561 nm laser. Stacks of 10,000 to 20,000 images were acquired at 50 Hz with oblique illumination, which was processed using NimOS software from ONI. Before every acquisition, stacks of 30 frames were acquired with the 473 nm excitation laser to visualize SEP-mGluR5 and PSD-95FingR-mEos3.2 expression. NimOS software from ONI was used for data processing and drift correction was performed. Before each imaging session, a bead sample was used to calibrate the system and align the two channels with a channel mapping precision >8 nm. The particle tables were exported to MATLAB for analysis and images were rendered in NimOS software with 11.7 nm output pixels (sigma 1) and filtered on a minimum photocount of 300 and xy localization precision ≤ 30 nm for figure display.

Single-molecule tracking with uPAINT

uPAINT for Figs. 3 and 4 was performed on the Nanoimager S from ONI (Oxford Nanoimaging; ONI), equipped with a x100/NA 1.4 oil immersion objective (Olympus Plan Apo), an XYZ closed-loop piezo stage, and with 405, 471, 561, and 640 nm wavelength excitation lasers. Fluorescence emission was detected using a sCMOS camera (ORCA Flash 4, Hamamatsu). Stacks of 5000 frames were acquired at 50 Hz with oblique illumination. NimOS software from ONI was used for data analysis and drift correction was performed.

uPAINT for Figs. 5 and 6 was performed on a Nikon Ti microscope with a Nikon x100/ NA 1.49 Apo TIRF objective, a Perfect Focus System, a 2.5× Optovar to achieve an effective pixel size of 64 nm and a DU-897D EMCDD camera (Andor). Imaging was performed with oblique laser illumination with a 405 nm diode laser (15 mW; Power Technology), a 491 nm DPSS laser (50 mW; Cobolt Calypso), a 561 nm DPSS laser (100 mW; Cobolt Jive), and a 640 nm diode laser (35 mW; Power Technology). Micromanager software⁸⁷ was used to control all these components. 5000 frames were acquired at 50 Hz in TIRF. Acquired image stacks were analyzed using the ImageJ plugin Detection of Molecules (DoM) v1.1.5 (https://github.com/ekatruxha/DoM_Utrecht) and drift correction was applied.

Neurons were imaged in extracellular imaging buffer containing 120 mM NaCl, 3 mM KCl, 10 mM HEPES, 2 mM CaCl₂, 2 mM MgCl₂ and 10 mM glucose, pH adjusted to 7.35 with NaOH. The GFP-booster Atto647N (Chromotek) was added before image acquisition in a concentration of 1:150.000 to 1:50.000 in extracellular imaging buffer while blocking with 0.5–1.5 % BSA. Low concentrations of the GFP-booster were used to achieve temporal separation of fluorescence emission of mGluR5 molecules. Due to the low dissociation rates of the nanobody, only being limited by photobleaching, we obtained long trajectories and used a minimum track length of 30 frames (20 ms interval) for visualization and quantification. PSD masks were created from a stack of 30 frames obtained for Homer1c-mCherry using the 561 nm excitation laser.

Live-cell spinning disk confocal imaging

The FKBP-rapalog-FRB heterodimerization assay and Ca²⁺ imaging were performed on a spinning disk confocal system (CSU-X1-A1 Yokogawa; Roper Scientific) mounted on an inverted Nikon Eclipse Ti microscope (Nikon) with a Plan Apo VC x100/1.40 NA objective (Nikon) with excitation from 491 nm Cobolt Calypso (100 mW), 561 nm Cobolt Jive (100 mW), 642 nm Vortran Stradus (110 mW) lasers and emission filters (Chroma). The microscope is equipped with a motorized XYZ stage (ASI; MS-2000), Perfect Focus System (Nikon), and Prime BSI sCMOS camera (Photometrics), and controlled by MetaMorph software (Molecular Devices). During the image acquisition neurons were kept in extracellular imaging buffer (with or without MgCl₂) in a closed incubation chamber (INUBG2E-ZILCS; Tokai Hit) at 37 °C in 5% CO₂.

For the FKBP-rapalog-FRB heterodimerization assay neurons were transfected with SEP-mGluR5-FRB and 2xFKBP-Homer1c and imaged at DIV18–22. After a 10-min baseline acquisition, recruitment of mGluR5 to Homer1c was induced by the addition of rapalog to a final concentration of 1 μM and the SEP-mGluR5 and Homer1c-mCherry signals were imaged every 5 min for another 40 min. Multiple Z stacks (seven planes) were obtained, with 0.5 μm intervals to acquire 3 μm image stacks.

For the heterodimerization assay combined with Ca²⁺ imaging, neurons were transfected with SNAP-mGluR5-FRB, 2xFKBP-Homer1c-mCherry, and GCaMP6f or SNAP-mGluR5, 2xFKBP-Homer1c-mCherry and GCaMP6f for control neurons. At DIV21–22, before each acquisition a coverslip with neurons was labeled with a SNAP JF646 cell-impermeable dye (JF646i; Janelia/ Tocris) diluted 1:2000 in supplemented medium for 30 min followed by a single wash with extracellular buffer. Neurons were transferred to the imaging chamber containing extracellular imaging buffer without MgCl₂ and with 3 μM tetrodotoxin citrate (TTX; Tocris) to block action potentials and relieve the NMDA receptor pore block. At the start, Z stacks (7 planes) were obtained of the SNAP-mGluR5-FRB JF646i and 2xFKBP-Homer1c-mCherry channels, with 0.5 μm intervals to acquire 3 μm image stacks. This was shortly followed by a 50-second stream of the GCaMP6f signal, acquired at 50 ms intervals (20 Hz) (referred to as “before” rapalog). Then, rapalog was added to the imaging chamber to a final concentration of 1 μM and incubated

for 30 min, the time we established is required for the synaptic recruitment of mGluR5 to reach a plateau. Again, this was followed by imaging stacks of SNAP-mGluR5 JF646i and Homer1c-mCherry and a stream of GCaMP6f (referred to as after rapalog). Maximum intensity projections were obtained of the mGluR5 and Homer1c stacks for image display and analysis.

For Ca^{2+} imaging experiments (without FKBP/FRB recruitment), neurons were transfected with GCaMP6f and mCherry as a fill marker and imaged at DIV21–22. Neurons were transferred to the imaging chamber containing extracellular imaging buffer without MgCl_2 and with 3 μM TTX (Tocris). A Z stack was obtained of mCherry and a 50-second baseline stream of GCaMP6f (same imaging settings as described above). In the drug treatment experiment, the baseline acquisition was followed by the application of 100 μM (S)-3,5-dihydroxyphenylglycine (DHPG; Tocris) for 5 min, a wash-out, 5 min recovery, and an additional 50-second stream of GCaMP6f. Then, this was followed by a 5-min incubation of 50 μM DL-2-Amino-5-phosphonopentanoic acid (DL-AP5; Tocris) and another 50-second stream of GCaMP6f.

Quantification and Statistical Analysis

Quantification of spine enrichment and mGluR5 expression

To assess the spine enrichment of surface mGluR5 and mGluR5/STGtail variants, the Atto647N intensity from confocal images were quantified as mean spine intensity divided by mean dendritic shaft intensity. For each neuron, circular regions of interest (ROIs) were traced on multiple dendritic spines to measure spine intensity and for each selected spine an ROI in the dendrite at the base of the spine was measured as dendritic shaft intensity. Background intensity was subtracted. For Figs. 1 and S7 the spine enrichment of mCherry and Homer1c-mCherry was determined using the same spine and dendrite ROIs as used for mGluR5. To analyze mGluR5 overexpression levels, the average intensity of mGluR5 staining was measured in dendritic segments of SEP-mGluR5 expressing neurons and neighboring untransfected neurons in the same field-of-view.

STED imaging analysis

To assess the localization of mGluR5 relative to Homer1c, PSD-95, GluA2, or Phalloidin, line profiles along spines were drawn using ImageJ software. To quantify the localization of mGluR5, mGluR5 ΔC , mGluR5WT-STGtail, and mGluR5 ΔC -STGtail in spines, all images were scrambled and blinded. Per neuron, a minimum of 20 spines were selected based on the Homer1c channel and the localization of mGluR5 was determined using the merged image of confocal-resolved Homer1c and gSTED-resolved mGluR5 in ImageJ software. The localization of mGluR5 could be categorized as spines with (1) synaptic enrichments, (2) synaptic and perisynaptic enrichments, (3) perisynaptic enrichments or (4) a homogeneous distribution of mGluR5. Per category, the percentage of spines was plotted and the statistical significance was determined within each category and all conditions were compared to mGluR5WT.

Single-molecule localization analysis

The maximum projections of the 30 frames acquired in the green channel were used to select all spines and save these as separate ROIs using ImageJ software. The molecules from the ROIs were extracted and used for further analysis and were filtered on a localization precision <20 nm. Furthermore, molecules that were in the fluorescent state longer than 1 frame were filtered out by tracking with a radius of 58.5 nm (0.5 pixels). PSD_{FingR} clusters were identified using DBScan²⁷ executed in MATLAB. PSD_{FingR} clusters with a density >1200 molecules per μm (epsilon 0.35 and >50 localizations) were used for further analysis and the PSD border was defined using the alpha shape. The distance of individual localizations to the nearest PSD border (up to 1 μm distance) were computed and plotted as a frequency distribution. Rings were calculated as a fraction of the PSD border polyshape (is 1) defined by DBScan with two rings inside the PSD: 0–0.5 and 0.5–1 and six rings outside the PSD, with three rings approximating the perisynaptic zone: 1–1.5, 1.5–2 and 2–2.5 and three rings defining the extrasynaptic region: 2.5–3, 3–3.5 and 3.5–4. Per ring, the number of mGluR5 localizations was determined and the fraction of mGluR5 localizations per ring was calculated. To correct for the different sizes of ring 1 to 8, we further calculated the fraction of the area covered by each ring. The fraction of mGluR5 localizations was divided by the fraction of ring area, and normalized to 1. Then we also assessed the existence of mGluR5 clusters using DBScan and a density of >480 molecules per μm (epsilon 0.35 and >20 localizations). The border-to-centroid distance from PSD to mGluR5 cluster was calculated and plotted as a frequency distribution. To detect clusters in spines using SR-Tesseler we set the criteria to >20 localizations and area >400 nm² (localization precision is 20 nm) and used a density factor of 2. To detect all objects in spines and dendrites we only applied a density factor of 2 and removed all other thresholds.

Single-molecule tracking analysis

Using MATLAB, molecules with a localization precision < 50 nm were selected for analysis and background localizations were removed by outlining the neuron based on the obtained SEP-mGluR5 widefield image. Tracking was achieved using custom algorithms in MATLAB described previously⁸⁸. For tracks consisting of ≥ 4 frames the instantaneous diffusion coefficient was estimated. The first three points of the MSD with the addition of the value 0 at MSD(0) were used to fit the slope using a linear fit. Tracks with a negative slope were not used for further analysis. The diffusion coefficient was estimated based on the fit using:

$$\text{MSD} = 4D\Delta t \quad (1)$$

Only tracks of at least 30 frames were selected for further analysis. Tracks were classified as immobile when the ratio between the radius of gyration and mean step size was smaller than 2.11⁹¹. This ratio was calculated using:

$$\text{ratio} = \frac{\sqrt{\pi/2} \cdot \text{radius of gyration}}{\text{mean stepsize}} \quad (2)$$

The PSD mask was created based on the maximum intensity projection of Homer1c-mCherry. Peaks in intensity were detected after which a FWHM-like boundary was defined for each PSD. An expanded PSD mask of 200 nm around the PSD mask was created to define the perisynaptic zone. Tracks were assigned to the synaptic group if $\geq 80\%$ of the localizations of the track overlapped with the PSD. Perisynaptic tracks had to overlap $\geq 60\%$ with the perisynaptic zone and $< 80\%$ with the PSD, and transient perisynaptic tracks overlapped $> 0\%$ and $< 60\%$ with the perisynaptic zone. Entries and exits per perisynaptic trajectory were derived based on their overlap with the PSD mask. The perisynaptic tracks were categorized into three groups: captured, returned or escaped. The ‘captured’ tracks were the tracks that started within the (peri)synaptic region or entered this region but never left. The ‘returned’ tracks were at least once outside the (peri)synaptic region over the course of the track but ended up within the (peri)synaptic region. Lastly the ‘escaped’ group contains the tracks that crossed the perisynaptic region, but ended outside.

Transient confinement analysis on mobile trajectories was done in MATLAB using slightly modified scripts from a previously published MATLAB implementation⁸⁹ based on the algorithm reported by^{33,90}. Briefly, transient confinement was detected in a trajectory based on the probability (ψ) of a molecule staying within a region of radius (R) for a period of time (t):

$$\log(\psi) = 0.2048 - 2.5117Dt/R^2 \quad (3)$$

where D is the maximum of the instantaneous diffusion coefficients estimated for each sub-trajectory of $\Delta 10$. This probability was translated into a confinement index L , the larger the value of L , the greater the probability that the observed part of the trajectory is not of Brownian origin. The regions where the confinement index is above the critical L for critical time T_c are identified as confinement zones. Parameters used in the analysis are: $L_c = 4$, $S_m = 15$, $\alpha = 0.5$, $T_c = 0.2$ s (10 frames). The confinement zones are further analyzed for size and duration of confinement and diffusion coefficient in and outside confinement zones.

Confinement maps were created based on the detected confinement radius for each confinement zone. Each confinement zone was stored as a 2D Gaussian with the radius as FWHM. The final matrix was plotted with a color code, where higher values indicate confinement hotspots because there are multiple Gaussians on top of each other. For the immobile tracks the center of the track coordinates was determined and a 2D Gaussian with a fixed FWHM of 75 nm was plotted. The distance between a confinement zone and a PSD was defined as the shortest distance between the center of a confinement zone or immobile track to the nearest PSD border.

mGluR5-FRB to FKBP-Homer recruitment analysis

The maximum intensity projections were corrected for XY drift over time using the ImageJ plugin ‘‘StackReg.’’ We quantified the SEP-mGluR5-FRB recruitment to 2xFKBP-Homer1c-mCherry over a time-period of 40 min, after a 10-min baseline period. The Homer1c timelapses were used to select ROIs using ImageJ. First, image noise was reduced by applying a gaussian blur with $\sigma = 1$ and background subtraction with a rolling ball of 50. Subsequently, the time-lapse images were subjected to thresholding based on the $t = -10$ min image to isolate all PSDs. Then, a mask followed by a selection of all PSDs was created for each timepoint and saved as ROIs. The raw time-lapse images of Homer1c and mGluR5 were used to measure the signal intensity within the ROIs at

the different time points. To obtain the change in relative fluorescence intensity ($\Delta F/F_0$) over time, the intensity relative to $t = -10$ min was calculated and for visualization all values were subtracted by 1. The increase in mGluR5 intensity upon rapalog application, measured within PSDs marked by Homer1c, was best explained by a one-phase association function, fitted using Graphpad Prism.

Ca²⁺ imaging analysis

To analyze the Ca²⁺ imaging data, a circular ROI was drawn around every spine within the field of view, clearly separated from the dendritic base and in focus, regardless of activity levels. Using ImageJ software, the mean intensity value within each ROI was measured for all 1000 frames (50 ms streams). Then, this data was analyzed using custom MATLAB scripts based on⁴⁶. Peaks of miniature spontaneous Ca²⁺ transients (mSCTs) were detected and measured if the 2-point slope was greater than $meanslope + 2 \times STDslope$, and amplitude greater than $0.035 \Delta F/F_0$. Using these and several other criteria described in more detail in Reese and Kavalali (2015), peaks were consistently detected, disregarding background noise or single high point artifacts. Then for each spine the mSCT frequency and for each peak the mSCT amplitude ($\Delta F/F_0$) was calculated. To measure average decay times, all $\Delta F/F_0$ values of detected peaks were loaded into Clampfit 10.3 (Molecular Devices) and average mSCT traces were made for each neuron by aligning all peaks before and all peak after rapalog application. Next, a single-exponential fit line was obtained from the decay phase of the average mSCT traces. The single-exponential fit lines were plotted in Graphpad Prism and the decay times (tau), the time in seconds required to decay to $(1/e)\Delta F$, were calculated. For measurements of mSCT frequency, tau, and amplitude spines with at least one mSCT were included and data is presented as the mean mSCT frequency (Hz) per neuron, mean mSCT tau (s) per neuron, and mean mSCT amplitude ($\Delta F/F_0$) per neuron, respectively. While in the frequency analysis correcting for the variability in the number of ROIs (spines) in the field of view, all spines (also without activity) were included and data are presented as the mean mSCT frequency (Hz) per spine. To test the statistical significance of the change in decay times and amplitude upon rapalog application, only neurons that had at least one mSCT both before and after rapalog application could be used.

Statistical analysis

All statistical tests used and significance in this study are described in the main text and figure legends. In the figures, * indicates significance based on the condition effect and when comparing more than two groups, * indicates significance based on the multiple comparison test. In all figures * was used to indicate a P value < 0.05 , ** for $p < 0.01$, and *** for $p < 0.001$. If normally distributed, data are represented as mean \pm SEM. Non-normal data are represented as median with 95% confidence interval (CI), with the [lower upper] limits of the 95% CI mentioned in the main text. Each experiment was replicated in cultures from at least three independent preparations of hippocampal neurons. The n indicated in the figure legends are the number of neurons used for analysis, unless stated otherwise. Statistical analysis and graphs were prepared in GraphPad Prism and figures were generated in Adobe Illustrator CC.

Reporting summary

Further information on research design is available in the Nature Portfolio Reporting Summary linked to this article.

Data availability

The data that support the findings of this study are available from the authors upon request. Source data are provided with this paper.

Code availability

The MATLAB code used in this study are based on previously published MATLAB algorithms as referenced accordingly. The custom MATLAB scripts are available from the authors upon request.

Acknowledgments

We would like to thank all members of the MacGillavry lab and Eline Penners for helpful discussions and Arthur de Jong, Yolanda Gutierrez and Lisa A.E. Catsburg for critical reading of the manuscript. This work was supported by the Netherlands Organization for Scientific Research (the Graduate Program of Quantitative Biology and Computational Life Sciences) to N.S. and the European Research Council (ERC-StG 716011) to H.D.M.

Author contributions

Conceptualization, methodology, N.S. and H.D.M.; validation & formal analysis, N.S. and M.W.; investigation, N.S.; resources, H.D.M.; writing – original draft, N.S.; writing – review, H.D.M. and M.W.; visualization, N.S.; supervision, H.D.M.; funding acquisition, H.D.M. and N.S.

Competing interests

The authors declare no competing interests.

References

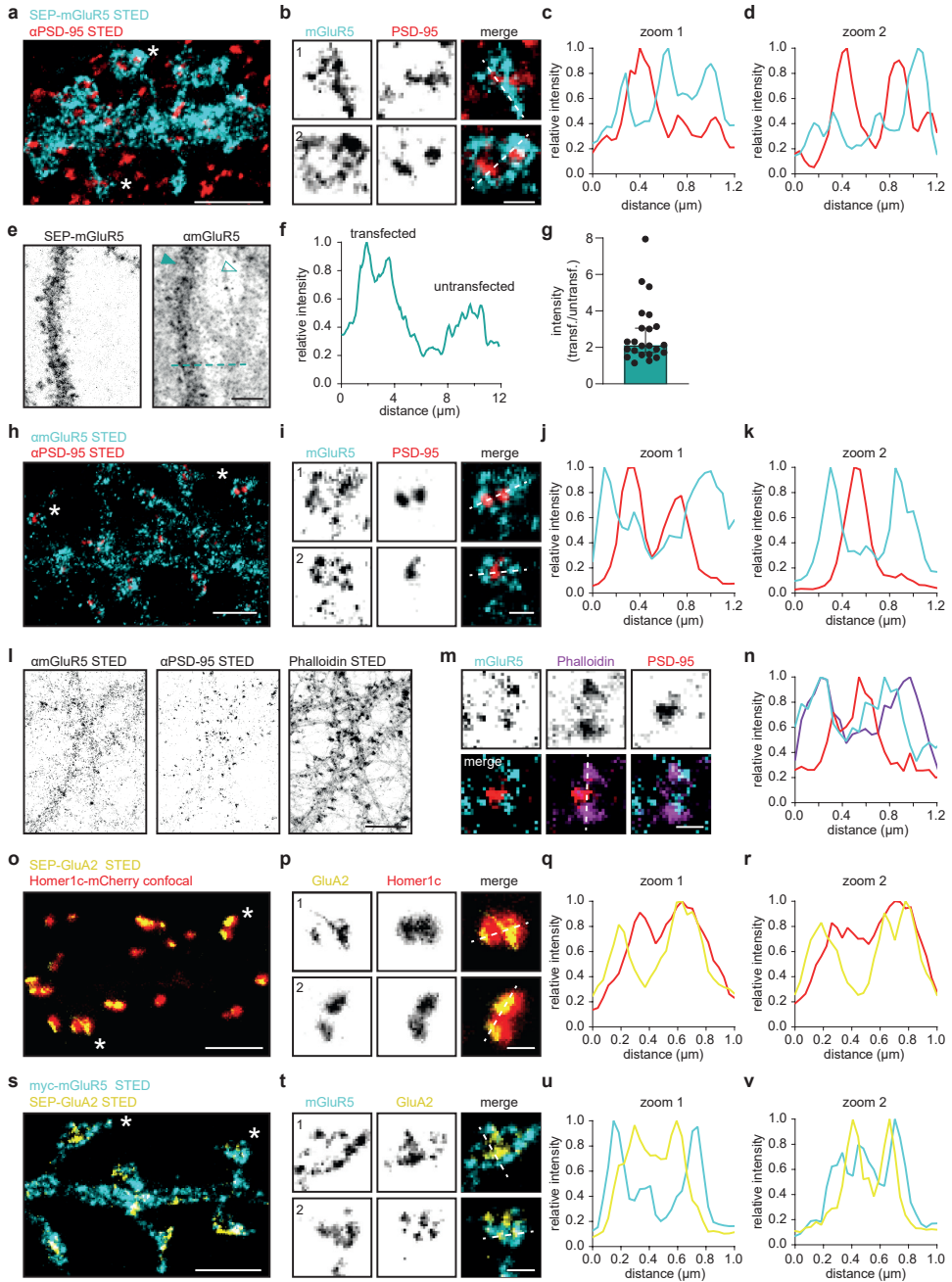
- Reiner A, Levitz J. Review Glutamatergic Signaling in the Central Nervous System : Ionotropic and Metabotropic Receptors in Concert. *Neuron* **98**, 1080-1098 (2018).
- Scheefhals N, MacGillavry HD. Functional organization of postsynaptic glutamate receptors. *Mol Cell Neurosci* **91**, 82-94 (2018).
- Bodzeta A, Scheefhals N, MacGillavry HD. Membrane trafficking and positioning of mGluRs at presynaptic and postsynaptic sites of excitatory synapses. *Neuropharmacology* **200**, 108799 (2021).
- Lüscher C, Huber KM. Group 1 mGluR-Dependent Synaptic Long-Term Depression: Mechanisms and Implications for Circuitry and Disease. *Neuron* **65**, 445-459 (2010).
- MacGillavry H, Song Y, Raghavachari S, Blanpied T. Nanoscale scaffolding domains within the postsynaptic density concentrate synaptic ampa receptors. *Neuron* **78**, 615-622 (2013).
- Nair D, *et al.* Super-resolution imaging reveals that AMPA receptors inside synapses are dynamically organized in nanodomains regulated by PSD95. *J. Neurosci* **33**, 13204-13224 (2013).
- Biederer T, Kaeser PS, Blanpied TA. Transcellular Nanoalignment of Synaptic Function. *Neuron* **96**, 680-696 (2017).
- Kellermayer B, *et al.* Differential Nanoscale Topography and Functional Role of GluN2-NMDA Receptor Subtypes at Glutamatergic Synapses. *Neuron* **100**, 106-119.e107 (2018).
- Willems J, *et al.* Orange: A CRISPR/Cas9-based genome editing toolbox for epitope tagging of endogenous proteins in neurons. *PLoS Biology* **18**, 1-41 (2020).
- Tang AH, Chen H, Li TP, Metzbowser SR, MacGillavry HD, Blanpied TA. A trans-synaptic nanocolumn aligns neurotransmitter release to receptors. *Nature* **536**, 210-214 (2016).
- Baude A, Nusser Z, Roberts JDB, Mulvihill E, McIlhinney RAJ, Somogyi P. The metabotropic glutamate receptor (mGluR1) is concentrated at perisynaptic membrane of neuronal subpopulations as detected by immunogold reaction. *Neuron* **11**, 771-787 (1993).
- Lujan R, Nusser Z, Roberts JD, Shigemoto R, Somogyi P. Perisynaptic location of metabotropic glutamate receptors mGluR1 and mGluR5 on dendrites and dendritic spines in the rat hippocampus. *Eur J Neurosci* **8**, 1488-1500 (1996).
- Nusser Z. Subsynaptic segregation of metabotropic and ionotropic glutamate receptors as revealed by immunogold localization. *Neuroscience* **61**, 421-427 (1994).
- Niswender CM, Conn PJ. Metabotropic glutamate receptors: physiology, pharmacology, and disease. *Annu Rev Pharmacol Toxicol* **50**, 295-322 (2010).
- Traynelis SF, *et al.* Glutamate receptor ion channels: structure, regulation, and function. *Pharmacol Rev* **62**, 405-496 (2010).
- Paoletti P, Bellone C, Zhou Q. NMDA receptor subunit diversity: impact on receptor properties, synaptic plasticity and disease. *Nat Rev Neurosci* **14**, 383-400 (2013).
- Greget R, *et al.* Simulation of postsynaptic glutamate receptors reveals critical features of glutamatergic transmission. *PLoS ONE* **6**, e28380 (2011).
- Marcaggi P, Mutoh H, Dimitrov D, Beato M, Knöpfel T. Optical measurement of mGluR1 conformational changes reveals fast activation, slow deactivation, and sensitization. *Proc Natl Acad Sci U S A* **106**, 11388-11393 (2009).
- Bodzeta A, Berger F, MacGillavry HD. Subsynaptic mobility of presynaptic mGluR types is differentially regulated by intra- and extracellular interactions. *Mol Biol Cell* **33**, ar66 (2022).
- Triller A, Choquet D. Surface trafficking of receptors between synaptic and extrasynaptic membranes: and yet they do move! *Trends Neurosci* **28**, 133-139 (2005).
- Choquet D, Triller A. The dynamic synapse. *Neuron* **80**, 691-703 (2013).
- Shrivastava AN, *et al.* beta-amyloid and ATP-induced diffusional trapping of astrocyte and neuronal metabotropic glutamate type-5 receptors. *Glia* **61**, 1673-1686 (2013).
- Renner M, *et al.* Deleterious Effects of Amyloid β Oligomers Acting as an Extracellular Scaffold for mGluR5. *Neuron* **66**, 739-754 (2010).
- Aloisi E, *et al.* Altered surface mGluR5 dynamics provoke synaptic NMDAR dysfunction and cognitive defects in Fmr1 knockout mice. *Nat Commun* **8**, 1103 (2017).
- Frost Na, Shroff H, Kong H, Betzig E, Blanpied Ta. Single-molecule discrimination of discrete perisynaptic and distributed sites of actin filament assembly within dendritic spines. *Neuron* **67**, 86-99 (2010).
- Gross GG, *et al.* Recombinant probes for visualizing endogenous synaptic proteins in living neurons. *Neuron* **78**, 971-985 (2013).
- Ester M, Krieger H-P, Sander J, Xu X. A density-based algorithm for discovering clusters in large spatial databases with noise. In: *Proceedings of the Second International Conference on Knowledge Discovery and Data Mining*. Portland, Oregon. AAAI Press (1996).
- Catsburg LA, Westra M, van Schaik AM, MacGillavry HD. Dynamics and nanoscale organization of the postsynaptic endocytic zone at excitatory synapses. *Elife* **11**, e74387 (2022).
- Levet F, *et al.* SR-Tesseler: a method to segment and quantify localization-based super-resolution microscopy data. *Nat Methods* **12**, 1065-1071 (2015).
- Giannone G, *et al.* Dynamic superresolution imaging of endogenous proteins on living cells at ultra-high density. *Biophys J* **99**, 1303-1310 (2010).
- Golan Y, Sherman E. Resolving mixed mechanisms of protein subdiffusion at the T cell plasma membrane. *Nat Commun* **8**, 15851 (2017).
- Saxton MJ. Lateral diffusion in an archipelago. Single-particle diffusion. *Biophys J* **64**, 1766-1780 (1993).
- Simson R, Sheets ED, Jacobson K. Detection of temporary lateral confinement of membrane proteins using single-particle tracking analysis. *Biophys J* **69**, 989-993 (1995).
- Westra M, MacGillavry HD. Precise Detection and Visualization of Nanoscale Temporal Confinement in Single-Molecule Tracking Analysis. *Membranes (Basel)* **12**, 650 (2022).
- Enz R. Structure of metabotropic glutamate receptor C-terminal domains in contact with interacting proteins. *Front Mol Neurosci* **5**, 52 (2012).
- Chang K, Roche KW. Neuropharmacology Structural and molecular determinants regulating mGluR5 surface expression. *Neuropharmacology* **115**, 10-19 (2017).
- Schnell E, Sizemore M, Karimzadegan S, Chen L, Bredt DS, Nicoll RA. Direct interactions between PSD-95 and stargazin control synaptic AMPA receptor number. *Proc Natl Acad Sci U S A* **99**, 13902-13907 (2002).
- Bats C, Groc L, Choquet D. The interaction between Stargazin and PSD-95 regulates AMPA receptor surface trafficking. *Neuron* **53**, 719-734 (2007).
- Hafner AS, *et al.* Lengthening of the stargazin cytoplasmic tail increases synaptic transmission by promoting interaction to deeper domains of PSD-95. *Neuron* **86**, 475-489 (2015).

40. Clackson T, et al. Redesigning an FKBP-ligand interface to generate chemical dimers with novel specificity. *Proc Natl Acad Sci U S A* **95**, 10437-10442 (1998).
41. Kato HK, Kassai H, Watabe AM, Aiba A, Manabe T. Functional coupling of the metabotropic glutamate receptor, InsP3 receptor and L-type Ca2+ channel in mouse CA1 pyramidal cells. *J Physiol* **590**, 3019-3034 (2012).
42. Skeberdis VA, Lan J, Opitz T, Zheng X, Bennett MV, Zukin RS. mGluR1-mediated potentiation of NMDA receptors involves a rise in intracellular calcium and activation of protein kinase C. *Neuropharmacology* **40**, 856-865 (2001).
43. Topolnik L, Azzi M, Morin F, Kougioumoutzakis A, Lacaille JC. mGluR1/5 subtype-specific calcium signalling and induction of long-term potentiation in rat hippocampal oriens/alveus interneurons. *J Physiol* **575**, 115-131 (2006).
44. Gerber U, Gee CE, Benquet P. Metabotropic glutamate receptors: intracellular signaling pathways. *Curr Opin Pharmacol* **7**, 56-61 (2007).
45. Chen T-W, et al. Ultrasensitive fluorescent proteins for imaging neuronal activity. *Nature* **499**, 295-300 (2013).
46. Reese AL, Kavalali ET. Spontaneous neurotransmission signals through store-driven Ca(2+) transients to maintain synaptic homeostasis. *Elife* **4**, 1-15 (2015).
47. Metzbower SR, Joo Y, Benavides DR, Blanpied TA. Properties of Individual Hippocampal Synapses Influencing NMDA-Receptor Activation by Spontaneous Neurotransmission. *eNeuro* **6**, 590141 (2019).
48. Goncalves J, et al. Nanoscale co-organization and coactivation of AMPAR, NMDAR, and mGluR at excitatory synapses. *Proc Natl Acad Sci U S A* **117**, 14503-14511 (2020).
49. Renner ML, Cognet L, Lounis B, Triller A, Choquet D. The excitatory postsynaptic density is a size exclusion diffusion environment. *Neuropharmacology* **56**, 30-36 (2009).
50. Li TP, Song Y, MacGillavry HD, Blanpied TA, Raghavachari S. Protein Crowding within the Postsynaptic Density Can Impede the Escape of Membrane Proteins. *J Neurosci* **36**, 4276-4295 (2016).
51. Stowell JN, Craig aM. Axon/dendrite targeting of metabotropic glutamate receptors by their cytoplasmic carboxy-terminal domains. *Neuron* **22**, 525-536 (1999).
52. De Blasi A, Conn PJ, Pin J, Nicoletti F. Molecular determinants of metabotropic glutamate receptor signaling. *Trends Pharmacol Sci* **22**, 114-120 (2001).
53. Das SS, Banker GA. The role of protein interaction motifs in regulating the polarity and clustering of the metabotropic glutamate receptor mGluR1a. *J Neurosci* **26**, 8115-8125 (2006).
54. Tu JC, et al. Coupling of mGluR/Homer and PSD-95 complexes by the Shank family of postsynaptic density proteins. *Neuron* **23**, 583-592 (1999).
55. Ciruela F, Soloviev MM, Chan WY, McIlhinney RA. Homer-1c/Vesl-1L modulates the cell surface targeting of metabotropic glutamate receptor type 1alpha: evidence for an anchoring function. *Mol Cell Neurosci* **15**, 36-50 (2000).
56. Kammermeier PJ. Surface clustering of metabotropic glutamate receptor 1 induced by long Homer proteins. *BMC neuroscience* **7**, 1 (2006).
57. Sergé A, Fourgeaud L, Hémar A, Choquet D. Receptor activation and homer differentially control the lateral mobility of metabotropic glutamate receptor 5 in the neuronal membrane. *J Neurosci* **22**, 3910-3920 (2002).
58. Tadokoro S, Tachibana T, Imanaka T, Nishida W, Sobue K. Involvement of unique leucine-zipper motif of PSD-Zip45 (Homer 1c/vesl-1L) in group 1 metabotropic glutamate receptor clustering. *Proc Natl Acad Sci U S A* **96**, 13801-13806 (1999).
59. Tao-Cheng JH, Thein S, Yang Y, Reese TS, Gallant PE. Homer is concentrated at the postsynaptic density and does not redistribute after acute synaptic stimulation. *Neuroscience* **266**, 80-90 (2014).
60. Westra M, Gutierrez Y, MacGillavry HD. Contribution of Membrane Lipids to Postsynaptic Protein Organization. *Front Synaptic Neurosci* **13**, 790773 (2021).
61. Dunn HA, Orlandi C, Martemyanov KA. Beyond the Ligand: Extracellular and Transcellular G Protein-Coupled Receptor Complexes in Physiology and Pharmacology. *Pharmacol Rev* **71**, 503-519 (2019).
62. Shi S-H, Hayashi Y, Esteban JA, Malinow R. Subunit-Specific Rules Governing AMPA Receptor Trafficking to Synapses in Hippocampal Pyramidal Neurons. *Cell* **105**, 331-343 (2001).
63. Anggono V, Haganir RL. Regulation of AMPA receptor trafficking and synaptic plasticity. *Curr Opin Neurobiol* **22**, 461-469 (2012).
64. Shepherd JD, Haganir RL. The cell biology of synaptic plasticity: AMPA receptor trafficking. *Annu Rev Cell Dev Biol* **23**, 613-643 (2007).
65. Diaz-Alonso J, Sun YJ, Granger AJ, Levy JM, Blankenship SM, Nicoll RA. Subunit-specific role for the amino-terminal domain of AMPA receptors in synaptic targeting. *Proc Natl Acad Sci U S A* **114**, 7136-7141 (2017).
66. Watson JF, Ho H, Greger IH. Synaptic transmission and plasticity require AMPA receptor anchoring via its N-terminal domain. *Elife* **6**, 1-20 (2017).
67. Watson JF, Pinggera A, Ho H, Greger IH. AMPA receptor anchoring at CA1 synapses is determined by N-terminal domain and TARPs $\gamma 8$ interactions. *Nat Commun* **12**, 5083 (2021).
68. Kusumi A, et al. Dynamic organizing principles of the plasma membrane that regulate signal transduction: commemorating the fortieth anniversary of Singer and Nicolson's fluid-mosaic model. *Annu Rev Cell Dev Biol* **28**, 215-250 (2012).
69. Kasai RS, Kusumi A. Single-molecule imaging revealed dynamic GPCR dimerization. *Curr Opin Cell Biol* **27**, 78-86 (2014).
70. Tanaka J, et al. Gq protein alpha subunits Galphaq and Galpha11 are localized at postsynaptic extra-junctional membrane of cerebellar Purkinje cells and hippocampal pyramidal cells. *Eur J Neurosci* **12**, 781-792 (2000).
71. Nakamura M, et al. Signaling complex formation of phospholipase Cbeta4 with metabotropic glutamate receptor type 1alpha and 1,4,5-trisphosphate receptor at the perisynapse and endoplasmic reticulum in the mouse brain. *Eur J Neurosci* **20**, 2929-2944 (2004).
72. Katona I, et al. Molecular composition of the endocannabinoid system at glutamatergic synapses. *J Neurosci* **26**, 5628-5637 (2006).
73. Olmo IG, Ferreira-Vieira TH, Ribeiro FM. Dissecting the Signaling Pathways Involved in the Crosstalk between Metabotropic Glutamate 5 and Cannabinoid Type 1 Receptors. *Mol Pharmacol* **90**, 609-619 (2016).
74. Westin L, Reuss M, Lindskog M, Aperia A, Brismar H. Nanoscopic spine localization of Norbin, an mGluR5 accessory protein. *BMC neuroscience* **15**, 45 (2014).
75. Blanpied Ta, Scott DB, Ehlers MD. Dynamics and regulation of clathrin coats at specialized endocytic zones of dendrites and spines. *Neuron* **36**, 435-449 (2002).
76. Lu J, et al. Postsynaptic Positioning of Endocytic Zones and AMPA Receptor Cycling by Physical Coupling of Dynamin-3 to Homer. *Neuron* **55**, 874-889 (2007).
77. Petrini EM, Lu J, Cognet L, Lounis B, Ehlers MD, Choquet D. Endocytic Trafficking and Recycling Maintain a Pool of Mobile Surface AMPA Receptors Required for Synaptic Potentiation. *Neuron* **63**, 92-105 (2009).

78. Scheefhals N, Catsburg LAE, Westerveld ML, Blanpied TA, Hoogenraad CC, MacGillavry HD. Shank Proteins Couple the Endocytic Zone to the Postsynaptic Density to Control Trafficking and Signaling of Metabotropic Glutamate Receptor 5. *Cell Rep* **29**, 258-269 e258 (2019).
79. Moutin E, et al. Restoring glutamate receptors dynamics at synapses rescues autism-like deficits in Shank3-deficient mice. *Mol Psychiatry* **26**, 7596-7609 (2021).
80. Moutin E, et al. Dynamic remodeling of scaffold interactions in dendritic spines controls synaptic excitability. *J Cell Biol* **198**, 251-263 (2012).
81. Hanson JE, Smith Y. Group I metabotropic glutamate receptors at GABAergic synapses in monkeys. *J Neurosci* **19**, 6488-6496 (1999).
82. Mansouri M, et al. Distinct subsynaptic localization of type I metabotropic glutamate receptors at glutamatergic and GABAergic synapses in the rodent cerebellar cortex. *Eur J Neurosci* **41**, 157-167 (2015).
83. Bertaso F, Roussignol G, Worley P, Bockaert J, Fagni L, Ango F. Homer1c-dependent crosstalk between NMDA and metabotropic glutamate receptors in mouse neurons. *PLoS One* **5**, e9755 (2010).
84. Kapitein LC, Yau KW, Hoogenraad CC. Microtubule dynamics in dendritic spines. *Methods Cell Biol* **97**, 111-132 (2010).
85. Kapitein LC, et al. Mixed microtubules steer dynein-driven cargo transport into dendrites. *Curr Biol* **20**, 290-299 (2010).
86. Sinnen BL, Bowen AB, Forte JS, Gibson ES, Acqua MLD, Kennedy MJ. Optogenetic Control of Synaptic Composition and Article Optogenetic Control of Synaptic Composition and Function. *Neuron* **93**, 646-660.e645 (2017).
87. ChazEAU A, Katrukha EA, Hoogenraad CC, Kapitein LC. Studying neuronal microtubule organization and microtubule-associated proteins using single molecule localization microscopy. *Methods Cell Biol* **131**, 127-149 (2016).
88. Lu HE, MacGillavry HD, Frost NA, Blanpied TA. Multiple spatial and kinetic subpopulations of CaMKII in spines and dendrites as resolved by single-molecule tracking PALM. *J Neurosci* **34**, 7600-7610 (2014).
89. Menchon SA, Martin MG, Dotti CG. APM_GUI: analyzing particle movement on the cell membrane and determining confinement. *BMC Biophys* **5**, 4 (2012).
90. Meilhac N, Le Guyader L, Salome L, Destainville N. Detection of confinement and jumps in single-molecule membrane trajectories. *Phys Rev E Stat Nonlin Soft Matter Phys* **73**, 011915 (2006).

Figure S1. mGluR5 is largely excluded from the synapse

a Representative two-color gSTED image of dendrite with SEP-mGluR5 expression, with anti-GFP staining (cyan; Atto647N) to label surface-expressed receptors and co-stained for anti-PSD-95 (red; Alexa594). Scale bar, 2 μ m. **b** Zooms of dendritic spines indicated in **a** with asterisks. Scale bar, 500 nm. **c** Line profile of spine 1 and **d** spine 2, indicated with dotted line in **b**. **e** Representative confocal images of total mGluR5 levels in SEP-mGluR5 transfected and untransfected neurons (anti-mGluR5 Millipore Alexa594). Scale bar, 5 μ m. **f** Line profile of anti-mGluR5 in a SEP-mGluR5 transfected dendrite (filled arrowhead) and an untransfected dendrite (open arrowhead), indicated with dotted line in **e**. **g** Quantification of the ratio of mGluR5 intensity in transfected over untransfected neurons ($n = 23$). Data is represented as median with 95% CI. **h** Representative two-color gSTED image of dendrite endogenously stained for total mGluR5 (cyan; anti-mGluR5 Millipore Atto647N) and PSD-95 (red; Alexa594). Scale bar, 2 μ m. **i** Zooms of dendritic spines indicated in **h** with asterisks. Scale bar, 500 nm. **j** Line profile of spine 1 and **k** spine 2, indicated with dotted line in **i**. **l** Representative three-color gSTED image of dendrite endogenously stained for total mGluR5 (cyan; anti-mGluR5 Alomone Atto647N), Phalloidin (magenta; Alexa594) and PSD-95 (red; Alexa488). Scale bar, 10 μ m. **m** Zoom of dendritic spine stained for mGluR5 (cyan), Phalloidin (magenta) and PSD-95 (red). Scale bar, 500 nm. **n** Line profile of spine, indicated with dotted line in **m**. **o** Representative gSTED image of dendrite expressing SEP-GluA2, additionally labeled with anti-GFP nanobody Atto647N to visualize surface-expressed receptors (yellow), and Homer1c-mCherry (red; confocal). Scale bar, 2 μ m. **p** Zooms of dendritic spines indicated in **o** with asterisks. Scale bar, 500 nm. **q** Line profile of spine 1 and **r** spine 2, indicated with dotted line in **p**. **s** Representative two-color gSTED image of dendrite expressing myc-mGluR5 (cyan; anti-myc Alexa594 surface labeling) and SEP-GluA2 (yellow, anti-GFP Atto647N surface labeling). Scale bar, 2 μ m. **t** Zooms of dendritic spines indicated in **s** with asterisks. Scale bar, 500 nm. **u** Line profile of spine 1 and **v** spine 2, indicated with dotted line in **t**. All experiments in this figure were replicated in cultures from at least 2 independent preparations of hippocampal neurons. Source data are provided as a Source Data file.



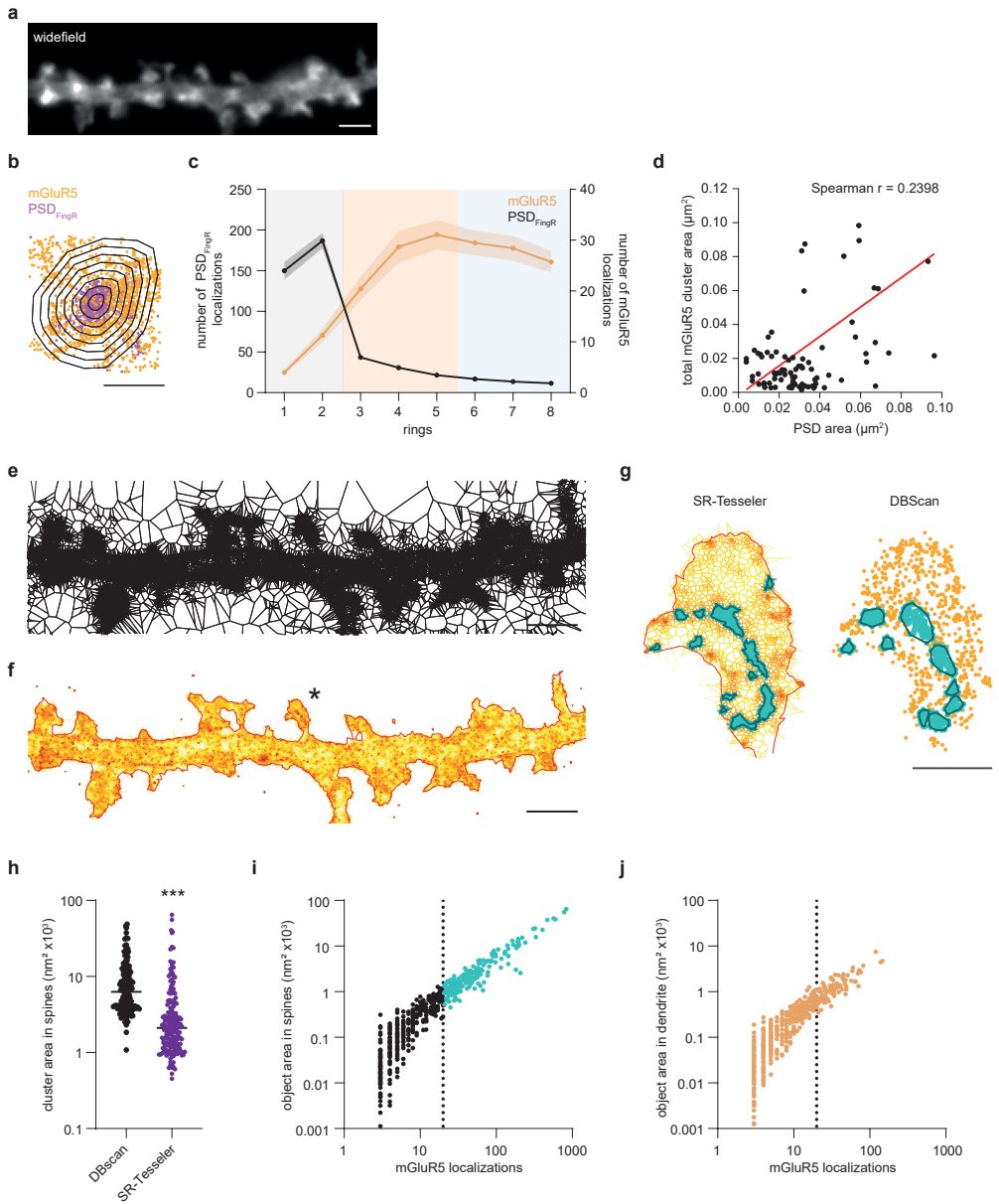


Figure S2. mGluR5 is enriched in distinct perisynaptic nanodomains

a Widefield of dendrite expressing SEP-mGluR5 and PSD_{FingR}-mEos3.2 (green channel). Scale bar, 2 μm . **b** The rings from *Fig. 2e* with the corresponding localizations of mGluR5 (orange) and PSD_{FingR} (cyan). Scale bar, 500 nm. **c** Absolute number of PSD_{FingR} (black; plotted on left y-axis) and mGluR5 (orange; plotted on right y-axis) localizations in rings 1 to 8. Data are represented as means \pm SEM. **d** Correlation between total mGluR5 cluster area and PSD area (in μm^2) (Correlation Spearman $r = 0.24$, $p = 0.03$). **e** Voronoi based segmentation performed with SR-Tesseler of the same dendrite shown in *Fig. 2a*. Scale bar, 2 μm . **f** Local density map created from the Voronoi diagrams, the red line represents the neuron outline. Scale bar, 2 μm . **g** Zooms of the dendritic spine indicated in **f** with an asterisk, showing the Voronoi polygons with detected clusters (cyan) using SR-Tesseler (left) and mGluR5 localizations belonging to clusters (cyan) detected using DBScan (right). Scale bar, 500 nm. **h** Quantification of median mGluR5 cluster area in spines as determined by DBScan and SR-Tesseler, shown in log 10 scale ($n = 18$ spines, $p < 0.0001$, two-sided Mann-Whitney test). Data are represented as median with 95% CI. **i** mGluR5 object area plotted as a function of number of localizations in spines and **j** dendrites determined using SR-Tesseler, shown in log10 scale. The dotted line at 20 localizations indicates the cut-off of minimum number of localizations per cluster otherwise set as criteria in the DBScan and SR-Tesseler analysis, and the cyan scatters are included for analysis in **h**. Source data are provided as a Source Data file.

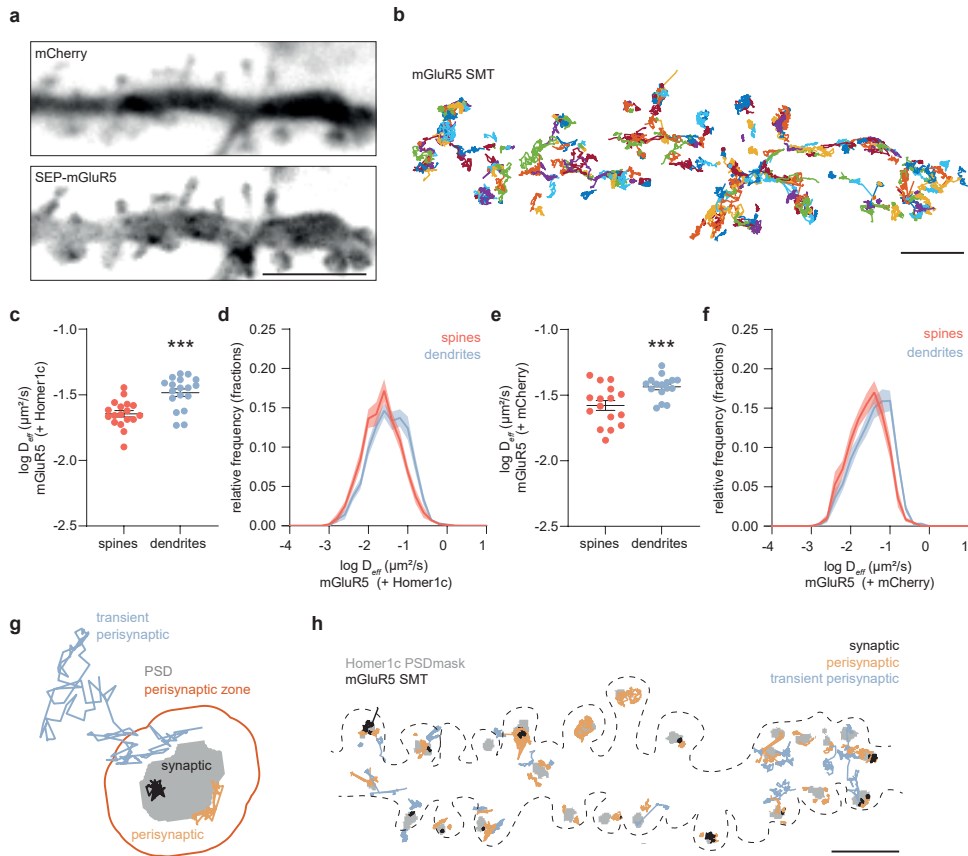


Figure S3. Single-molecule tracking resolves the subsynaptic dynamics of mGluR5

a Widefield of dendrite expressing mCherry and SEP-mGluR5. Scale bar, 5 μm . **b** SMTs of mGluR5 (random colors) in the same dendrite as shown in **a**. Scale bar, 2 μm . **c** Mean $\log D_{\text{eff}}$ per neuron ($p < 0.0001$, two-sided paired t test) and **d** relative frequency distributions of D_{eff} s of mGluR5 trajectories in spines and dendrites co-transfected with Homer1c-mCherry ($n = 18$). **e** Mean $\log D_{\text{eff}}$ per neuron ($p = 0.0006$, two-sided paired t test) and **f** relative frequency distributions of D_{eff} s of mGluR5 trajectories in spines and dendrites co-transfected with mCherry ($n = 16$). **g** mGluR5 trajectories are assigned to different categories based on the degree of colocalization with the PSD (gray) and perisynaptic zone (orange): synaptic trajectories (black; $\geq 80\%$ overlap with PSD), perisynaptic trajectories (orange; $\geq 60\%$ overlap with the perisynaptic zone and $< 80\%$ overlap with PSD) and transient perisynaptic trajectories (blue; $> 0\%$, but $< 60\%$ overlap with the perisynaptic zone). **h** Synaptic (black), perisynaptic (orange) and transient perisynaptic (blue) SMTs of mGluR5 relative to the Homer1c PSD mask (gray) in the dendrite shown in **Fig. 3a** and **b**. This dendrite is an example of the mGluR5 trajectories that are included for analysis, compared to the same dendritic stretch in **Fig. 3b** with all obtained trajectories shown. Scale bar, 5 μm . Data are represented as means \pm SEM. *** $p < 0.001$. Source data are provided as a Source Data file.

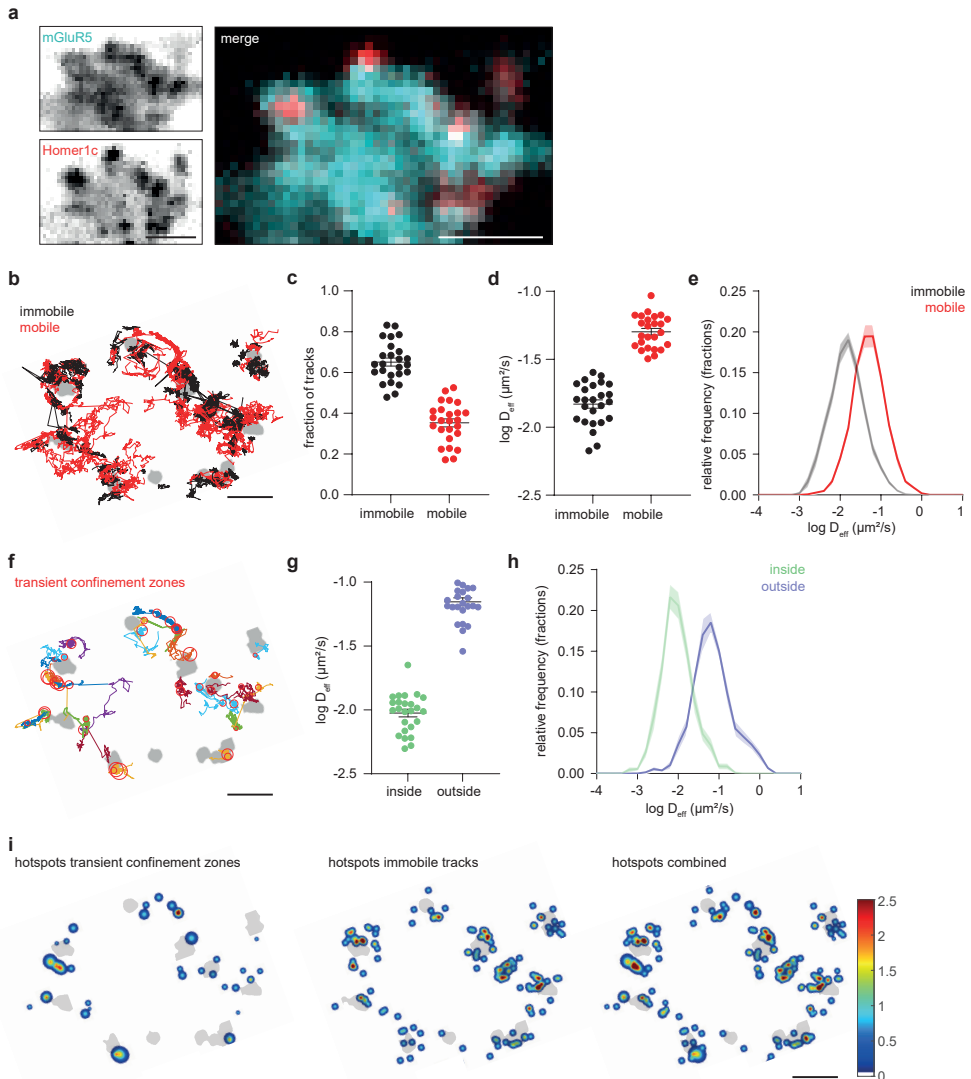


Figure S4. mGluR5 is not stably anchored, but dynamically exchanges at perisynaptic nanodomains

a Widefield image of a dendrite expressing SEP-mGluR5 (cyan) and Homer1c-mCherry (red). Scale bar, 2 μm . **b** The same dendrite, with SMTs color-coded for immobile (black) and mobile (red) mGluR5 relative to the Homer1c PSD mask. Scale bar, 1 μm . **c** Fraction of immobile and mobile mGluR5 trajectories ($n = 25$ neurons). **d** Mean $\log D_{\text{eff}}$ per neuron and **e** relative frequency distributions of D_{eff} of immobile and mobile mGluR5 trajectories ($n = 25$). **f** Transient confinement zones (red circles) of the mobile mGluR5 trajectories (random colors) shown in **b**. Scale bar, 1 μm . **g** Mean $\log D_{\text{eff}}$ per neuron and **h** relative frequency distributions of D_{eff} of mGluR5 trajectories inside (green) and outside (blue) confinement zones ($n = 25$). **i** Hotspots of transient confinement zones (left), immobile track centers (middle) and both images combined (right), color-coded for the frequency of confinement zones and/or immobile tracks. Scale bar, 1 μm . Data are represented as means \pm SEM. Source data are provided as a Source Data file.

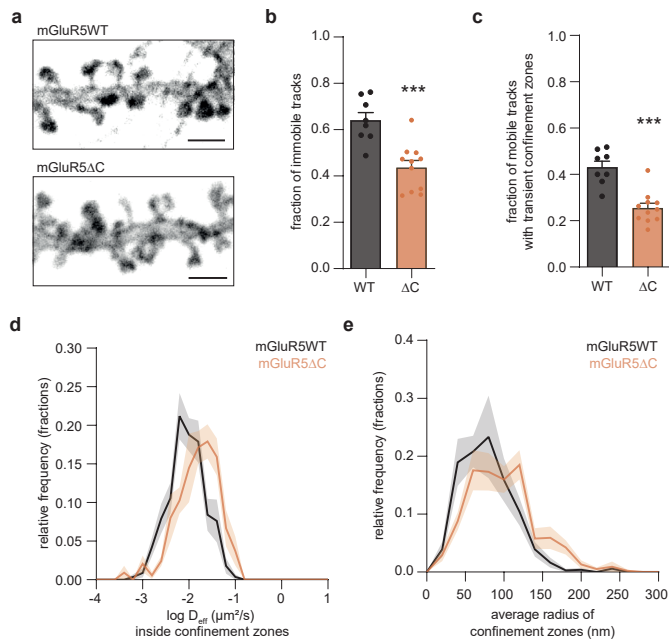
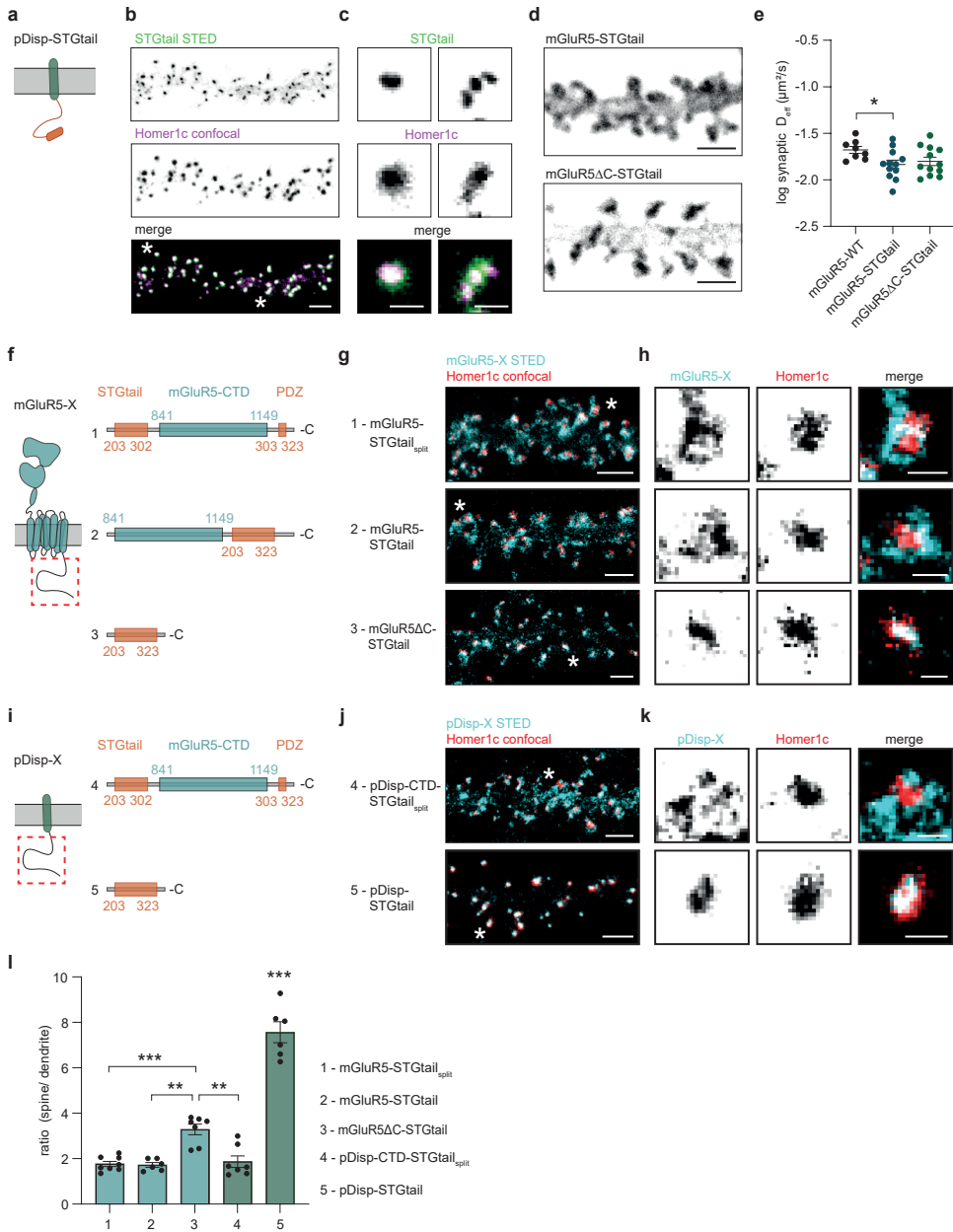


Figure S5. The C-terminal domain of mGluR5 regulates transient confinement

a Representative confocal images of dendrite with SEP-mGluR5WT (top) and SEP-mGluR5 Δ C (bottom) expression, surface-labeled with an anti-GFP nanobody Atto647N. Scale bar, 2 μ m. **b** Fraction of immobile trajectories of mGluR5WT ($n = 8$) and mGluR5 Δ C ($n = 11$; $p = 0.0004$, two-sided unpaired t test). **c** Fraction of mobile trajectories with transient confinement zones for mGluR5WT ($n = 8$) and mGluR5 Δ C ($n = 11$; $p < 0.0001$, two-sided unpaired t test). **d** Relative frequency distributions of D_{eff} of individual mGluR5WT and mGluR5 Δ C trajectories inside confinement zones. **e** Relative frequency plot of the average radius of confinement zones for mGluR5WT and mGluR5 Δ C trajectories. Data are represented as means \pm SEM. *** $p < 0.001$. Source data are provided as a Source Data file.

Figure S6. The mGluR5-Stargazin chimera is efficiently targeted to the PSD

a Schematic of pDisp-TM-STGtail. **b** Representative gSTED image of dendrite expressing SEP-TM-STGtail, additionally labeled with an anti-GFP nanobody Atto647N (green), and Homer1c-mCherry (magenta; confocal). Scale bar, 2 μ m. This experiment was replicated in cultures from more than 3 independent preparations of hippocampal neurons. **c** Zooms of spines indicated in **b** with asterisks. Scale bar, 500 nm. **d** Representative confocal images of dendrite with SEP-mGluR5-STGtail (top) and SEP-mGluR5 Δ C-STGtail (bottom) expression, surface-labeled with an anti-GFP nanobody Atto647N. Scale bar, 2 μ m. **e** Mean log D_{eff} per neuron of synaptic trajectories of mGluR5WT ($n = 8$), mGluR5-STGtail ($n = 12$) and mGluR5 Δ C-STGtail ($n = 12$; $p = 0.0705$, one-way ANOVA with Dunnett's multiple comparisons test: compared to WT $p = 0.0459$ for mGluR5-STGtail and $p = 0.1270$ for mGluR5 Δ C-STGtail). The mGluR5WT dataset shown **e** is also shown in Fig. 5g, as these figures show different aspects of the same experiment. **f** Schematic of mGluR5 with the CTD domain structure of three variants: 1 – mGluR5-STGtail_{split}, 2 – mGluR5-STGtail and 3 – mGluR5 Δ C-STGtail **g** Representative gSTED images of dendrite expressing mGluR5-X, additionally labeled with an anti-GFP nanobody Atto647N (cyan), and Homer1c-mCherry (red; confocal). Scale bar, 2 μ m. **h** Zooms of spines indicated in **g** with asterisks. Scale bar, 500 nm. **i** Schematic of pDisp with the CTD domain structure of two variants: 4 – pDisp-CTD-STGtail_{split} and 5 – pDisp-STGtail. **j** Representative gSTED images of dendrite expressing pDisp-X, additionally labeled with an



anti-GFP nanobody Atto647N (cyan), and Homer1c-mCherry (red; confocal). Scale bar, 2 μm . **k** Zooms of spines indicated in **j** with asterisks. Scale bar, 500 nm. **l** Quantification of the ratio of spine over dendrite intensity of mGluR5-STGtail_{split} ($n = 8$), mGluR5-STGtail ($n = 6$), mGluR5 Δ C-STGtail ($n = 7$), pDisp-CTD-STGtail_{split} ($n = 7$) and pDisp-STGtail ($n = 6$; $p < 0.0001$, one-way ANOVA with Tukey's multiple comparisons test: $p > 0.9999$ for 1 vs. 2, $p = 0.0009$ for 1 vs. 3, $p = 0.0015$ for 3 vs. 2, $p = 0.9981$ for 4 vs. 1, $p = 0.0029$ for 4 vs. 3 and $p < 0.0001$ for 5 vs. 1, 2, 3 and 4). Data are represented as means \pm SEM. * $p < 0.05$, ** $p < 0.01$ and *** $p < 0.001$. Source data are provided as a Source Data file.

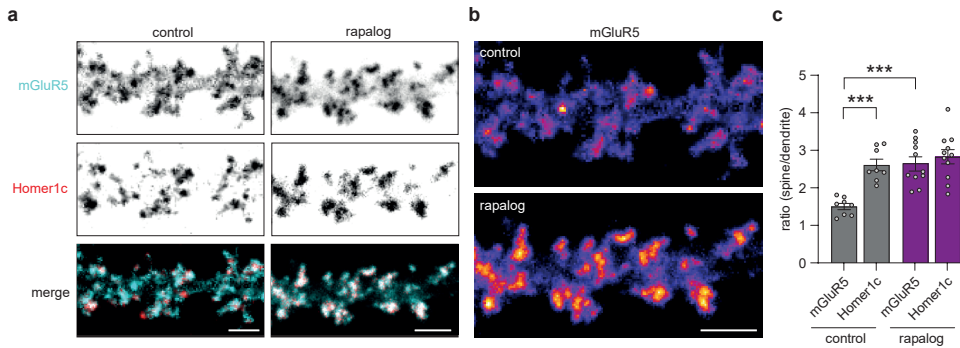
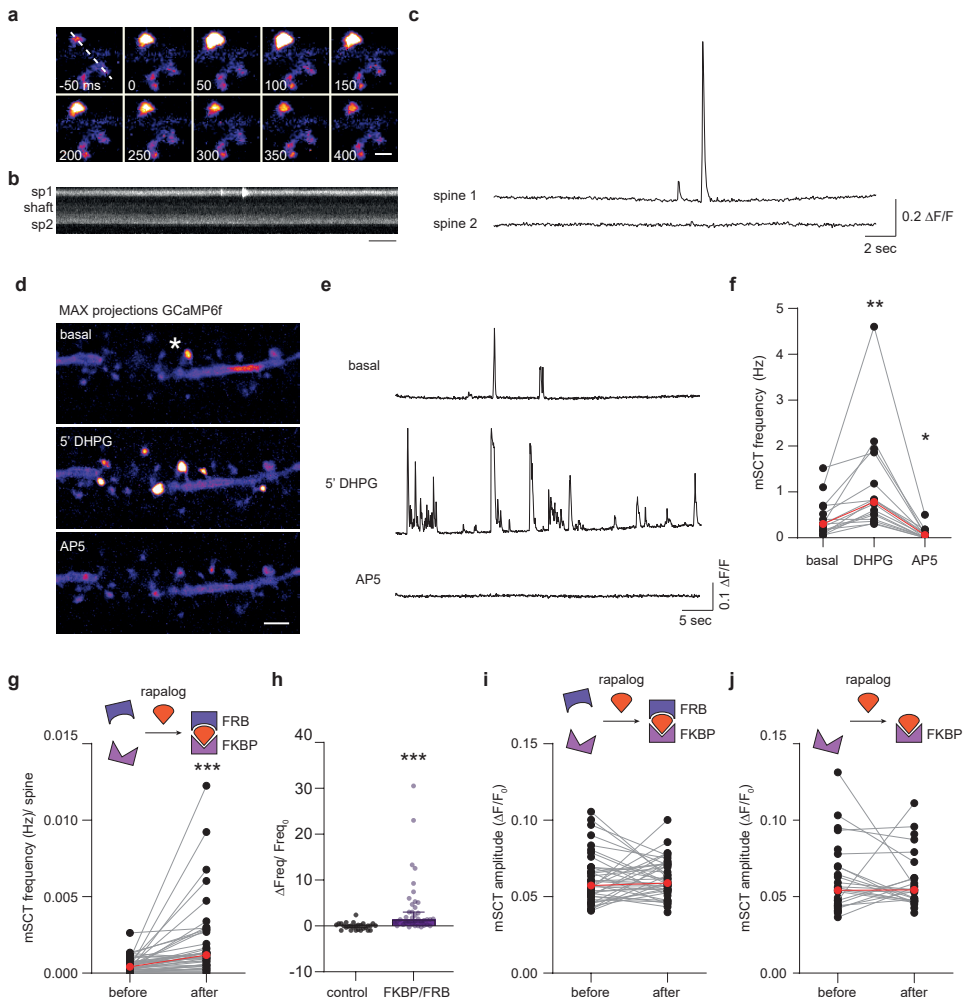


Figure S7. The inducible dimerization system acutely relocated mGluR5 to the synapse

a Representative image of SEP-mGluR5-FRB and 2xFKBP-Homer1c-mcherry after vehicle (control) and rapalog application for 50 minutes. Scale bars, 2 μm . **b** SEP-mGluR5-FRB color-coded for fluorescence intensity in control and rapalog neurons. Scale bar, 2 μm . **c** Quantification of the ratio of spine over dendrite intensity of SEP-mGluR5-FRB and 2xFKBP-Homer1c-mCherry after vehicle (control; $n = 8$) and rapalog ($n = 11$) application for 50 minutes ($p < 0.0001$, one-way ANOVA with Tukey's multiple comparisons test: $p = 0.0002$ for mGluR5 control vs. mGluR5 rapalog, $p = 0.0007$ for mGluR5 control vs. Homer1c control, $p = 0.8598$ for mGluR5 rapalog vs. Homer1c rapalog and $p = 0.7935$ for Homer1c control vs. Homer1c rapalog). Data are represented as means \pm SEM. *** $p < 0.001$. Source data are provided as a Source Data file.

Figure S8. Synaptic recruitment of mGluR5 deregulated synaptic calcium signaling

a Representative time-lapse of a spine with GCaMP6f expression showing one mSCT (scale bar, 1 μm), and **b** the kymograph showing two consecutive events at the same spine (sp1), and no detected Ca^{2+} increases at the dendritic shaft and neighboring spine (sp2). Scale bar, 2 sec. This experiment was replicated in cultures from more than 3 independent preparations of hippocampal neurons. **c** The two successive mSCTs from spine 1 with different amplitudes and the absence of mSCTs in spine 2 **d** Maximum projections of the GCaMP6f stream (50 s) in a representative dendrite at baseline, upon 5 minute DHPG application and after the addition of AP5. Scale bar, 2 μm . **e** $\Delta F/F_0$ traces of GCaMP6f signal from the spine indicated with an asterisk in **d** during baseline, upon DHPG and AP5 application. **f** Quantification of mSCT frequencies during baseline and after DHPG (5') and AP5 application in neurons without mGluR5 overexpression ($n = 16$ neurons, $p < 0.0001$, Friedman test with Dunn's multiple comparisons test: compared to basal $p = 0.0094$ for DHPG and $p = 0.0207$ for AP5). **g** Quantification of mSCT frequencies upon application of rapalog in neurons expressing SNAP-mGluR5-FRB and 2xFKBP-Homer1c-mCherry, corrected for spine number ($n = 43$ neurons, $p < 0.0001$, two-sided Wilcoxon matched-pairs signed rank test). **h** mSCT frequencies per neuron before and after application of rapalog for 30 minutes in control



(FKBP only) and FKBP/FRB neurons. The scatter plot with bar (median with 95% CI) shows the change in mSCT frequency 30 minutes after rapalogs application (ΔFreq), divided by the baseline value (Freq_0) (control: $n = 28$ and FKBP/FRB: $n = 39$ neurons; $p < 0.0001$, two-sided Mann-Whitney test, only neurons included with minimum of one mSCT at baseline). **i** Quantification of mSCT amplitudes upon application of rapalogs in neurons expressing SNAP-mGluR5-FRB and 2xFKBP-Homer1c-mCherry ($n = 39$ neurons, $p = 0.9395$, two-sided Wilcoxon matched-pairs signed rank test) and **j** in neurons expressing SNAP-mGluR5 and 2xFKBP-Homer1c-mCherry (control) ($n = 22$ neurons, $p = 0.4628$, two-sided Wilcoxon matched-pairs signed rank test). Medians are indicated by the red lines. * $p < 0.05$, ** $p < 0.01$ and *** $p < 0.001$. Source data are provided as a Source Data file.

7



Methods to study the dynamic lipid organization in the postsynaptic membrane

Manon Westra and Harold D. MacGillavry

Cell Biology, Neurobiology and Biophysics, Department of Biology,
Faculty of Science, Utrecht University, Utrecht, The Netherlands

Abstract

Synaptic membrane organization is highly important for proper synaptic functioning. Particularly, the precise organization of neurotransmitter receptors in membrane domains determines synaptic efficacy. Receptors are embedded in a complex mixture of lipids, and it is thus likely that the composition and organization of the synaptic membrane contribute to receptor organization. Nevertheless, we know surprisingly little about the contribution of lipids to neuronal functioning and their organization within the postsynaptic membrane. Therefore, in this study we set out to develop different experimental approaches to study the dynamic organization of the synaptic membrane. To investigate the lipid organization in the synaptic membrane, we took two different approaches. First, we aimed to determine the dynamic nanoscale organization of synaptic lipids by labeling lipids directly. Second, we aimed to determine the functional contribution of membrane lipid organization to synaptic structure and signaling. This study demonstrated that single-molecule tracking can distinguish the diffusive behavior of different membrane probes including phospholipids. Environment-sensitive dyes made it possible to observe global changes in neuronal membrane ordering. Furthermore, we found no effect of cholesterol on the diffusive behavior of mGluR5 and GluA2. Finally, we discovered the presence of endogenously expressed sphingomyelin-modifying enzymes within spines.

Introduction

The membrane organization of glutamatergic synapses is highly important for proper synaptic functioning. At the postsynaptic membrane, glutamate receptors are organized in nanodomains that align with the presynaptic release site of neurotransmitters to efficiently mediate synaptic transmission (MacGillavry et al., 2013; Nair et al., 2013; Tang et al., 2016). Because the receptors have a low affinity for glutamate, this property can be used to fine-tune synaptic signaling and allow for plasticity. The ionotropic glutamate receptors like AMPARs are concentrated in the postsynaptic density (PSD) whereas the metabotropic glutamate receptor mGluR5 is concentrated in the perisynaptic area (Nusser et al., 1994; Luján et al., 1996; Scheefhals et al., 2023). Because of this segregation of the receptors and their low affinity for glutamate, mGluR5 receptors will only be activated when there is enough release of glutamate to diffuse further than the PSD. This exemplifies the importance of the heterogeneous organization of the postsynaptic membrane. However, how this organization is established and maintained remains largely unknown. Particularly, even though these receptors are embedded in a complex mixture of lipids that could modulate their positioning and functioning, we know surprisingly little about the contribution of lipids to neuronal functioning and their organization within the postsynaptic membrane.

The plasma membrane exists of a wide variety of lipid types with each their own biophysical properties. This mixture leads to a non-uniform organization of the membrane. Phase separation in the membrane is observed between the tightly packed saturated lipids and cholesterol, the so-called liquid-ordered phase, and on the other hand the unsaturated lipids that segregate in liquid-disordered phases. The existence of those ordered domains consisting of cholesterol and sphingolipids led to the idea that these so-called lipid rafts could promote the clustering of proteins at the plasma membrane (Simons and Ikonen, 1997). This



membrane domain theory also stresses the importance of lipid-protein interactions. Based on lipidomic studies the synaptic membrane is found to be enriched in specific lipids such as cholesterol, sphingomyelin, and polyunsaturated fatty acids (PUFAs) (Cotman et al., 1969; Breckenridge et al., 1972; Igbavboa et al., 2002). Furthermore, their dynamics appear to be of great influence on neuronal functioning (Dotti et al., 2014; Westra et al., 2021). However, it is unknown how the different lipids are distributed within the synapse.

It would be interesting to learn if the dynamic formation of lipid domains at the postsynaptic membrane contributes to the compartmentalization of glutamate receptor complexes. Do AMPARs and mGluR5 receptors reside in membrane domains enriched in cholesterol and sphingomyelin? Does the amount and localization of cholesterol influence synaptic transmission? Is the lipid organization of larger importance for mGluR5 than for AMPARs because AMPARs are already bound by numerous scaffold molecules?

Different techniques have been used to study lipids and membrane organization within the plasma membrane. Labeling lipids with small probes allows for the investigation of their distribution and dynamics within the membrane (Eggeling et al., 2009; Fujiwara et al., 2016). The development of polarity-sensitive dyes led to the study of phase separation in cellular membranes (Owen et al., 2012; Klymchenko and Kreder, 2014; Danylchuk et al., 2020). And membrane modifications like cholesterol or sphingolipid depletion helped the investigation of the effect of membrane organization on cellular functioning (Hering et al., 2003; Lenne et al., 2006; Guo et al., 2021). However, not many of these techniques have been specifically applied to the postsynaptic plasma membrane.

Therefore, in this study we set out to adapt different methods to study the organization of these synaptic lipids and their contribution to synaptic transmission. To investigate the lipid organization in the synaptic membrane, we took two different approaches. First, we aimed to directly label lipids and thereby study their organization and dynamics in the membrane. The second goal was to modify lipid composition and investigate the effects of those modifications on membrane organization and the dynamics of glutamate receptors.

Results

Labeling of gangliosides in the neuronal plasma membrane

To investigate the more ordered regions in the neuronal plasma membrane, we used cholera toxin subunit B (CTxB) to label ganglioside GM1. This probe can bind up to five GM1 gangliosides and is reported to label so-called lipid rafts (Merritt et al., 1994; Day and Kenworthy, 2015). Neurons were live labeled with CTxB conjugated to the dye CF640R, which resulted in labeling of the plasma membrane (Figure 1A). To study the ganglioside organization at the postsynaptic membrane, we also transfected the neurons with PSD95.FingR-GFP to label the postsynaptic density (PSD) (Figure 1B). However, the density of neighboring axons and dendrites was too high to distinguish individual spines, making it difficult to study the distribution of CTxB specifically at postsynaptic sites. Furthermore, it was not possible to perform STED microscopy to achieve better resolution, because the CF640R dye did not have high photostability. This also made it difficult to perform single-molecule tracking on CTxB, as it resulted only in very short trajectories.

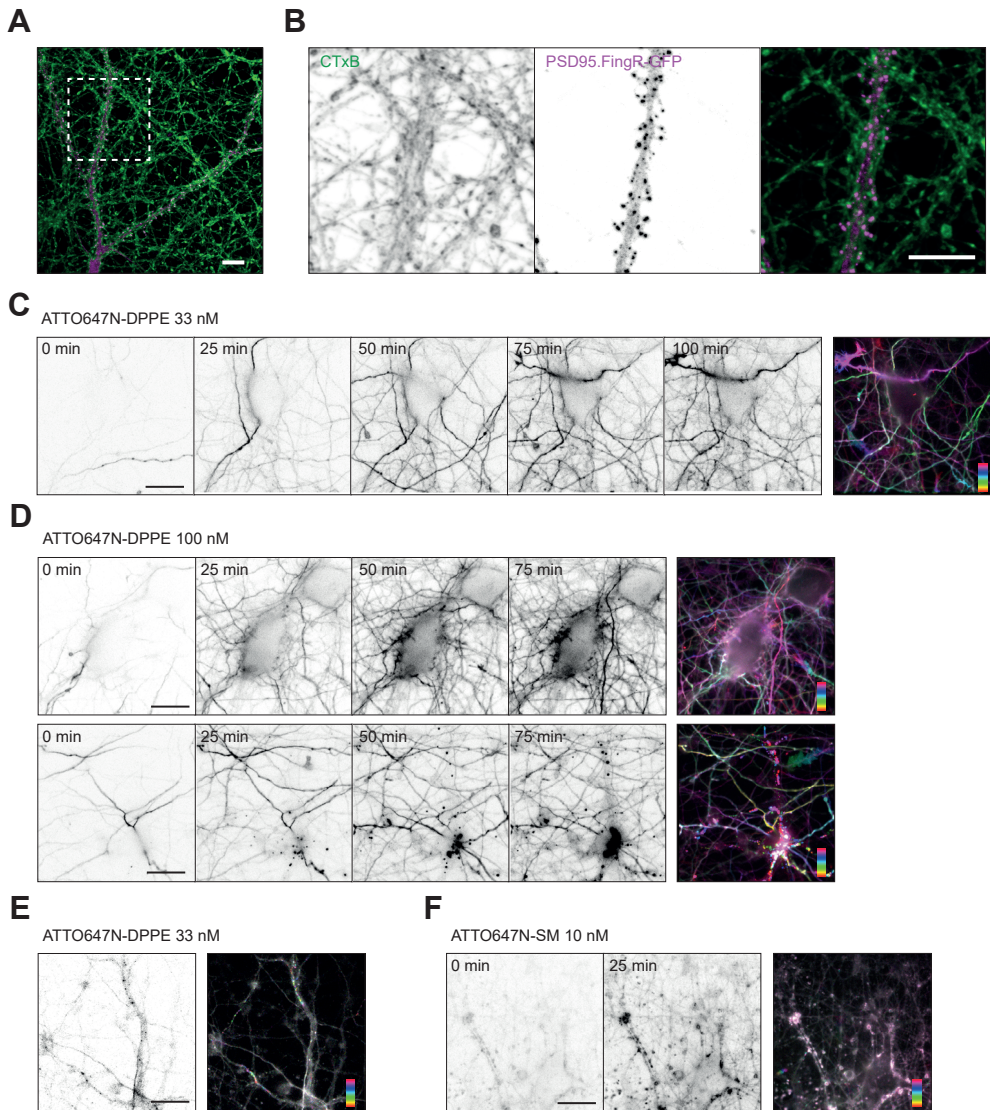


Figure 1. Lipid labeling in the neuronal plasma membrane

(A) Cholera toxin subunit B (CTxB) conjugated to dye CF640R labels membrane of hippocampal neurons. Scale bar, 10 μm . (B) CTxB labeling in combination with PSD95.FingR-GFP expression. Zoom of (A), scale bar, 10 μm . (C) Time-lapse imaging of ATTO647N-DPPE labeling of hippocampal neurons with a concentration of 33 nM. Image on the right is color-coded for frame number. One frame every minute. Scale bar, 20 μm . (D) Time-lapse imaging of ATTO647N-DPPE labeling of hippocampal neurons with a concentration of 100 nM. Images on the right are color-coded for frame number. One frame every minute. Scale bar, 20 μm . (E) Internalized ATTO647N-DPPE travels through the dendrites. Image on the right is color-coded for frame number. One frame every ten seconds. Scale bar, 20 μm . (F) Time-lapse imaging of ATTO647N-SM labeling of hippocampal neurons with a concentration of 10 nM. Image on the right is color-coded for frame number. One frame every minute. Scale bar, 20 μm .



Fluorescently-labeled phospholipids mainly label the axonal plasma membrane

Next, we aimed to investigate the dynamics of labeled phospholipids in the neuronal membrane. We made use of phosphatidyl ethanolamine (PE) with unsaturated (DOPE) or saturated (DPPE) fatty acids and sphingomyelin (SM), all labeled with the photostable dye ATTO647N. First, we performed time-lapse imaging to investigate how the dye-coupled lipids would label the membrane. The DPPE lipids spread over the plasma membrane of the neurons; over time more neurites gradually became fluorescent (Figure 1C, D). However, first, we noticed that the lipids would primarily label axons and to a lesser extent the soma and dendrites. Even after longer, overnight labeling with ATTO647N-DPPE, lipid labeling of the plasma membrane of soma and dendrites was almost absent. Second, we noticed internalized aggregates moving through dendrites and accumulating in the soma (Figure 1D, E). The internalization and aggregation were more apparent when adding higher concentrations of the lipids (Figure 1D). To prevent internalization of labeled lipids, we also performed labeling on ice, but that did not improve the results. In contrast to DPPE, SM did not label neurons by spreading over the plasma membrane. SM labeling intensity seemed to increase over time, but we could not clearly distinguish the outline of neurons and the dye-coupled lipids mainly seemed to aggregate over time (Figure 1F).

Single-molecule tracking of different membrane components

To study the diffusion coefficient of membrane components in the neuronal membrane, we performed single-molecule tracking on different membrane probes. First of all, we could track ATTO647N-DOPE and ATTO647N-DPPE in axons and found a few dendrites with plasma membrane labeling (Figure 2A, B). For comparison, we tracked other membrane probes with expected different diffusion coefficients: the AMPAR subunit GluA2, an artificial protein with a single-spanning transmembrane domain (GT46), and GPI-anchored GFP (GFP-GPI). All of these proteins were coupled to a fluorescent protein that could be tracked with an anti-GFP or anti-RFP nanobody coupled to ATTO647N (Figure 2C). We detected that the diffusion coefficient of GluA2 ($0.0218 \pm 0.0014 \mu\text{m}^2/\text{s}$, mean \pm SEM) was significantly lower than GT46 ($0.0334 \pm 0.0031 \mu\text{m}^2/\text{s}$, $p = 0.003$), whereas the diffusion coefficient of GPI ($0.0547 \pm 0.0041 \mu\text{m}^2/\text{s}$, $p < 0.001$) was significantly higher than GT46, and the diffusion of the phospholipids ($0.2857 \pm 0.026 \mu\text{m}^2/\text{s}$, $p < 0.001$) was substantially higher as expected (Figure 2D, E).

Cholesterol depletion with MBCD

Another approach to learn more about the role of lipids in the synaptic membrane was to study the effect of changing membrane composition on the dynamic membrane organization. We used the special properties of polarity-sensitive membrane dye di-4-ANEPPDHQ to investigate the membrane ordering of the neuronal plasma membrane (Owen et al., 2012). Di-4-ANEPPDHQ excites at 488 nm and has a 60-nm spectral blue shift between the liquid-disordered and liquid-ordered membrane phases. This shift in the emission profile can be described by the generalized polarization (GP) value, calculated as a ratiometric measurement of the fluorescence intensity in the two spectral channels corresponding to the ordered and disordered phase. First, we applied the dye on U2OS cells, where we could distinguish the plasma membrane from the intracellular membranes based on the GP value

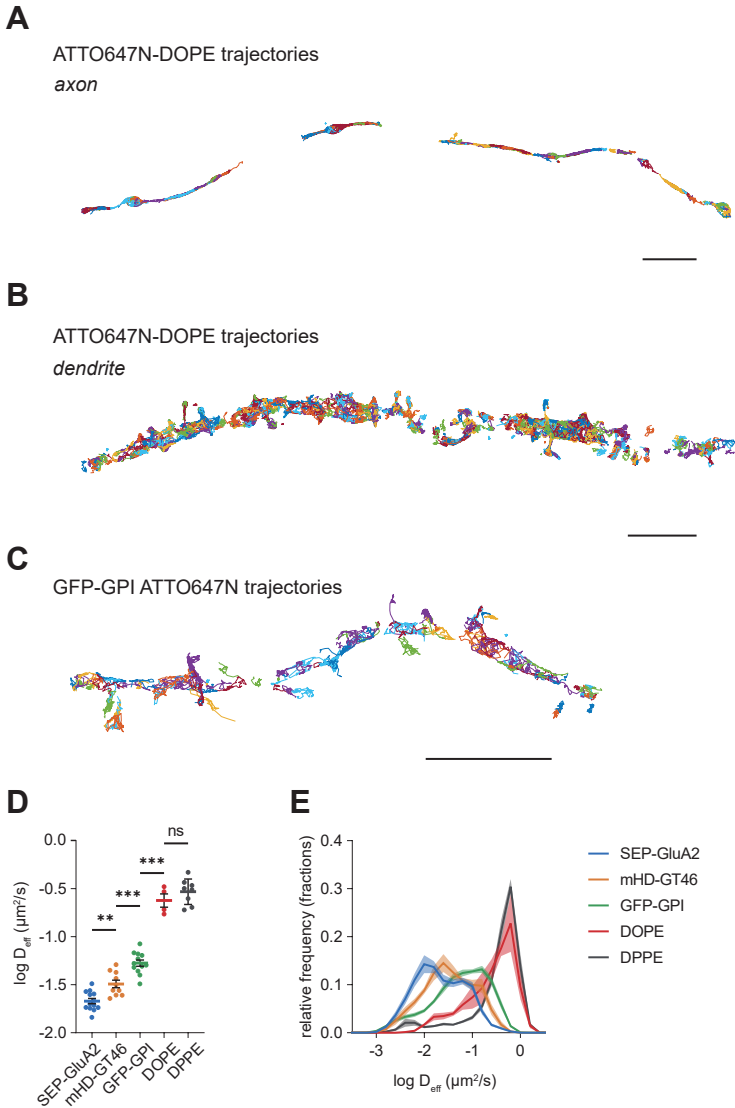


Figure 2. Single-molecule tracking of different membrane probes

(A) ATTO647N-DOPE tracking in an axon. (B) ATTO647N-DOPE tracking in a dendrite. (C) GFP-GPI ATTO647N single-molecule tracking in a dendrite. (D) Mean log D_{eff} per neuron of trajectories of SEP-GluA2, mHD-GT46, GFP-GPI, DOPE, and DPPE. (E) Relative frequency distributions of log D_{eff} of the individual trajectories from (D). The data from one neuron per membrane component from this complete dataset was also published in (Westra and MacGillavry, 2022). Data are represented as means \pm SEM. ** $p < 0.01$, *** $p < 0.001$. Scale bars, 5 μm .

(Figure 3A, B). This is similar to what has been reported before, confirming that the plasma membrane is more ordered than intracellular membranes because of the high cholesterol content (Niko et al., 2016). Next, we applied the dye on hippocampal neurons where it

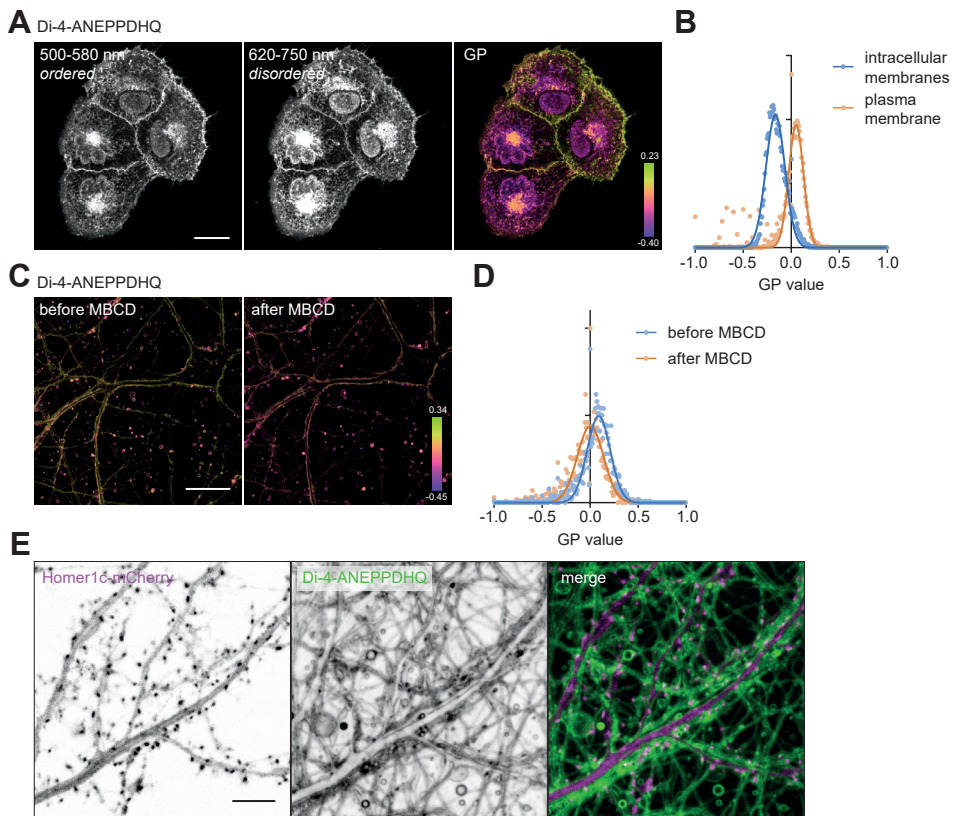


Figure 3. Labeling of membranes with polarity-sensitive dye di-4-ANEPPDHQ

(A) Di-4-ANEPPDHQ labels U2OS cells. The two separate spectral channels are shown with, next to it, the GP image. Scale bar, 20 μm . (B) Distribution of GP values with a Gaussian fit for the intracellular membranes and the plasma membrane of (A). (C) GP images of di-4-ANEPPDHQ labeling of neurons before and after cholesterol depletion with 2 mM MBCD. Scale bar, 20 μm . (D) Distribution of GP values with a Gaussian fit of the neuronal membrane before and after MBCD in (C). (E) Confocal image of dendrites expressing Homer1c-mCherry and labeled with di-4-ANEPPDHQ. Scale bar, 5 μm .

labeled the plasma membrane (Figure 3C). To study the effect of cholesterol depletion on membrane ordering in the neuronal plasma membrane, we incubated neurons with 2 mM methyl- β -cyclodextrin (MBCD) for 30 minutes. After incubation with MBCD a reduction in GP values could be observed along the plasma membrane, indicating an overall shift to a less ordered plasma membrane (Figure 3C, D). The follow-up question would be to study the change in membrane ordering in more detail at the postsynaptic membrane. We transfected the neurons with Homer1c-mCherry to be able to investigate the distribution of di4-ANEPPDHQ at the PSD. However, similar to CTxB, di-4-ANEPPDHQ labeled all membranes, and it was almost impossible to distinguish individual spines from the axons tangled around (Figure 3E).

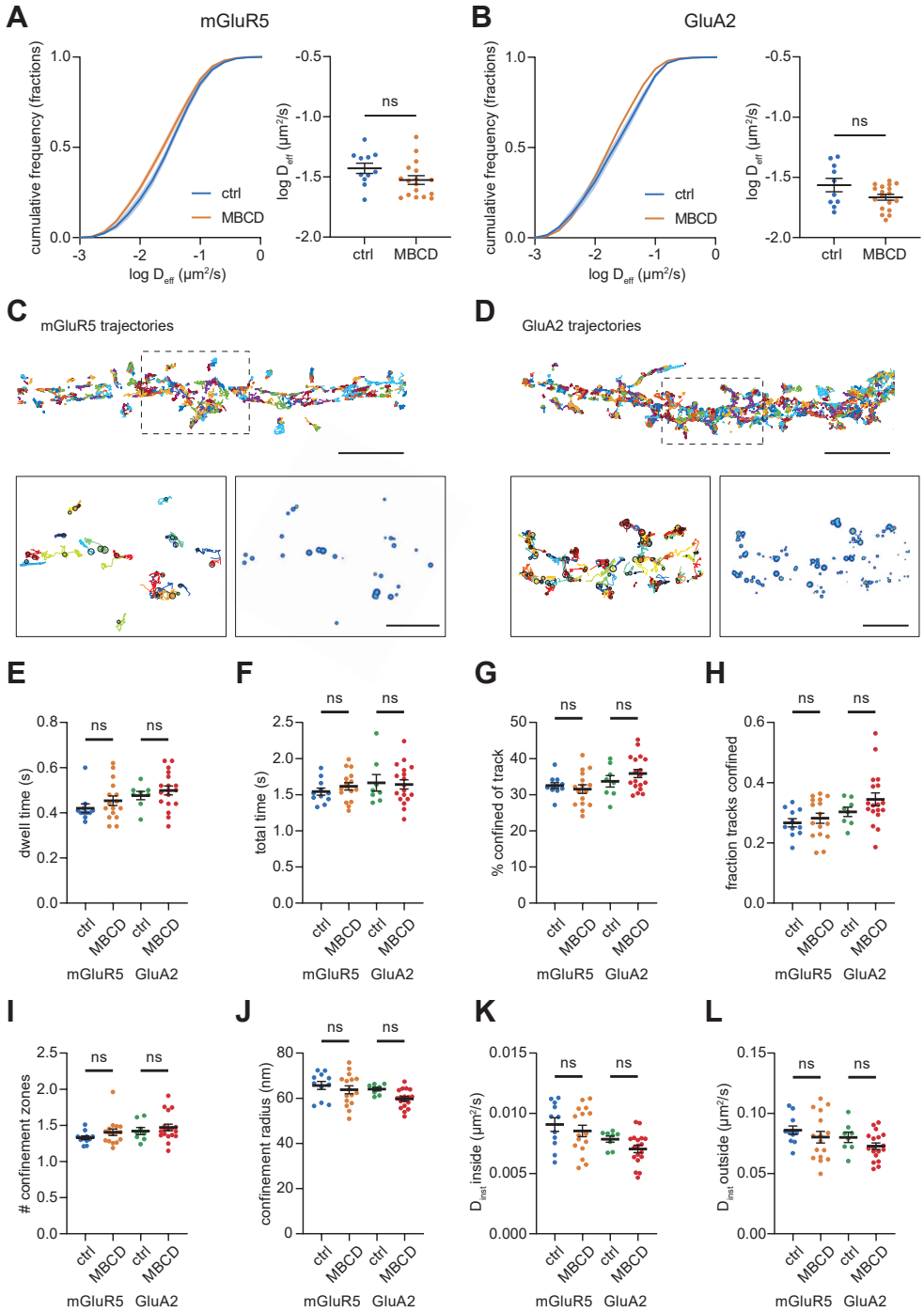




Figure 4. Single-molecule tracking of glutamate receptors after cholesterol depletion

(A) Cumulative frequency distribution of the $\log D_{\text{eff}}$ for mGluR5 trajectories with on the right the median $\log D_{\text{eff}}$ per neuron. Both control condition and after cholesterol depletion. (B) Cumulative frequency distribution of the $\log D_{\text{eff}}$ for GluA2 trajectories with on the right the median $\log D_{\text{eff}}$ per neuron. Both control condition and after cholesterol depletion. (C) Single-molecule trajectories of mGluR5 in a dendrite. Zooms reveal the trajectories that displayed transient confinement indicated by the black circles (left) and a confinement heatmap displaying the confinement zones. Scale bar, 5 μm . (D) Single-molecule trajectories of GluA2 in a dendrite. Zooms reveal the trajectories that displayed transient confinement indicated by the black circles (left) and a confinement heatmap displaying the confinement zones. (E-L) Transient confinement analysis of mGluR5 and GluA2 in control conditions and after cholesterol depletion with MBCD. (E) Dwell time per trajectory, median per neuron. (F) Total time of the trajectory, median per neuron. (G) Average percentage of a trajectory that displayed transient confinement, median per neuron. (H) Fraction of all the trajectories that displayed at least one period of transient confinement per neuron. (I) Average number of confinement zones per trajectory, mean per neuron. (J) Average confinement radius per trajectory, median per neuron. (K) Diffusion coefficient inside confinement zones, median per neuron. (L) Diffusion coefficient outside confinement zones, median per neuron. The transient confinement data from the control conditions from mGluR5 and GluA2 was also published in (Westra and MacGillavry, 2022). Data are represented as means \pm SEM, ns, $p > 0.05$. Scale bar is 5 μm and in zooms 2 μm .

Single-molecule tracking of glutamate receptors after cholesterol depletion

Next, we questioned what influence the depletion of cholesterol would have on the dynamics of different glutamate receptors. For AMPARs it is known that they are bound to various scaffold molecules that concentrate them in the PSD, however, for mGluR5 it is less well-known what keeps them in domains in the perisynaptic area. Therefore, we hypothesized that if cholesterol is an important component of membrane domains, mGluR5 dynamics would be influenced by cholesterol depletion whereas the effect on AMPARs would be less. To investigate the effect of cholesterol depletion on the dynamics of glutamate receptors mGluR5 and GluA2, we studied the diffusion using single-molecule tracking. Hippocampal neurons were transfected with either SEP-mGluR5 or SEP-GluA2 and labeled with anti-GFP nanobody coupled to ATTO647N to track the receptors. To deplete cholesterol, neurons were incubated with 2 mM MBCD for 15–30 minutes. First, we estimated the diffusion coefficient of mGluR5 and GluA2 in control and cholesterol-depleted conditions from the MSD versus time lag curve. The diffusion coefficient after cholesterol depletion (mGluR5: $0.0317 \pm 0.0031 \mu\text{m}^2/\text{s}$, GluA2: $0.0222 \pm 0.0012 \mu\text{m}^2/\text{s}$) did not differ significantly from the control condition (mGluR5: $0.0391 \pm 0.0038 \mu\text{m}^2/\text{s}$, GluA2: $0.0293 \pm 0.0037 \mu\text{m}^2/\text{s}$) for both mGluR5 and GluA2 (Figure 4A, B, Supplementary Figure 1A, C). A higher concentration of MBCD also did not lead to a larger effect (Supplementary Figure 1B, D). Next, we studied the dynamics of the receptors in more detail by inspecting periods of transient confinement (Figure 4C, D) (Westra and MacGillavry, 2022). However, we did not observe significant differences after cholesterol depletion in the period of confinement (Figure 4E, F, G), the fraction of tracks that displayed transient confinement (Figure 4H), the number of confinement zones per trajectory (Figure 4I), the size of confinement zones (Figure 4J), or the diffusion coefficient inside and outside confinement zones (Figure 4K, L) for both mGluR5 and GluA2. Altogether, in our experiments we could not find evidence for a specific role of cholesterol in the diffusive behavior of both mGluR5 and GluA2.

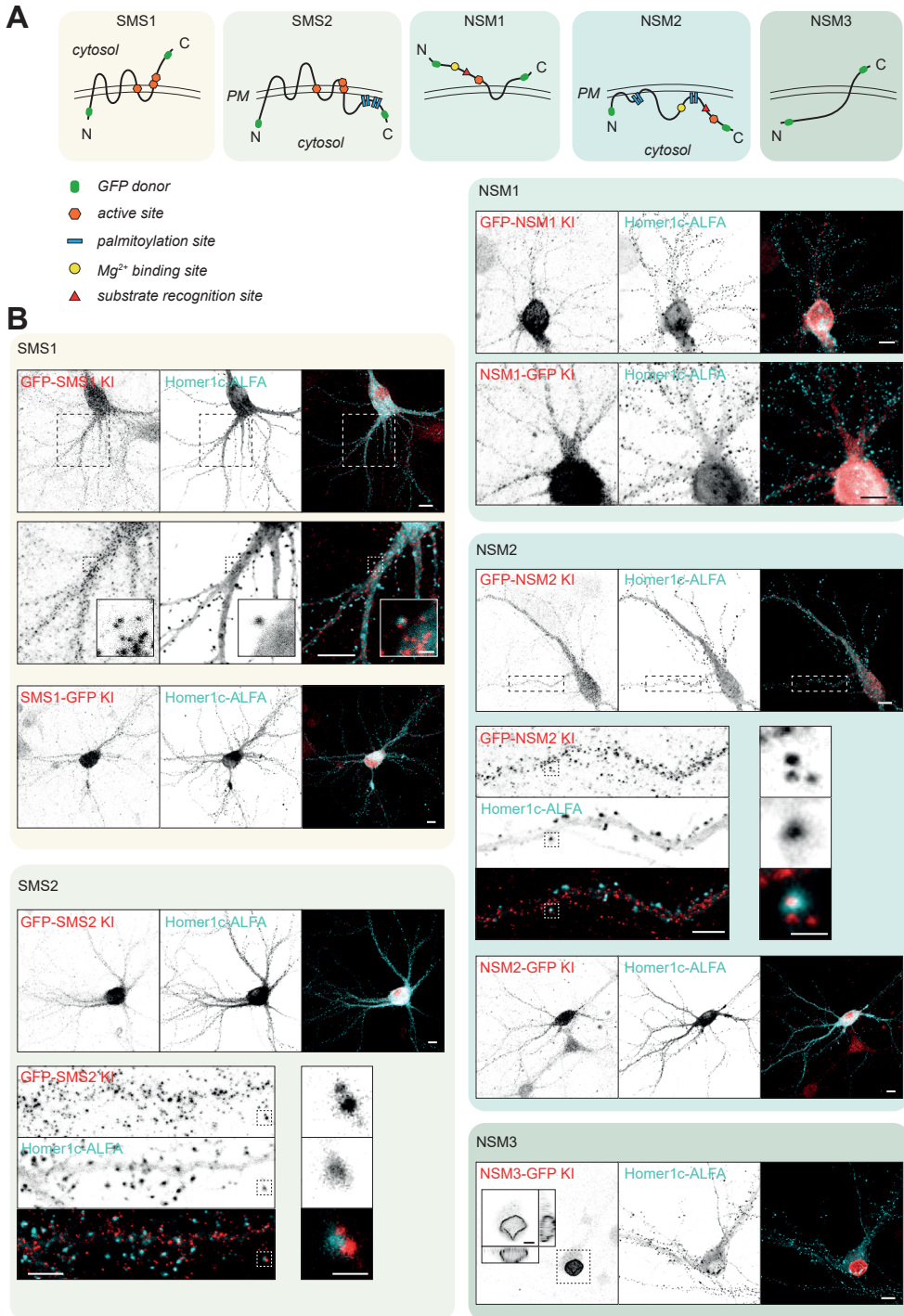




Figure 5. Endogenous localization of sphingomyelin-modifying enzymes in hippocampal neurons

(A) Schematic representation of the hypothesized localization of the different sphingomyelin-modifying enzymes around the (plasma) membrane based on the Uniprot protein database. Important sites such as palmitoylation sites and the location of the GFP donor in our knock-ins are indicated and referred to in the legend. (B) Representative confocal images of the knock-ins GFP-SMS1, SMS1-GFP, GFP-SMS2, GFP-NSM1, NSM1-GFP, GFP-NSM2, NSM2-GFP, and NSM3-GFP all co-transfected with Homer1c-ALFA to reveal co-localization with the PSD. Scale bars are 10 μm , in zooms 5 μm , and in the zooms of only one spine 1 μm .

Endogenous localization of sphingomyelin-modifying enzymes

Sphingomyelin is enriched at the PSD (Cotman et al., 1969; Breckenridge et al., 1972), to begin to study processes that could underlie this enrichment, we first developed tools to visualize endogenous localization of sphingomyelin-modifying enzymes. Several sphingomyelin-modifying enzymes are involved in the sphingomyelin metabolism: sphingomyelin synthase 1 (SMS1) and 2 (SMS2) are responsible for the synthesis of sphingomyelin and neutral sphingomyelinase 1 (NSM1), 2 (NSM2) and 3 (NSM3) are involved in the breakdown of sphingomyelin. We endogenously tagged the sphingomyelin-modifying enzymes with a GFP tag using the ORANGE CRISPR/Cas9-based knock-in toolbox (Willems et al., 2020). We designed knock-ins with the GFP tag at the C-terminal or N-terminal to test for a possible effect of the tag on the localization (Figure 5A). We co-transfected neurons with Homer1c-ALFA to mark the PSD. We could find knock-ins for all the enzymes except for SMS2-GFP and GFP-NSM3 (Figure 5B). In general, we did not observe remarkably different distributions between the C-terminally and N-terminally tagged knock-ins. For SMS1, SMS2 and NSM2 we could observe overlap of enzyme localization with the PSD, however no specific enrichment of any of the enzymes in the spines (Figure 5B). NSM1 appeared to be mainly around the nucleus and in low abundance in neurites, whereas NSM3 localized exclusively in the nuclear membrane (Figure 5B). In summary, these results show that SMS1, SMS2, and NSM2 localize inside spines and might locally regulate the amount of sphingomyelin in the postsynaptic membrane.

Discussion

In this study we applied different methods to investigate both the dynamic lipid organization in the neuronal membrane and the contribution of those lipids to the membrane organization and dynamics. We could track phospholipids in both axons and dendrites but also noticed that they almost did not label the plasma membrane of soma and dendrites. Single-molecule tracking allows for detecting differences in the diffusion coefficient of different membrane probes. Polarity-sensitive dyes make it possible to observe global changes in membrane ordering of the neuronal membrane. We observed no large effect of cholesterol depletion on the diffusive behavior of glutamate receptors mGluR5 and GluA2. We were able to study the endogenous localization of sphingomyelin-modifying enzymes and discovered the presence of some of them within spines.

The problem with studying lipid organization directly is the visualization of lipids. One cannot overexpress or genetically label lipids with a fluorescent tag like with proteins. Several probes are available with a fluorescent dye attached that bind to specific lipid types. The membrane-binding subunit of cholera toxin (CTxB) is one of them and binds up to five GM1

gangliosides, which are considered lipid raft components. In this study we found that the probe is not very suitable for visualizing GM1 localization specifically in the postsynaptic membrane as it is labeling all the membranes. Furthermore, we labeled the neurons live, which could induce clustering of GM1 gangliosides and might thus not visualize the native condition. However, the property of CTxB to crosslink GM1 gangliosides could be used as an approach to modify membrane composition. Indeed, the probe has been reported to induce phase separation in model membrane systems and giant plasma membrane vesicles (GPMVs) (Hammond et al., 2005; Johnson et al., 2010).

In addition to labeling endogenous lipids with specific probes, there is the possibility to add exogenous lipids that have a dye conjugated to them. The idea is that these lipids will incorporate into the membrane and behave as their non-labeled counterparts. Although single-molecule tracking requires sparse labeling and the concentration was thus relatively low, we cannot rule out that adding the exogenous lipids modified the native membrane composition. Furthermore, it is not entirely clear why the phospholipids mainly labeled the axons and did not enter the soma and dendrites. Possibly, the axon initial segment (AIS) acted as a diffusion barrier between the axons and the somatodendritic compartment (Kobayashi et al., 1992; Winckler et al., 1999; Nakada et al., 2003). However, then it is still expected that some of the phospholipids would incorporate into the dendritic plasma membrane directly instead of spreading over the membrane from the axonal compartments, which did almost not happen. In addition to the visualized internalized molecules this prompts the speculation that in the dendritic compartments exogenous lipids are immediately internalized and transported to the soma where they accumulate.

The contribution of lipid organization to glutamate receptor dynamics and synaptic functioning could be investigated by modifying the lipid composition. Cholesterol depletion with MBCD is a method used in previous research, where it for example resulted in a smaller immobile synaptic pool of NMDARs (Korinek et al., 2020). MBCD is not entirely specific for cholesterol but has the advantage that it does not generate additional metabolites, whereas cholesterol oxidase is more specific but generates byproducts (Ohtani et al., 1989; Leventis and Silviu, 2001). In this study we hypothesized that cholesterol depletion with MBCD would affect the dynamics of mGluR5 because they reside in membrane domains that are also enriched in cholesterol. Cholesterol depletion would lead to the loss of those domains and therefore less confined periods of mGluR5. On the other hand, we expected the effect on AMPAR dynamics to be lower because they are already trapped in the PSD by numerous scaffold molecules. However, we did not observe any of these differences after cholesterol depletion in the dynamics for both mGluR5 and GluA2. The next step would be to measure the levels of cholesterol in the neurons after the incubation with MBCD to investigate if cholesterol was indeed depleted before concluding that cholesterol does not influence glutamate receptor dynamics (Mahammad and Parmryd, 2015). Although we did observe a change in membrane order after cholesterol depletion with the polarity-sensitive dye di-4-ANEPPDHQ, indicating that MBCD did change membrane composition. Another approach would be to modify membrane composition in a more specific and compartmentalized manner.

One of those approaches would be to recruit or deplete certain enzymes important for lipid metabolism to the postsynaptic membrane. In this study we generated several knock-ins for sphingomyelin-modifying enzymes. It has been reported that for example NSM2 plays a role in memory; inhibition of NSM2 resulted in increased PSD95 and AMPARs and changed the subunit composition of NMDARs (Tabatadze et al., 2010). We found that a few of the



sphingomyelin-modifying enzymes did localize near the synapses but were not specifically enriched in those compartments. To recruit specific enzymes to the PSD, knock-ins could be generated with the rapalog-inducible dimerization domain FRB and PSD95 with FKBP after which the addition of rapalog would lead to recruitment of the enzymes to the PSD (Clackson et al., 1998). The hypothesis is that recruitment of sphingomyelinase or sphingomyelin synthase could lead to decreased or increased levels of sphingomyelin within the postsynaptic membrane, respectively. Knockouts of these enzymes could also be generated, but the question is how redundant the enzymes are if another enzyme can take over the task of the depleted enzyme. With these tools, the role of sphingomyelin in the dynamics of glutamate receptors could be investigated. It is important to note, however, that increasing or decreasing sphingomyelin levels by modifying their enzymes will also lead to a decrease or increase in ceramide. Thus, it will be difficult to ascribe any observed effect solely to sphingomyelin.

In summary, we set out to adapt different methods to study the lipid organization in the postsynaptic membrane and the contribution of lipid composition to the dynamics of glutamate receptors. We assessed the advantages and disadvantages of these techniques to specifically study membrane organization at excitatory synapses. Further development of these techniques and novel tools are required to efficiently study the organization of lipids at the postsynaptic membrane. Thus, while the exact lipid organization remains to be resolved, this and future studies can help towards a better understanding of the contribution of synaptic lipid organization to synaptic functioning.

Methods

Animals

All animal experiments were performed in compliance with the guidelines for the welfare of experimental animals issued by the Government of the Netherlands (Wet op de Dierproeven, 1996) and European regulations (Guideline 86/609/EEC). All animal experiments were approved by the Dutch Animal Experiments Review Committee (Dier Experimenten Commissie; DEC), performed in line with the institutional guidelines of Utrecht University.

Primary neuron cultures and transfections

Dissociated hippocampal cultures were prepared from mixed-sex embryonic day 18 (E18) pups from Wistar rats (Janvier Labs) (Kapitein et al., 2010). Dissociated neurons were plated on Ø18-mm coverslips coated with poly-L-lysine (37.5 µg/mL, Sigma-Aldrich) and laminin (1.25 µg/mL, Roche Diagnostics) at a density of 50,000 (low-density) or 100,000 neurons per well. Neurons were grown in Neurobasal medium (NB) supplemented with 1% penicillin/streptomycin (Gibco), 2% B27 (Gibco), and 0.5 mM L-glutamine (Gibco) at 37 °C in 5% CO₂. From days in vitro (DIV) 1 onward, medium was refreshed weekly by replacing half of the medium with BrainPhys Neuronal Medium (BP, STEMCELL Technologies) supplemented with 2% NeuroCult SM1 (STEMCELL Technologies) and 1% penicillin/streptomycin. At DIV3 (knock-ins) or DIV14–18 (overexpression), neurons were transfected with indicated constructs using Lipofectamine 2000 (Invitrogen). For each well, 1–2 µg DNA was mixed with 3.3 µL Lipofectamine 2000 in 200 µL BP, incubated for 30 min at room temperature (RT). Then, 400 µL conditioned medium was transferred to a new culture plate and replaced by 260 µL BP supplemented with 0.5 mM L-glutamine. The DNA mix was added to the neurons and incubated at 37 °C in 5% CO₂. After 1 to 2 h, neurons were briefly washed with BP and transferred to the new culture plate with conditioned medium supplemented with an additional 400 µL BP with SM1 and penicillin/streptomycin and kept at 37 °C in 5% CO₂.

DNA plasmids

The following plasmids have been described before in previous studies: SEP-GluA2 (MacGillavry et al., 2013), SEP-mGluR5 and Homer1c-mCherry (Scheefhals et al., 2019), Homer1c-ALFA (Catsburg et al., 2022), PSD95.FingR-GFP (Gross et al., 2013). The GFP-GPI and mHD-GT46 constructs are kind gifts from Dr. Ewers (Albrecht et al., 2015).

The sphingomyelin-modifying enzyme CRISPR/Cas9 knock-in constructs were designed as described in (Willems et al., 2020). GFP was inserted into the different genes at the locations described in the table below resulting in the N-terminal and/or C-terminal tagging of the proteins.

Gene	Protein		Target sequence	Exon
<i>SGMS1</i>	Sphingomyelin synthase 1 (SMS1)	N	5'-GTTGTCTGCCAGTACCATGA-3'	6
		C	5'-GTTAGGTGTCGTTTACCAGC-3'	10
<i>SGMS2</i>	Sphingomyelin synthase 2 (SMS2)	N	5'-CTCCGAAGGCTGGCGGACAA-3'	2
<i>SMPD2</i>	Neutral sphingomyelinase 1 (NSM1)	N	5'-ACAACCTTTTCTCTGCGGCTG-3'	1
		C	5'-CCGCCTCCTGCTGCCGGCAG-3'	10
<i>SMPD3</i>	Neutral sphingomyelinase 2 (NSM2)	N	5'-CGGCGCCCAGTGAGCTGCAA-3'	2
		C	5'-TGACAGACACCATCAGCCGCA-3'	8
<i>SMPD4</i>	Neutral sphingomyelinase 3 (NSM3)	C	5'-TGACACTGCTCACTGAGCGG-3'	20

Cholesterol depletion

Cholesterol was depleted in different experiments using methyl- β -cyclodextrin (MBCD; Sigma Aldrich). For every experiment the solution was freshly prepared, dissolved in extracellular medium and used in concentrations of 2–5 mM and incubated for 15–30 minutes.

Confocal imaging Cholera Toxin Subunit B

Neurons were transfected with PSD95.FingR-GFP at DIV18 as described. At DIV21 neurons were labeled live with Cholera Toxin Subunit B (CTxB) coupled to the dye CF640R (Biotium) with a concentration of 1 μ g/mL in extracellular medium for 30 minutes at room temperature (RT) while blocking with 0.5% BSA. Next, neurons were washed five times with extracellular buffer with 0.5% BSA. Finally, the neurons were fixed with 4% paraformaldehyde (PFA) and 4% sucrose in PBS for 15 minutes at RT, washed three times with PBS and mounted in Mowiol mounting medium (Sigma).

Confocal images were acquired with a Zeiss LSM 700 microscope and imaging was performed with a Plan-Apochromat 63 \times oil (NA 1.40) objective. A Z-stack containing 8 planes at a 0.56- μ m interval was acquired and maximum intensity projections were made for display.

Time-lapse imaging phospholipid labeling

Imaging was performed on an inverted Nikon Eclipse TE2000 microscope equipped with mercury lamp (Nikon). Fluorescence emission was detected using a 40 \times oil-immersion objective (Nikon Apo, NA 1.3), together with an EMCCD camera (Evolve 512, Photometrics) controlled by MetaMorph 7.7 software (Molecular Devices). During imaging, neurons were kept in extracellular imaging buffer in a closed incubation chamber (Tokai Hit) at 37 $^{\circ}$ C. Timelapse imaging was performed on low-density neurons at DIV9. ATTO647N-DPPE or ATTO647N-SM (ATTO-TEC) in complex with defatted BSA (Eggeling et al., 2009) was added to the extracellular medium in a concentration of 33–100 nM or 10 nM, respectively. Images were acquired every minute or every 10 seconds using the 647 nm laser for a maximum period of 2 hours after the addition of the labeled lipids.

Single-molecule tracking

Single-molecule tracking was performed on the Nanoimager S from ONI (Oxford Nanoimaging; ONI), equipped with a 100 \times /NA 1.4 oil immersion objective (Olympus Plan Apo), an XYZ closed-loop piezo stage, and with 471-, 561-, and 640-nm wavelength excitation lasers. Fluorescence emission was detected using an sCMOS camera (ORCA Flash 4, Hamamatsu). Stacks of 5000 frames were acquired at 50 (GluA2, GT46, GPI, mGluR5) or 100 Hz (DOPE, DPPE) with oblique illumination using the 640-nm laser. NimOS software (version 1.18.3) from ONI was used for localization and drift correction was performed. Neurons were imaged in extracellular imaging buffer containing 120 mM NaCl, 3 mM KCl, 10 mM HEPES, 2 mM CaCl₂, 2 mM MgCl₂, and 10 mM glucose, pH adjusted to 7.35 with NaOH. The GFP/RFP-booster ATTO647N (Chromotek) was added before image acquisition in a concentration of 1:200,000 in extracellular imaging buffer while blocking with 1% BSA. For the tracking of phospholipids DOPE and DPPE, ATTO647N-DOPE or ATTO647N-DPPE (ATTO-TEC) in complex with



defatted BSA (Eggeling et al., 2009) was added before image acquisition at a final concentration of 5–10 nM. We used a minimum track length of 30 frames (10- or 20-ms intervals) for visualization and quantification.

Single-molecule tracking analysis

Using MATLAB (version 2021b), molecules with a localization precision of <50 nm were selected for analysis. Tracking was achieved using custom algorithms in MATLAB described previously with a tracking radius of <500 nm (Lu et al., 2014). The first three points of the MSD with the addition of the value 0 at $MSD(0)$ were used to fit the slope using a linear fit. Tracks with a negative slope were not used for further analysis. The diffusion coefficient was estimated based on the fit using the formula: $MSD = 4 \times D \times \Delta t$. Only tracks of at least 30 frames were selected for further analysis. Tracks were classified as immobile when the ratio between the radius of gyration and mean step size ($\frac{\sqrt{\pi/2 \times \text{radius of gyration}}}{\text{mean stepsize}}$) was smaller than 2.11 (Golan and Sherman, 2017).

Transient confinement analysis on mobile trajectories was done in MATLAB as described in (Westra and MacGillavry, 2022). Parameters used in the analysis are: $L_c = 5.5$, $S_m = 15$, $\alpha = 0.5$, $T_c = 0.2$ s. The confinement zones are further analyzed for size and duration of confinement and diffusion coefficient in and outside confinement zones. Confinement maps were created based on the detected confinement radius for each confinement zone. Each confinement zone was stored as a two-dimensional Gaussian distribution with the radius as FWHM. The final matrix was plotted with a color code, where higher values indicate confinement hotspots because there are multiple Gaussians on top of each other.

Di-4-ANEPPDHQ imaging

U2OS cells were plated on 18-mm diameter coverslips 2–4 days before imaging. Di-4-ANEPPDHQ (ThermoFisher) was added in a concentration of 5 μM to live U2OS cells or 200 nM to live hippocampal neurons in extracellular medium 30 minutes before imaging. Images were acquired with a Leica TCS SP8 STED 3X microscope using an HC PL APO 100 \times /NA1.4 oil-immersion objective. Di-4-ANEPPDHQ was excited by the 488 nm laser and the fluorescence emission was detected using two PMT detectors with a range of 500–580 nm and 620–750 nm. The used concentration of MBCD was 2 mM.

For the images of di-4-ANEPPDHQ in combination with transfected Homer1c-mCherry, first, an acquisition of Homer1c-mCherry was made, after which the dye was added and 30 minutes later an acquisition of the same field of view was made to be able to observe the relative distribution.

The GP values and images were calculated with an ImageJ macro based on (Owen et al., 2012). Briefly, for every pixel the intensity value of the disordered channel (620–750 nm) is subtracted from the intensity value from the ordered channel (500–580 nm) and then divided by the sum of the two channels. To create the GP image, the pseudocolored pixels are merged with the mean intensity image using the HSB color space, where the GP value is assigned to hue, the mean intensity to brightness, and saturation set to 1. For the discrimination between intracellular membranes and the plasma membrane, ROIs were drawn around the plasma membrane and intracellular membranes and the GP values inside were used for the comparison.

Confocal imaging sphingomyelin-modifying enzyme knock-ins

Hippocampal neurons were transfected with the different sphingomyelin-modifying enzyme knock-ins in combination with Homer1c-ALFA at DIV3 as described. At DIV 15, neurons were fixed using 4% paraformaldehyde (PFA) with 4% sucrose in PBS for 10 minutes at 37 °C and washed three times in PBS containing 0.1 M glycine (PBS/Gly). Neurons were blocked in blocking buffer (10% [v/v] normal goat serum (NGS) (Abcam) in PBS/Gly) and permeabilized with 0.1% [v/v] Triton X100 for 1 hour at 37 °C. Next, coverslips were incubated with rabbit anti-GFP to enhance the signal (MBL Sanbio, 598, RRID AB_591819) in a concentration of 1:2000 and FluoTag-X2 anti-ALFA coupled to ATTO647N (NanoTag) in a concentration of 1:500 diluted in incubation buffer (5% [v/v] NGS in PBS/Gly with 0.1% [v/v] Triton X100) for 2 hours at RT. Coverslips were washed three times with PBS/Gly and incubated with Alexa488-conjugated secondary antibodies (Life Technologies) diluted 1:200 in incubation buffer for 1 hour at RT. Coverslips were washed three times in PBS/Gly, dipped in Milli-Q water (MQ), and mounted in Mowiol mounting medium (Sigma).

Confocal images were acquired with a Zeiss LSM 700 microscope and imaging was performed with a Plan-Apochromat 63 \times oil (NA 1.40) objective. A Z-stack containing 7–12 planes at a 0.56- μm interval was acquired and maximum intensity projections were made for display.

Statistical Analysis

Data is represented by mean \pm standard error of the mean (SEM). Statistical significance was tested using a Student's *t*-test when comparing two groups and a one-way ANOVA followed by Sidak's multiple comparisons test when comparing more than two groups. Statistical tests with a *p*-value below 0.05 were considered significant. Significance is indicated as follows: *p* < 0.05 is indicated by *, *p* < 0.01 by **, and *p* < 0.001 by ***. Data are shown as average values, error bars represent SEM. Analysis was performed on neurons originating from 1–3 individual preparations of hippocampal neurons. Statistical analysis and graphs were prepared in GraphPad Prism (version 9, Graphpad Software) and figures were generated in Adobe Illustrator 2022 (Adobe Systems).

Acknowledgements

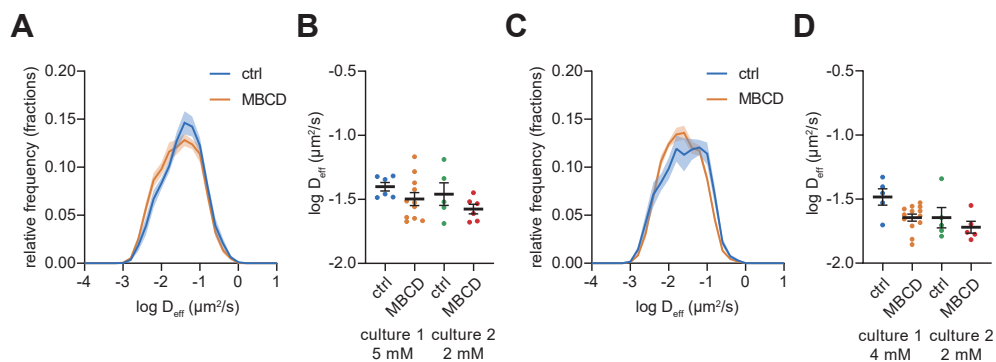
We would like to thank Maya Haaker for her help with creating the lipid-BSA complexes and all members of the MacGillavry lab for helpful discussions. This work was supported by the Netherlands Organization for Scientific Research (ALW-VIDI 171.029 to H.D.M.).



References

- Albrecht, D., Winterflood, C. M., and Ewers, H. (2015). Dual color single particle tracking via nanobodies. *Methods Appl. Fluoresc.* 3, 024001.
- Breckenridge, W. C., Gombos, G., and Morgan, I. G. (1972). The lipid composition of adult rat brain synaptosomal plasma membranes. *Biochim. Biophys. Acta - Biomembr.* 266, 695–707.
- Catsburg, L. A. E., Westra, M., van Schaik, A. M. L., and MacGillavry, H. D. (2022). Dynamics and nanoscale organization of the postsynaptic endocytic zone at excitatory synapses. *Elife* 11.
- Clackson, T., Yang, W., Rozamus, L. W., Hatada, M., Amara, J. F., Rollins, C. T., et al. (1998). Redesigning an FKBP–ligand interface to generate chemical dimerizers with novel specificity. *Proc. Natl. Acad. Sci.* 95, 10437–10442.
- Cotman, C. W., Blank, M. L., Mochl, A., and Snyder, F. (1969). Lipid composition of synaptic plasma membranes isolated from rat brain by zonal centrifugation. *Biochemistry* 8, 4606–4612.
- Danylchuk, D. I., Sezgin, E., Chabert, P., and Klymchenko, A. S. (2020). Redesigning Solvatochromic Probe Laurdan for Imaging Lipid Order Selectively in Cell Plasma Membranes. *Anal. Chem.* 92, 14798–14805.
- Day, C. A., and Kenworthy, A. K. (2015). Functions of cholera toxin B-subunit as a raft cross-linker. *Essays Biochem.* 57, 135–145.
- Dotti, C. G., Esteban, J. A., and Ledesma, M. D. (2014). Lipid dynamics at dendritic spines. *Front. Neuroanat.* 8, 1–11.
- Eggeling, C., Ringemann, C., Medda, R., Schwarzmann, G., Sandhoff, K., Polyakova, S., et al. (2009). Direct observation of the nanoscale dynamics of membrane lipids in a living cell. *Nature* 457, 1159–1162.
- Fujiwara, T. K., Iwasawa, K., Kalay, Z., Tsunoyama, T. A., Watanabe, Y., Umemura, Y. M., et al. (2016). Confined diffusion of transmembrane proteins and lipids induced by the same actin meshwork lining the plasma membrane. *Mol. Biol. Cell* 27, 1101–1119.
- Golan, Y., and Sherman, E. (2017). Resolving mixed mechanisms of protein subdiffusion at the T cell plasma membrane. *Nat. Commun.* 8, 15851.
- Gross, G. G., Junge, J. A., Mora, R. J., Kwon, H.-B., Olson, C. A., Takahashi, T. T., et al. (2013). Recombinant Probes for Visualizing Endogenous Synaptic Proteins in Living Neurons. *Neuron* 78, 971–985.
- Guo, Y., Zou, G., Qi, K., Jin, J., Yao, L., Pan, Y., et al. (2021). Simvastatin impairs hippocampal synaptic plasticity and cognitive function in mice. *Mol. Brain* 14, 41.
- Hammond, A. T., Heberle, F. A., Baumgart, T., Holowka, D., Baird, B., and Feigenson, G. W. (2005). Crosslinking a lipid raft component triggers liquid ordered–liquid disordered phase separation in model plasma membranes. *Proc. Natl. Acad. Sci.* 102, 6320–6325.
- Hering, H., Lin, C., and Sheng, M. (2003). Lipid Rafts in the Maintenance of Synapses, Dendritic Spines, and Surface AMPA Receptor Stability. *J. Neurosci.* 23, 3262–3271.
- Igbavboa, U., Hamilton, J., Kim, H.-Y., Sun, G. Y., and Wood, W. G. (2002). A new role for apolipoprotein E: modulating transport of polyunsaturated phospholipid molecular species in synaptic plasma membranes. *J. Neurochem.* 80, 255–261.
- Johnson, S. A., Stinson, B. M., Go, M. S., Carmona, L. M., Reminick, J. I., Fang, X., et al. (2010). Temperature-dependent phase behavior and protein partitioning in giant plasma membrane vesicles. *Biochim. Biophys. Acta - Biomembr.* 1798, 1427–1435.
- Kapitein, L. C., Yau, K. W., and Hoogenraad, C. C. (2010). “Microtubule Dynamics in Dendritic Spines,” in *Methods in Cell Biology* (Amsterdam, The Netherlands: Elsevier Inc.), 111–132.
- Klymchenko, A. S., and Kreder, R. (2014). Fluorescent Probes for Lipid Rafts: From Model Membranes to Living Cells. *Chem. Biol.* 21, 97–113.
- Kobayashi, T., Storrie, B., Simons, K., and Dotti, C. G. (1992). A functional barrier to movement of lipids in polarized neurons. *Nature* 359, 647–650.
- Korinek, M., Gonzalez-Gonzalez, I. M., Smejkalova, T., Hajdukovic, D., Skrenkova, K., Krusek, J., et al. (2020). Cholesterol modulates presynaptic and postsynaptic properties of excitatory synaptic transmission. *Sci. Rep.* 10, 12651.
- Lenne, P.-F., Wawrzyniec, L., Conchonaud, F., Wurtz, O., Boned, A., Guo, X.-J., et al. (2006). Dynamic molecular confinement in the plasma membrane by microdomains and the cytoskeleton meshwork. *EMBO J.* 25, 3245–3256.
- Leventis, R., and Silviu, J. R. (2001). Use of Cyclodextrins to Monitor Transbilayer Movement and Differential Lipid Affinities of Cholesterol. *Biophys. J.* 81, 2257–2267.
- Lu, H. E., MacGillavry, H. D., Frost, N. A., and Blanpied, T. A. (2014). Multiple Spatial and Kinetic Subpopulations of CaMKII in Spines and Dendrites as Resolved by Single-Molecule Tracking PALM. *J. Neurosci.* 34, 7600–7610.
- Luján, R., Nusser, Z., Roberts, J. D. B., Shigemoto, R., and Somogyi, P. (1996). Perisynaptic Location of Metabotropic Glutamate Receptors mGluR1 and mGluR5 on Dendrites and Dendritic Spines in the Rat Hippocampus. *Eur. J. Neurosci.* 8, 1488–1500.
- MacGillavry, H. D., Song, Y., Raghavachari, S., and Blanpied, T. A. (2013). Nanoscale Scaffolding Domains within the Postsynaptic Density Concentrate Synaptic AMPA Receptors. *Neuron* 78, 615–622.
- Mahammad, S., and Parmryd, I. (2015). “Cholesterol Depletion Using Methyl- β -cyclodextrin,” in *Methods in molecular biology (Clifton, N.J.)* (Humana Press, New York, NY), 91–102.
- Merritt, E. A., Sarfaty, S., Akker, F. Van Den, L’Hoir, C., Martial, J. A., and Hol, W. G. J. (1994). Crystal structure of cholera toxin B-pentamer bound to receptor GM1 pentasaccharide. *Protein Sci.* 3, 166–175.
- Nair, D., Hossy, E., Petersen, J. D., Constals, A., Giannone, G., Choquet, D., et al. (2013). Super-Resolution Imaging Reveals That AMPA Receptors Inside Synapses Are Dynamically Organized in Nanodomains Regulated by PSD95. *J. Neurosci.* 33, 13204–13224.
- Nakada, C., Ritchie, K., Oba, Y., Nakamura, M., Hotta, Y., Iino, R., et al. (2003). Accumulation of anchored proteins forms membrane diffusion barriers during neuronal polarization. *Nat. Cell Biol.* 5, 626–632.
- Niko, Y., Didier, P., Mely, Y., Konishi, G., and Klymchenko, A. S. (2016). Bright and photostable push-pull pyrene dye visualizes lipid order variation between plasma and intracellular membranes. *Sci. Rep.* 6, 18870.
- Nusser, Z., Mulvihill, E., Streit, P., and Somogyi, P. (1994). Subsynaptic segregation of metabotropic and ionotropic glutamate receptors as revealed by immunogold localization. *Neuroscience* 61, 421–427.
- Ohtani, Y., Irie, T., Uekama, K., Fukunaga, K., and Pitha, J. (1989). Differential effects of alpha-, beta- and gamma-cyclodextrins on human erythrocytes. *Eur. J. Biochem.* 186, 17–22.
- Owen, D. M., Rentero, C., Magenau, A., Abu-Siniyah, A., and Gaus, K. (2012). Quantitative imaging of membrane lipid order in cells and organisms. *Nat. Protoc.* 7, 24–35.
- Scheefhals, N., Catsburg, L. A. E., Westerveld, M. L., Blanpied, T. A., Hoogenraad, C. C., and MacGillavry, H. D. (2019). Shank Proteins Couple the Endocytic Zone to the Postsynaptic

- Density to Control Trafficking and Signaling of Metabotropic Glutamate Receptor 5. *Cell Rep.* 29, 258-269.e8.
- Scheefhals, N., Westra, M., and MacGillavry, H. D. (2023). mGluR5 is transiently confined in perisynaptic nanodomains to shape synaptic function. *Nat. Commun.* 14, 244.
- Simons, K., and Ikonen, E. (1997). Functional rafts in cell membranes. *Nature* 387, 569–572.
- Tabatadze, N., Savonenko, A., Song, H., Bandaru, V. V. R., Chu, M., and Haughey, N. J. (2010). Inhibition of neutral sphingomyelinase-2 perturbs brain sphingolipid balance and spatial memory in mice. *J. Neurosci. Res.* 88, 2940–2951.
- Tang, A.-H., Chen, H., Li, T. P., Metzbower, S. R., MacGillavry, H. D., and Blanpied, T. A. (2016). A trans-synaptic nanocolumn aligns neurotransmitter release to receptors. *Nature* 536, 210–214.
- Westra, M., Gutierrez, Y., and MacGillavry, H. D. (2021). Contribution of Membrane Lipids to Postsynaptic Protein Organization. *Front. Synaptic Neurosci.* 13, 7903773.
- Westra, M., and MacGillavry, H. D. (2022). Precise Detection and Visualization of Nanoscale Temporal Confinement in Single-Molecule Tracking Analysis. *Membranes (Basel)*. 12, 650.
- Willems, J., de Jong, A. P. H., Scheefhals, N., Mertens, E., Catsburg, L. A. E., Poorthuis, R. B., et al. (2020). ORANGE: A CRISPR/Cas9-based genome editing toolbox for epitope tagging of endogenous proteins in neurons. *PLOS Biol.* 18, e3000665.
- Winckler, B., Forscher, P., and Mellman, I. (1999). A diffusion barrier maintains distribution of membrane proteins in polarized neurons. *Nature* 397, 698–701.



Supplementary Figure 1. Single-molecule tracking of glutamate receptors after cholesterol depletion

(A) Relative frequency distribution of the $\log D_{\text{eff}}$ of mGluR5 trajectories in control condition and after cholesterol depletion with MBCD. (B) The median $\log D_{\text{eff}}$ split per culture with a different concentration of MBCD: 5 mM or 2 mM. (C) Relative frequency distribution of the $\log D_{\text{eff}}$ of GluA2 trajectories in control condition and after cholesterol depletion with MBCD. (D) The median $\log D_{\text{eff}}$ split per culture with a different concentration of MBCD: 4 mM or 2 mM.

8



General discussion

Manon Westra

The dynamic organization of glutamate receptors within the postsynaptic membrane plays a vital role in both basal synaptic transmission and synaptic plasticity. However, there is still much to be understood about the subsynaptic organization and diffusive behavior of specific glutamate receptor subtypes and the contribution of membrane lipids to the overall organization of the postsynaptic membrane. In this thesis, we aimed to shed more light on these topics.

In **Chapter 2**, we reviewed our current understanding of the role of membrane lipids in the organization of the postsynaptic membrane. In **Chapter 3**, we described a protocol for studying synaptic protein distribution at high resolution using single-molecule localization microscopy (SMLM). In **Chapter 4**, we delved into the analysis of temporal confinement within single-molecule trajectories. In **Chapter 5**, we compared the dynamics and localization of AMPAR subunits GluA1 and GluA3. In **Chapter 6**, we demonstrated that metabotropic glutamate receptor mGluR5 is transiently confined in perisynaptic domains. And in **Chapter 7**, we presented preliminary work on different approaches to investigate both the lipid organization in the postsynaptic membrane and their contribution to protein organization. In this final chapter, we discuss the key findings of this thesis, contextualize them within the current literature, and make recommendations for future studies.

The lateral organization of glutamate receptors in the postsynaptic membrane

For both AMPARs and mGluR5 it has been previously described where they reside relative to the PSD. mGluR5 was found in a perisynaptic ring surrounding the PSD, whereas AMPARs are concentrated in the PSD (Nusser et al., 1994; Luján et al., 1996; Scheefhals and MacGillavry, 2018). It was also shown that AMPARs are enriched in PSD95 nanodomains and are organized in domains themselves (MacGillavry et al., 2013; Nair et al., 2013; Haas et al., 2018; Hruska et al., 2022). However, information on the subsynaptic organization of mGluR5 and the distinct AMPAR subtypes was lacking. With the use of super-resolution imaging, in **Chapters 5** and **6** we reported the organization of mGluR5, GluA1, and GluA3 in subsynaptic domains at the postsynaptic membrane. Thus in addition to the previously described GluA1 nanodomains, GluA3 is also organized in nanodomains and both subunits are enriched inside PSD95 nanodomains, whereas mGluR5 is organized in perisynaptic domains.

The relevance of subsynaptic domains of glutamate receptors became clear from studies that revealed the low affinity of glutamate receptors for glutamate and the brief, local and steep peak of glutamate after release in the synaptic area (Diamond and Jahr, 1997; McAllister and Stevens, 2000; Franks et al., 2003; Raghavachari and Lisman, 2004; Traynelis et al., 2010). During glutamate release, only glutamate receptors in close proximity to the release become activated (Liu et al., 1999; Lisman et al., 2007), therefore the clustered organization is highly beneficial for efficient synaptic transmission. In our studies, we did not investigate the alignment between the detected postsynaptic nanodomains and the presynaptic release site. However, previous studies showed evidence for the existence of this transsynaptic nanocolumn (Tang et al., 2016; Martinez-Sanchez et al., 2021). Furthermore, it has been described that the misalignment of glutamate receptor domains with glutamate release sites decreases synaptic efficiency (Haas et al., 2018; Ramsey et al., 2021).

The organization of AMPARs into subsynaptic domains has been previously established, however in **Chapter 6**, we demonstrate that mGluR5 is also organized in nanodomains



surrounding the PSD. The alignment of AMPARs with the presynaptic release site, as facilitated by their domain organization, is critical for efficient synaptic transmission. However, what would be the relevance of the domain organization of mGluR5? The clustering of mGluR5 into nanodomains may indicate signaling hotspots, potentially facilitating efficient signaling through the clustering of signaling machinery components (Suzuki and Yao, 2013). Multiple nanodomains of mGluR5 around the PSD could also indicate the spatial segregation of distinct signaling pathways initiated by the activation of mGluR5. Future research could investigate the localization of components of mGluR5's downstream signaling pathways and their potential colocalization with mGluR5 nanodomains, which would support the idea of these perisynaptic signalosomes. Furthermore, in addition to mGluR5 nanodomains, the perisynaptic area contains the endocytic zone (EZ), a clathrin-coated structure that is stably associated with the PSD and regulates the trafficking of glutamate receptors, which is crucial for synaptic plasticity (Blanpied et al., 2002; Petrini et al., 2009; Scheefhals et al., 2019; Catsburg et al., 2022). Activated mGluR5 is quickly desensitized and internalized via endocytosis to prevent overstimulation (Dhami and Ferguson, 2006). If nanodomains of mGluR5 are in close proximity to the EZ, their clustering into nanodomains would be an efficient method to rapidly internalize desensitized mGluR5 receptors.

We investigated the subsynaptic organization of AMPAR subtypes GluA1/2 and GluA2/3 by single-molecule imaging of the subunits GluA1 and GluA3. Both of the subunits are organized in nanodomains and enriched in PSD95 nanodomains. However, we do not know if the subunits localize in the same nanodomains. It could be that some PSD95 nanodomains are enriched with GluA1/2 and others with GluA2/3. For future studies, it would be interesting to explore their relative localization and even more interesting, combine that with the localization of PSD95 nanodomains. We did try to perform SMLM for GluA1 and GluA3 at the same time, however, the differences detected in their localization could be mainly ascribed to the dye they were labeled with, because when we switched the dyes the results also shifted. Therefore, it is still important to continue the development of new dyes, tags, and techniques to perform reliable super-resolution imaging of multiple proteins at the same time (Jimenez et al., 2020; Mund and Ries, 2020). Another important consideration is the size of the probe, as this can also be of great influence on the obtained localization results when studying proteins inside the crowded synaptic area (Lelek et al., 2021). We, for instance, noticed that when glutamate receptors were labeled with antibodies, the obtained localizations were less enriched inside the synapse, therefore we performed most experiments with nanobodies.

Although we did not observe differences in the nanodomain characteristics of GluA1 and GluA3, the results from our single-molecule tracking experiments reveal a difference in the diffusion of GluA1 and GluA3, where GluA3 is diffusing significantly slower compared to GluA1. Surface diffusion of AMPARs was found to be critical for hippocampal LTP (Penn et al., 2017). Another study did investigate the diffusion of different AMPAR subunits including GluA3, and concluded that GluA2/3 receptors diffuse faster than GluA1/2 (Kropf et al., 2008). However, they did not investigate the diffusion of single molecules but ensembles of molecules. Furthermore, we investigated the diffusive behavior in more detail and found that GluA3 dwells longer in the PSD area compared to GluA1. We thus picked up some differences between GluA1- and GluA3-containing AMPARs, however, it might be interesting for future studies to be more selective in the size of the spines included in the analysis of lateral organization, because at small spines the lateral organization might be less relevant as glutamate will quickly diffuse through the whole synaptic cleft and activate all

postsynaptic AMPARs. At larger spines, the lateral organization could be of more influence and therefore reveal different patterns of nanodomain organization between the AMPAR subtypes. Furthermore, it was shown before that GluA1 is less mobile inside active synapses compared to GluA1 in neighboring inactive synapses (Ehlers et al., 2007). This might be another interesting classification for future research, to study the dynamic lateral organization of glutamate receptors specifically in active synapses. These studies could result in a clearer picture of the lateral organization of receptors in and around the PSD to learn more about the relevance of synaptic transmission.

A special role for AMPAR subunit GluA3?

We were specifically interested in AMPAR subunit GluA3, as recent studies discovered a special role for this AMPAR subunit. Earlier studies revealed that synaptic currents and plasticity are significantly reduced in the absence of GluA1, but essentially unaffected in the absence of GluA3 (Andrásfalvy et al., 2003; Meng et al., 2003; Lu et al., 2009). And later it was discovered that during basal conditions GluA3-containing receptors almost do not contribute to synaptic currents in the hippocampus (Renner et al., 2017a). However, upon the increase of intracellular cAMP, GluA3 receptors increase their open probability, leading to synaptic potentiation. A similar role for GluA3 in cAMP-dependent plasticity has been described in the cerebellum (Gutierrez-Castellanos et al., 2017). Furthermore, synapses expressing GluA3 were found to have increased susceptibility for $A\beta$ -mediated synapse loss (Reinders et al. 2016).

As the alignment between presynaptic release of neurotransmitters and postsynaptic receptors is of great importance for efficient synaptic transmission, we were wondering if the lateral distribution of GluA3 also contributed to its role in cAMP-mediated potentiation. We hypothesized that GluA3 receptors are not inside the transsynaptically aligned nanodomains and therefore contribute little to nothing to the excitatory currents. Upon the increase of cAMP levels, GluA3 would move from a more homogeneous distribution into the subsynaptic domains. Another option would be that GluA3 was localized in nanodomains that misalign, and by the increase in cAMP, they move towards the aligned nanodomains and contribute to synaptic currents. However, in our experiments, we could not find evidence for such a mechanism. The number and size of the detected nanodomains did not change after increasing cAMP levels. Furthermore, we did not observe any differences in the dynamics of GluA3 receptors, including their subdiffusive behavior like temporal confinement. Important to note that in our experiments we did not specifically test for the last hypothesis, as we did not colocalize the GluA3 enrichment with presynaptic release sites of glutamate. This is an interesting suggestion for future studies.

The only change we observed was the recruitment of both GluA1 and GluA3 to the spines. This is in contrast to the results reported in the previous study (Renner et al., 2017a). In that study, no change in the levels of AMPARs at the spines was observed. This discrepancy could come from the fact that we studied the AMPAR subtypes in dissociated hippocampal cultures, whereas the study by Renner et al. was performed in cultured slices. The increase in AMPARs we detected was significant but minimal and therefore might not have been picked up in the slice cultures. In conclusion, we did not observe any GluA3-specific changes in the dynamic subsynaptic organization after increasing cAMP levels.

A suggestion for future research would be to be more specific in the selection of synapses or AMPAR subtypes when studying subsynaptic organization, as the results we obtained



show large variations. As mentioned before, at small synapses the lateral organization might be of less importance as the release of glutamate would cover the complete PSD, therefore it would be interesting to focus on larger PSDs. Second, we are studying the whole population of GluA3 subunits, however, it might be a smaller population that is bound to specific auxiliary subunits and underwent posttranslational modifications, revealing the importance of different AMPAR subtypes (Diering and Haganir, 2018). By looking at the complete pool of GluA3-containing AMPARs we might overlook subtle but crucial differences in their dynamics and lateral organization. Auxiliary subunits are important for the trafficking of AMPARs and their anchoring within the PSD (Bissen et al., 2019). Recently, it has been shown that the AMPAR subtypes have their own specific interactome, further emphasizing the relevance of different AMPARs (van der Spek et al., 2022). For the GluA1/2 receptors, the most abundant interactors were TARP- γ 8, CNIH-2, and SynDIG4, whereas the GluA2/3 receptors revealed the strongest interaction with TARP- γ 2, CNIH-2, and Noelin1. Lastly, it would be relevant to study the lateral organization in slices as it might be that activity levels in our dissociated hippocampal cultures are too low to pick up the specific effect of GluA3 in cAMP-mediated potentiation. Altogether, more research has to be performed to rule out any effect of lateral organization in the special role of GluA3 in cAMP-mediated potentiation.

Contribution of membrane lipids to protein organization

In the previous sections we mainly discussed proteins and protein-protein interactions in the postsynaptic membrane. However, lipids are the main component of membranes and therefore also contribute to the dynamic organization of glutamate receptors. In **Chapter 2** we reviewed the current literature on how membrane lipids could contribute to postsynaptic protein organization. There is still a lack of understanding of the organization of lipids themselves in neuronal membranes and their contribution to protein organization. To learn more about the diffusive behavior of membrane lipids in the postsynaptic membrane, in **Chapter 7**, we aimed to track fluorescently labeled phospholipids within the membrane. These phospholipids did incorporate into membranes and their diffusion coefficient was higher compared to the diffusion coefficient from proteins tracked in the previous chapters, as expected. Unfortunately, the phospholipids mainly labeled the axons and not so much the soma and dendrites. Therefore it became difficult to study their diffusive behavior in the postsynaptic membrane. On the other hand, a positive outcome was that the labeling was sparse and therefore it was possible to investigate individual neurons. Other studies also used these labeled phospholipids and other lipid types to investigate the diffusion of lipids in cellular membranes (Eggeling et al., 2009; Honigsmann et al., 2014; Komura et al., 2016; Schneider et al., 2017), studying something similar in the neuronal membrane might just be another challenge to overcome. The development of other more suitable lipid probes would be helpful to investigate the dynamic lipid organization in the synaptic membrane. When single-molecule tracking of different lipids within the postsynaptic membrane is possible, we could apply the confinement analysis described in **Chapter 4** on those trajectories. This would give insight into the location of certain confinement hotspots and their location relative to the PSD or glutamate receptors.

The other approach we took in studying the influence of membrane lipids on postsynaptic protein organization was to modify the lipid composition of the membrane. In **Chapter 7**, we depleted cholesterol using methyl- β -cyclodextrin (MBCD). This method has been used in

previous studies and revealed profound effects on the synapse (Hering et al., 2003; Zidovetzki and Levitan, 2007; Choi et al., 2015). Therefore, we were interested in the effect of cholesterol depletion on the diffusive behavior of glutamate receptors. As mentioned earlier, AMPARs have been demonstrated to be captured in the PSD by numerous scaffold molecules, however, as shown in **Chapter 6**, mGluR5 resides in domains in the perisynaptic region surrounding the PSD, which is considerably less protein dense. Although we found that the cytoplasmic tail domain (CTD) of mGluR5 is important for this perisynaptic domain organization, it is not entirely clear yet how the CTD leads to the clustering of mGluR5. Cholesterol was found to be involved in the heterogeneous organization of the membrane by packing lipids into tightly-packed ordered regions. Therefore, we hypothesized that cholesterol could contribute to the perisynaptic domain organization of mGluR5, whereas the effect on AMPARs would be minor. However, as shown in **Chapter 7**, we did not observe any significant effect of cholesterol depletion on the diffusive behavior of both mGluR5 and GluA2. Neither the diffusion coefficient of the receptors changed, nor did their temporal confinement. It has been suggested that by mild depletion of cholesterol, membrane lipids change their membrane organization, preserving the segregation of cholesterol in membrane domains (Ottico et al., 2003). Thus, it could be that the membrane domains were maintained and therefore we did not observe an effect. Furthermore, it might still be that other lipids contribute to the domain organization of mGluR5, which could be a subject of future studies.

Another possibility is to create novel ways for modifying membrane composition with high spatial and temporal control. In **Chapter 7**, we made a start with this approach by studying the endogenous localization of sphingomyelin-modifying enzymes. Sphingomyelin is enriched in synapses, and therefore an interesting candidate to investigate their contribution to synaptic organization (Cotman et al., 1969). Lipid metabolism might be a promising target. If you could manipulate the metabolism of lipids at specific locations, you would have a great tool in hands for future studies into the influence of membrane composition. Among the sphingomyelin-modifying enzymes we found a few candidates that localize inside spines and could be recruited to the PSD. Several methods have been described to move proteins to a specific location by chemically induced dimerization (Clackson et al., 1998; Guntas et al., 2015; Voß et al., 2015; Dang, 2022). One of those methods is also described in **Chapter 6**, where mGluR5 is recruited to the PSD. This could be performed by chemicals but also with the use of light, thereby creating the possibility for reversible dimerization (Sinnen et al., 2017). Interestingly, a recent study developed a method to manipulate sphingolipid biosynthesis with optical control (Kol et al., 2019). Optogenetics would allow for the necessary temporal and spatial control. An intriguing future experiment would be to recruit lipid-modifying enzymes to the PSD while tracking receptors to evaluate the effect on their diffusion. Important control experiments would be to determine whether lipid composition indeed changes like predicted, which might be accomplished by tailored lipidomics investigations that explore distinct neuronal compartments in great detail (Iuliano et al., 2021).

Areas of temporal confinement

Within the synaptic membrane, the organization of receptors into subsynaptic domains can be detected by single-molecule localization microscopy in fixed cells or tissues. Proteins with higher density can be identified and associated with other spatial markers to learn more about their unique localization. However, as previously stated, proteins and lipids are highly dynamic



in the membrane and constantly in motion, exhibiting Brownian, confined, or anomalous diffusion. When studying the static picture of the localization of proteins, we do not obtain information on how long proteins reside in such a nanodomain, how much exchange there is, or on which timescale they move in and out of domains. To answer those kinds of questions, live-cell imaging is indispensable. Using single-molecule tracking we can follow individual molecules and learn more about their subdiffusive behavior. Combined with a spatial marker this can give great insight into their biology. In **Chapter 4**, we focused on the analysis of temporal confinement. Much research before has been investigating the subdiffusive behavior of molecules using different analyses based on distinct parameters (Simson et al., 1995; Meilhac et al., 2006; Renner et al., 2017b; Sikora et al., 2017; Lanois  e et al., 2021). The difficulty with these analyses is setting the parameters. Therefore we studied the parameters of one of the previously described confinement analyses in great detail (Simson et al., 1995). We described that the user-defined parameters can have a great influence on the results of the analysis, thus confinement results should be interpreted with caution.

We were interested in temporal confinement because for that process we know the molecule is mobile; it did move before or after but at some point in its trajectory gets trapped for a while. The molecule could be completely trapped there, but may also resume its route again after some time. These areas of confinement could indicate areas of higher organization, where for example the specific lipid organization is more favorable for the molecule, or certain other proteins bind to the molecule of interest so that it cannot continue its path in a Brownian way. It has been reported before that a relationship exists between lipid rafts and transient confinement zones detected with single-molecule tracking (Dietrich et al., 2002). It would be interesting to map these areas of confinement and thereby learn more about where and how the diffusion of molecules is influenced by other factors. In **Chapter 4** we visualized confinement areas with a heatmap and could thereby correlate this to another cellular spatial marker. In **Chapter 5** we used this feature to investigate the areas of confinement for GluA1 and GluA3 and detected more confinement inside the PSD for GluA3 compared to GluA1. Furthermore, in **Chapter 6** the use of this map revealed transient confinement areas just around the PSD for mGluR5, providing extra evidence for its residence in perisynaptic nanodomains. More research is needed to fully understand the underlying biological mechanisms responsible for those confinement periods. Another remaining question is the timescale of the detected confinement zones. Does it indicate an area that exists for a longer time and represents for example the location of nanodomains like we hypothesized, or is it only a transient zone that disappears as soon as the molecule continues its journey because the membrane is continuously reorganizing? If confinement zones represent areas of higher organization that exist for a slightly longer period, this analysis could be a helpful tool for learning more about the heterogeneity in membrane organization.

Although a wide variety of methods have been published, the research into detecting anomalous diffusion seems to be still in its early stages. Alongside the classical statistical methods mentioned in **Chapter 4**, new methodologies have been proposed that extend beyond the computation of the mean squared displacement or radius of gyration. The advent of machine learning has greatly facilitated these advancements. These new techniques have shown promise in detecting anomalous diffusion in short, irregularly sampled trajectories from single-molecule tracking experiments. Examples include Bayesian inference (Thapa et al., 2018), recurrent neural networks (Bo et al., 2019), and deep neural networks (Kowalek et al., 2019). Currently, there is even an ongoing challenge to objectively evaluate and compare

various methodologies for characterizing anomalous diffusion (Muñoz-Gil et al., 2021). While machine learning-based approaches have demonstrated superior performance to classical statistical models, no one method has emerged as a clear winner. Finally, in addition to their accuracy, a significant challenge is to make these new methods user-friendly and thus more widely available to the scientific community.

Concluding remarks

Over the past several decades, our understanding of membrane organization and its importance for synaptic function has significantly improved. However, there remained a lack of detailed knowledge on the dynamic subsynaptic organization of individual glutamate receptor subtypes and the contribution of membrane lipids to the postsynaptic membrane organization. In this thesis, we utilized super-resolution imaging to gain new insights into the dynamic nanoscale organization of both glutamate receptors and membrane lipids, thereby contributing to our understanding of the architecture of the postsynaptic membrane. While we have made significant progress in this field, there are still challenges to be addressed to obtain a complete and detailed picture of postsynaptic membrane organization. In the coming years, it will be interesting to see how the field of membrane lipid research evolves, particularly with the advancement of techniques for directly investigating lipids within the postsynaptic membrane in conjunction with the investigation of postsynaptic protein organization. The combination of these efforts, coupled with technological advances in microscopy, has the potential to yield significant breakthroughs in this area of research.

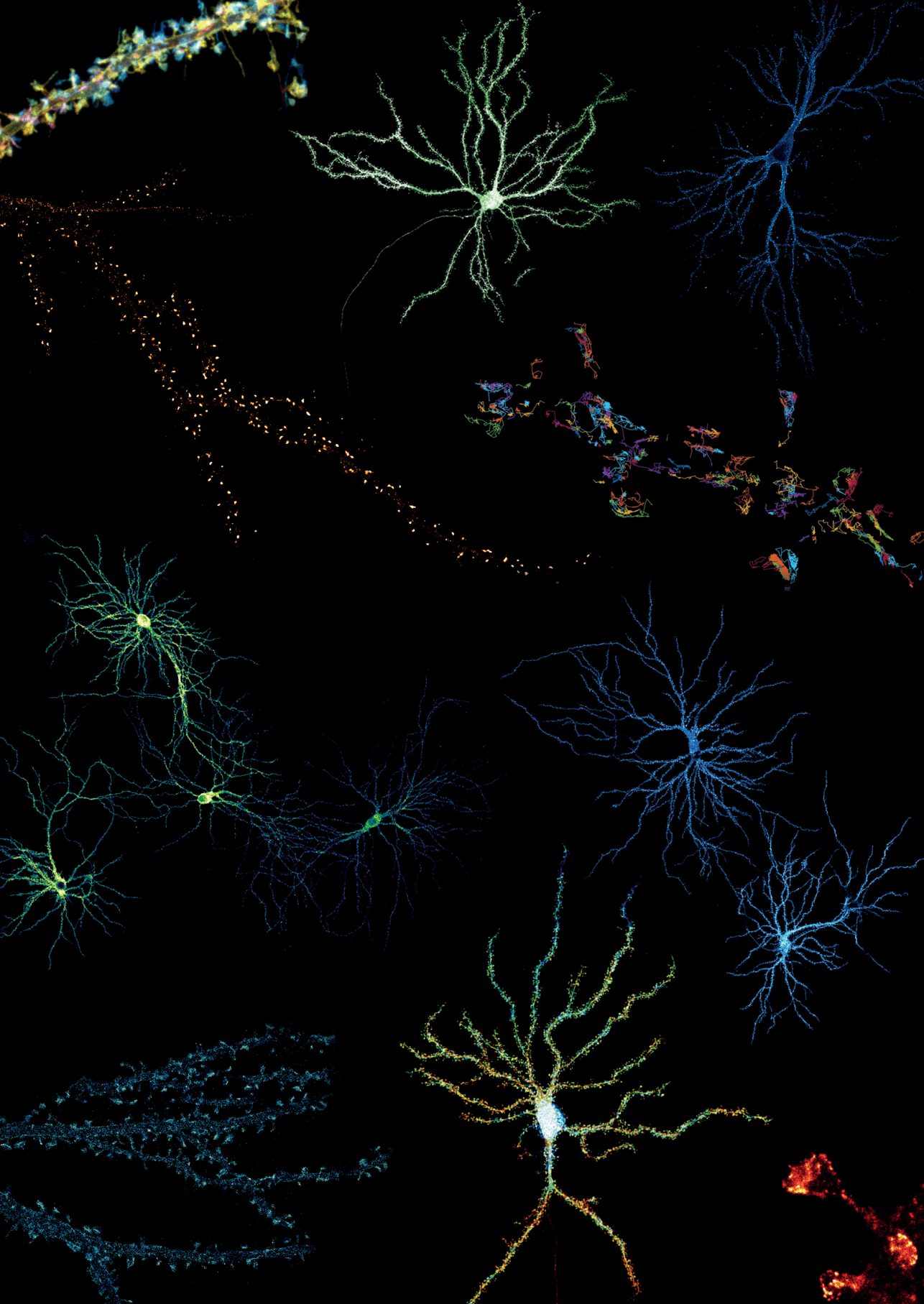


References

- Andrásfalvy, B. K., Smith, M. A., Borchardt, T., Sprengel, R., and Magee, J. C. (2003). Impaired Regulation of Synaptic Strength in Hippocampal Neurons from GluR1-Deficient Mice. *J. Physiol.* 552, 35–45.
- Bissen, D., Foss, F., and Acker-Palmer, A. (2019). AMPA receptors and their minions: auxiliary proteins in AMPA receptor trafficking. *Cell. Mol. Life Sci.* 76, 2133–2169.
- Blanpied, T. A., Scott, D. B., and Ehlers, M. D. (2002). Dynamics and Regulation of Clathrin Coats at Specialized Endocytic Zones of Dendrites and Spines. *Neuron* 36, 435–449.
- Bo, S., Schmidt, F., Eichhorn, R., and Volpe, G. (2019). Measurement of anomalous diffusion using recurrent neural networks. *Phys. Rev. E* 100, 010102.
- Catsburg, L. A. E., Westra, M., van Schaik, A. M. L., and MacGillavry, H. D. (2022). Dynamics and nanoscale organization of the postsynaptic endocytic zone at excitatory synapses. *Elife* 11.
- Choi, T.-Y., Jung, S., Nah, J., Ko, H.-Y., Jo, S.-H., Chung, G., et al. (2015). Low levels of methyl β -cyclodextrin disrupt GluA1-dependent synaptic potentiation but not synaptic depression. *J. Neurochem.* 132, 276–285.
- Clackson, T., Yang, W., Rozamus, L. W., Hatada, M., Amara, J. F., Rollins, C. T., et al. (1998). Redesigning an FKBP–ligand interface to generate chemical dimerizers with novel specificity. *Proc. Natl. Acad. Sci.* 95, 10437–10442.
- Cotman, C. W., Blank, M. L., Mochl, A., and Snyder, F. (1969). Lipid composition of synaptic plasma membranes isolated from rat brain by zonal centrifugation. *Biochemistry* 8, 4606–4612.
- Dang, D. T. (2022). Molecular Approaches to Protein Dimerization: Opportunities for Supramolecular Chemistry. *Front. Chem.* 10, 62.
- Dhami, G. K., and Ferguson, S. S. G. (2006). Regulation of metabotropic glutamate receptor signaling, desensitization and endocytosis. *Pharmacol. Ther.* 111, 260–271.
- Diamond, J. S., and Jahr, C. E. (1997). Transporters Buffer Synaptically Released Glutamate on a Submillisecond Time Scale. *J. Neurosci.* 17, 4672–4687.
- Diering, G. H., and Haganir, R. L. (2018). The AMPA Receptor Code of Synaptic Plasticity. *Neuron* 100, 314–329.
- Dietrich, C., Yang, B., Fujiwara, T., Kusumi, A., and Jacobson, K. (2002). Relationship of Lipid Rafts to Transient Confinement Zones Detected by Single Particle Tracking. *Biophys. J.* 82, 274–284.
- Eggeling, C., Ringemann, C., Medda, R., Schwarzmann, G., Sandhoff, K., Polyakova, S., et al. (2009). Direct observation of the nanoscale dynamics of membrane lipids in a living cell. *Nature* 457, 1159–1162.
- Ehlers, M. D., Heine, M., Groc, L., Lee, M.-C., and Choquet, D. (2007). Diffusional Trapping of GluR1 AMPA Receptors by Input-Specific Synaptic Activity. *Neuron* 54, 447–460.
- Franks, K. M., Stevens, C. F., and Sejnowski, T. J. (2003). Independent Sources of Quantal Variability at Single Glutamatergic Synapses. *J. Neurosci.* 23, 3186–3195.
- Guntas, G., Hallett, R. A., Zimmerman, S. P., Williams, T., Yumerefendi, H., Bear, J. E., et al. (2015). Engineering an improved light-induced dimer (iLID) for controlling the localization and activity of signaling proteins. *Proc. Natl. Acad. Sci.* 112, 112–117.
- Gutierrez-Castellanos, N., Da Silva-Matos, C. M., Zhou, K., Canto, C. B., Renner, M. C., Koene, L. M. C., et al. (2017). Motor Learning Requires Purkinje Cell Synaptic Potentiation through Activation of AMPA-Receptor Subunit GluA3. *Neuron* 93, 409–424.
- Haas, K. T., Compans, B., Letellier, M., Bartol, T. M., Grillo-Bosch, D., Sejnowski, T. J., et al. (2018). Pre-post synaptic alignment through neuregulin-1 tunes synaptic transmission efficiency. *Elife* 7, e31755.
- Hering, H., Lin, C., and Sheng, M. (2003). Lipid Rafts in the Maintenance of Synapses, Dendritic Spines, and Surface AMPA Receptor Stability. *J. Neurosci.* 23, 3262–3271.
- Honigsmann, A., Mueller, V., Ta, H., Schoenle, A., Sezgin, E., Hell, S. W., et al. (2014). Scanning STED-FCS reveals spatiotemporal heterogeneity of lipid interaction in the plasma membrane of living cells. *Nat. Commun.* 5, 5412.
- Hruska, M., Cain, R. E., and Dalva, M. B. (2022). Nanoscale rules governing the organization of glutamate receptors in spine synapses are subunit specific. *Nat. Commun.* 13, 920.
- Iuliano, M., Seeley, C., Sapp, E., Jones, E. L., Martin, C., Li, X., et al. (2021). Disposition of Proteins and Lipids in Synaptic Membrane Compartments Is Altered in Q175/Q7 Huntington’s Disease Mouse Striatum. *Front. Synaptic Neurosci.* 13.
- Jimenez, A., Friedl, K., and Letierrier, C. (2020). About samples, giving examples: Optimized Single Molecule Localization Microscopy. *Methods* 174, 100–114.
- Kol, M., Williams, B., Toombs-Ruane, H., Franquelim, H. G., Korneev, S., Schroer, C., et al. (2019). Optical manipulation of sphingolipid biosynthesis using photoswitchable ceramides. *Elife* 8.
- Komura, N., Suzuki, K. G. N., Ando, H., Konishi, M., Koikeda, M., Imamura, A., et al. (2016). Raft-based interactions of gangliosides with a GPI-anchored receptor. *Nat. Chem. Biol.* 12, 402–410.
- Kowalek, P., Loch-Olszewska, H., and Szwabiński, J. (2019). Classification of diffusion modes in single-particle tracking data: Feature-based versus deep-learning approach. *Phys. Rev. E* 100, 032410.
- Kropf, M., Rey, G., Glauser, L., Kulangara, K., Johnsson, K., and Hirling, H. (2008). Subunit-specific surface mobility of differentially labeled AMPA receptor subunits. *Eur. J. Cell Biol.* 87, 763–778.
- Lanoiselée, Y., Grimes, J., Koszegi, Z., and Calebiro, D. (2021). Detecting Transient Trapping from a Single Trajectory: A Structural Approach. *Entropy* 23, 1044.
- Lelek, M., Gyparaki, M. T., Beliu, G., Schueder, F., Griffié, J., Manley, S., et al. (2021). Single-molecule localization microscopy. *Nat. Rev. Methods Prim.* 1, 39.
- Lisman, J. E., Raghavachari, S., and Tsien, R. W. (2007). The sequence of events that underlie quantal transmission at central glutamatergic synapses. *Nat. Rev. Neurosci.* 8, 597–609.
- Liu, G., Choi, S., and Tsien, R. W. (1999). Variability of Neurotransmitter Concentration and Nonsaturation of Postsynaptic AMPA Receptors at Synapses in Hippocampal Cultures and Slices. *Neuron* 22, 395–409.
- Lu, W., Shi, Y., Jackson, A. C., Bjorgan, K., During, M. J., Sprengel, R., et al. (2009). Subunit Composition of Synaptic AMPA Receptors Revealed by a Single-Cell Genetic Approach. *Neuron* 62, 254–268.
- Luján, R., Nusser, Z., Roberts, J. D. B., Shigemoto, R., and Somogyi, P. (1996). Perisynaptic Location of Metabotropic Glutamate Receptors mGluR1 and mGluR5 on Dendrites and Dendritic Spines in the Rat Hippocampus. *Eur. J. Neurosci.* 8, 1488–1500.
- MacGillavry, H. D., Song, Y., Raghavachari, S., and Blanpied, T. A. (2013). Nanoscale Scaffolding Domains within the Postsynaptic Density Concentrate Synaptic AMPA Receptors. *Neuron* 78, 615–622.

- Martinez-Sanchez, A., Laugks, U., Kochovski, Z., Papantoniou, C., Zinzula, L., Baumeister, W., et al. (2021). Trans-synaptic assemblies link synaptic vesicles and neuroreceptors. *Sci. Adv.* 7, eabef6204.
- McAllister, A. K., and Stevens, C. F. (2000). Nonsaturation of AMPA and NMDA receptors at hippocampal synapses. *Proc. Natl. Acad. Sci.* 97, 6173–6178.
- Meilhac, N., Le Guyader, L., Salomé, L., and Destainville, N. (2006). Detection of confinement and jumps in single-molecule membrane trajectories. *Phys. Rev. E* 73, 011915.
- Meng, Y., Zhang, Y., and Jia, Z. (2003). Synaptic Transmission and Plasticity in the Absence of AMPA Glutamate Receptor GluR2 and GluR3. *Neuron* 39, 163–176.
- Mund, M., and Ries, J. (2020). How good are my data? Reference standards in superresolution microscopy. *Mol. Biol. Cell* 31, 2093–2096.
- Muñoz-Gil, G., Volpe, G., Garcia-March, M. A., Aghion, E., Argun, A., Hong, C. B., et al. (2021). Objective comparison of methods to decode anomalous diffusion. *Nat. Commun.* 12, 6253.
- Nair, D., Hossy, E., Petersen, J. D., Constals, A., Giannone, G., Choquet, D., et al. (2013). Super-Resolution Imaging Reveals That AMPA Receptors Inside Synapses Are Dynamically Organized in Nanodomains Regulated by PSD95. *J. Neurosci.* 33, 13204–13224.
- Nusser, Z., Mulvihill, E., Streit, P., and Somogyi, P. (1994). Subsynaptic segregation of metabotropic and ionotropic glutamate receptors as revealed by immunogold localization. *Neuroscience* 61, 421–427.
- Ottico, E., Prinetti, A., Prioni, S., Giannotta, C., Basso, L., Chigorno, V., et al. (2003). Dynamics of membrane lipid domains in neuronal cells differentiated in culture. *J. Lipid Res.* 44, 2142–2151.
- Penn, A. C., Zhang, C. L., Georges, F., Royer, L., Breillat, C., Hossy, E., et al. (2017). Hippocampal LTP and contextual learning require surface diffusion of AMPA receptors. *Nature* 549, 384–388.
- Petrini, E. M., Lu, J., Cognet, L., Lounis, B., Ehlers, M. D., and Choquet, D. (2009). Endocytic Trafficking and Recycling Maintain a Pool of Mobile Surface AMPA Receptors Required for Synaptic Potentiation. *Neuron* 63, 92–105.
- Raghavachari, S., and Lisman, J. E. (2004). Properties of Quantal Transmission at CA1 Synapses. *J. Neurophysiol.* 92, 2456–2467.
- Ramsey, A. M., Tang, A.-H., LeGates, T. A., Gou, X.-Z., Carbone, B. E., Thompson, S. M., et al. (2021). Subsynaptic positioning of AMPARs by LRRTM2 controls synaptic strength. *Sci. Adv.* 7, eabf3126.
- Renner, M. C., Albers, E. H., Gutierrez-Castellanos, N., Reinders, N. R., van Huijstee, A. N., Xiong, H., et al. (2017a). Synaptic plasticity through activation of GluA3-containing AMPA-receptors. *Elife* 6, e25462.
- Renner, M., Wang, L., Levi, S., Hennekinne, L., and Triller, A. (2017b). A Simple and Powerful Analysis of Lateral Subdiffusion Using Single Particle Tracking. *Biophys. J.* 113, 2452–2463.
- Scheefhals, N., Catsburg, L. A. E., Westerveld, M. L., Blanpied, T. A., Hoogenraad, C. C., and MacGillavry, H. D. (2019). Shank Proteins Couple the Endocytic Zone to the Postsynaptic Density to Control Trafficking and Signaling of Metabotropic Glutamate Receptor 5. *Cell Rep.* 29, 258–269.e8.
- Scheefhals, N., and MacGillavry, H. D. (2018). Functional organization of postsynaptic glutamate receptors. *Mol. Cell. Neurosci.* 91, 82–94.
- Schneider, F., Wäithe, D., Clausen, M. P., Galiani, S., Koller, T., Ozhan, G., et al. (2017). Diffusion of lipids and GPI-anchored proteins in actin-free plasma membrane vesicles measured by STED-FCS. *Mol. Biol. Cell* 28, 1507–1518.
- Sikora, G., Wyłomańska, A., Gajda, J., Solć, L., Akin, E. J., Tamkun, M. M., et al. (2017). Elucidating distinct ion channel populations on the surface of hippocampal neurons via single-particle tracking recurrence analysis. *Phys. Rev. E* 96, 062404.
- Simson, R., Sheets, E. D., and Jacobson, K. (1995). Detection of temporary lateral confinement of membrane proteins using single-particle tracking analysis. *Biophys. J.* 69, 989–993.
- Sinnen, B. L., Bowen, A. B., Forte, J. S., Hiester, B. G., Crosby, K. C., Gibson, E. S., et al. (2017). Optogenetic Control of Synaptic Composition and Function. *Neuron* 93, 646–660.e5.
- Suzuki, T., and Yao, W.-D. (2013). Molecular and structural bases for postsynaptic signal processing: interaction between postsynaptic density and postsynaptic membrane rafts. *J. Neurorestoratology* 2, 1.
- Tang, A.-H., Chen, H., Li, T. P., Metzbower, S. R., MacGillavry, H. D., and Blanpied, T. A. (2016). A trans-synaptic nanocolumn aligns neurotransmitter release to receptors. *Nature* 536, 210–214.
- Thapa, S., Lomholt, M. A., Krog, J., Cherstvy, A. G., and Metzler, R. (2018). Bayesian analysis of single-particle tracking data using the nested-sampling algorithm: maximum-likelihood model selection applied to stochastic-diffusivity data. *Phys. Chem. Chem. Phys.* 20, 29018–29037.
- Traynelis, S. F., Wollmuth, L. P., McBain, C. J., Menniti, F. S., Vance, K. M., Ogden, K. K., et al. (2010). Glutamate Receptor Ion Channels: Structure, Regulation, and Function. *Pharmacol. Rev.* 62, 405–496.
- van der Spek, S. J. F., Pandya, N. J., Koopmans, F., Paliukhovich, I., van der Schors, R. C., Otten, M., et al. (2022). Expression and Interaction Proteomics of GluA1- and GluA3-Subunit-Containing AMPARs Reveal Distinct Protein Composition. *Cells* 11, 3648.
- Voß, S., Klever, L., and Wu, Y.-W. (2015). Chemically induced dimerization: reversible and spatiotemporal control of protein function in cells. *Curr. Opin. Chem. Biol.* 28, 194–201.
- Zidovetzki, R., and Levitan, I. (2007). Use of cyclodextrins to manipulate plasma membrane cholesterol content: Evidence, misconceptions and control strategies. *Biochim. Biophys. Acta - Biomembr.* 1768, 1311–1324.







Addendum

Nederlandse samenvatting

Curriculum vitae

List of publications

Dankwoord

Nederlandse samenvatting

Het menselijk brein is een fascinerend orgaan dat bestaat uit een complex netwerk van miljarden zenuwcellen, neuronen genaamd. Neuronen zijn opgebouwd uit meerdere uitlopers, waarvan het axon verantwoordelijk is voor signaaltransmissie, terwijl de dendrieten fungeren als signaalontvangers. De synaps, het punt waarop het axon van een neuron in nauw contact komt met de dendriet van een ander neuron, faciliteert de communicatie tussen neuronen. Elk neuron kan honderden tot duizenden van dergelijke contactpunten maken met verschillende andere neuronen. Neurotransmitters worden gebruikt om signalen over te brengen van het ene neuron naar het andere. Ze worden vrijgegeven door het presynaptische neuron en binden aan specifieke receptoren op het synaptische membraan van het postsynaptische neuron, waardoor de activiteit van het ontvangende neuron gestimuleerd of geremd kan worden. Glutamaat, een van de meest voorkomende stimulerende neurotransmitters, bindt aan glutamaat receptoren op het postsynaptische membraan. Echter, alleen glutamaatreceptoren die zich recht tegenover de locatie van neurotransmittervrijgave bevinden, worden geactiveerd vanwege hun lage affiniteit voor glutamaat. Dit benadrukt het belang van de organisatie van het postsynaptische membraan voor efficiënte signaaloverdracht en dus de functionaliteit van de hersenen. Het postsynaptische membraan bestaat uit transmembraan glutamaatreceptoren en synaptische eiwitcomplexen die zijn ingebed in een diversiteit aan lipiden. Desalniettemin is er weinig bekend over de subsynaptische organisatie van individuele glutamaatreceptor-subtypen en de dynamiek van synaptische membraanlipiden, en hun bijdrage aan synaptische transmissie. Het doel van het onderzoek beschreven in dit proefschrift is dan ook om een dieper inzicht te verkrijgen in de dynamische organisatie van verschillende glutamaatreceptor-subtypen en membraanlipiden, en hun rol in de complexe architectuur van het postsynaptische membraan.

Hoofdstuk 2 biedt een overzicht van de bestaande kennis omtrent de invloed van membraansamenstelling op de eiwitorganisatie in de postsynaps, evenals de uitdagingen die dit onderzoeksveld met zich meebrengt. Het membraan bestaat uit een diversiteit van honderden lipiden met unieke biofysische eigenschappen. Het wordt verondersteld dat de heterogene organisatie van deze lipiden invloed heeft op de subsynaptische organisatie van glutamaatreceptoren en daarmee op de synaptische functie. Om de membraanorganisatie te onderzoeken, maken we gebruik van geavanceerde superresolutie microscopietechnieken, waarmee we op nanometerschaal de distributie en dynamiek van eiwitten en lipiden kunnen visualiseren. Deze superresolutie microscopie is essentieel, aangezien conventionele microscopietechnieken niet voldoende resolutie bieden om de specifieke verdeling van individuele eiwitten en lipiden binnen de synaps (met een diameter van ongeveer 1 micrometer) zichtbaar te maken. In **hoofdstuk 3** presenteren we een protocol om microscopie met lokalisatie van individuele moleculen uit te voeren, waarbij we voorbeelden laten zien van de subsynaptische lokalisatie van diverse synaptische eiwitten. Vervolgens richten we ons op de dynamiek van lipiden en eiwitten binnen het synaptische membraan. Met behulp van de eerdergenoemde superresolutie microscopietechniek kunnen we ook individuele moleculen in levende cellen in de tijd volgen. Op deze manier kunnen we de beweging van deze moleculen traceren en hun diffusie analyseren. In **hoofdstuk 4** concentreren we ons specifiek op periodes van langere immobilisatie van moleculen binnen hun bewegingstraject, wat kan wijzen op gebieden met een complexere organisatie. Hoewel er al verschillende analysemethoden bestaan om dit gedrag



te beschrijven, zijn deze vaak afhankelijk van meerdere parameters die kunnen variëren per experiment. Daarom hebben we door middel van gesimuleerde bewegingen van moleculen de invloed van verschillende parameters en hun effect op de resultaten onderzocht, om zo de parameters te optimaliseren voor diverse experimentele omstandigheden.

Met de gereedschappen uit de vorige hoofdstukken kunnen we vervolgens aan de slag met de biologische vraagstukken van dit proefschrift. In **hoofdstuk 5** wordt de focus gelegd op een specifieke glutamaatreceptor, namelijk de AMPA-receptor (AMPA), in het bijzonder de GluA3-bevattende AMPAR. AMPARs bevinden zich hoofdzakelijk in het centrum van het postsynaptische membraan, binnen de postsynaptische dichtheid (PSD), een geconcentreerd netwerk van eiwitten dat onder andere AMPARs verankert. Het wordt verondersteld dat het toevoegen en verwijderen van AMPARs in het synaptische membraan, evenals hun subsynaptische positionering, een belangrijke rol spelen in het reguleren van langdurige veranderingen in de sterkte van synaptische verbindingen (synaptische plasticiteit), die geassocieerd zijn met leren en geheugen. De specifieke rol van de GluA3-bevattende receptor is tot op heden beperkt onderzocht, omdat deze voorheen als marginaal werd beschouwd. Recent onderzoek heeft echter aangetoond dat GluA3 een specifieke rol zou kunnen spelen bij bepaalde vormen van synaptische plasticiteit en hersengerelateerde aandoeningen. Daarom hebben we met behulp van superresolutie microscopie de distributie en dynamiek van dit AMPAR-subtype onderzocht in vergelijking met GluA1-bevattende AMPARs. We tonen aan dat beide AMPAR-subtypen georganiseerd zijn in nanodomeinen en verrijkt zijn in de subsynaptische domeinen van het postsynaptisch verbindingseiwit PSD95.

Hoofdstuk 6 richt zich op metabotrope glutamaatreceptor mGluR5, waarvan de activatie leidt tot langdurige postsynaptische veranderingen door een cascade van intracellulaire gebeurtenissen. mGluR5 bevindt zich in een circulaire zone rondom de PSD, maar de precieze regulatie en de specifieke reden voor de aanwezigheid op deze locatie waren onbekend. Met behulp van superresolutie microscopietechnieken hebben we zowel de distributie als de dynamiek van deze receptor in het postsynaptische gebied onderzocht. We laten zien dat mGluR5 georganiseerd is in nanodomeinen net buiten de PSD, en we beschrijven het specifieke domein van de receptor dat verantwoordelijk is voor deze perisynaptische lokalisatie.

In **hoofdstuk 7** beschrijven we de verschillende methoden om de dynamische lipidenorganisatie in het postsynaptische membraan te bestuderen. Eén benadering betrof het direct labelen van lipiden en het analyseren van hun diffusiegedrag en distributiepatronen. Door gebruik te maken van superresolutie microscopie in levende cellen, tonen we aan dat het mogelijk is om het diffusiegedrag van verschillende membraancomponenten, waaronder fosfolipiden, te bestuderen. De andere benadering betrof het veranderen van de lipidenamenstelling van het membraan en het bestuderen van het effect daarvan op de organisatie van receptoren binnen het postsynaptische membraan. Door cholesterol te verwijderen uit het membraan, konden we onder andere met behulp van zogenaamde omgevingsgevoelige markers veranderingen in de ordening van het neuronale membraan waarnemen.

Samenvattend heeft het onderzoek in dit proefschrift geleid tot nieuwe inzichten in de dynamische nanoschaal-organisatie van zowel glutamaatreceptoren als membraanlipiden. De verworven fundamentele kennis draagt bij aan ons begrip van de architectuur van het postsynaptische membraan en de invloed daarvan op de functionaliteit van het brein.

Curriculum vitae

Manon Westra was born on the 10th of February, 1994 in Amstelveen and grew up in Uithoorn. In 2012 she finished her secondary education (Gymnasium, Alkwin Kollege, Uithoorn). Because of her interest in biology, especially the brain, she decided to study Biomedical Sciences at VU University in Amsterdam that same year. Her interest in the brain grew during the minor Biomolecular & Neurosciences. In 2015, she finalized her education with an internship in the lab of dr. Ronald van Kesteren at the Center for Neurogenomics and Cognitive Research, studying the role of perineuronal nets and PV+ interneurons in memory impairments in an Alzheimer's disease model and obtained her Bachelor's degree cum laude. Manon continued her education that same year with the research master Neurosciences at VU University, where she pursued the Fundamental Neurosciences track. During this two-year Master's program she performed her first internship in the group of Linda Douw at the department Anatomy & Neurosciences of the VUmc, studying the relationship between network topology and molecular characteristics in brain tumor patients. She then performed her second internship in the lab of dr. Harold MacGillavry at Utrecht University, studying the dynamic subsynaptic distribution of AMPAR subunits. In 2017, she finalized her Master's education with a literature review under the supervision of dr. Wiep Scheper on the propagation of protein aggregates in the progression of neurodegenerative diseases. Driven by her interest in the brain's fundamental working mechanisms, Manon started her PhD research at the end of 2017 in the lab of dr. Harold MacGillavry at the department of Cell Biology, Neurobiology and Biophysics of Utrecht University, the results of which are presented in this dissertation.

List of publications

Scheefhals, N., Westra, M., & MacGillavry, H. D. (2023). mGluR5 is transiently confined in perisynaptic nanodomains to shape synaptic function. *Nature Communications*, 14(1), 244.

Westra, M., & MacGillavry, H. D. (2022). Precise Detection and Visualization of Nanoscale Temporal Confinement in Single-Molecule Tracking Analysis. *Membranes*, 12(7), 650.

Willems, J.*, Westra, M.*, & MacGillavry, H. D. (2022). Single-Molecule Localization Microscopy of Subcellular Protein Distribution in Neurons. *Methods in Molecular Biology* (Clifton, N.J.), 2440, 271–288.

Catsburg, L. A., Westra, M., van Schaik, A. M., & MacGillavry, H. D. (2022). Dynamics and nanoscale organization of the postsynaptic endocytic zone at excitatory synapses. *eLife*, 11, e74387.

Westra, M.*, Gutierrez, Y.*, & MacGillavry, H. D. (2021). Contribution of Membrane Lipids to Postsynaptic Protein Organization. *Frontiers in Synaptic Neuroscience*, 13, 790773.

* Authors contributed equally

Dankwoord

Dat was het dan... De mensen die mij de afgelopen maanden gesproken hebben, weten vast dat schrijven niet mijn favoriete bezigheid was, maar ik kan dit traject natuurlijk niet afsluiten zonder een aantal mensen te bedanken. Zonder jullie was ik niet zo ver gekomen! Dus — omdat een spraakbericht inbouwen in dit boekje iets te ingewikkeld is — nog een paar geschreven woorden van mijn kant.

Allereerst wil ik Harold bedanken, in 2016 kwam je college geven tijdens mijn studie en toen wist ik, dat is wat ik wil doen, superresolutie microscopie op synapsen. Ik vroeg of het mogelijk was om stage te lopen op de afdeling en zo opende de wereld van AMPA-receptoren en superresolutie microscopie zich voor mij. Wat fijn dat ik daarna ook mocht beginnen aan mijn PhD onderzoek in jouw lab. Bedankt voor je enthousiasme altijd, als ik nog duizend dingen zag die beter moesten voordat ik een echte conclusie kon geven, liet jij me altijd inzien dat ik ook blij moest zijn met wat ik al had. Ik mis nu toch wel die momenten dat er, zonder dat ik het door heb, iemand op mijn scherm meekijkt en opeens op jouw typische manier ‘Wow!’ zegt vanwege een mooi resultaat. Ook bedankt dat jij me vrijliet om verder door te gaan met dingen waar ik voldoening uit haalde, en me dus de kans gaf om lekker te wroeten in MATLAB-analyses. Ik wens je heel veel succes met je lab en ben benieuwd naar alle mooie resultaten die er nog gaan komen! Lukas, bedankt voor je kritische blik en de feedback de afgelopen jaren. Zeker tijdens mijn stage en het begin van mijn PhD toen we als labs nog vaak gezamenlijke meetings hadden, heb ik op wetenschappelijk gebied veel van je geleerd. Ik heb bewondering voor jouw enthousiasme over wetenschap en je innovatieve ideeën. Verder wil ik de leden van mijn beoordelings- en promotiecommissie bedanken voor het beoordelen van mijn proefschrift en verdediging, Bela Mulder, Anna Akhmanova, Helmut Kessels, Elly Hol, Madelon Maurice en Anne-Sophie Hafner.

Dear paranymphs, so happy that you will be next to me on this special day! Lieve Lisa, bedankt voor alle gezellige jaren en vooral ook alle wandelingetjes door het ‘prachtige’ park Transwijk tijdens de corona periode en daarna. Dat heeft me zeker door die periode heen gesleept. Fijn om met iemand de leuke dingen maar ook zeker de struggles van het PhD bestaan te bespreken. Verder heb ik zo gelachen om alle songteksten op bekende nummers die je me elke keer stuurde over ons leven als PhD-student. Dit resulteerde uiteindelijk natuurlijk in ‘The Lab Girls’ met het schitterende nummer ‘Wannabe a Lab Girl’. Het Cell paper waar we over zongen is er niet gekomen, maar wat een lol hebben we gehad en het heeft wel een award opgeleverd! Dear Yolanda, you’re such a sweet and caring person. I’m still amazed by the lab escape game you made for me on my birthday, it was such a nice surprise. Thanks for all the support and sweet cards throughout the years, they were invaluable to me! And what a relief it was to finally have someone to talk about lipids with, I didn’t have to feel alone anymore on my lipid island :) Really enjoyed working with you on the lipid review, couldn’t have done it without you!

The lovely Maclab, I enjoyed working with you the past few years so much! We really were a nice group together with our fun lab quizzes, dinners, and the lab poems are also still a



highlight! I learned a lot from all of you, in and outside the lab. It was difficult for me to say goodbye to such an amazing group of people. Nicky, in 2017 werd jij zomaar met deze stagestudent opgezadeld, bedankt voor alles wat je me toen geleerd hebt en de fijne samenwerkingen daarna. Het mGluR5 hoofdstuk in dit boekje is daar natuurlijk het hoogtepunt van, heerlijke discussies hebben we gehad over hoe de verschillende soorten tracks nou het beste geassocieerd konden worden. Ik heb al die jaren veel gehad aan jouw adviezen en doelgerichte feedback. En ik wil zeker niet jouw bijdrage aan de sfeer in het lab vergeten te benoemen, jij kwam vaak met ideeën voor leuke activiteiten en dat heeft een hele positieve invloed gehad op hoe ik mijn tijd op de afdeling heb beleefd! Jelmer, volgens mij heb ik met jou toch de langste periode op kantoor gezeten, na wat verhuizingen kwamen we op het einde toch weer in hetzelfde kantoor terecht. Wat heb ik genoten van onze lange discussies over o.a. MATLAB-scripts en hoe we die toch weer iets sneller konden maken, maar zeker ook van alle verhalen over je hardloop- en fietsavonturen. Fijn dat ik altijd op jou kon rekenen als er iets leuks als een borrel of PhD activiteit te doen was. Maar ook bedankt dat ik je altijd alle lab dingen kon vragen als ik bijvoorbeeld weer eens niet wist hoe ik moest beginnen met kloneren omdat het alweer zo lang geleden was. Anna, my office mate from the beginning in the abandoned west wing. I enjoyed all the fun talks in the office about the most random topics, and probably a lot about the Nanoimager ;) I do miss the Polish chocolate a lot actually... Thanks for all your honest feedback and sharing your thoughts when I was planning new experiments. I admire your passion for science and your perseverance! I wish you all the best in Bristol! Wouter, mijn 'buddy' tijdens de corona periode. Wat ben jij heerlijk ambitieus, volgens mij zou jij het liefst honderd projecten tegelijkertijd doen. Er staat jou nog een mooie carrière te wachten! Arthur, de meester in het verzinnen van acroniemen, ook met jou heb ik aardig wat tijd op kantoor doorgebracht en kon ik altijd nuttige en eerlijke feedback van jou verwachten. Jij weet altijd de juiste vragen te stellen om iemand echt even goed na te laten denken over zijn/haar verhaal. Niels, wij hadden sowieso altijd een gespreksonderwerp, GluA3 natuurlijk. Thanks voor al je feedback en het meedenken over dat project. Zehra, you started just after I left, but I want to wish you all the best for your PhD! Dear Maclab people, I wish you all the very best in your future careers and will follow your paths! It was a fun ride!

And of course, there are and were many more people in the lab that helped me during my experiments and/or made my time in the lab a lot more fun. Robbelien, Carlijn, Klara en Lotte, ooit begonnen we tijdens een pub quiz als team neurotische neurdo's en gelukkig kon ik tijdens mijn hele PhD op jullie rekenen voor een goed gesprek en een hoop gezelligheid. Lieve Robbelien, we leerden elkaar kennen tijdens stage en begonnen daarna gelukkig allebei onze PhD op dezelfde afdeling. Bedankt voor je oprechte interesse, de fijne gesprekken en je eindeloze support, waardeer ik echt enorm! Zo fijn ook af en toe ons klaagwandelingetje rond de Botanische Tuinen, dan was alle frustratie er weer even uit. En zeker bedankt voor al je InDesign tips! Carlijn, zo leuk dat ik jou nu nog steeds vaak zie tijdens een wandelingetje in de buurt, we zijn er bijna! Klara, de gesprekken met jou richting het einde van ons contract waren heel behulpzaam en ik wil je ook heel erg bedanken dat ik jou als ervaringsdeskundige alles kon vragen over het afronden van mijn PhD. Wendy, na onze stage was er even een pauze, maar toen je terugkwam, was het alsof je nooit was weggeweest, zo gezellig. Wat ben jij heerlijk eerlijk, heb vertrouwen in je eigen kunnen! Daphne, ook jou ken ik al sinds stage en ik was blij dat we weer samen op een kantoor terecht kwamen. Bedankt voor het organiseren van de leuke PhD activiteiten ook op afstand tijdens de corona tijd (sorry nog voor de zoi

in je keuken tijdens de pizzaworkshop haha). En ondanks dat de lab outing voorbereidingen na een geslaagde 70's party in de prullenbak konden door corona, hebben we samen met Joyce toch nog een leuke online pub quiz en escaperoom georganiseerd, bedankt allebei voor die leuke afleiding rondom het werk. Thanks to my other five office mates in the past few years, Snježana, Anna and Albert, the best of luck for your PhD projects. Wilco, zo fijn dat jij eigenlijk overal een antwoord op weet of het nou over labzaken of politiek gaat, en Marijn, bedankt voor de hulp met het starten van de confinement simulaties. Ik weet nog hoe je zo enthousiast was over de color mapping in de tracks, het concept zit er zeker nog in, met iets andere kleurtjes :) Mithila, our Dutch chats during covid times were definitely a fun distraction in the evening. Malina en Emma, ik heb ook genoten van jullie aanwezigheid, van het maken van PFA tot de leuke door jullie georganiseerde activiteiten tijdens de lockdown. En dat jullie mij enthousiast mee bleven trekken naar alle IB-activiteiten ook al was ik al weg van de afdeling. Feline en Jessica, door jullie ging ik elke donderdagochtend veel te vroeg mijn bed uit voor een yoga sessie bij Olympos, maar als ik er eenmaal was, was het toch een fijne start van de dag. Phebe en Bart jullie zijn in meerdere opzichten onmisbaar voor de afdeling. Phebe, ik heb heel veel waardering voor hoe jij altijd je best doet om een zo goed mogelijke sfeer op het lab te creëren door het organiseren van allerlei activiteiten. Bart, zo fijn dat ik tijdens al die lunches mijn film en serie kennis wat heb kunnen bijspijkeren. Ilya and Eugene, thank you so much for all the help with the microscopes in the department. Esther en Lena, bedankt voor het organiseren van alle IB-activiteiten! Maya, bedankt voor je hulp bij mijn experimenten met die o zo lastige lipiden. Dennis, Anne, Roderick, Sybren, Robin, Chiung-Yi and Peter Jan, thanks for the fun wine & cheese evenings, board games, bowling and canoeing activities. It was nice to not discuss work for a while and to do fun things with colleagues, I have always really appreciated that the atmosphere was so good! A big thank you to all the members of the neuron culture team during my years in the department. You made it possible to do all my experiments and were thus invaluable for my research. And thanks to all other members and previous members of the department that I enjoyed lunches, borrels, IB evenings, retreats, conferences, and good discussions with: Dipti, Lilian, Corette, Martin, Frederik, Amélie, Florian, René, Bart, Max, Jey, Boris, Cyntha, Hugo, Derk, Liu, Noortje, Giel, Josiah, Fangrui, Chun Hei, Ha, Mai Dan, Nazmiye, Milena, Katerina, Cátia, Dieudonée, Jian, Yujie, Xingxiu, York, Ate, Inês, Desiree, Saishree, Funso, Eitan and Babet.

En dan zijn er naast collega's gelukkig nog veel lieve mensen die mij vanaf de zijlijn hebben bijgestaan de afgelopen jaren.

Lieve Willemijn, Michelle, Diana, Tara, Marianne en Tiffany, oftewel de world-famous Alkwinpaaldanseresjes. Bedankt voor al jullie gezelligheid! De weekendjes weg, jaarlijkse (kerst) hightea's, escaperooms en spelletjesavonden waren altijd een fijne afleiding tussen het werk door. Ik ben heel blij met jullie! Ook al bestond de eerste zin van een abstract al voor het grootste deel uit woorden die voor jullie abracadabra waren, jullie juichten het hardst met me mee als er een paper gepubliceerd was! Willemijn, bedankt voor al onze fijne gesprekken, ik waardeer onze etentjes, veel te luide thuis karaoke sessies of juist het oplossen van een ingewikkelde online escaperoom enorm. Michelle, zo leuk dat jij nu ook een PhD bent gaan doen, we wisselden elkaar mooi af, fijn dat we daar ook onze ervaringen over kunnen uitwisselen! Je doet het super goed en mag echt heel erg trots op jezelf zijn hoe je het allemaal doet!



Lieve opa en oma's, bedankt voor jullie interesse altijd. Ook al is het een ver van jullie bed show dat wetenschappelijk onderzoek, en bleef ik in jullie ogen de eeuwige student, jullie probeerden toch altijd te begrijpen waar ik mee bezig was en leefden enorm mee. Oma die vroeg: "Maar wat ben je dan nu, hoe kan ik nou aan anderen vertellen wat je doet?" En opa en oma die rustig gingen luisteren toen ik mijn literature review probeerde uit te leggen en altijd wat lieten weten als er iets over de hersenen op tv was. Wat fijn dat jullie er ook bij kunnen zijn op deze speciale dag.

Lieve familie, ooms, tantes, neven en nichten, jullie ook bedankt voor jullie interesse en de pogingen om te begrijpen waar ik mee bezig was. Ik kan me nog een gesprek over een poster die ik voor een congres had gemaakt, herinneren, waarbij de conclusie van een van jullie uiteindelijk was: "Oh dus veel nanodomeinen is goed, ik denk dat ik veel van die nanodomeinen in mijn hersenen heb."

Lieve Robin, niet meer zo klein broertje van me, bedankt dat ik je altijd kan bellen als ik even mijn verhaal kwijt moet. Ik ben zo trots op wat je allemaal al bereikt hebt! En je hebt stiekem toch ook best een bijdrage aan het lab geleverd door mij al je kennis over git door te spelen en mij te enthousiasmeren om meer te doen met programmeren.

Lieve papa en mama, ik kan jullie niet in een paar woorden bedanken, dus ik hoop dat ik jullie genoeg laat voelen hoe belangrijk jullie voor me zijn en hoe dankbaar ik ben. Jullie hebben mij altijd de vrijheid gegeven om volledig mijn eigen pad te kiezen en me daarbij vervolgens altijd ondersteunt. Ik kan altijd bij jullie terecht als ik het even niet meer weet. Bedankt voor al jullie liefde!

Manon



